Patient-specific computational haemodynamics in the arteriovenous fistula and aorta of a chronic kidney disease cohort

George Hyde-Linaker

Supervisor: Dr. A. Kazakidi

Department of Biomedical Engineering
University of Strathclyde

This dissertation is submitted for the degree of
Doctor of Philosophy

January 2024

I would like to dedicate this thesis to my family and all those close to me throughout my studies. Thank you all very much for all your support.

Declaration

I hereby declare that except where specific reference is made to the work of others, the contents of this thesis are original and have not been submitted in whole or in part for consideration for any other degree or qualification in this, or any other university. This thesis is my own work and contains nothing which is the outcome of work done in collaboration with others, except as specified in the text and Acknowledgements.

George Hyde-Linaker
January 2024

Acknowledgements

I would like to acknowledge my supervisors, Dr. A Kazakidi and Dr. R Black, in addition to the other members of my research group Scott Black, Lauren Johnston, Maria Boumpouli, and Ioanna Syntouka. I would also like to thank Pauline Hall Barrientos (Imaging Centre of Excellence, Glasgow), Sokratis Stoumpos, and David Brian Kingsmore (Renal and Transplant Unit, Queen Elizabeth University Hospital, Glasgow), for providing the image data, without which this research would not have been possible. Additionally, Siemens Digital Industries is thanked for providing licenses of Simcenter AMEsim and Simcenter STAR-CCM+, which were used for completing the simulations within this research.

This work is supported in part from the University of Strathclyde International Strategic Partner (ISP) Research Studentships, and the European Union's Horizon 2020 research and innovation programme under the Marie Sklodowska-Curie grant agreement No 749185. I would like to thank Vittoria Flamini (New York University) for being a key partner in this research for receiving the ISP funding.

Abstract

End-stage renal disease (ESRD) patients require renal replacement therapy (RRT) for filtering wastes and excess fluids from blood, often due to kidney transplant waiting times. Haemodialysis, the most common RRT, requires a vascular access for an efficient and repeatable procedure. An arteriovenous fistula (AVF) is widely considered the 'gold-standard' vascular access. However, AVFs suffer from poor patency rates, and their non-maturation is a key issue in failing cases. Localised haemodynamics and flow patterns are hypothesised to be prevalent factors behind AVF success. In addition to this, the impact of AVF creation on other parts of the haemodynamic network requires further elucidation. For example, the presence of an AVF is known to increase cardiac load and alter resistances in the vascular network.

CFD enables a robust investigation into haemodynamic metrics that are not easily measurable in-vivo, such as wall shear stress (WSS) and oscillatory shear index (OSI). CFD can therefore play a vital role in the pre-operative planning of AVFs, in addition to the post-surgical assessment. Despite the breadth of AVF research that has utilised CFD, there is still no clear consensus on the mechanisms of AVF failure that result in fistula re-intervention or abandonment. Neointimal hyperplasia, the gradual loss of luminal patency due to the thickening of the vascular wall, and inadequate outward remodelling, an insufficient increase in venous diameter and elasticity, are the two major mechanisms behind AVF failure.

Considering the highly patient-specific nature of AVF, vascular access guidelines have proposed a patient-centred care approach for determining an AVF site and morphology. Evaluating the localised haemodynamics in such patient-specific anatomy requires the acquisition and segmentation of high-quality images, a traditional blocker in this research area due to the contraindicating nature of historic contrast agents in the ESRD community.

In this research, high-quality images from ferumoxytol-enhanced magnetic resonance angiography (FeMRA) were segmented for a cohort of chronic kidney disease (CKD) patients. These segmentations were then subsequently used for three CFD investigations, which is the first time FeMRA and CFD have been coupled together.

The principal aims of this research were to i) investigate the influence of a successful AVF on a patient's proximal haemodynamics, ii) replicate haemodynamics within a cohort of patient-specific AVF vessels to examine the impact of several metrics on future outcomes, and iii) to examine the haemodynamic differences in the subclavian arteries between successful and unsuccessful AVF cases within a cohort. The novelty in this research is four-fold, i) the segmentation and dataset registration workflow used for generating a patient-specific model (from aorta to AVF), ii) the use of computational fluid dynamics (CFD) for investigating proximal haemodynamics to an AVF, iii) the use of ferumoxytol as the contrast agent for generating patient-specific 3D vasculature models for a set of juxta-anastomosis CFD simulations, and iv) aortic haemodynamic CFD investigations in an ESRD cohort with AVFs.

The investigations of this research demonstrated that i) the changes in vascular resistances induced from the creation of the AVF were found to markedly increase the WSS in the proximal vasculature of a 19-year-old patient with a radiocephalic AVF (Chapter 3), ii) the influence of cross-sectional juxta-anastomosis vessel characteristics (notably the feeding artery curvature) are the most prominent factor in determining AVF future success (Chapter 4), and iii) the WSS in the subclavian artery of the arm used for the AVF is 3-4 times higher than the opposite subclavian artery (Chapter 5).

Having demonstrated the feasibility of generating patient-specific anatomy (using FeMRA) for CFD analysis, the future possibilities of research area are greatly increased. It is proposed that segmenting the AVF of several more cohorts can contribute to a repository/library of reference AVF models with haemodynamic analysis. Additionally, segmentation of further cohorts can open the doors to statistical shape modelling (SSM). Completing the workflow within this research for multiple cohorts, or by implementing SSM for the generation of multiple patient-specific derived anatomies of successful and unsuccessful AVF anatomies, can improve pre-surgical planning, as the surgeon can have a library of prior AVF in-silico trials to refer to.

Table of contents

List of figures **12**

List of tables **21**

Nomenclature **23**

1 Introduction **25**
- 1.1 Background . . . 25
- 1.2 Thesis aim and overview . . . 27
  - 1.2.1 Research questions and Aim . . . 27
  - 1.2.2 Overview . . . 28
- 1.3 Resulting publications . . . 28
  - 1.3.1 Journal Submissions . . . 29
  - 1.3.2 Conference Presentations . . . 29
- 1.4 COVID-19 Impact Statement . . . 30

2 Literature review **31**
- 2.1 Clinical background . . . 31
  - 2.1.1 Chronic kidney disease and renal replacement therapies . . . 31
  - 2.1.2 Haemodialysis and vascular access . . . 34
- 2.2 Arteriovenous fistulae . . . 36
  - 2.2.1 AVF development . . . 37
  - 2.2.2 AVF complications . . . 39
- 2.3 AVF imaging protocols and model generation methods . . . 46
  - 2.3.1 Vascular imaging for AVF creation . . . 46
  - 2.3.2 Image-based model generation . . . 48
  - 2.3.3 State of the art for AVF model generation for CFD . . . 50
- 2.4 State of the art for AVF CFD investigations . . . 50
  - 2.4.1 The credibility of computational modelling through verification and validation . . . 50

2.4.2 Rheology 51
2.4.3 CFD studies 52
2.4.4 Fluid-structure interaction investigations and wall models 54
2.4.5 Haemodynamic parameters 55
2.4.6 Systematic reviews and non-CFD studies 55
2.5 Gaps in the current literature 56

3 Proposed workflow for investigating the proximal haemodynamics to an AVF 57
3.1 Introduction 57
3.2 Materials and Methods 59
3.2.1 Ferumoxytol-enhanced Magnetic Resonance Angiography 60
3.2.2 Generation of computational domain 61
3.2.3 Validation of segmentation approach 62
3.2.4 Hybrid mesh generation 64
3.2.5 Numerical modelling 65
3.2.6 Boundary conditions 67
3.3 Results 68
3.3.1 Pre- and post-fistula geometry characterisation 68
3.3.2 Aorta-to-radial artery haemodynamics 69
3.3.3 Localised haemodynamics at the AVF anastomosis 75
3.4 Discussion 77
3.4.1 Limitations 78
3.4.2 Comparisons to prior work 79
3.4.3 Clinical relevance 80
3.4.4 Conclusions and further work 82

4 Investigating juxta-anastomosis haemodynamics related to AVF success and failure in 6-week post-AVF geometries: a pilot study 83
4.1 Introduction 83
4.2 Materials and methods 84
4.2.1 Ferumoxytol-enhanced magnetic resonance angiography (FeMRA) 85
4.2.2 Conversion of FeMRA images data to three-dimensional computational models 86
4.2.3 Model details and haemodynamic metrics 89
4.2.4 Haemodynamic parameter defintions 90
4.2.5 ROC analysis 91
4.3 Results 92
4.3.1 Vessel characteristics and flow waveforms 92

4.3.2 Biometric factors 101
4.3.3 CFD analyses 105
4.4 Discussion 111
4.4.1 Novelty and contribution to knowledge 111
4.4.2 Influence of biometric, vessel, and haemodynamics variations on AVF performance 112
4.4.3 Clinical relevance and limitations 113
4.4.4 Limitations 114
4.4.5 Future work 115

5 Computational aortic haemodynamics in relation to the influence of AVF on CVD risk 116
5.1 Introduction 116
5.2 Materials and methodologies 118
5.2.1 Extraction of phase contrast data and boundary conditions 118
5.3 Flow-splitting methodology 120
5.4 Model details and haemodynamic metrics 124
5.4.1 Modelling details 124
5.4.2 CFD post-processing 125
5.5 Results 125
5.6 Discussion and conclusions 142
5.6.1 Novelty and contribution 142
5.6.2 Limitations 144
5.6.3 Clinical relevance 144
5.6.4 Conclusions and further work 145

6 Discussion 148
6.1 Key results, novelty, and contribution 148
6.1.1 Key results 148
6.2 Workflows and limitations 150
6.2.1 Limitations 150
6.2.2 Verification and validation 151
6.2.3 Computational resource 152
6.3 Discussion related to the investigations within this research 153
6.3.1 Computational haemodynamic conclusions 153
6.4 Future outlook of AVF computational haemodynamics for clinical AVF generation 155
6.4.1 Summary of current state of AVFs 155

6.4.2 AVFs in in-silico trials 155
6.4.3 Simulation of AVF in current and future research 156

References **160**

Appendix A Materials and methods pertaining to all investigation chapters **185**
A.1 Ferumoxytol-enhanced MRA (FeMRA) 185
A.2 Segmentation and model generation 186
A.2.1 Segmentation and reconstruction 186
A.2.2 Intra-software segmentation validation 189
A.2.3 Iterative smoothing and remeshing 190
A.3 Geometry characterisation 190
A.4 Computational fluids modelling theory 191
A.4.1 Fundamental laws and governing equations 191
A.4.2 Numerical solutions of fluid flow 193
A.4.3 Turbulence and transition 197
A.4.4 Wall treatment 199
A.5 Mesh generation pipeline 200
A.5.1 Surface mesh import and region assignment 200
A.5.2 Mesh element composition 201
A.5.3 Meshing parameters and validation 202
A.5.4 Grid convergence 203
A.6 Boundary conditions 205
A.7 Haemodynamic parameter defintions 205
A.8 Volume renderings of DICOM data 206
A.9 Turbulence model comparison 207

Appendix B Supplementary material for Chapter 3 **211**
B.1 Wall shear stress estimation at inlet computation 211
B.2 Calculation of initial prism layer height 212
B.3 Grid convergence calculation equations 212
B.4 Mesh base size validation 213
B.5 Calculated physiological flow-splits using the ‘splitting method’ 216
B.6 Windkessel model information 217
B.6.1 Windkessel models 220
B.7 Calculated windkessel values in proximal-to-fistula study 223
B.8 Phase-contrast waveforms assigned to draining vessels in the post-AVF case 225
B.9 Non-Newtonian Blood model 226
B.10 Scale-resolving hybrid model 226

B.11 Resource required for the workflow 227
B.12 Boolean methodologies implemented within Meshmixer 227

Appendix C Supplementary material for Chapter 4 231
C.1 Boundary conditions 231
C.2 Mesh independence analysis 233
C.3 Interpolation of data using polynomials for ROC analysis: Separate excluded data 234
C.4 Code used for ROC analysis 237
C.5 Vessel diameter and velocity waveforms applied at the computational domain patches 239
C.6 AVF contour plots not presented in main body of thesis 242
C.7 Further details of cohort in Chapter 4 244

Appendix D Supplementary material for Chapter 5 245
D.1 Boundary conditions 245
  D.1.1 Prescribed flow-splits 245
D.2 Mesh independence analysis 246
D.3 Velocity streamline figures 246
D.4 Pressure figures 254

List of figures

2.1 The structure of the kidney and nephron (National Institute of Diabetes and Digestive and Kidney Diseases, National Institutes of Health) [1]. . . 32
2.2 Prognosis of Chronic Kidney Disease by Glomerular Filtration Rate and Albuminuria Categories [2, 3], where: Green: low risk (if no other markers of kidney disease, no chronic kidney disease [CKD]); Yellow: moderately increased risk; Orange: high risk; Red, very high risk. 33
2.3 Schematic diagram of haemodialysis procedure [4]. 34
2.4 Vascular access options for haemodialysis: Central venous catheter (CVC), Arteriovenous fistula (AVF), and Arteriovenous graft (AVG) [5]. 35
2.5 The differing AVF classifications: radiocephalic (left), brachiocephalic (centre), and brachiobasilic (right) [6]. 37
2.6 The differing AVF anastomoses [7]. Where A is side-to-side, B is end-to-end, C is artery side to vein end, and D is artery end to vein side. 37
2.7 The 3 stages of extracellular matrix (ECM) changes. These phases are referred to as the Early, Transition, and Late phase. [8]. 39
2.8 Visual explanation of patency rates. Primary patency is the intervention-free access survival. Assisted primary patency is the thrombosis-free access survival. Secondary patency ends when the access is abandoned [9]. 40
2.9 Different modalities of the vascular remodelling response after fistula creation [10]. Where favourable outward remodelling is exhibited in the left image, outward remodelling and intimal hyperplasia is shown centre, and unfavourable intimal hyperplasia without sufficient outward remodelling is shown in the right image. 43
2.10 The stages of AVF maturation, where early or late failure can occur pre- or post- AVF maturation [11]. 44
2.11 ASME V & V 40 workflow [12]. 51

3.1 Simplified schematic of the vessels and boundary conditions of the computational domains used in the pre- and post-AVF simulations, where the solid line represents the common vessels in both domains and the dashed line represents vessels only in the post-AVF simulation. Three-element Windkessel models were used for the majority of outlets (in both simulations), the only exceptions being the cephalic vein and radial artery in the post-AVF simulation (which used prescribed outflows). The inlet velocity waveforms are displayed in the inset (where the blue waveform is the pre-AVF inlet, and the red waveform is the post-AVF inlet). 60

3.2 Framework used for the segmentation, reconstruction, geometry unification and volume extraction of the patient-specific geometry based on ferumoxytol-enhanced magnetic resonance angiography (FeMRA) multi-stack images and subsequent CFD analysis. 61

3.3 Pre- (blue) and post-AVF (red) domains and centerlines of the 19-year-old radicephalic fistula case studied. 62

3.4 Simvascular (blue) and ITK-SNAP (pink) segmentations of the aorta used for computing the DICE score intra-software segmentation validation. . . 63

3.5 Simvascular (blue) and ITK-SNAP (pink) segmentations of the AVF used for computing the DICE score intra-software segmentation validation. . . 64

3.6 Pre- (blue) and post-AVF (red) centreline characteristics, where (a) and (b) show inscribed vessel diameter and centreline curvature from the aortic inlet to the radial artery, and (c) shows the curvature, diameter, and torsion box plots of the centerline from the ascending aorta (AscA) to descending aorta (DSA) and left radial artery (LRA) outlets. 70

3.7 Change in inscribed vessel diameter (normal to vessel centrelines) near the AVF with respect to the distance along the domain centreline from the feeding (radial) artery (starting from 195mm proximal to the anastomosis) to the draining vessels. 71

3.8 (a) Velocity streamlines pre- and post-AVF at peak systole (where arrows represent flow direction), (b) flow rate waveforms in the vasculature at (α, α') the left subclavian, (β, β') brachial, and (γ, γ') radial arteries pre- and post-AVF creation. 72

3.9 Box and whisker plots of the Re_{max} values at the outlets of the simulated vasculature induced over the analysed (5th) cardiac cycle in the common simulated vasculature between the pre- and post-AVF cases. The Remean values are denoted with a straight line within each box. 73

3.10 Comparison between the patient-specific phase-contrast FeMRA-obtained volumetric flow rate at the radial (feeding) artery (red dot dash line) and the flow waveform generated computationally in the radial artery (red dash line). The radial artery was assessed at location δ as shown at the inset of Fig. 3.8a. The cephalic vein (blue dot dash line) prescribed waveform at the venous outlet is also presented. 73
3.11 (a) Normalised TAWSS and (b) OSI contour plots prior-to (top) and after (bottom) fistula creation. 75
3.12 (a-c) Velocity streamlines and flow directions (arrows) in the radiocephalic fistula anastomosis at (a) T1 (peak systole), (b) T2 (mid-deceleration), and (c) T3 (peak diastole). (d) Normalised TAWSS, (e) OSI. 77

4.1 The workflow utilised in this study, from image acquisition to CFD modelling. Where FA: Feeding artery; DV: Draining vein; DA: Distal artery. . 85
4.2 Example AVF vessel segmentation using ITK-SNAP, A) The process of applying the ‘snake-evolution’ tool in the 2D view, where the blue region represents the excluded greyscale values, B) Evolving segmentations using the tool, C) Manual segmentation at the AVF anastomosis, D) Resulting segmentation with gaussian smoothing in ITK-SNAP. 87
4.3 AVF surface file example prior to (left) and following (right) iterative remeshing and smoothing operations with OpenFlipper. 88
4.4 Example of subdivided AVF computational domain (FA: Feeding artery; DV: Draining vein; DA: Distal artery). The number assigned to each 1cm segment corresponds to its distance from the anastomosis, i.e. DA1, FA1, DV1 are the 1cm-segments nearest to the anastomosis, DA2, FA2, DV2 are the second-nearest 1cm-segments to the anastomosis and so on. The final segment of each vessel is not a region analysed (DA4, FA6, DV9). The arrows indicate the direction of blood flow for each artery/vein. . . . 89
4.5 The cohort of AVF anatomies studied within Chapter 4. 93
4.6 Mean feeding artery (FA) and draining vein (DV) flow-rate (Q_{FA} and Q_{DV}) waveform of each sub-group (defined by success and morphology), normalised with respect to time. A further breakdown of the case-by-case flow waveforms and inscribed diameters (in addition to centerline curvature and torsion) are given in Appendix C.5. 94

4.7 The inscribed diameters along the centrelines of the plotted in sub-groups (defined by success and morphology). Where distance = 0 is the centrepoint of the anastomosis (the centreline intersection point of the anastomosis vessel centrelines), blue lines represent the draining vein, red lines represent the feeding artery, and orange lines represent the draining artery. A further breakdown of the case-by-case flow waveforms and inscribed diameters (in addition to centerline curvature and torsion) are given in Appendix C.5. 95

4.8 AVF venous outflows of the cohort (classified by venous outflow flowrate). Where flowrates in excess of 1000ml/min are considered high, flowrates between 600-1000ml/min are considered medium, and flowrates below 600ml/min are considered low. 99

4.9 ROC curves for vessel curvature, diameter, patient characteristics, and anastomosis angle using original datasets (n=17). The binary classification between ‘successful’ and ‘unsuccessful’ cases was a venous flow rate greater than or equal to $1000 ml/min$. 100

4.10 ROC curves for Feeding artery curvature, Feeding artery diameter, Draining vein diameter, and the combined ROC curve of the three aforementioned metrics using original datasets (n=17). The binary classification between ‘successful’ and ‘unsuccessful’ cases was a venous flow rate greater than or equal to $1000 ml/min$. 101

4.11 Biometric graphs: Venous (outflow) flow rates against biometric factors measured on the same day as scan. 103

4.12 Biometric graphs: Venous flow rates against biometric factors (2). (top row) Feeding artery mean flow rate and outflow flow rate vs age, (middle row) cannulation length vs vein depth and venous flow rate vs cannulation length, and (bottom row) venous flow rate against vein depth and feeding artery flow rate. 104

4.13 Peak-systole flow (LNH and Velocity Magnitude) and WSS (TAWSS and WSSG) contour plots for the successful brachio-basilic fistulae (BBF) sub-group of the cohort (n=17). 105

4.14 Peak-systole flow (LNH and Velocity Magnitude) and WSS (TAWSS and WSSG) contour plots for the successful brachio-cephalic fistulae (BCF) sub-group of the cohort (n=17). 106

4.15 Peak-systole flow (LNH and Velocity Magnitude) and WSS (TAWSS and WSSG) contour plots for the unsuccessful brachio-cephalic fistulae (BCF) sub-group of the cohort (n=17). 106

4.16 Peak-systole flow (LNH and Velocity Magnitude) and WSS (TAWSS and WSSG) contour plots for the successful radio-cephalic fistulae (RCF) sub-group of the cohort (n=17). 107
4.17 Peak-systole flow (LNH and Velocity Magnitude) and WSS (TAWSS and WSSG) contour plots for the unsuccessful radiocephalic fistulae (RCF) sub-group of the cohort (n=17). 108
4.19 Mean radial velocity and LNH (and error bars (right)) for each sub-group at 1cm cross-sectional plane intervals (n=17). Note that the segments presented follow the segments along the centreline from the feeding artery and draining vein. 109
4.18 Mean WSS metrics (and error bars (right)) for each sub-group at 1cm segments for the computational AVF domains (n=17). Note that the segments presented follow the segments along the centreline from the feeding artery and draining vein. 110

5.1 Schematic of computational domain of the vasculature (red) studied within the investigation of this chapter. Where Asc A is the ascending aorta, DA is the descending aorta, RSA is the right subclavian artery, RVA is the right vertebral artery, RCC is the right common carotid artery, LCC is the left common carotid artery, LVA is the left vertebral artery, and LSA is the left subclavian artery. 119
5.2 Inlet (ascending aorta) waveforms for each patient within the cohort studied in Chapter 5. Each waveform was calculated using patient-specific cardiac output values. 120
5.3 Flow chart used for assigning the flow split percentages for the boundary conditions of the geometries in this Chapter. 122
5.4 Flow rate in each AVF-arm subclavian against cardiac output for each case studied in Chapter 5. Each case is plotted according to the sub-group. . . 123
5.5 Flow split percentage in each AVF-arm subclavian against cardiac output for each case studied in Chapter 5. Each case is plotted according to the sub-group. 123
5.6 Configuring the arbitrary probe derived parts for each case (example shown is case #6). Where lilac shaded regions represent the clipped .stl files used for defining the subclavian artery regions, and the blue points represent the points of the arbitrary probes generated. 125
5.7 TAWSS, OSI and transWSS contour plots plotted on the wall of each computational for subject IDs 6, 18, and 34. 126

5.8 TAWSS, OSI and transWSS contour plotted on the wall of each computational for subject IDs 40, 44, and 45. 127
5.9 TAWSS, OSI and transWSS contour plotted on the wall of each computational for subject IDs 48, 51, and 57. 128
5.10 TAWSS, OSI and transWSS contour plotted on the wall of each computational for subject IDs 60, 61, and 64. 129
5.11 TAWSS, OSI and transWSS contour plotted on the wall of each computational for subject IDs 65, 67, and 69. 130
5.12 TAWSS, OSI and transWSS contour plotted on the wall of each computational for subject IDs 71, 72, and 74. 131
5.13 TAWSS, OSI and transWSS contour plotted on the wall of each computational for subject IDs 77, 79, and 80. 132
5.14 TAWSS, OSI and transWSS contour plotted on the wall of each computational for subject IDs 87, 94, and 96. 133
5.15 Mean TAWSS, OSI, and transWSS metrics in the subclavian artery (in AVF-arm) plotted against cardiac output measured and prescribed at the ascending aorta (inlet). 136
5.16 Mean TAWSS, OSI, and transWSS metrics in the subclavian artery (in AVF-arm) plotted against mean flowrate within the AVF-arm subclavian artery. 137
5.17 Box plots of the ratio of WSS and OSI metrics (Table 5.2) between the subclavian arteries of the AVF and non-AVF arms. 140
5.18 Mean WSS and OSI metrics in the AVF-arm subclavian sub-groups within the cohort. 141

6.1 Example figure of the quantity of cases generated in an in-silico trial workflow when considering multiple boundary condition, blood model, and FSI model approaches. 156

A.1 Computation of the DICE score. Where the DICE score is equal to 2 × the number of intersecting voxels divided by the sum of the voxels in both segmentations 190
A.2 Centreline generated in VMTKlab, where the green point represents the inlet seed point, and the red point represents the outlet seed points. The example shown is case 60 in Chapter 4. 191
A.3 Example volume renderings (in Osirix, www.osirix-viewer.com) of vessels of interest within chest (left), upper arm (middle), and lower arm (right) DICOM stack obtained using FeMRA. 206

A.4 Comparison of maximum velocity magnitude observed using laminar and Scale-resolving hybrid turbulence model in 19-year-old RCF case studied in Chapter 3. 208
A.5 Velocity streamline contour plots at A) Peak systole, B) Mid deceleration, C) Peak diastole, and D) Mid-late diastole using laminar and Scale-resolving hybrid turbulence model in 19-year-old RCF case studied in Chapter 3. 209
A.6 Normalised TAWSS contour plots generated using laminar and Scale-resolving hybrid turbulence model in 19-year-old RCF case studied in Chapter 3. 210

B.1 Parabolic flow profile between two plates. 212
B.2 Wall Y+, Taylor Mirco scale, and Kolmogorov length scale of the pre-AVF geometry. 214
B.3 Mesh configuration for the post-AVF simulation, where (A) shows the mesh density in the aortic region and at the ascending aorta inlet patch (red), (B) shows the mesh density at the cephalic vein outlet (orange), and (C) shows the mesh density at the anastomosis. 215
B.4 Example of increasing mesh density using base size characteristics of the mesh. 216
B.5 Flow-splitting methodology example using daughter vessel bifurcation workflows. 216
B.6 Bounds for φ and λ that satisfy the estimation of windkessel parameters methodology documented in Alastruey Arimon (2006). 219
B.7 Implementation of windkessel model in Simcenter Amesim. 222
B.8 Pressure waveforms over cardiac cycles for cylindrical tube simulation for validating windkessel discretisation in Simcenter Amesim and STAR-CCM+222
B.9 Normalised pressure figure at peak-systole for (a) pre- and (b) post-AVF case, where normalised pressure is calculated through dividing pressure by half of the fluid density ($\frac{P}{0.5\rho}$). 224
B.10 Annotated post-AVF geometry, where AscaA - Ascending aorta, DescA - Descending aorta, RSA - Right subclavian artey, RCC - Right common carotid, RVA - Right vertebral artery, LCC - Left common carotid, LVA - Left vertebral artery, LSA - Left subclavian artery, DBA - Deep brachial artery, BA - Brachial artery, RA - Radial artery, IA - Interosseous artey, UA - Ulnar artery, CV - Cephalic vein, γ' is the feeding artery phase-contrast scan location. 225

B.11 Phase-contrast waveforms ascertained through FeMRA scanning, in addition to flow obtained through CFD simulation at feeding artery cross section (γ' in Fig. B8) 226
B.12 Positioning of segmentations for constructing the computational domain. Where the blue labels represent the locations for positioning the upper arm segmentation towards the chest segmentation, and the red label represent the locations for positioning the lower arm segmentation towards the upper arm segmentation. Positions 1 and 2 represent common points between the segmentations of the daughter bifurcations, whereas position A represents a position where the angle of the parent bifurcation is changed so that the segmentations align. 229
B.13 The boolean process for generating the surface of the computational domain. Where (A) shows the position of the segmentations, (B) shows the combined segmentation following manual 'clean up' of segmentation, (Ci-iii) shows the boolean process of unifying multiple segmentation surface into a singular computational domain. 230

C.1 Phase contrast waveforms extracted at the point of the AVF vessels (example of case 6 shown). 232
C.2 Flow waveform profile example from the PC-MRI using FeMRA. 232
C.3 Mesh independence study completed for the BBF and BCF sub-groups. Demonstrated on test case (subject 69). 233
C.4 Mesh independence study completed for the RCF sub-groups. Demonstrated on test case (subject 87). 234
C.5 Low-flow polynomials fitted to the low-flow (<1000ml/min) datapoints . . 235
C.6 High-flow polynomials fitted to the high-flow (>1000ml/min) datapoints . 236
C.7 Interpolated vs Original dataset datapoints 237
C.8 ROC code used for vessel curvature, diameter, patient characteristics, and anastomosis angle. Note: Lines included which are commented out during running the code for various characteristics. 238
C.9 Vessel diameter and velocity waveforms and computational domain patches (for cases 6-44) 239
C.10 Vessel diameter and velocity waveforms and computational domain patches (for cases 45-65) 240
C.11 Vessel diameter and velocity waveforms and computational domain patches(for cases 69-79) 241
C.12 Vessel diameter and velocity waveforms and computational domain patches(for cases 80-87) 242

C.13 OSI contour plots for AVFs for subjects 6-64. 242
C.14 OSI contour plots for AVFs for subjects 65-87. 243

D.1 Mesh independence study for Chapter 5, demonstrated on the test case (subject 65). 246
D.2 Velocity magnitude streamline contour plots for peak systole (left), mid-deceleration (centre), and peak diastole (right) for datasets 6-34. 247
D.3 Velocity magnitude streamline contour plots for peak systole (left), mid-deceleration (centre), and peak diastole (right) for datasets 40-45. 248
D.4 Velocity magnitude streamline contour plots for peak systole (left), mid-deceleration (centre), and peak diastole (right) for datasets 48-57. 249
D.5 Velocity magnitude streamline contour plots for peak systole (left), mid-deceleration (centre), and peak diastole (right) for datasets 60-64. 250
D.6 Velocity magnitude streamline contour plots for peak systole (left), mid-deceleration (centre), and peak diastole (right) for datasets 65-69. 251
D.7 Velocity magnitude streamline contour plots for peak systole (left), mid-deceleration (centre), and peak diastole (right) for datasets 71-74. 252
D.8 Velocity magnitude streamline contour plots for peak systole (left), mid-deceleration (centre), and peak diastole (right) for datasets 77-80. 253
D.9 Velocity magnitude streamline contour plots for peak systole (left), mid-deceleration (centre), and peak diastole (right) for datasets 87-96. 254
D.10 Normalised pressure contour plot at peak systole for datasets 6-45. 255
D.11 Normalised pressure contour plot at peak systole for datasets 48-64. . . . 256
D.12 Normalised pressure contour plot at peak systole for datasets 65-74. . . . 257
D.13 Normalised pressure contour plot at peak systole for datasets 77-96. . . . 258

List of tables

2.1 Description of CKD severity 32

3.1 DICE score validation check 63

4.1 Subject population used for the current study (M: Male; F: Female; L: Left arm; R: Right arm; BCF: Brachiochephalic Fistula; RCF: Radiocephalic Fistula; BBF: Brachiobasilic fistula; S: Successful AVF outcome; U: Unsuccessful AVF outcome). 86

4.2 Subject population centreline characteristics (where **mean** feeding artery and draining vein characteristics were evaluated up to 10cm along centreline length, and draining artery characteristics were evaluated up to 5cm along centreline length). Where FA is feeding artery, DV is draining vein, DA is draining artery, S is successful, U is unsuccessful, and D is inscribed diameter. 96

4.3 Classification of venous flowrates for the cohort used in the ROC analysis of the AVF. Where a flowrate greater or equal to 1000 ml/min is considered high (H), a flowrate between 600-1000ml/min is considered medium-low (M-L), and a flowrate less than 600 ml/min is considered low. 98

4.4 Area under curve (AUC) values of ROC curves presented in 4.9-4.10 . . . 99

5.1 The CKD cohort classification of inlet (cardiac output) information and the calculated flow splits for each case. 121

5.2 Pearson correlation coefficient (r) for WSS metrics in the subclavian artery of each subgroup (presented in Fig. 5.16). 135

5.3 Mean flow rate, TAWSS, OSI, and transWSS metrics induced in the subclavian artery of the arm proximal to the AVF. 138

5.4 Ratio of mean flow rate, TAWSS, transWSS, WSSG, and OSI metrics induced in the subclavian artery of the arm proximal to the AVF compared to the values induced in the subclavian artery of the non-AVF arm. 139

A.1 FeMRA imaging details 186
A.2 Mesh characteristics consistent between different cases. 203
A.3 Percentage difference between the maximum velocity induced through computational domain using laminar and scale-resolving hybrid turbulence model 207

B.1 Values used for the initial hybrid mesh generation 212
B.2 Maximum length scale values ascertained from a steady-state RANS simulation using the mesh calculated from performing GCI calculations. . . . 214
B.3 Calculated physiological flow-splits for the pre-AVF case 217
B.4 Calculated Windkessel values for proximal-to-fistula case 224
B.5 Time required for completing the workflow 228

C.1 Area under curve (AUC) of ROC curves using raw and interpolated data. . 235
C.2 Cohort information referred to in Chapter 4 and presented within Figs. 4.11-4.12. 244

Nomenclature

Acronyms / Abbreviations

μ	Blood viscosity
ρ	Blood density
AVF	Arteriovenous fistula
AVG	Arteriovenous graft
BBF	Brachio-Basalic Fistula
BCF	Brachio-Cephalic Fistula
CFD	Computational Fluid Dynamics
CVC	Central venous catheter
DAO	Distal arterial outlet
DVO	Distal venous outlet
ESRD	End-stage renal disease
HD	Haemodialysis
IH	Intimal Hyperplasia
OSI	Oscillatory Shear Index
OSI	Oscillatory shear index
PAI	Proximal artery inlet
RCF	Radio-cephalic fistula
Re	Reynolds Number

RRTime	Relative Residence Time
RRT	Renal Replacement Therapy
SMC	Smooth Muscle Cells
TAWSS	Time-averaged wall shear stress
WSS	Wall Shear Stress

Chapter 1

Introduction

1.1 Background

End-stage renal disease (ESRD), also known as stage 5 chronic kidney disease (CKD), refers to the declination of renal function to a glomerular filtration rate (GFR) of 15 $mL/min/1.73m^2$ or less [3, 13]. ESRD patients with kidney damage to this extent would ideally receive a kidney transplant within the months following their diagnosis. Kidney transplantation yields superior survival rates over dialysis [14], the most common renal replacement therapy (RRT). Furthermore, transplantation is more cost-effective and provides better quality of life for the ESRD patient [15, 16]. However, due to the number of available kidneys and kidney transplant waiting times, the supply of organs does not meet the demand [17]. In addition to this, the number of elderly and fragile ESRD patients is increasing [18]. With RRT being a necessity for survival in the majority of ESRD patients, improving RRT strategies presents the most immediate solution to improving patient quality of life and survival.

Haemodialysis, the most prevalent RRT modality, requires a well-functioning vascular access for a repeatable and efficient procedure [19]. An arteriovenous fistula (AVF), a surgically created native connection between the artery and vein (commonly in the arm), is considered the preferential vascular access [20]. This is due to AVFs having a comparably better patient survival and access longevity statistics. Additionally, AVFs have lower risks of infection, thrombosis, and endovascular interventions [21]. These considerations also make AVFs more cost effective. AVFs also have superior patency rates following successful cannulation than the alternative vascular accesses [19], which are arteriovenous grafts (AVG) and central venous catheters (CVC). The clinical preference of AVFs is stated in the latest vascular access guidelines published by the National Kidney Foundation's (NKF) Kidney Disease Outcomes Quality Initiative (KDOQI) [3], which promote an increase in the adoption of AVFs and a patient-care centred focus towards AVF creation.

In successful AVFs, the venous segment becomes ‘arterialised’ over 4-6 weeks and the resulting direct flow from the artery to the vein provides consistently high flow rates in excess of $1000 mL/min$, permitting rapid filtering of the blood upon cannulation [22]. However, despite AVFs being widely considered as the ‘gold-standard’ vascular access [23], a significant percentage of AVFs fail and require re-intervention procedures. Due to the increasing number of elderly and fragile ESRD patients, the early failure of AVFs have been observed in up to 53% of patients [24, 25]. Re-interventions in order to produce a successful AVF are also commonplace (44%) [26]. These statistics place significant strain on medical resources in addition to decreasing patient quality-of-life.

The principal causes of AVF failure are failure to mature (FTM) and a subsequent venous stenosis, which often results in thrombosis [27]. AVF (and other VA) failure has been described as a multifactorial process [28], whereby an amalgamation of events result in the failure etiologies. AVF failure has two major etiologies; neointimal hyperplasia (NH) and inadequate outward remodelling (IOR) [29]. Both of these etiologies and the presence of calcifications cause a reduction in luminal area following the creation of the AVF anastomosis. IOR refers to cases where outward remodelling is present, but insufficient to prevent luminal stenosis [30]. NH refers to a pathological excess of negative vascular remodelling, this arises due to the proliferation and migration of vascular smooth muscle cells into the tunica intima [31].

Despite the pathophysiology for inadequate maturation and NH currently being incomplete, the haemodynamic environment and flow patterns proximal and distal to the AVF anastomosis are hypothesised to play a vital role [10, 32–38]. However, the relative impact of the contributing haemodyanmic factors with respect to the biological background and risk factors for each patient remains unclear. Studying the localised haemodynamics in-vivo is extremely challenging in clinical practice, especially in the post-surgical evaluation.

Computational fluid dynamics (CFD), a subset of numerical modelling, permits a wide and thorough investigation into haemodynamic parameters that are not-easily measurable in-vivo. This research utilises CFD methods to study the biological, vessel, and flow characteristics influencing favourable AVF flow conditions.

The justification behind this research is that despite there being a number of previous CFD studies investigating the haemodynamics related to AVFs [34, 39, 40], there is lack of patient-specific geometries that have been used, resulting in tentative conclusions being drawn. Additionally, despite NH being present in failed AVFs, there is skepticism on the associated haemodynamics in the existing literature [41, 42]. In order to conduct patient-specific AVF CFD simulations, geometries were segmented from ferumoxytol-enhanced magnetic resonance angiography (FeMRA). This imaging protocol avoids the contraindicating-nature of typical contrast agents, which has been a blocker to segmenting and generating large numbers of patient-specific AVF geometries for CFD. This has the potential of being a crucial element in a patient-specific care focus approach proposed in the KDOQI guidelines [3].

The coupling of FeMRA and CFD for AVF anatomies is the first time this has been completed, and provides the framework (with reference to ASME V&V 40) for studying patient-specific haemodynamics in AVF with known outcomes. This is vital for the existing bank of AVF literature. Moreover, minimal research has been completed on the influence of successful AVF on the proximal (upstream) haemodynamic environment. These are both areas addressed in this research.

1.2 Thesis aim and overview

1.2.1 Research questions and Aim

The aim of this research was to investigate the haemodynamic parameters and flow characteristics relating to the flow induced by patient-specific AVF anastomoses so as to inform and improve the clinical outcomes of patient-care centered AVF generation. This was achieved using datasets obtained using a FeMRA imaging protocol. The research questions of this doctoral research were:

- can a ‘scan-to-simulation’ workflow be established for patient-specific AVF from FeMRA? Can this be used for a patient-care focused AVF planning approach?
- can this workflow be used to study the influence of an AVF on the proximal haemodynamic environment?
- can vessel and or fluid flow markers in a cohort of AVF cases establish whether biological or haemodynamic flow factors are more crucial to AVF success?
- what is the influence of the AVF on the wall shear stress (WSS) metrics in the proximal subclavian artery? How does the WSS values compare to the opposite subclavian vessel?

It is proposed that answering these questions enhances the current state of the art of AVF CFD studies and can contribute to superior patient-centred care, a focus proposed by the KDOQI guidelines [3]. Superior patient-centred care can result in an increase in patient quality of life due to a minimised haemodialysis time and a decrease in the likelihood of AVF re-intervention or abandonment for a given patient. Additionally, despite the known increase in cardiovascular risk following the creation of an AVF [43, 44], this is a neglected area of research and the completed simulations highlight why careful evaluation of the resulting upstream haemodynamics is required in AVF planning [45].

1.2.2 Overview

This thesis aims to elucidate the haemodynamics in the arterial vasculature (AVF and aorta) of CKD patients. Following a thorough literature review (Chapter 2), three main studies are presented, each described in a separate chapter (Chapters 3, 4, and 5). Each of these chapters are structured in the form of research papers, which include a review of current literature, a description of the question of interest, details on the materials and methods used, the results, and concluding remarks.

Chapter 3 "Proposed workflow for investigating the proximal haemodynamics to an AVF" was published in Medical Engineering & Physics, Chapter 4 "Investigating juxta-anastomosis haemodynamics related to AVF failure in 6-week post-AVF geometries", and Chapter 5 "Computational aortic haemodynamics studying the influence of AVF on CVD risk" are in the process of being submitted at the time of writing. Chapter 6 of the thesis details the discussion and overall conclusions behind this research, in addition to the future outlook of AVF research and modelling strategies. Appendix A details common materials and methodologies for Chapters 3-5, Appendix B details the supplementary material for Chapter 3, Appendix C documents the further information and detials to the investigations completed within Chapter 4 and Appendix D details supplementary material behind Chapter 5.

1.3 Resulting publications

Various aspects of the work reported in this research have been presented in the following journal submissions and conference presentations.

1.3.1 Journal Submissions

- Patient-specific computational haemodynamics associated with the surgical creation of an arteriovenous fistula. (2022) Hyde-Linaker, G., Hall Barrientos, P., Stoumpos, S., Kingsmore, D. B., Kazakidi, A. Medical Engineering & Physics, 105. 103814. ISSN 1873-4030 (https://doi.org/10.1016/j.medengphy.2022.103814) [46]

- Haemodynamic factors associated with arteriovenous fistula outcomes: can they predict AVF success or failure? (2023) Hyde-Linaker, G., Hall Barrientos, P., Stoumpos, S., Kingsmore, D. B., Kazakidi, A. (under submission)

1.3.2 Conference Presentations

- Hyde-Linaker, G. Black, R. Kazakidi, A. Fluid-structure interaction simulation of flow-mediated dilation of a straight arterial conduit, BioMedEng19, 4-5 September 2019, University College London, UK.

- Hyde-Linaker, G. Black, R. Kazakidi, A. Fluid-structure interaction simulation of flow-mediated dilation of the brachial artery, BME Multilateral Symposium, November 2019, Beihang University, China.

- Hyde-Linaker, G. Black, R. Kazakidi, A. Multi-scale model of the fluid-structure interaction during flow mediated dilation for assessing vasodilation, 33rd Scottish Fluid Mechanics Meeting 2020, 28 May 2020, Edinburgh UK.

- Hyde-Linaker, G. Black, R. Kazakidi, A. Fluid-Structure Interaction simulation of multiple bifurcations in arm under transient boundary conditions due to Flow mediated dilation, Scottish Cardiovascular Forum - 23rd annual meeting, 1 February 2020, Glasgow, UK.

- Hyde-Linaker, G. Black, R. Kazakidi, A. Multi-parameter computational model of Flow mediated dilation with fluid-structure interaction capabilities and lumped parameter boundaries, 14th WCCM-ECCOMAS Congress 2020, January 11-15, 2021, Virtual congress.

- Hyde-Linaker, G. Hall Barrientos P. Sokratis, S. Brain Kingsmore, D. Kazakidi, A. Comparing the pre- and post-operative haemodynamics associated with arteriovenous fistula creation using computational fluid dynamics, BioMedEng21,6-7 September 2021, Sheffield, UK.

- Hyde-Linaker, G. Kazakidi, A. Best practices for CFD haemodynamic modelling of an arteriovenous fistula, Siemens webinar, April 2021.

- Hyde-Linaker, G. Hall Barrientos P. Sokratis, S. Brain Kingsmore, D. Kazakidi, A. A pilot study of juxta-anastomosis AVF haemodynamic analysis using ferumoxytol-enhanced magnetic resonance angiography and computational fluid dynamics, BioMedEng23, 14˘15 September 2023, Swansea, UK.

1.4 COVID-19 Impact Statement

A significant part of the research completed in the first year of the funding period was focused on flow-mediated dilation (FMD). The FMD assessment indicates the endothelial health of a patient by ultrasonically assessing the dilation of the brachial artery in response to a period of distal ischemia. The peak percentage dilation of the brachial artery diameter corresponds to the endothelial health of the patient. The aim of this part of the research was to simulate the varying haemodynamics across a cohort of patients.

A collaboration was established between the University of Strathclyde and Bangor University to accomplish these investigations. Bangor University was responsible for completing the FMD assessments, and the University of Strathclyde would use this data for computational modelling.

Unfortunately due to the COVID-19 pandemic lockdown restrictions being imposed in the data collection period, the FMD assessments were unable to be completed. With the AVF research chapters being subdivided into three clear chapters, the FMD elements have been omitted due to their incompleteness. The collaboration between the universities remains open to revisit this research topic.

Chapter 2

Literature review

This section details the prior literature at the time of writing related to the investigations of this research. Section 2.1 details the clinical context behind AVFs, section 2.2 details AVF pathogenesis and complications, section 2.3 details AVF imaging protocols and considered segmentation methods, section 2.4 discusses the state of the art of AVF CFD investigations, and section 2.5 describes the gaps in prior literature that this research seeks to address.

2.1 Clinical background

2.1.1 Chronic kidney disease and renal replacement therapies

Chronic kidney disease

The principal function of the kidneys (a pair of ‘bean-shaped’ organs situated either side of the spine) is to remove excess water and metabolic wastes from the blood [47]. This controls the composition and volume of body fluids. In order to filter blood each kidney has approximately 1 million nephrons (fine and complex filtering structures) which are composed of the glomerulus and the renal tubule, the former filters solutes and the later reabsorbs the filtrates [48] (Fig. 2.1).

Chronic kidney disease (CKD) is a syndrome defined by persistent alterations to kidney structure and or function. These alterations lead to the gradual and permanent loss of kidney function over a patient-variable time horizon [49, 50]. The majority of kidney diseases attack the nephrons of each kidney gradually over time [51], resulting in a diminished filtering capacity which often only becomes apparent in late stages [52]. Kidney dysfunction can manifest in multiple ways, such as hypertension, oedema, and decreased urine quality

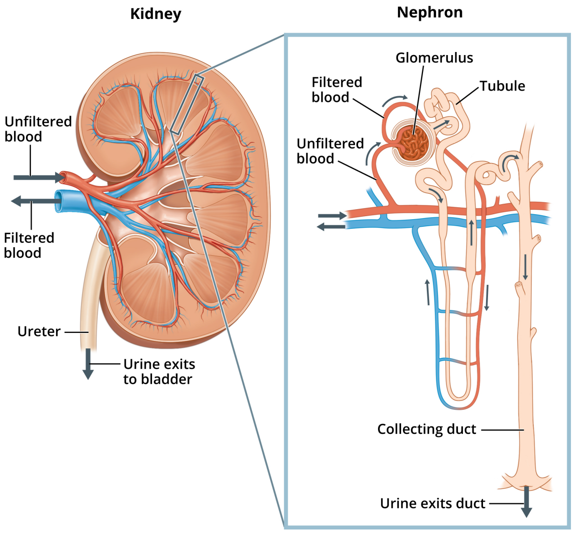

Fig. 2.1 The structure of the kidney and nephron (National Institute of Diabetes and Digestive and Kidney Diseases, National Institutes of Health) [1].

[53]. Ultimately, the failure to filter blood results in a build-up of liquids and toxins in tissues, which leads to uremia, and subsequently death [54]. Diabetes, high blood pressure, hypertension, and glomerulonephritis (an inflammation of the glomeruli) are the three major conditions causing CKD in developed countries [55, 56]. There are a multitude of risk factors behind these causations (Appendix), including cardiovascular disease (CVD) and genetics. Lifestyle changes and medicines may alleviate CKD [57], but renal replacement therapy (RRT) is usually a necessity for survival, particularly in late stages. Monitoring and categorisation of kidney health is achieved using the glomerular filtration rate (GFR) [58], an accepted index of overall kidney function. The Kidney Disease Outcomes Quality Initiative (KDOQI) guidelines [3] define the several stages in the progression of CKD, this is summarised in Figure 2.2 and Table 2.1. ESRD patients are considered to be in either stage IV or stage V (Table 2.1), where kidney function is less than $15mL/min/1.73m^2$ [59].

Table 2.1 Description of CKD severity

Stage	Description
I	a normal eGFR above 90ml/min/1.73m^2, but other tests have detected signs of kidney damage
II	a slightly reduced eGFR of 60 to 89ml/min/1.73m^2, with other signs of kidney damage
IIIa	an eGFR of 45 to 59ml/min/1.73m^2
IIIb	an eGFR of 30 to 44ml/min/1.73m^2
IV	an eGFR of 15 to 29ml/min/1.73m^2
V	an eGFR below 15ml/min/1.73m^2, meaning the kidneys have lost almost all of their function

Predictably, CKD places considerable demand on national medical resources. CKD costs the National Health Service (NHS) in England £1.4 billion per year, which equates

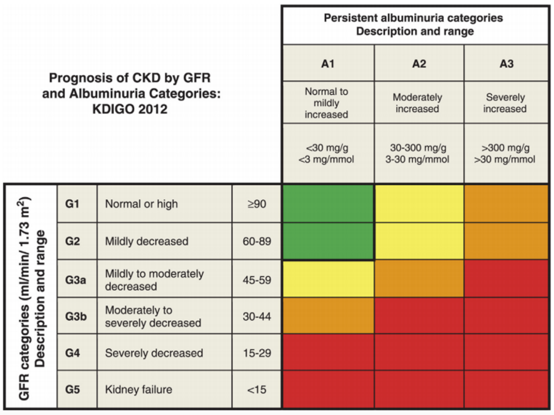

Prognosis of CKD by GFR and Albuminuria Categories: KDIGO 2012

				Persistent albuminuria categories Description and range		
				A1	A2	A3
				Normal to mildly increased	Moderately increased	Severely increased
				<30 mg/g <3 mg/mmol	30-300 mg/g 3-30 mg/mmol	>300 mg/g >30 mg/mmol
GFR categories (ml/min/ 1.73 m^2) Description and range	G1	Normal or high	≥90	🟩	🟨	🟧
	G2	Mildly decreased	60-89	🟩	🟨	🟧
	G3a	Mildly to moderately decreased	45-59	🟨	🟧	🟥
	G3b	Moderately to severely decreased	30-44	🟧	🟥	🟥
	G4	Severely decreased	15-29	🟥	🟥	🟥
	G5	Kidney failure	<15	🟥	🟥	🟥

Fig. 2.2 Prognosis of Chronic Kidney Disease by Glomerular Filtration Rate and Albuminuria Categories [2, 3], where: Green: low risk (if no other markers of kidney disease, no chronic kidney disease [CKD]); Yellow: moderately increased risk; Orange: high risk; Red, very high risk.

to £1 in every £77 spent [60]. In addition to this, CKD manifests in 7,000 extra strokes and 12,000 extra myocardial infarctions from the CKD population [61]. Approximately 3 million persons in the UK have CKD, approximately 63,000 of these are in ESRD treatment, and there are approximately 45,000 premature CKD annual deaths in the UK [60].

Renal replacement therapy

The two RRT strategies for ESRD patients are chronic dialysis or renal transplantation [62]. Renal transplantation is the treatment of choice for most ESRD patients as successful transplantation improves quality of life in addition to reducing cardiovascular risk in ESRD patients [63–65]. However, despite a decrease in kidney transplant waiting time, the average kidney waiting time is 2.5 years in the UK [66]. The shortage of kidneys available for transplantation is highlighted by 80% of the people on the transplant list being in need of a kidney [67]. Due to the number of ESRD patients and the number of donated kidneys there exists a supply-demand problem. There are approximately 3600 renal transplants every year in the UK, however, there is a backlog of 5000 persons on the transplant list and 10 people are added to the transplant list everyday [68]. This gives rise to both the thorough assessment of potential kidney transplant recipients (KTRs) and the widespread adoption of dialysis where transplantation is unavailable in the short- and long-term [69].

Due to the backlog of renal transplantations and with over 30,000 patients are currently receiving dialysis in UK [70], improving the dialysis RRT procedures would have most immediate impact to the CKD population. Haemodialysis (HD) is the most common dialysis treatment, with 89% of all dialysis RRT patients receiving HD [71], the usual alternative to HD is peritoneal dialysis (PD). Despite the wide implementation of HD, issues still exist with this treatment, usually arising from the vascular access (Section 2.1.2).

2.1.2 Haemodialysis and vascular access

HD first became available in 1962, and the the first HD fistula was created in 1966 [72]. HD involves the external filtering of blood using a extracorporeal circuit and a haemodialyser (Fig. 2.3) [73]. Haemodialysers utilise an exchange chamber with a semi-permeable membrane to separate blood and dialysate, much like the nephrons in functioning kidneys [74]. Blood is withdrawn from the patient via an arterial needle situated at the vascular access using a peristalic pump, filtered blood is then returned to the patient via a venous needle inserted into the vascular access (Fig. 2.3) [75]. In order to avoid coagulation, heparin is often infused downstream from the blood pump. This procedure replaces the three main functions of the kidney, the removal of wastes from the blood, restoring the balance of electrolytes, and the elimination of extra fluid. The HD procedure is traditionally performed 3-4 times a week for a period of approximately 4 hours [76]. As such, the vascular access created must provide consistently high flow rates whilst being durable and permitting an efficient and repeatable HD procedure [77]. Additionally, risk of infections should be minimised.

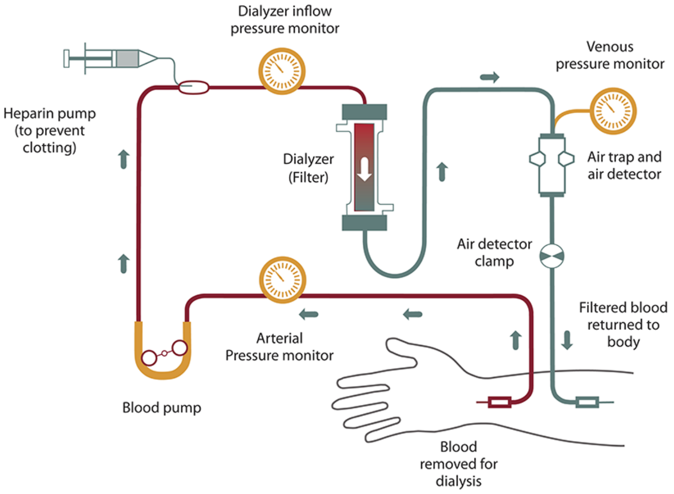

Fig. 2.3 Schematic diagram of haemodialysis procedure [4].

The three standard vascular accesses utilised in clinical practice are arteriovenous fistulae (AVF), arteriovenous grafts (AVG), and central venous catheters (CVC) (Fig. 2.4) [78, 5]. An AVF is a surgically created native connection between an artery and vein,

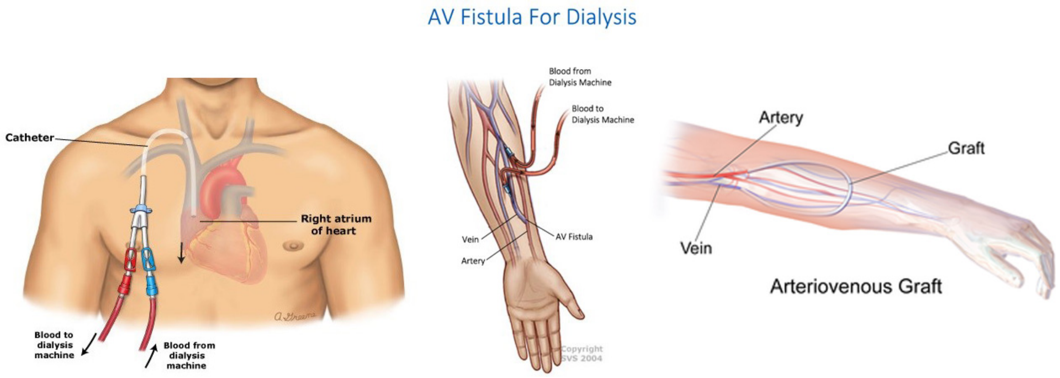

Fig. 2.4 Vascular access options for haemodialysis: Central venous catheter (CVC), Arteriovenous fistula (AVF), and Arteriovenous graft (AVG) [5].

usually in the patient’s arm [79]. AVGs involve connecting the artery and vein via an artificial prosthetic (often a polytetrafluroethylene, PTFE) segment [80]. CVCs are a synthetic device peripherally inserted into a large central vein, this avoids the need for surgically creating the VA [81]. However, CVCs have the highest mortality risk from cardiovascular and infectious diseases, followed by AVGs, and then native AVFs [82].
In 1997, the National Kidney Foundation Kidney Disease Outcomes Quality Initiative (KDOQI) published a set of evidence-based practice guidelines for vascular accesses. These have since been updated [3]. The KDOQI guidelines have promoted the use of AVFs over AVGs due to their reliability and lower risk of infection and thrombosis [83]. Additionally, the native AVF is considered the preferential VA to initiate patients onto haemodialysis due to its comparably longer survival and lower complication rates. Moreover, the cost of vascular access care has been reported to be significantly lower in patients who began treatment with AVFs [3]. Despite AVFs being widely considered the ‘gold-standard’ vascular access, AVFs still have challenges, such high primary failure and patency rates. Furthermore, several papers have debated AVF being the preferrential vascular access, as stated in the KDOQI guidelines. A wide consensus it that each vascular access has advantages and disadvantages associated with them [84]. Also, Allon (2019) [78] proposes that the lower rate of AVF (over AVG) infections is counterbalanced by a higher rate of catheter-related bloodstream infections prior to AVF maturation (4-6 weeks). The same paper mentions that the overall cost of access management is actually higher in patients receiving an AVF in patients who have started dialysis with a CVC. Whilst the debate of the drawbacks of vascular accesses and the selection of the most appropriate access on a per patient basis continues, the need for identifying the common characteristics of low and high flow rates in AVFs remains. As such, the focus of this research is the clinically preferred AVF.

2.2 Arteriovenous fistulae

Despite the clinical preference of AVFs [85], the increasing proportion of elderly and frail patients on haemodialysis has resulted in an increase in the number of AVFs failing to mature and a decrease in patency rates. With the desired patient-centered approach for these patients [3], vascular screening is completed to determine the most suitable AVF location and morphology.

The three potential AVF locations in the arm are referred to by the vessels used to create the anastomosis (the surgical connection between the artery and vein). The AVF locations are described as either radiocephalic (radial artery to the cephalic vein), brachiocephalic (brachial artery to the cephalic vein), or brachiobasilic (brachial artery to the basalic vein) (Fig. 2.5) [20]. The specific AVF site is selected to give the best chance for the fistula to develop to the extent where it is of adequate size and depth for successful repetitive cannulation and there is sufficient blood flow for HD. However, typically the anastomosis is sought to be generated as distal as possible, with a radiocephalic AVF (near the wrist) being preferred. This is so more proximal AVF sites can be implemented thereafter if the original AVF fails. However, with the aforementioned aging CKD population, published data has demonstrated superior maturation of upper arm versus forearm AVFs, likely explaining the progressive increase in upper arm AVFs in the United States [78]. In addition to this and surgical preferences, AVF location is dependent on the dimensions of the pre-surgical vessels and vessel calibre, which are vital to the development of the AVF. For example, brachiobasilic transposition has been increasingly implemented in patients possessing veins of insufficient caliber to support the preferred radiocephalic or brachiocephalic fistulas.

Differing anastomosis morphologies are also implemented in AVF creation (Fig. 2.6). The four anastomoses used for AVFs are termed side-to-end (side of vein connected to the end of the artery), end-to-side (end of vein is connected to the side of the artery), side-to-side (side of artery is connected to the side of the vein), and end-to-end (terminations of vein and artery are connected). The end-to-side AVF morphology is the most common morphology implemented clinically, and the AVF morphology of the patient-specific geometries studied in this research.

As stated previously, the AVF should have adequate size and depth for successful repetitive cannulation and there is sufficient blood flow for HD. This is formalised by the so-called ‘rule of six’ [3]. This states that at 6 weeks post-creation the AVF should have the following characteristics to be considered ‘successful’:

- a minimum diameter of 6mm

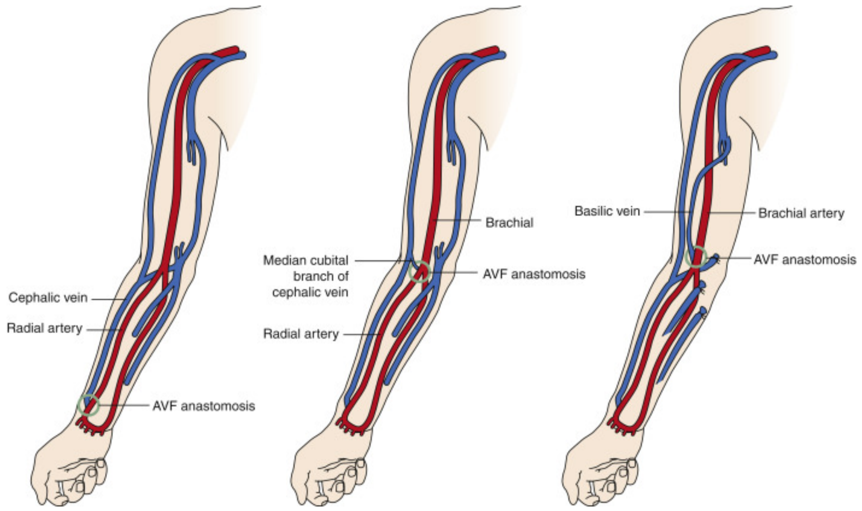

Fig. 2.5 The differing AVF classifications: radiocephalic (left), brachiocephalic (centre), and brachiobasilic (right) [6].

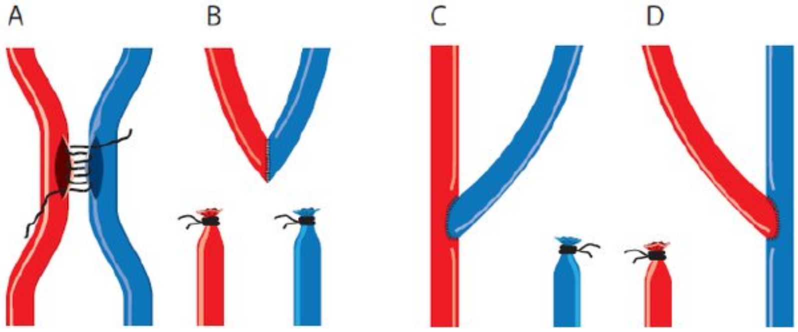

Fig. 2.6 The differing AVF anastomoses [7]. Where A is side-to-side, B is end-to-end, C is artery side to vein end, and D is artery end to vein side.

- have a depth (from the skin surface) no greater than 0.6cm
- a volumetric blood flow rate exceeding 600mL/min
- a minimum length of 6cm to permit two-needle dialysis

2.2.1 AVF development

Pre-surgical planning

Successful AVF maturation is thought to be dependent on multiple biological and haemodynamics factors, which are dependent on the vessel characteristics prior to AVF creation. Despite there being no minimum-diameter threshold to create an AVF, arteries and veins of <2mm in diameter should undergo thorough evaluation for feasibility and quality to create a functioning AVF [3]. This minimum diameter threshold (2mm) is commonly quoted from Silva et al. (1998) [86]), which demonstrated an increased rate of AVF creation (63 vs 14%) with a lower primary failure rate (8 vs 36%) using a minimum radial artery diameter threshold of 2mm [87]. It is also reasonable when possible to evaluate the multiple characteristics of the vessel, these include size, distensibility, and flow. These parameters are assessed in pre-surgical planning using either ultrasound or some form of magnetic resonance imaging (MRI). This vascular mapping is preformed prior to AVF creation in all patients.

The artery selected for the AVF must be capable of delivering sufficient blood flow for HD. Common arterial AVF arterial occlusive issues arise from diabetes and hypertension, particularly with the increasing age of the HD population. Additionally, the artery selected must not compromise the viability of the blood received from the distal arteries of the hand. With venous issues being more likely to compromise AVF success, detailed evaluation of venous anatomy is vital. Similarly to the criteria for the artery of the fistula, there is no recognised standard for vein size. Silva et al. 1998 [86] quoted a 2.5mm venous diameter threshold at the anastomosis location. Additioanlly, venous distensibility has be reported as a predictor of AVF success rather than venous luminal diameter [88].

AVF maturation

The development of the AVF occurs due to the process known as 'maturation' (Section 2.2.1), a complex vascular remodeling process initiated from the creation of the anastomosis [89]. Upon surgical creation of the AVF anastomosis, a shunt is established between the high pressure (low capacitance) arterial system and the low pressure (high capacitance) venous system. This induces a significant quantity of high pressure blood to flow directly into the vein from the artery. The flow rates induced in the venous segment of the AVF are order of magnitudes higher, for example non-AVF cephalic vein flow rates of 14-42ml/min jump to over 600ml/min in successful cases [89]. The increased flow produces an increased wall shear stress (WSS) in the AVF vessels upon anastomosis creation. The WSS values normalise with the 'maturation' and outward remodelling of the AVF vessel walls, this is a Poiseuille's law mechanism. In accordance with Laplace's law, the increased pressure and tensile stresses within the AVF vessels imply medial thickening.

The biochemical explanation of these processes is that increased velocities induced in the vessels implies disturbed flow, which can be characterised as non-laminar, disordered, and often turbulent. The increased flow and the flow patterns trigger a series physiological reactions, where haemodynamic changes are translated in endothelial and adventitial signaling. This signaling results in passive vascular distension, nitric oxide (NO) synthesis, and vascular smooth muscle cell (VSMC) relaxation. These factors cause vasodilation, a widening of blood vessels as a result of the relaxation of vessel muscular walls. In addition to the endothelial cells, changes occur in the extracellular matrix (ECM) in each layer of the venous vessel wall (the tunica intima, media and adventitia). The changes in the ECM are summarised in Figure 2.7. A successful AVF maturation process occurs over 6-8 weeks, with successful cases being visible at 4-6 weeks [90].

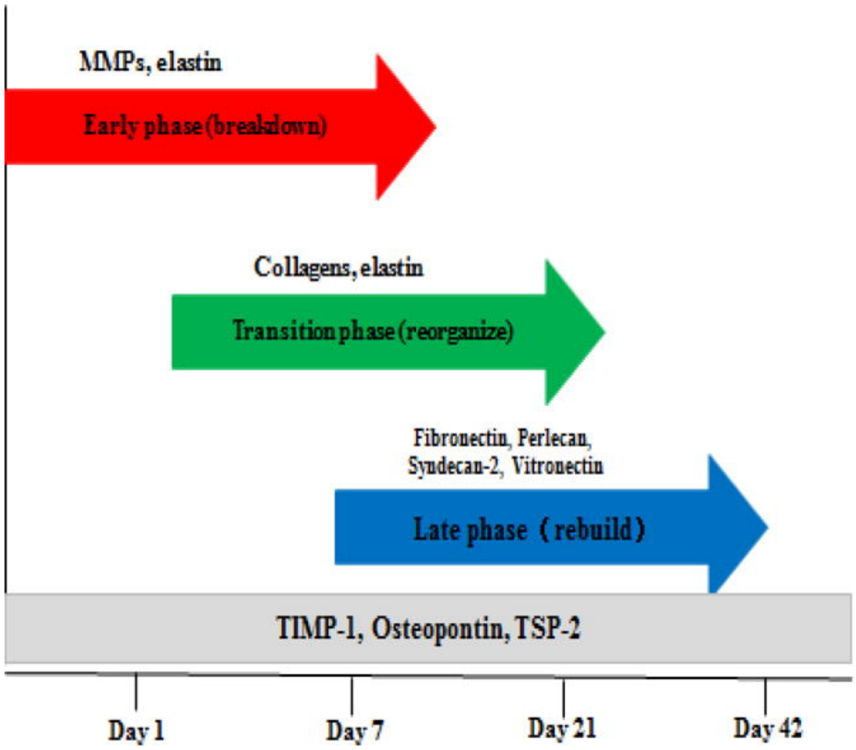

Fig. 2.7 The 3 stages of extracellular matrix (ECM) changes. These phases are referred to as the Early, Transition, and Late phase. [8].

2.2.2 AVF complications

AVF failure and patency

Adequate AVF maturation occurs in 60-80% of all created fistulae [91]. Of the remaining percentage of cases, there are various categories of AVF 'failure' and patency (Fig. 2.8). These failures and AVF dysfunction (low AVF flow rates) are one of the leading causes of morbidity and mortality among ESRD patients [92].

Primary AVF failure is usually defined by a fistula that is never usable, or fails within the first three months of its use. This definition includes inadequate maturation, thrombosis, failure of first and subsequent cannulations, and other complications leading to nonfunctional AVFs [93]. Secondary failure is defined as failure after the AVF has met the dialysis suitability criteria. Primary patency and functional patency are defined as the time from access placement until an intervention is required, and the time from first dialysis use respectively. Secondary patency is defined as the interval from time of access placement to access abandonment, with or without an intervention procedure [9]. Huijbregts et al. (2008) [94] covers these definitions in greater detail.

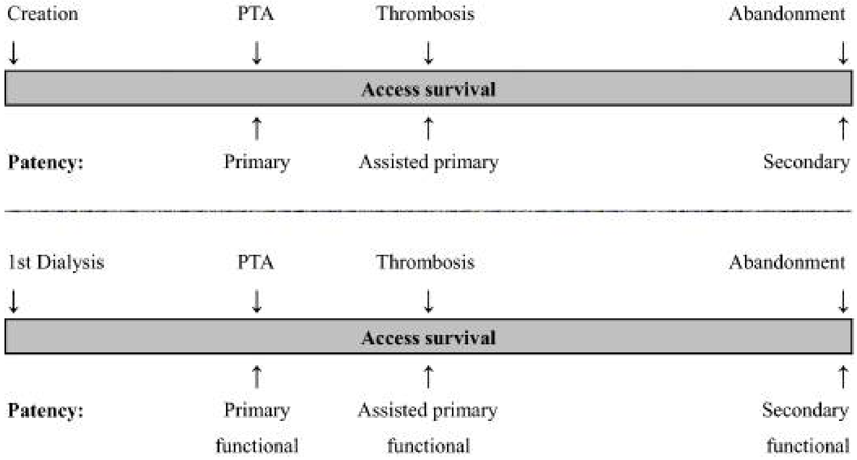

Fig. 2.8 Visual explanation of patency rates. Primary patency is the intervention-free access survival. Assisted primary patency is the thrombosis-free access survival. Secondary patency ends when the access is abandoned [9].

A multi-centre, observational cohort study completed by Stoumpos et al. 2019 [95] showed only 37.3% of pre-dialysis and 48.3% dialysis patients were using AVFs for HD 1-year after creation. Primary patency rate was estimated to be approximately 60% in year one, and 51% in year two. Therefore, almost half of AVFs require a re-intervention to maintain or restore blood flow within 2 years post-creation. This study also looked at primary patency, primary assisted patency, the interval between VA placement and VA thrombosis, and secondary patency. The 1-year primary patency was 48%, the primary assisted patency was 67%, and the secondary patency was 69%. Other examples of 1-year patency rates found in two meta-analyses were 60-64% and 71-79% respectively [96, 97]. This highlights the need for evaluating patient vasculature to maximise the chance of AVF maturation to minimise AVF interventions and abandonment, as even with successful AVF creation, the maintenance of AVF patency can be compromised by structural or problems that emerge during usage of the AVF [98].

Despite the exact pathophysiology behind failing AVFs being unclear, the cellular mechanisms of proliferation, migration, and stenosis have common pathways with inflammation and increased thrombogenicity. These pathways can lead to intimal hyperplasia and the narrowing of the AVF venous vessel, which can subsequently cause AVF thrombosis [10]. This has been the traditional consensus behind failing AVFs, which often fail due to juxta-anastomotic stenoses. However, recent evidence suggests that many AVFs mature despite neointimal hyperplasia, and that suboptimal arterial vasodilation may be an equally important contributor to AVF non-maturation. As such, the conditions behind both neointiaml hyperplasia and inadequate outward remodelling are key to understand for improving AVF outcomes.

The following sub-sections details both of the aforementioned failure causations, in addition to other complications associated with the generation of the AVF in the ESRD population, and common characteristics behind failing AVFs. These include:

- Neointimial hyperplasia
- Inadequate outward remodelling
- Calcifications in the vascular wall
- Thrombosus from lesions
- Cardiovascular and proximal vasculature complications
- Common characteristics behind failing AVFs

Additionally, although not a failure in the maturation of the AVF, arterial steal syndrome can be regarded as a condition where a reusable AVF has not been generated. In this condition distal arteries receive insufficient blood flow, resulting in ischemia in the patients hand.

Flow and haemodynamic parameters

The pressure gradient induced from connecting the high-pressure artery to the low-pressure vein produces increased haemodynamics, promoting AVF adaptation. Prior image-based CFD studies have demonstrated laminar flow in the arterial AVF segment and complex disturbed flow in the venous swing segment of the AVF [99]. Wall thickening occurs in the inner wall of the venous segment. The degree of thickening is related to flow patterns and is hypothesised to have a strong inverse correlation with shear stress magnitudes [33]. However, there is scarce literature of venous vasculature and venous cells. The arterial vasculature demonstrates that disturbed flow and low and reciprocating WSS induces atherogenic and thrombogenic genes which are proinflammatory and procoagulant in endothelial cells [100, 101]. Additionally, these conditions stimulate VSMC migration and proliferation, which can enhance wall thickening [102, 103]. However, the flow conditions which lead to wall thickening can also produce the conditions for NH and IOR.

Neointimal Hyperplasia

Neointimal hyperplasia (NH) is defined as the accumulation of SMCs and ECM in the intima, and is one of the main contributors in the failing pathophysiology of AVFs. NH is typically located juxta-anastomosis in the venous AVF segment. Following anastomosis creation, wall thickening occurs in the vessel wall to accommodate the increased pressures and the ‘non-physiological’ WSS distribution. The stimuli behind NH in AVFs arises from repeated cannulation trauma and the VA creation [104]. The process of wall thickening involves the expansion of the vessel layers by ECM deposition and VSMC proliferation and migration [105]. The current consensus describes NH arising from the direct results of SMC migration from medial layer to the tunica intima layer. The SMC layer penetrates through the internal elastic lamina, resulting in the secretion of substances such as collagen, elastin and proteoglycans. This was proposed by Spaet et al. (1975) [106] and is popular in the literature. Alternate theories of intimal thickening place a greater emphasis on the migration of fibroblasts from the tunica adventitia to the media [28, 107]. Prevention of excessive NH occurs with high laminar shear stress, which triggers endothelial quiescence (the endothelial alignment to be parallel to the flow). Endothelial quiescence leads to the secretion of anti-inflammatory, antiplatelet, and anti-coagulant substances, which counteract NH. Somewhat conversely, intimal hyperplasia is desirable in the AVF maturation phase (the 4-6 weeks following creation), but becomes undesirable once the AVF is matured due to the undesirable consequences of excessive NH. The reason for the high occurrence of NH in AVFs, is the naturally disturbed flow in the venous segment of AVFs.

The majority if fistula failures are focused on effect of several parameters on IH, due to IH being considered as the pathognomonical lesion in fistula failure. However, luminal calibre can be preserved by adequate outward remodelling (Fig 2.9.). This suggests promoting sufficient outward remodelling should be a greater focus than preventing NH. Anticoagulatory interventions have been considered an eligible strategy to inhibit IH. Prior murine vascular endothelial injury studies demonstrated reduced IH following treatment with human soluble CD39 [108].

Inadequate outward remodelling

The non-maturation of AVFs accounts for the most early AVF failure, with 30–60% of newly created fistulas being abandoned because of maturation failure [109, 95]. The

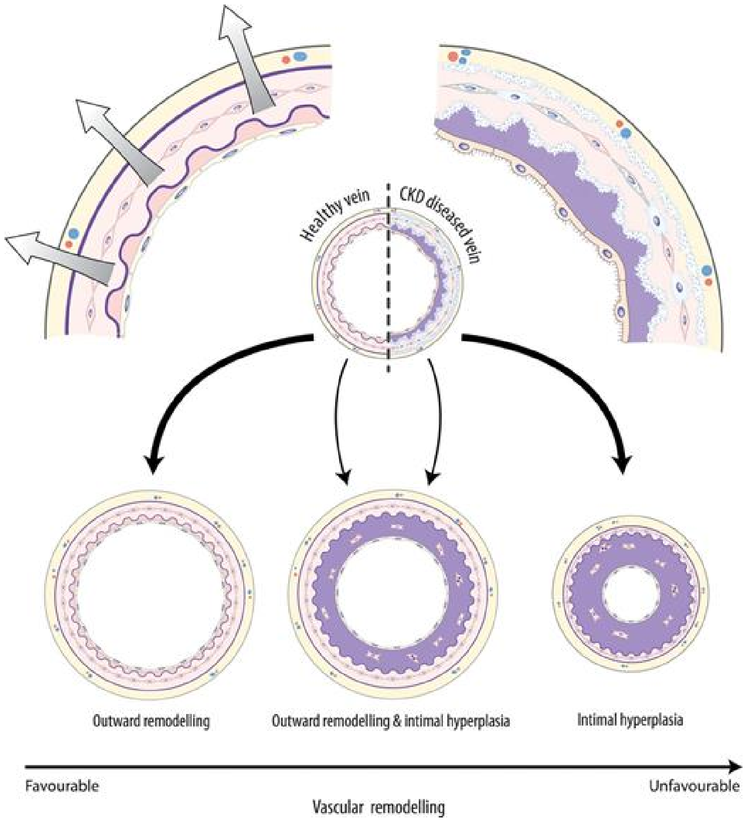

Fig. 2.9 Different modalities of the vascular remodelling response after fistula creation [10]. Where favourable outward remodelling is exhibited in the left image, outward remodelling and intimal hyperplasia is shown centre, and unfavourable intimal hyperplasia without sufficient outward remodelling is shown in the right image.

consequence of this is a poor primary (1-year) patency rate of 60–65% [110, 111]. A key challenge to resolving and improving the 'failure-to-mature' AVF cases is that the pathophysiology is incomplete. Despite the limited knowledge on AVF failure pathophysiology, most research has focused on NH as opposed to IOR. However, sufficient outward remodelling could be invaluable for AVF maturation due to its ability to preserve luminal calibre (Fig. 2.9) [10]. For AVFs, luminal calibre is determined by the net result of the outward expansion due to remodelling and any luminal narrowing. This luminal calibre may determine long-term AVF patency. As such, impaired or inadequate outward remodelling can be considered an important but overlooked contributor towards AVF failure. The wide consensus in prior literature is that more information and studies are required to elucidate this area [112], which is a focus of this research. The net resultant of IH and outward remodelling may determine ultimate luminal calibre, and if IH outbalances outward remodelling, this could result in stenosis and fistula failure [10].

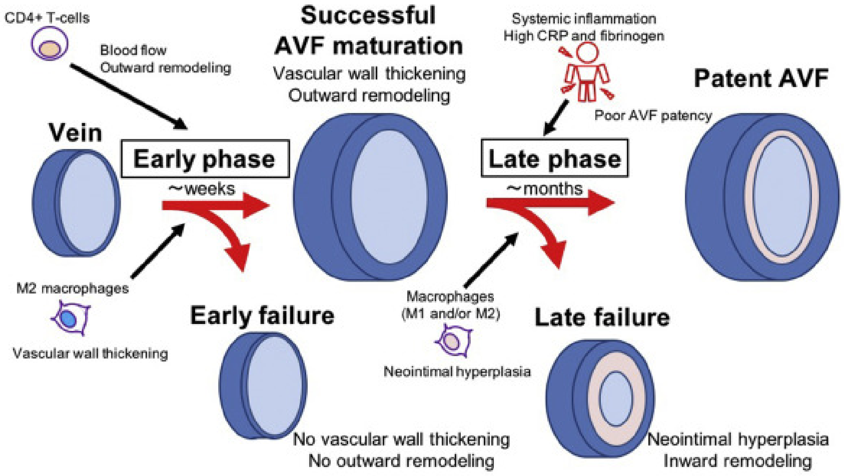

Fig. 2.10 The stages of AVF maturation, where early or late failure can occur pre- or post-AVF maturation [11].

Despite the incomplete pathophysiology behind IOR, several hypthesises exist in the literature. AVF maturation is triggered from a cascade of processes after the AVF anastomosis creation. The processes lead to the reorganization of the ECM [10]. This process, a matrix metalloproteinase (MMP) mediated process, permits vascular remodelling. Wong et al. (2015) [29] hypothesized that elastin might be an important regulator in outward remodeling in AVF, in large part due to collagen and elastin being the main ECM components that are involved in outward remodeling. Additionally, elastic fibers give the elasticity and resilience to vessel walls, supplying the resistance to haemodynamic pressures and stresses [113]. Elastin homeostasis has emerged as an important determinant of vascular outward remodeling [29].

Clinical studies have shown that forearm venous distensibility (luminal diameter increase due to upper arm cuff inflation) is a superior predictor of successful AVF maturation than baseline venous diameter [88, 10]. Medial calcifications in the AVF feeding artery have not been associated with maturation failure [114], however this is somewhat anticipated due to the significant proportation of outward remodelling and lunminal expansion occuring in the draining vein of the AVF [115].

Manifestations of NH & IOR: Stenosis, lesions, and calcifications

Juxta-anastomotic stenosis (within 2 cm of the anastomosis) are the most common abnormality following AVF creation. These stenoses are common and can result in insufficient HD and potentially fistula thrombosis (complete vessel occlusion due to non-circulating blood) in extreme cases. Stenoses can arise from both excessive NH and vessel repair following repeated AVF cannulation, and are treated using intervention procedures which employ balloon angioplasty. Thrombosis is the leading cause for AVF primary failure, whilst also being the leading cause (65-85%) of permanent access loss [116]. Early thrombosis occurs in 5-30% of all created fistulae within 24 hours [117].

In addition to stenoses, the presence of lesions can result in inadequate HD. Lesions are often found in the mid-forearm and elbow/upper arm of the AVF, in addition to the venous swing segment in the AVF [118]. Swing segment lesions are equivalent in each AVF location [98]. Additionally, the cephalic arch is often a problematic area in both BCF and RCF [119]. However, theres is an increase in the prevalence of issues in BCF AVF than RCF due to the flow differentials. Also, feeding artery lesions occur commonly in distal radiocephalic AVFs (8% lesions and 21% stenosis in 101 dysfunctional AVFs) [120]. The importance of understanding the NH and IOR pathophysiologies and manifestations is highlighted by almost all AVFs failing to mature having an anatomic problem of some type and one or more lesions frequently being present when an AVF fails [121].

Calcifications in AVF vessels are common, and jeopardize the longevity and survival of AVFs [122]. Despite the arterialisation of the vein, there is uncertainty on whether calcifications in venous vessels are governed by the same mechanisms as arterial vessels. However, disturbed blood flow from calcifications in AVFs promotes dysfunctional endothelial phenotypes, and inflammation plays a crucial role in calcification development. Choi et al. (2015) [123] found that AVF patients with microcalcifcations had a significantly lower AVF patency rate than patients without. However, Allon et al. (2011) [114] performed a similar study, concluding that arterial microcalcifcations had no impact on AVF maturation, stenosis and time to first intervention.

Cardiovascular and arterial network complications

ESRD patients are predisposed to a dramatically increased cardiovascular (CV) risk compared to the general population [124, 50]. Additionally, there is limited literature on the effects of AVF on cardiovascular remodeling and cardiac function [125]. However, it is noted that a vascular access contributes to CVD mortality through a number of mechanisms [45]. Macrae et al. (2006) [45] notes the varying relationships between vascular access and CVD risk, which ranges from inflammation promoting atherosclerosis, to vascular remodelling, stenosis formation and left ventricular hypertrophy. In addition to these categories, the presence of a functioning AVF has been found to have a significant impact on cardiac mass, cardiac index and left ventricular dimensions [126]. Another aspect that links CVD and CKD is the prediction of CVD risk using traditional CKD markers. Large meta-analyses have demonstrated GFR, a key measure of CKD, improve cardiovascular risk prediction beyond traditional risk factors [127].

Despite the known commonalities between the pathophysiologies of atherosclerosis in cardiovascular diseases and the complications of vascular accesses in CKD patients, there is an absence of CFD studies on the haemodynamics generated in CKD patients with a vascular access. This area is a question of interest, as immediately after creation of an AVF in CKD patients there is a 10–20% increase in cardiac output [45]. This is a consequence of a reduction in peripheral resistance, an increase in sympathetic nervous system activity (increasing contractility), and an increase in stroke volume and heart rate [128]. With these considerations and CVD being the largest cause of death in the CKD population, the repercussions of generating the AVF on the proximal haemodynamics and WSS metrics required elucidation. This is particularly the case with the wide consensus that endothelial exposure to low and or oscillatory time-averaged wall shear stress (TAWSS) plays an important role in initiating vessel lesions and atherosclerotic development [129].

2.3 AVF imaging protocols and model generation methods

2.3.1 Vascular imaging for AVF creation

Pre-operative evaluations, clinical surveillance, and vascular mapping are used for screening the vasculature of the patient pre- and post-surgery. This is useful for informing the selection of the location of the AVF at the pre-operative stage [130], in addition to identifying any stenotic lesions following the creation of the AVF in the post-surgical stage. AVFs are evaluated by experienced clinicians 4-6 weeks post-creation to assess whether the AVF is clinically usable [131] as it is apparent if AVF maturation will occur without interventions at this stage [90]. Moreover, AVFs are examined during HD sessions to inform the practitioner if there are any problems. In addition to visualising abnormalities and noting problems during dialysis, the post-operative imaging enables the analysis of unexplained decreases in delivered dialysis.

Traditional CT imaging protocols are not applicable in the CKD population due to the associated risks and complications of traditional contrast agents. Gadolinium-based and iodine-based contrast agents (GBCA, IBCA) can cause ‘nephrogenic systemic fibrosis’ (NSF) [132] and declining kidney function respectively [133, 134]. Non-contrast MRA has emerged as a feasible alternative in ESRD patients for imaging central vasculature prior to VA creation [135], however, non-contrast techniques can often yield poor diagnostics whilst also being time-consuming for assessing multi-directional flow. As such, non-contrast MRI is not applicable on the cohort level. Planken et al. (2008) [136] demonstrated that contrast-enhanced MRA accurately detected upper limb arterial and venous stenosis and occlusions prior to AVF creation. Alternative imaging methods such as Duplex US can be difficult to interpret and are vulnerable to high intra-operator variability. Additionally, ESRD patients have an increased risk of complications using catheter-based x-ray angiography.

Ultrasound is the most common imaging modality for vascular mapping prior to AV creation, the main benefits being its non-invasive method without intravenous contrast agents. Angiography has been a preferred method in ESRD patients with prior AVF access attempts and obese patients. However, its disadvantage is that an intravenous access is necessary, which is difficult in CKD patients. Whilst angiography is the most sensitive modality for characterising stenotic vascular lesions, it is expensive and invasive [137].

High-quality imaging is desirable for indicating conditions specific to CKD, as well as conditions within the CKD population that are not vascular access based. With the difficulties associated imaging the CKD population, the reemergence of ferumoxytol as a contrast agent is notable in the ESRD community.

Ferumoxytol

Ferumoxytol (Feraheme, AMAG Pharmaceuticals, Waltham, Massachusetts) was originally designed as an intravascular contrast agent for MRI [138]. Ferumoxytol is an ultrasmall superparamagnetic iron oxide (USPIO) nanoparticle encapsulated by a semisynthetic carbohydrate [139], this prevents redistribution outside the vascular space. Each millilitre of ferumoxytol contains 30mg of elemental iron. Ferumoxytol's large molecular weight (750 kD) [139] is responsible for it not diffusing out of the extracellular fluid space. The drug was strategically licensed as a therapeutic iron supplement, which superseeded its use as an MRI contrast agent. However, the risks posed by GBCAs in advanced CKD patients has lead to a resurfaced interest in ferumoxytol as a contrast agent ([140–142].

Ferumoxytol has high relaxivity at 1.5T and 3.0T [143] and a high intravascular halflife (>14 hours) [144], which avoids bolus timing and permits longer data acquisition time window. This also allows repeat imaging with negligible loss of intravascular signal intensity [141]. The drawbacks are that ferumoxytol can be present in the blood pool for weeks, and in the liver and spleen for months. This can complicate follow-up studies [145]. Additionally, a susceptibility artefact similar to thrombosis has been described with higher ferumoxytol concentrations [146].

The use of ferumoxytol-enhanced magnetic resonance angiography (FeMRA) has not been 'validated' by a comparison of image-data obtained used in traditional contrast agents for the same patient as of the time-of-writing. Despite this, the image data obtained using FeMRA meets the qualitative requirements for the imaging modality to be adopted in the clinical setting [95]. The vessels throughout the vasculature are of similar visibility between FeMRA and the traditional contrast agents used in non-CKD populations[95], hence its reemergence [147]. In order to complete a quantitative comparison between traditional contrast agents and FeMRA, a study using both imaging methodologies per-patient in a cohort non-CKD patients should be completed. A comparison of the vessel structures obtained using both techniques can be subsequently be completed using a dataset registration workflow. Segmenting the vessels upon registering the datasets would permit the computation of a DICE score, which can be used as a quantitative comparison between the imaging modality. With the varying clincial preferences however, acquiring the required image data may be challenging. This is considered further work. Lastly, the underlying image resolution is a factor that limits the "precision" of the subsequent segmentations and geometries, rather than the "accuracy" of the segmentation and meshing protocol. This makes a validation stud difficult to perform across varying patient vessel sizes, which may infer different image resolutions.

As of writing, ferumoxytol is currently not licensed for clinical diagnostic imaging, used in an off-label capacity despite its imaging capabilities. Ferumoxytol has attracted interest as an MRI contrast agent in advanced CFD patients where there is a clinical question without an alternative viable angiographic option. There is an expanding body of literature demonstrating the safety and application of ferumoxytol in adult and paediatric patients for a plethora of applications ([141, 87].

2.3.2 Image-based model generation

The output of a 3D imaging scan is a stack of 2D Cartesian grids of greyscale image data, the greyscale intensity within each 2D image corresponds to the relative signal strengths within the scanned region. The common format of the scan output is a DICOM (Digital Imaging and Communications in Medicine) stack of 2D images. Most approaches for converting 3D image data into meshes for FE and CFD require significant user interaction, and often model simplification [148, 149].

In order to generate accurate computational models, the identification and classification of the volumes of interest (VOI) within the image data is completed. This involves classifying voxels in the DICOM stacks belonging to the vessel(s) of interest, this process is called segmentation. Segmentation techniques vary from manually 'painting' the voxels belonging to the vessels of interest, to the use of level set methods [150]. Crucially, the accuracy of the resultant model is largely dependent of the accuracy of the initial segmentation. This is dependent on the image resolution, noise, poor contrast between tissues, motion of vessels, and inter-operator preferences of interpreting images.

Some segmentation software (e.g. Simvascular [151, 152]) use the approach of extracting contours and several slices and then to subsequently loft a surface through the contours [152]. The limitations of this approach are that the spline around segmentated 2D slices are based on manual selection of control points, yielding pronounced geometry discrepancies between bounding curve and previously segmented data. Additionally, stacking contours has issues at bifurcations due to the connectivity between adjacent slices, these have to resolved manually. This can cause loss of surface detail and geometric accuracy. Recently, the most popular surface extraction methods are based on the marching cubes algorithm [149].

ITK-SNAP (itksnap.org) is an open-source application that uses a level set-based approach [153] for segmentation. ITK-SNAP was initially applied to the segmentation of brain structures for planning medical interventions. Within ITK-SNAP, a region growing algorithm can be implemented for growing defined segmentation bubbles within a specified greyscale threshold over a specified number of iterations. This is referred to as a semi-automatic algorithm, as the resulting segmentation is manually modified if desired following the completion of the region growing algorithm. This approach is advantageous for producing a repeatable segmentation workflow, with less scope for inter-user interpretation of the vessel segmentation. ITK-SNAP produces a segmentation from stacking contours, meaning attention is given to bifurcations. The use of the gaussian smoothing operators within ITK-SNAP aid this process.

AI- and machine learning-based fully automatic segmentation methodologies are advantageous when implemented for many biomedical model generation scenarios. However, the number of ground-truth segmentations required to train such a segmenter is not feasible within the scope of this research.

The output of ITK-SNAP phase of the workflow is a Stereolithographic (STL) surface mesh, which then has to be processed prior to the generation of the computational mesh.

Meshmixer is a manual application for manipulating 3D meshes, which is extremely useful in tidying up 3D meshes. This is useful in processing the Stereolithographic (STL) meshes resulting from segmentation protocols. O'Hara 2016 et al. [154] demonstrated the use of Meshmixer for manufacturing patient-specific vascular flow phantoms. The smoothing functionalities and Boolean operations within Meshmixer make the process of generating computational models in this research much more efficient. The smoothing operators are particular useful for modifications at bifurcations. The boolean union operators aid unifying differing segmentations when required.

2.3.3 State of the art for AVF model generation for CFD

Despite the challenges associated with imaging the ESRD population there have been several studies which produced patient-specific geometries for CFD. MRI and CFD has been coupled in previous work [39] and Bozzetto et al. (2016, 2018) [155, 156] also demonstrated good quality images in a short scan duration when coupling contrast-free MRI and CFD. Kharboutly et al. [157–162] has completed numerous CFD investigations regarding the performance of AVFs, and has reconstructed patient-specific AVF from CT images using a contrast bolus (OMERON 400) [159]. Carroll et al. [163] completed a 3D reconstruction using 2D MRI scans of a healthy vein and fully matured patient-specific AVF. Sigovan et al. (2013) [39] utilised CFD in conjunction with MRI scan data in order to investigate the evolution of three AVF over ten months and identify the haemodynamic factors that contribute to AVF failure. This research presents the first time FeMRA has been used in conjunction with CFD for characterising AVF haemodynamics.

2.4 State of the art for AVF CFD investigations

2.4.1 The credibility of computational modelling through verification and validation

One major benefit of computational model (and in-silico trials more generally) is that the user can assess aspects of in vivo performance without subjecting patients or animal to harm or unnecessary risk. Additionally, the performance of the medical device (or procedure) can assessed throughout the product life cycle.

A key aspect of the use of computational models is the model credibility, which can be established through verification and validation. Due to the inheriant risk of depending on computational simulations, the ASME V&V 40 [12] subcommittee developed a risk-informed credibility assessement framework. In this framework, the question of interest and the context of use of the computational simulation is critical to its credibility and application (Fig. 2.8).

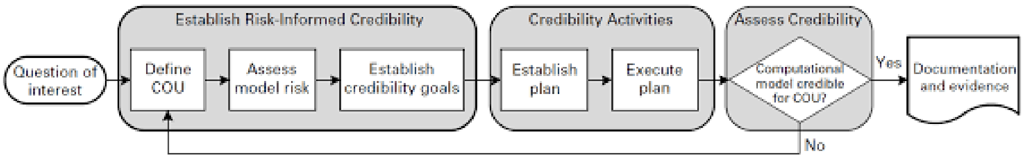

Fig. 2.11 ASME V & V 40 workflow [12].

In the case of generating AVFs, we are not discussing a medical device, but a medical procedure. Despite this, the model credibility assessments mentioned in the ASME V&V 40 documentation are relevant and pertain to the computational simulations of this research.

2.4.2 Rheology

Since the origins of fluid mechanical studies, simplifications regarding blood properties have been made. These include defining blood, the fluid continua, as laminar, steady, and Newtonian fluid. The assumption of Newtonian rheology omits the ‘shear-thinning’ property of blood, which manifests at shear rates below 50-100s^{-1} [164]. The assumption of Newtonian rheology is frequently considered reasonable due to the significant exposure to high shear throughout the domain at some stage during the cardiac cycle, which suppresses the rouleaux formation. This assumption has been widely used in prior blood flow studies [165–167]. The physiologically relevant values used when implementing a Newtonian fluid are usually dynamic viscosity of (0.0035$Pa.s$) and a density of (1060kgm^{-3}). However, the Newtonian fluid assumption does not account for the true behaviour of blood. Particle image velocimetry (PIV) experimentation has demonstrated the non-Newtonian nature of blood. This is particular the case in smaller vessels. There have been several non-Newtonian blood viscosity models utilised in prior CFD haemodynamic investigations (Carreau, Cross, Quemade, modified-Casson, Walburn-Schneck, Power law, Casson, generalised power law), demonstrating the reduction in shear stress to be greater when considering the effects of blood viscosity models. Furthermore Halder et al. (2019) [168] demonstrated the significant differences in the WSS, velocity, strain and vortex distribution when considering non-Newtonian and Newtonian models. This concludes a non-Newtonian fluid should be utilised when considering AVF blood flow.

2.4.3 CFD studies

There have been several AVF haemodynamic studies that utilised CFD for analysing the metrics relating to AVF maturation and functionality. In the majority of prior AVF CFD studies, the haemodynamic environment arising from the generation of the AVF anastomosis has been the research area.

The time-averaged wall shear stress (TAWSS) and oscillatory shear index (OSI) metrics are utilised in the majority of hameodynamic CFD studies for quantifying the effect of flow-induced mechanical stress on the vascular endothelium. A dysfunctional endothelial layer is a harbinger of several complications, such as IH and atherosclerosis, which has implications regarding calcifications. Both high and low WSS regions have been proposed as locations of atherosclerotic development [169], particularly depending on age [170]. However, the current consensus is that lesions occur most frequently at low and oscillating WSS locations [171, 172]. The multi-directional nature of blood flow has also been proposed as a leading factor in atherosclerosis [173]. A majority of authors have observed an association between calcification and areas of low and oscillating WSS, others have suggested an association between calcification and high temporal WSS gradients. In addition to WSS-orientated metrics, helical flow has been hypothesised to influence AVF maturation in prior studies. Caro and Coppola studied the flow characteristics and O_2 mass transfer in a helical vessel configuration, ascertaining that the induced helical flow has favourable results in stented arteries.

Idealised geometries

Idealised models have been used in several papers to examine flow fields and WSS patterns induced by an side-to-end AVF, such studies demonstrated the significant influence of geometry on the flow field and the influence of flow pulsatility on flow separation [174–176, 35, 99]. Ene-Iordache et al. (2012) [177] completed numerical simulations of the haemodynamics in idealised AVF models to characterise the patterns of haemodynamic shear stress; low and oscillating WSS in the juxta-anastomotic vein in both side-to-end and end-to-end AVF configurations. Secondary blood flows are also a evident part of the hameodynamics induced by the AVF [178]. Laminar flow is typical of the proximal artery and secondary flow and local vortexes are common in the venous segment.

Hull et al. (2013) [40] completed a CFD evaluation of a side-to-side AVF anastomosis, concluding that IH correlated with WSS, in addition to high WSS regions are desirable to the initiating positive vessel remodelling. Furthermore, diverse WSS was suggested to be a cause behind IH development in areas of relatively low WSS. Conversely, uniform and high WSS regions should yield the least IH.

The influence of differing AVF morphologies was analysed by Remuzzi et al. (2013) [179] and Ene-Iordache et al. (2013) [102], who investigated the blood flow in both end-to-end and side-to-end AVF idealised morphologies with varied anastomosis angles. A straight artery with a 30°angle was found to be optimal so as to reduce unsteady flow and stagnation regions. Additionally, it has been demonstrated that a smaller angle correlates to smaller areas of low and oscillating WSS [180]. This has lead to suggestions that anastomosis angle, curvature, planarity, and local changes in cross-sectional areas are strong contributors to local AVF haemodynamics. Iori et al. (2015) [181] used idealised geometries to suggest AVF anastomoses should be created on the outer-curve of an arterial bend if the link between unsteady flow and IH is valid. However, it is also noted a straight segment or an inner-curve of the artery is beneficial should the low WSS hypothesis theory of IH be correct. Cunnane et al. (2019) [182] studied varying anastomosis angles and their influence on the WSS distribution, and Niemann et al. (2011) [176] studied WSS in six different fistula morphologies.

Patient-specific geometries

Bozzetto et al. (2016) [155] studied 4 patient-specific AVF imaged 6-weeks post-creation. High frequency unsteady flow was observed in the venous segment of 2 BCF and 2 RCF, disturbed flow was also evident in the arterial segment of the anastomoses. Browne et al. concluded the pressure drop in a patient-specific AVF simulated was due to the high-frequency flow in the vein. As expected, Carroll et al. [163] observed maximum and mean WSS magnitudes were significantly elevated in the vein following AVF creation. Flow reversal was found in the juxta-anastomotic and efferent vein. Additionally, Remuzzi et al. [183] reviewed the role of haemodynamics proximal to the AVF as an upstream event in the ignition and formation of neointimal hyperplasia in AVF. This highlights the necessity for accounting for proximal haemodynamics.

Several CFD investigations have sought to investigate the flow inside the AVF following surgical AVF creation at different time intervals. Translating the haemodynamics simulated at a single instance into a specific outcome can be very challenging and is somewhat limited. Lee et al. (2015) [32], and Sigovan et al. (2013) [39] sought to investigate the vascular remodelling of differing anastomoses through CFD simulations. Sigovan et al. (2013) [39] found the venous areas of the anastomosis that experienced recirculation or flow instability were more prone to remodelling. However, the limited patient cohort minimises the interpretation of the findings.

Limitations of CFD

Ng et al. (2022) [184] studied the influence of boundary conditions and highlighted the necessity of selecting the appropriate boundary conditions for the AVF being simulated. The study correctly described patient-specific data, usually in the form of waveforms, being required for accurate and representative patient-specific haemodynamics.

All of the prior studies discussed simplify the behaviour of the vessel wall using rigid walls, although a reasonable approach in a large percentage of computational haemodynamic studies [39, 179, 185], this approach omits the compliance of vessel walls and the influence of the surrounding tissue. These previously discussed studies model atmospheric pressure surround the vessel wall. In reality the force of the fluid (blood) interacts with the structure of the vessel wall. This is known as fluid-structure interaction (FSI). This influence of the vessel wall and the surrounding tissue may have a significant impact in the vessel remodelling.

2.4.4 Fluid-structure interaction investigations and wall models

McGah et al. (2014) [186] used CFD and a compliant wall model for modelling the haemodynamics in four mature AVF. The findings were that modelling the distensibility of arterial and venous walls may influence the TAWSS magnitudes, but not the flow patterns.

The FSI between the blood and vessel wall is modelled using either a one-way or a two-way coupling. A one-way FSI coupling means the force of the fluid acts on the solid continua, but not vice versa. A two-way coupling means the fluid exerts a force on the solid and the displacement of the solid continua influences the fluid field. The selection of the software utilised becomes imperative in FSI simulations, often the fluid and solid continua are resolved in separate software. The information between the continua are exchanged at each timestep. Additionally, the selection of the most appropriate model for the modelling the behaviour of the vessel walls is varied in prior studies. The hyperelastic nature of the vessel wall has given rise to several differing modelling approaches. Additionally, the differing properties of the tunica intima, media, and adventitita require consideration.

Decorato et al. (2014) [187] investigated the FSI in a patient-specific AVF in order to establish the model complexity required for providing clinically relevant information. This FSI simulation investigation utilised non-Newtonian blood model in addition to variations in the mechanical properties of vascular walls through simulated solid domain.

Colley et al. (2016) [188] completed a one-way FSI simulation of the AVF within ANSYS.

A hyperelastic Yeoh 3rd order model was utilised in conjunction with a vessel wall density of $1060 kgm^{-3}$. Additionally, the surrounding tissue of was modelled using a linear elasiticity (E = 1MPa, Poissons ratio = 0.3). The vessel wall was reconstructed utilising Simpleware software (Synopsys, Exeter).

2.4.5 Haemodynamic parameters

There is a wide consensus that endothelial exposure to low and or oscillatory WSS plays an important role in initiating vessel lesions and atherosclerotic development [189]. These conditions initiate both atherosclerosis and IH, despite their differing pathologies. Dimensionless haemodynamics metrics such as oscillatory shear index (OSI) and relative residence time (RRTime) have been used in order to correlate low and oscillatory shear stress to atherosclerotic plaque. However, some reviews [190] have found the use of these metrics to yield conflicting results, with there being split opinion on the link beween OSI and RRTime and atherosclerotic plaque. As such Peiffer et al. (2013) [191] introduced the transverse WSS metric (transWSS), which measures multi-directional disturbed flow, finding a correlation between high transWSS and the formation of atherosclerotic plaques. Chiu et al. (2011) [100] reviewed the state of the art on experimental in-vivo and in-vitro data that correlated disturbed flow and endothelial outcomes. Specifically, on how WSS distributions influence the regulation of gene expression on endothelial cells. Chiu et al. (2011) [100] concluded surgical procedure improvement can be made so as to generate favoured flow patterns via controlling the morphology of the AVF geometry.

2.4.6 Systematic reviews and non-CFD studies

Browne et al. (2015) [99] completed a systematic review of the impact of shear stress on the outward remodelling during maturation, evaluating the evidence supporting the location and development of intimal hyperplasia (IH). The review highlighted a growing body of evidence suggesting that low and oscillating shear stress stimulates the initiation of intimal medial thickening of AVFs. Despite this, further evidence is required for the ‘disturbed flow’ theory and the outward remodelling finding prior to surgical configurations and treatment strategies are optimised to adhere to them [99].

Caroli et al. (2013) [192] reviewed the potential use of a patient-specific vascular low-order network model for predicting haemodynamic changes in the network six weeks after AVF creation. However, 3D investigations permit a more comprehensive analysis of the haemodynamics than low-order models. The drawback of CFD is increased computational expense compared to low-order models, however, CFD has a lower computational cost than FSI simulations. A key aspect addressed in Chapter 5 is the increased cardiac output generated due to the creation of the AVF. This is highlighted by Reddy et al. (2017) [193], which presented evidence for left ventricle remodelling and dysfunction following AVF creation [193].

2.5 Gaps in the current literature

In presenting the literature behind AVFs and the prior CFD-based studies, it is evident low and oscillatory WSS regions are potentially problematic. Additionally, it is hypothesised that helical flow in the venous segment of the AVF is desirable. These two criterion are somewhat contrary to the other, with helical flow likely causing low and oscillating WSS regions. Considering the current hypothesis of the desirable flow conditions and the hypothesis behind the failure etiologies, this research seeks to add to the 'bank of knowledge' that can be referred to it future AVF mapping and planning.

Additionally, the majority of CFD studies on AVF haemodynamics have focused on the juxta-anastomosis environment [185, 39]. In addition to simulating the haemodynamics at the anastomosis, this research has composed a workflow for generating patient-specific geometries from the ascending aorta to the AVF. This workflow can be implemented for investigating the blood flow dynamics proximal to the fistula. This is a neglected area of prior research which may be crucial to long-term patient quality of life, with conditions being produced from an increased cardiac load.

Moreover, there still exist potential improvements that can be made in the selection, creation, and patient-centered care of AVFs in the ESRD population. Minimising the fistula complications associated with morbidity, mortality and increased costs is beneficial to the individual patients, surgeons and the ESRD healthcare community. With an individualised approach, the selection of the most appropriate fistula location is crucial to the success and performance of the AVF. A key component of this is the knowledge of whether haemodynamics or biological factors are more determinant of AVF success.

Chapter 3

Proposed workflow for investigating the proximal haemodynamics to an AVF

The majority of the content presented in this chapter was published in Hyde-Linaker et al. (2022) [46].

3.1 Introduction

In 2017, the global prevalence of chronic kidney disease (CKD) was 9.1%, which is roughly 700 million cases [194]. Patients with CKD experience a gradual decline in renal function to the extent that renal replacement therapy (RRT) is required for survival in end-stage kidney disease (ESKD). Over 85% of the global ESKD population is haemodialysis (HD) dependent [195], requiring a reliable access to the systemic circulation to achieve mechanical blood filtering and replace the kidney function. The preferred vascular access for ESKD patients is an arteriovenous fistula (AVF), a native vessel segment created by surgically joining a vein and an artery, commonly in the patient's non-dominant arm [196]. Creation of an AVF establishes a shunt from the high pressure, low capacitance arterial system, to the low pressure, high capacitance venous system [197], causing an increase in the arterial diameter and the 'arterialisation' (thickening and increased elasticity) of the vein. This process takes approximately 6-8 weeks [198] and, when successful, permits consistently high blood flow rates in excess of 600mL/min [26] whilst providing a durable vascular access for delivery of efficient and repeatable dialysis. The 6-week arterialisation period and 600mL/min minima flow rate fall under the successful AVF 'rule of six' criterion detailed in vascular guidelines [3]. In addition to flow rate, the AVF venous diameter should exceed 6mm and the AVF should have a depth from the skin surface no greater than 0.6cm.

A major problem with AVFs is the high frequency of primary failure as a result of either poor maturation or early thrombosis. As such, vascular access dysfunction is one of the leading causes of morbidity and mortality among ESKD patients [199, 200]. Neointimal hyperplasia (NH) and inadequate outward venous remodelling are the two leading causes of AVF failure [201]. However, the exact mechanisms underlying these processes remain mostly unknown, highlighting the need for exploring further the haemodynamic environment caused by vascular access surgery [185, 40, 39]. Moreover, it has been reported that the successful creation of AVF may result in cardiac failure due to the marked increase in cardiac output over time [202].

This increase in cardiac output is the result of two principal factors. Firstly, the shunt produced by the presence of the AVF causing a reduced systemic vascular resistance and increased venous return. In a compensatory response to this, heart rate, contractility, and systemic filling, pressures increase, increasing cardiac output [202]. Additionally, due to blood through the AVF bypassing the capillary bed, peripheral perfusion is maintained by the increase in cardiac output being equal or greater than the flow diverted through the AVF. This cycle continues as increased cardiac output increases venous return [203, 204]. The increased venous return initiates the increase in the left ventricle end-diastolic volume, resulting in left ventricle hypertrophy. Secondly, reduced systemic vascular resistance activates the sympathetic nervous system, further inducing pathologic cardiac remodeling.

The dual influence of increased cardiac output and reduced systemic vascular resistance post-AVF creation is an area of limited prior research. In this work, we aim to investigate these changes in a 20-year-old ESKD patient by combining novel vascular imaging (through ferumoxytol-enhanced magnetic resonance angiography, FeMRA) with high-fidelity computational fluid dynamics (CFD) analysis of the entire proximal vasculature to the arteriovenous fistula. This patient received a radiocephalic AVF, which is the clinically preferred AVF location [205].

CFD is a useful tool for assessing patient-specific haemodynamic predictors of AVF success or failure [206] beyond the traditional demographic, clinical and biological factors. This is due to the haemodynamics and wall shear stress (WSS) influencing the AVF environment being difficult to measure in-vivo. The use of CFD has been demonstrated in prior studies [155, 177, 178], which have described AVF flow characteristics in addition to proposing the conditions associated with luminal reduction. These sites are zones of low and oscillatory shear stress. CFD allows a wide range of calculations into such haemodynamic metrics [207–209, 172, 171]. This is key for assessing regions of patient-specific anatomical characteristics that are susceptible to abnormal WSS distributions and disturbed flow [210–212].

Here, we present a new framework for generating 3D reconstructions of the arterial vasculature, pre- and post-AVF creation. The reconstructions presented are based on ferumoxytol-enhanced magnetic resonance angiography (FeMRA) data. Ferumoxytol is a superparamagnetic iron oxide nanoparticle preparation, developed firstly as a contrast agent in 2000 [213]. The use of FeMRA avoids the risks that historic contrast-enhanced methods pose in ESKD patients. For example, gadolinium-based contrast agents (GBCAs) are linked with a risk of nephrogenic systemic fibrosis in ESKD. In this study, the haemodynamics of the 3D arterial reconstructions generated from multiple FeMRA scans were simulated using an established finite-volume implementation in Simcenter STAR-CCM+ (Siemens Industries Digital Software). A Scale-Resolving Hybrid (SRH) turbulence model was utilised to capture the potentially transitional-flow in the AVF. The use of CFD with FeMRA in this study demonstrates the potential for more thorough explanation of the complexities behind AVF maturation, NH, and cardiovascular impact. The aims of this study were to analyse WSS distributions at the peri-anastomotic region, the velocity profile in the proximal artery and venous outflow segments, and to elucidate haemodynamic changes in the proximal vasculature to the AVF (from the ascending aorta to the radial artery). Prior AVF CFD studies concentrated primarily on localised AVF haemodynamics, neglecting the consequences of increased cardiac output on the proximal vasculature to the AVF. The novelty of this study lies in elucidating the haemodynamics in this region, in addition to being the first study according to our knowledge that couples FeMRA with CFD in a workflow.

3.2 Materials and Methods

In this research, we completed CFD investigations of two domains (pre- and post-AVF) that were each generated from three sets of FeMRA-obtained DICOM stacks (chest, upper arm, and lower arm). The pre-operative simulated vasculature extends from the ascending aorta to the radial artery, while the post-surgical reconstruction commences at the ascending aorta and terminates distally to the ‘draining’ vessels of the patient’s ‘end-to-side’ radiocephalic AVF. Fig. 3.1 displays a simplified schematic of the centrelines within the computational domains used in the pre- and post-AVF simulations, along with the applied

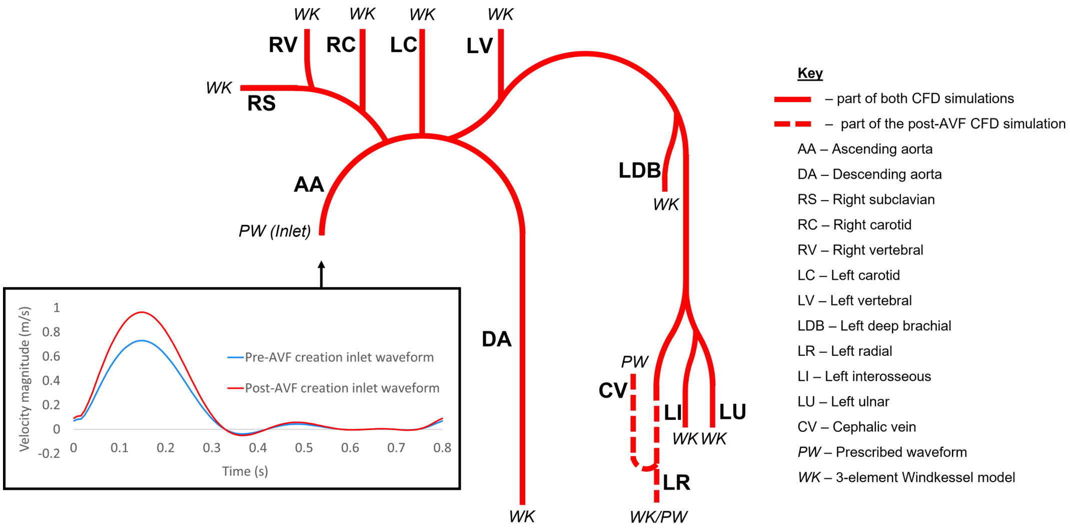

Fig. 3.1 Simplified schematic of the vessels and boundary conditions of the computational domains used in the pre- and post-AVF simulations, where the solid line represents the common vessels in both domains and the dashed line represents vessels only in the post-AVF simulation. Three-element Windkessel models were used for the majority of outlets (in both simulations), the only exceptions being the cephalic vein and radial artery in the post-AVF simulation (which used prescribed outflows). The inlet velocity waveforms are displayed in the inset (where the blue waveform is the pre-AVF inlet, and the red waveform is the post-AVF inlet).

boundary conditions.

In order to generate the pre-operative and post-surgery computational domains, each of the DICOM stacks were segmented, reconstructed, and then combined using a Boolean unification workflow in Meshmixer (Autodesk Meshmixer). These domains were then meshed and numerically modelled (Fig. 3.2).

3.2.1 Ferumoxytol-enhanced Magnetic Resonance Angiography

Due to the differing scales of the vasculature in this study, three separate scans for the chest, left upper arm, and left lower arm were acquired (Fig. 3.2). This is due to the varying resolutions required when scanning smaller vessels as opposed to larger ones (Appendix A.1). The scans of the patient were performed before surgery and six weeks after AVF creation on a 3.0T Prisma MRI scanner (Magnetom, Siemens Medical Solutions) with local phased-array imaging coils using a standardised protocol similar to that of standard MRA studies with GBCAs. The patient was imaged in the supine position [213]. In addition to scans of the vasculature, FeMRA was the modality by phase contrast MRI was acquired proximal and distal to the AVF anastomosis. Phase contrast MRI is useful for quantify

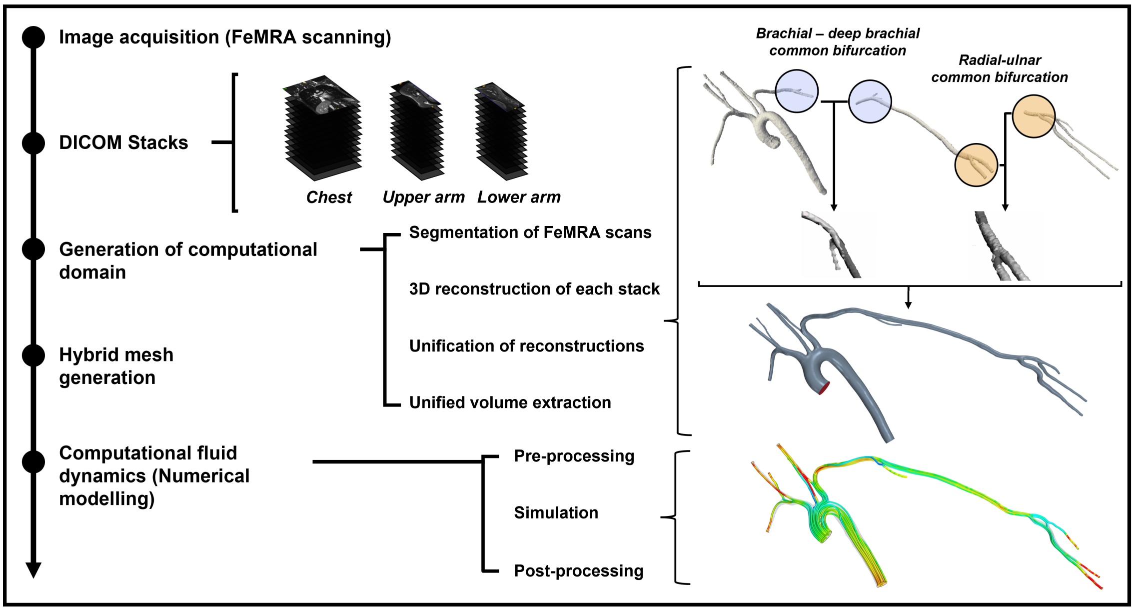

Fig. 3.2 Framework used for the segmentation, reconstruction, geometry unification and volume extraction of the patient-specific geometry based on ferumoxytol-enhanced magnetic resonance angiography (FeMRA) multi-stack images and subsequent CFD analysis.

flow velocity. Through the use of bipolar gradients, degrees of phase shift are encoded and correlation with the velocity of protons [214] (and subsequently the flow). Correct acquisition of the flow waveform data requires selection of the correct imaging plane to ensure accurate measurement and to achieve the highest signal-to-noise ratio [214].

3.2.2 Generation of computational domain

Volume renderings of each DICOM stack were initially generated in order to visualise the vessels of interest. The key areas to assess visually were the common bifurcations between the three FeMRA scans of each visit, these being i) the body and upper arm scans, and ii) the upper arm and lower arm scans (Fig. 3.2). The two respective regions selected were the deep brachial artery bifurcation and the radial-ulnar bifurcation. These anatomical landmarks were used to align and unite the geometries and to create a single domain from the three DICOM stacks. Following this, each unified stack was segmented and reconstructed 'semi-automatically' using the open-source ITK-SNAP algorithms (www.itksnap.org). This involved manual editing following automatic segmentations that used a common threshold ratio [215]. These unstructured surface meshes of the reconstructions were exported into Meshmixer and manipulated so that the common areas (the deep brachial artery bifurcation and the radial-ulnar bifurcation) overlapped (Fig. 3.2). The daughter bifurcation vessels between scans were made colinear (Appendix B.12). The geometries were then combined using a 'Boolean Union' function in Meshmixer

(Appendix B.12), with overlapping areas being smoothed to preserve the dimensions of the geometry whilst ensuring that the transition from one reconstruction to the other was valid anatomically. The dimensions of the STL surface mesh were compared to the initial DICOM files at various intervals for verification. The open-source ‘Hole Filler’ tool in OpenFlipper (RWTH Aachen), a framework for processing geometric data, was then used for resolving any areas of missing elements. Following this, the mesh was iteratively refined and ’smoothed’ in OpenFlipper to ensure the mesh quality was sufficient at each bifurcation. The centrelines of the domain were subsequently computed utilising the VMTK libraries (http://www.vmtk.org) before clipping the inlet and outlets of the domain, normal to the vessel centreline, in Paraview (http://www.paraview.org). The domain was clipped normally at distances of 0.5D (inlet) and 1.5D (outlet) in a similar manner to prior studies [211], where D is the diameter of each respective patch. This approach mitigates potential boundary effects. Finally, the clipped inlet and outlet boundaries of the geometry were closed normal to the centreline in STAR-CCM+ in order to define the boundaries and volume of the domains (Fig. 3.3).

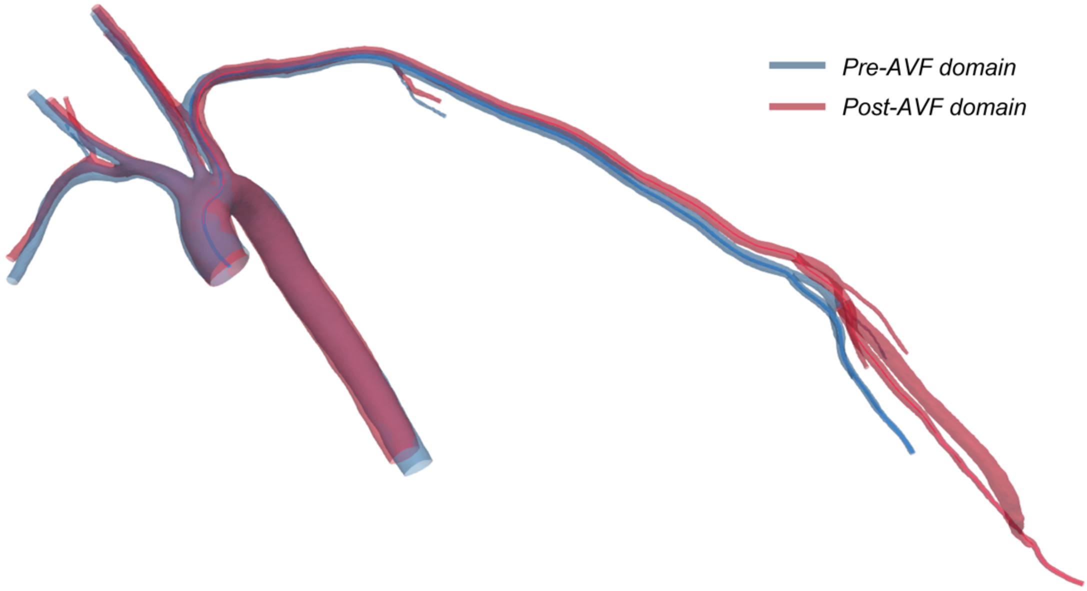

Fig. 3.3 Pre- (blue) and post-AVF (red) domains and centerlines of the 19-year-old radi-cephalic fistula case studied.

3.2.3 Validation of segmentation approach

The DICE score (Appendix A.2.2) was computed within this chapter to validate the segmentation methodology used in ITK-SNAP (approach A). A comparative segmentation was completed within Simvascular (approach B). The post-AVF chest and lower arm scans of the patient studied in this chapter were used for the comparison.

DICE score is computed as follows:

$$\text{DICE score} = \frac{2 \times \text{overlapping voxels between A and B}}{\text{Number of voxels in segmentation A} + \text{Number of voxels in segmentation B}} \tag{3.1}$$

The DICE scores of the aorta and AVF anatomies was 0.930 and 0.918 respectively (Table 3.1). These values are within the accepted DICE score numbers reported in literature for ground-truth segmentations when training AI segmentation methods [216].

Table 3.1 DICE score validation check

Metric	ITK-SNAP segmentation	SimVascular segmentation	Intersecting voxels	DICE score
Aorta voxel count	120606	107743	106135	0.930
AVF (lower arm) voxel count	76864	78504	71280	0.918

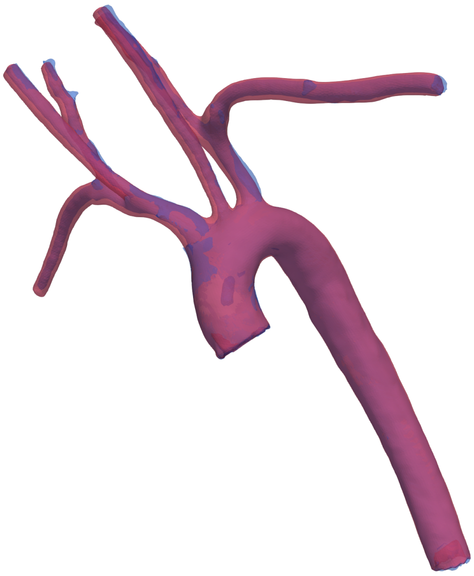

Fig. 3.4 Simvascular (blue) and ITK-SNAP (pink) segmentations of the aorta used for computing the DICE score intra-software segmentation validation.

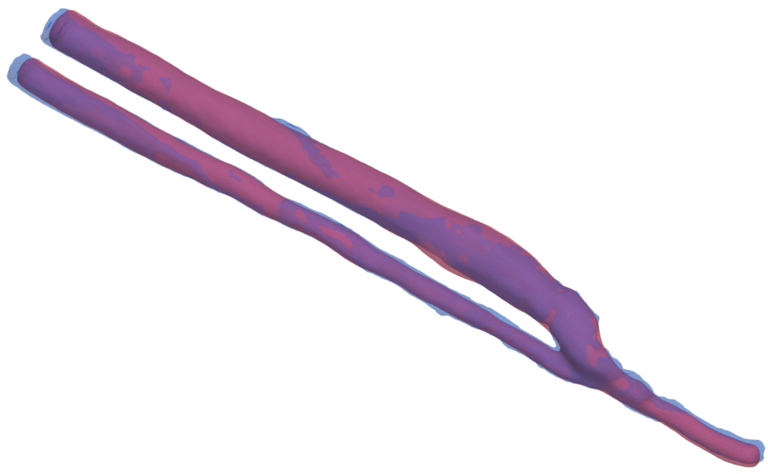

Fig. 3.5 Simvascular (blue) and ITK-SNAP (pink) segmentations of the AVF used for computing the DICE score intra-software segmentation validation.

3.2.4 Hybrid mesh generation

A hybrid mesh with prism layers and polyhedral elements was used for discretising the computational domain (Appendix A.5.2, B.4). Polyhedral meshes contain approximately five times fewer cells than a comparable tetrahedral mesh and are less sensitive to stretching. Prism layers were incorporated to reduce numerical diffusion adjacent to the wall and capture viscous effects. The height of the first prism layer, y, was calculated assuming a y+ value of 1 [208], given by:

$$y+ = \frac{\rho u_T y}{\mu} \tag{3.2}$$

where $y+$ is a dimensionless distance for describing the mesh density adjacent to domain walls, ρ is fluid density, u_T is the friction velocity, y is the height of the first prism layer, and μ is the dynamic viscosity of the fluid.

Following the calculation of the initial prism layer height, a mesh independence study was completed for the pre-AVF case. The number of prism layers and cell base size was varied, whilst the prism layer total thickness was kept constant. The most suitable mesh had 8 prism layers and base size of 3.8E-4m, resulting in a hybrid mesh with 3776730 elements and a maximum y+ value of 0.36. The mean grid convergence index (GCI) [217] at 16 locations in the vasculature was computed as 0.99, which was deemed appropriate. This same mesh specification was applied for the post-AVF case. The mesh characteristics for each case were validated for the SRH model by computation of the maximum wall y+, and the Taylor Mirco-, and Kolmogorov length scales (Appendix B.4), which are measures of turbulent flow structures that infer the required mesh resolution of the domain.

3.2.5 Numerical modelling

Scale-Resolving Hybrid Turbulence Model

The SRH turbulence model (STAR-CCM+, Appendix A.4.3) is a hybrid RANS-LES (Reynolds-Averaged Navier-Stokes, Large Eddy Simulation) model which permits the computation of unsteady large-scale turbulence structures whilst having a computational expense similar to a RANS model. The equations solved in the SRH model are ascertained using a spatial-temporal filtering, i.e. each variable φ is decomposed into a filtered $\overline{\tilde{\varphi}}$ and a subfiltered value φ' as per:

$$\varphi = \overline{\tilde{\varphi}} + \varphi' \tag{S29}$$

where ϕ is representative of quantities such as velocity components, pressure, and energy. Duffal et al. (2019) [218] details further information relating to the SRH model utilised in the CFD investigations.

The decomposed solution variables from the SRH model are input into the Navier-Stokes equations to yield filtered transport equations of mass, momentum, and energy. The time-dependent Navier-Stokes (governing) equations of the flow-field are defined as:

$$\nabla . u = 0 \tag{3.3}$$

$$\rho \frac{\partial u}{\partial t} + \rho (u . \nabla) u + \nabla p = \mu \nabla^2 u \tag{3.4}$$

where u is the velocity vector, and p is the pressure.

The investigations were completed using a segregated pressure-based flow solver on a finite volume implementation in Star-CCM+ with a timestep of 0.001s. A SIMPLE (Semi-Implicit method for pressure-linked equations) pressure-velocity coupling algorithm was used, in addition to optimised 2nd-order temporal discretisation. This reduces the leading-order truncation error by a factor of 2, compared to base-level 2nd-order temporal discretisation [219].

Non-Newtonian model and haemodynamic metrics

Often it is reasonable to use a Newtonian fluid model to approximate the rheology of blood in computational haemodynamics. This is applicable when the areas of interest are exposed to high shear throughout the domain during the cardiac cycle, which suppresses the rouleaux formation. A Newtonian rheology assumption omits the ‘shear-thinning’ property of blood, which manifests at shear rates below $50 - 100s^1$. Due the size of the AVF vessels, the produced shear rates would stretch the Newtonian rheology assumption. Therefore, a generalised Carreau-Yasuda non-Newtonian model [209] was implemented with values from literature (Appendix A.4.2). The time-averaged WSS (TAWSS) and oscillatory shear index (OSI) [172, 171, 212] are key haemodynamic metrics, described as:

$$TAWSS = \frac{1}{T}\int_0^T |\tau_w| dt \tag{3.5}$$

$$OSI = \frac{1}{2}(1 - \frac{|\int_0^T \tau_w dt|}{\int_0^T |\tau_w| dt}) \tag{3.6}$$

where t is the time, T is the cardiac cycle time, and τ_w is the wall shear stress.

TAWSS evaluates shear stress exerted on the vessel walls during the cardiac cycle, whereas OSI assesses the directional change of WSS during the cardiac cycle. We present TAWSS as a normalised quantity, where the TAWSS values are normalised with respect to the predicted TAWSS generated at the ascending aorta inlet in the pre-AVF case. The value of TAWSS predicted at the inlet was 27.5Pa via the computation of:

$$\tau_w = \mu \frac{du}{dy} = [\frac{-4\mu u_{max}}{D_{inlet}}] \tag{3.7}$$

where u_{max} is the peak fluid velocity maxima, and D_{inlet} is the inlet vessel diameter.

Additionally, the Reynolds number (Re), a dimensionless ratio of fluid momentum to viscous shear force, was computed for flow analysis at various locations within the fistula. Mean and maximum Re values were calculated, respectively, according to:

$$Re_{mean} = \frac{u_{mean} D}{\mu} \tag{3.8}$$

$$Re_{max} = \frac{u_{max} D}{\mu} \tag{3.9}$$

where u_{mean} is the mean flow velocity, and D is the local cross-sectional diameter normal to the centreline of the domain.

3.2.6 Boundary conditions

Triphasic velocity inlet waveforms based on the cardiac output measured at the pre-surgical ($CO_{pre-AVF} = 6.49L/min$) and post-operative ($CO_{post-AVF} = 8.03L/min$) visits were assigned at the aortic root in each respective simulation (Fig. 3.1). A no-slip rigid wall condition was assumed in each of the simulations. The majority of arterial outlet branches in both the pre- and post-AVF simulations were treated as pressure outlets, with each of them being coupled to lumped-parameter three-element Windkessel (WK) models [220] (Appendix B.6). The exceptions were the venous and arterial vessels distal to the created AVF in the post-AVF case (the cephalic vein and radial artery outlets), which were assigned flow waveforms based on post-operative FeMRA scanning (Appendix A.1). With regard to the WK models, the capacitance (C) and resistance (R) parameters account for the compliance and peripheral resistance of the terminal branch, respectively, while the characteristic impedance element (Z) represents the resistance of the terminal vessel. The expression relating the flow rate (Q) and pressure (p) in the 3-element WK model with respect to time (t) [221] is expressed by:

$$\frac{\partial p}{\partial t} + \frac{p}{RC} = \frac{Q}{C}(1 + \frac{Z}{R}) + Z(\frac{\partial Q}{\partial t}) \tag{3.10}$$

The discretisation of this model in the time-domain for purposes of a time-discretised CFD study, yields:

$$p^{n+1} = \frac{\frac{\tau}{\Delta t}p^n + Q^{n+1}(R + Z(1 + \frac{\tau}{\Delta t})) - Z\frac{\tau}{\Delta t}Q^n}{1 + \frac{\tau}{\Delta t}} \tag{3.11}$$

where $\tau = RC$, p and p^{n+1} are the pressure at the current and next timestep, Q and Q^{n+1} are the volumetric flow rates at the current and next timestep, and Δt is the timestep.

The use of 3-element WK models produced physiologically relevant pressure values (120/80 mmHg) in both simulations. This approach compared favourably with respect to the ‘splitting method’ [222] (22/-8mmHg), which involved computing branch diameters immediately following a bifurcation (see Appendix B.5). The capacitance and resistive values of each 3-element WK model are dependent on the artery’s characteristics in addition to the distal vasculature. An estimate for the characteristic impedance (Z) and capacitance of each terminal artery (C_0) is given by:

$$Z = \frac{\rho c_d}{A_d} \tag{3.12}$$

$$C_0 = \frac{A_d L}{\rho(c_d)^2)} \tag{3.13}$$

where L, c_d, and A_d are the vessel length, pulse wave velocity (PWV) and vessel area at diastolic pressure, respectively.

Characteristic R and C values for each 3-element WK model can subsequently be calculated with the methodology detailed in Alastruey (2006) [223] (Appendix B.6), using the following equations:

$$R = (\frac{1}{1 - \frac{\lambda}{2\phi^4}})Z = \frac{\lambda}{2\phi^4 - \lambda}Z \tag{3.14}$$

$$C = (\frac{1}{1 - 2\lambda\phi^3} - 1)C_0 = (\frac{2\lambda\phi^3}{1 - 2\lambda\phi^3})C_0 \tag{3.15}$$

where $\lambda = 0.7$ and $\varphi = \sqrt{0.6}$ are estimated using the technique described in Alastruey (2006) [223].

Further information is provided in the Appendix B.6. The 3-element Windkessel models coupled to the outlets of the computational domain were implemented via the use of reports, monitors, and field functions within Simcenter STAR-CCM+ (Appendix A.7).

3.3 Results

The results are presented in three parts: a geometrical characterisation of the pre- and post-fistula geometries is described first (Figs. 3.6, 3.7), an analysis of the global haemodynamics from the aorta to the radial artery (pre-AVF) and radiocephalic AVF (post-AVF) is provided second (Figs. 3.8-3.11), followed by the localised flow development in the remodelled patient-specific arteriovenous fistula, 6-weeks post-surgery (Fig. 3.12) at three intervals of the cardiac cycle: peak systole (T1), mid-deceleration (T2), and peak diastole (T3).

3.3.1 Pre- and post-fistula geometry characterisation

In order to characterise the geometries, the centrelines of each computational domain were computed utilising the VMTK libraries (http://www.vmtk.org). The changes in inscribed diameter and curvature along the length of the centreline from the ascending aorta (inlet) to the left radial artery is presented for both cases in Fig. 3.6a and 3.6b, respectively, to ensure valid comparisons can be made between the reconstructed geometries due to consistent segmentation. With the same imaging protocol (Appendix A.1) and segmentation method being used, differences in the proximal vasculature characteristics are considered to be due to minor differences in the original image acquisition and segmentation. However, the haemodynamic origins and remodeling are thought to be the causations of increased radial artery diameters in the post-AVF. Box plots of curvature, diameter, and torsion for these centrelines also confirm that the geometries do not differ greatly (Fig. 3.6c).

The localised dimensions of the patient-specific AVF studied here are presented in Fig. 3.7, demonstrating successful AVF maturation with respect to the ‘rule of six’, i.e. the venous diameter exceeding 6mm at 6-weeks post-AVF creation. This is in accordance with the National Kidney Foundation’s Kidney Disease Outcomes Quality Initiative (KDOQI) vascular access guidelines [3]. The anatomical characteristics of the AVF is of crucial importance to AVF success and usability.

3.3.2 Aorta-to-radial artery haemodynamics

Figure 3.8a demonstrates the changes in the haemodynamic environment proximal to the fistula for the pre- and post-AVF vasculatures through velocity streamlines at peak systole. Figure 3.8b displays the flow rate waveforms at three locations along the left arm (the left subclavian, brachial and radial arteries) before and after the creation of the AVF. The velocity streamline and flow rate values in the post-AVF case reflect the decrease in peripheral resistance and increased flow rate, particularly in the radial artery, arising from the anastomosis creation. Between the pre-operative and post-surgical simulation, the maximum localised Reynolds number (Re_{max}) in the left subclavian, brachial, and radial arteries was significantly influenced, increasing by over a factor of 2 in each case (Fig. 3.9). The value of Re_{max} (calculated using the flowrates in Fig. 3.8b) in the left subclavian artery (at location α,α’) increased by a factor of 2.13 (706 to 1504), the left brachial Re_{max} value (at location β,β’) increased by a factor of 2.47 (537 to 1328), and the value of left radial Re_{max} (at location γ,γ’) increased by a factor of 2.37 (890 to 2106).

The overall trend in the proximal haemodynamics is demonstrated through analysis of the Re_{max} numbers at the outlets of the simulated vasculature (Fig. 3.9). Despite the increased cardiac output in the post-AVF case, the vessels not associated with the left arm (i.e. the vessels not on the centreline trajectory towards the AVF) have less flow when compared to the pre-AVF case. The mean Re_{mean} number in the left common carotid, right common carotid, left vertebral, right vertebral, and right subclavian arteries is lower in the post-AVF case than the pre-AVF case. The opposite is true for the left deep brachial, left interosseous, left ulnar, and left radial arteries, where the Re_{mean} number is significantly increased.

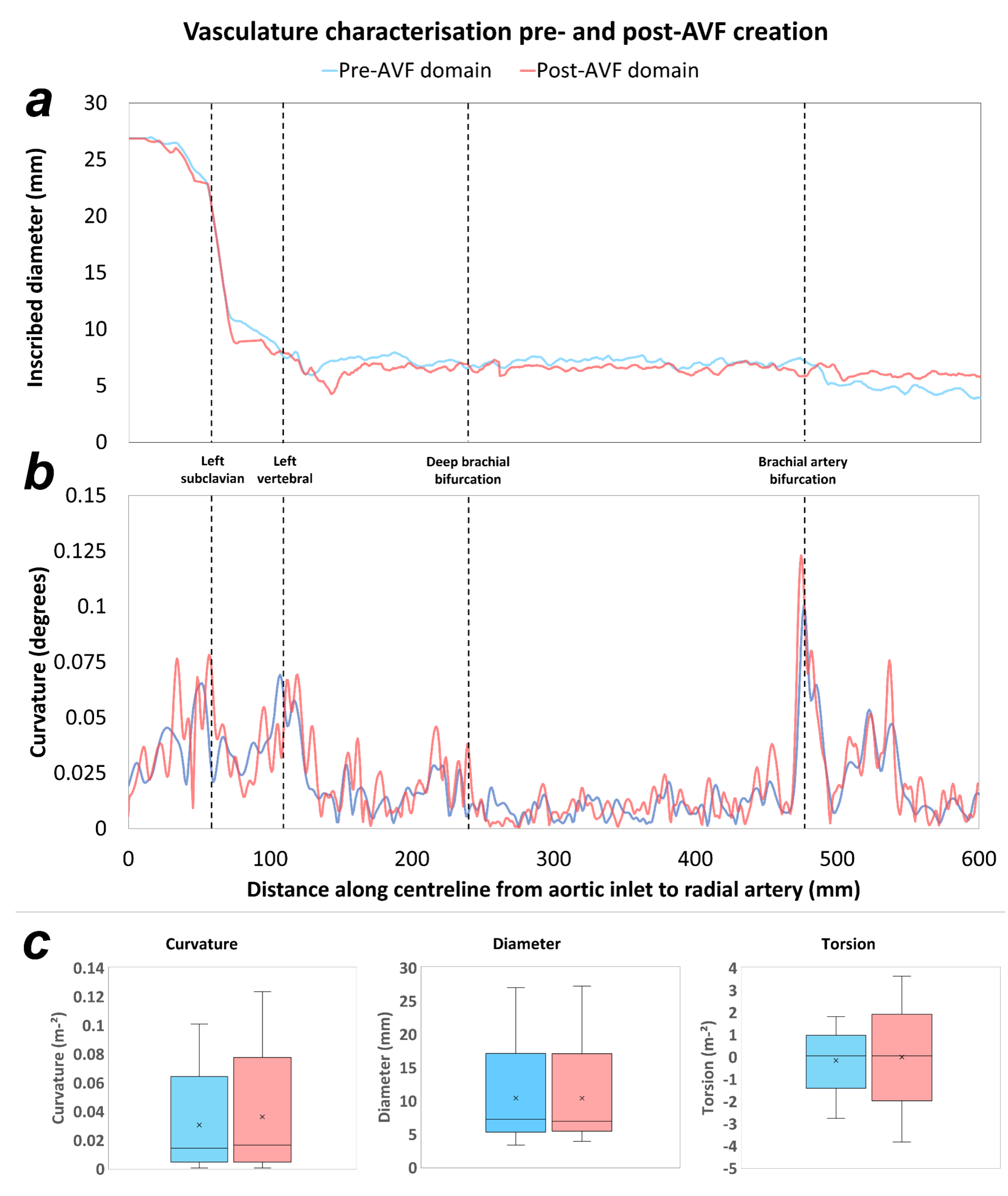

Fig. 3.6 Pre- (blue) and post-AVF (red) centreline characteristics, where (a) and (b) show inscribed vessel diameter and centreline curvature from the aortic inlet to the radial artery, and (c) shows the curvature, diameter, and torsion box plots of the centerline from the ascending aorta (AscA) to descending aorta (DSA) and left radial artery (LRA) outlets.

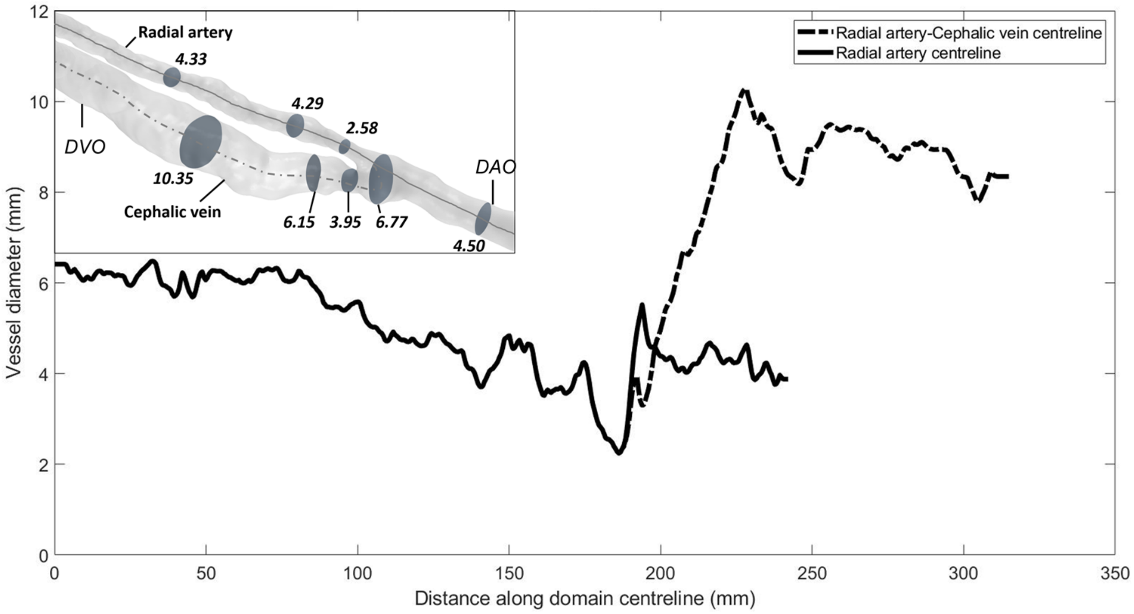

Fig. 3.7 Change in inscribed vessel diameter (normal to vessel centrelines) near the AVF with respect to the distance along the domain centreline from the feeding (radial) artery (starting from 195mm proximal to the anastomosis) to the draining vessels.

The results from this simulation have been validated through analysis and comparison of the CFD results and phase-contrast FeMRA-obtained data in the left radial artery following anastomosis creation (Fig. 3.10). The mean percentage difference between the CFD and phase-contrast FeMRA in the radial (feeding) artery was calculated to be 2.52%.

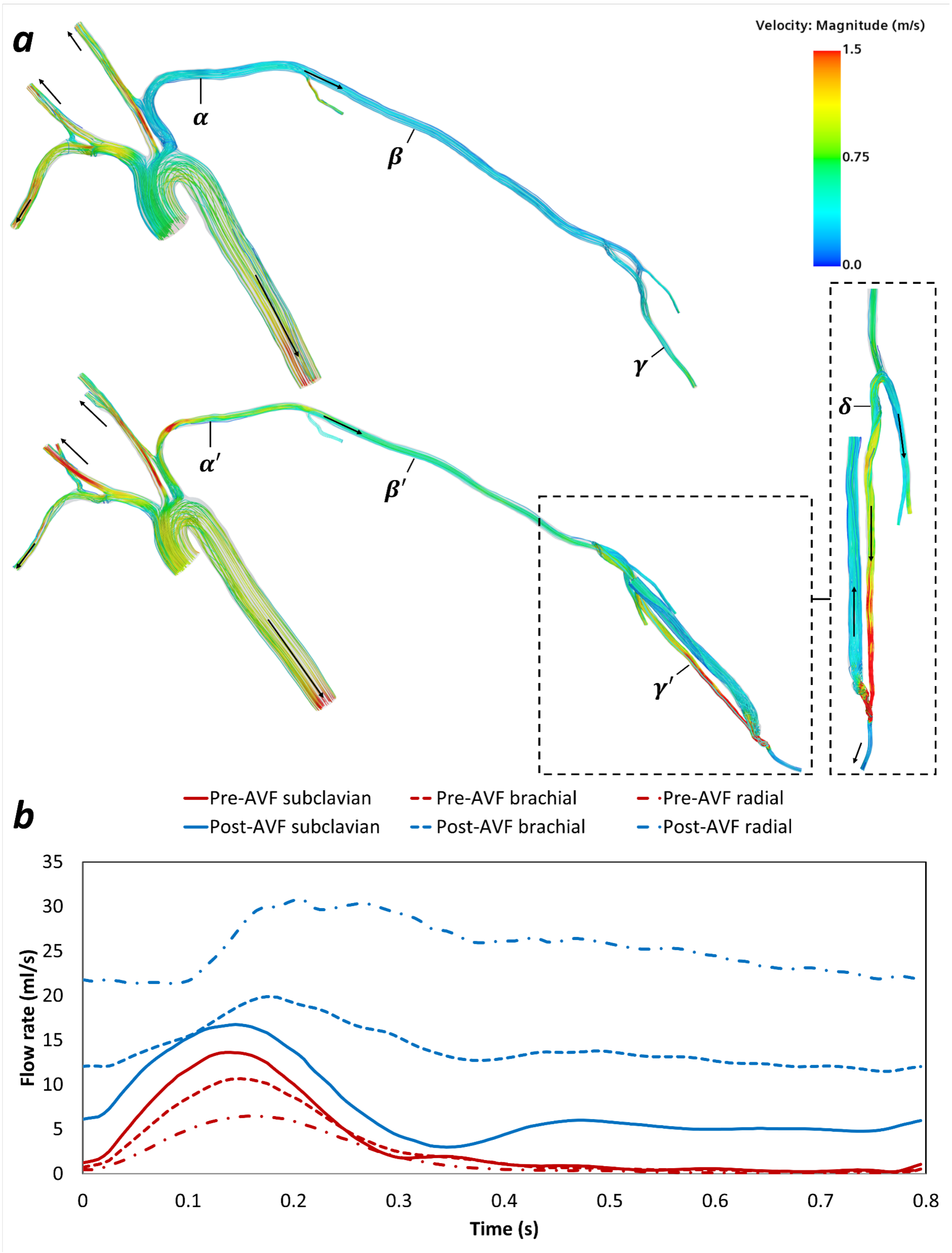

Fig. 3.8 (a) Velocity streamlines pre- and post-AVF at peak systole (where arrows represent flow direction), (b) flow rate waveforms in the vasculature at (α, α’) the left subclavian, (β, β’) brachial, and (γ, γ’) radial arteries pre- and post-AVF creation.

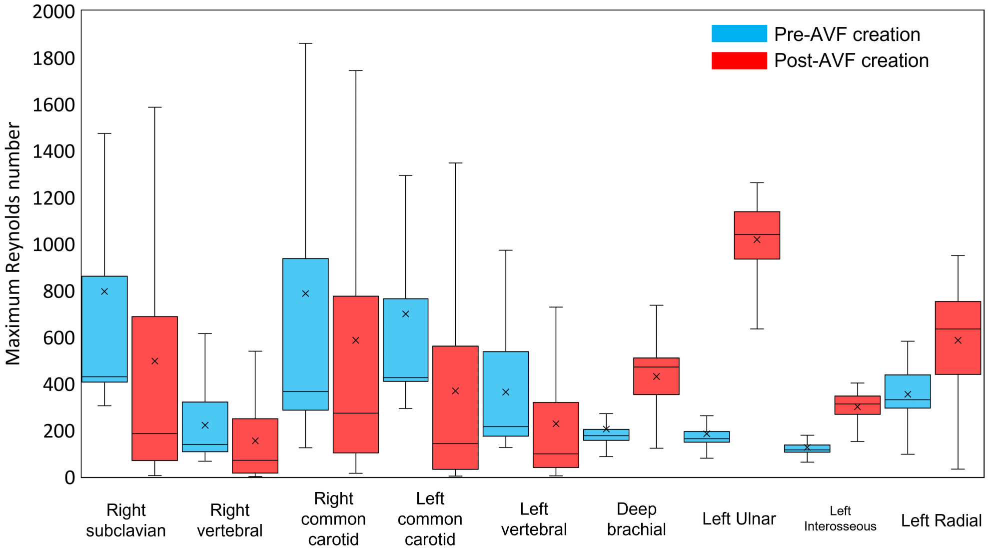

Fig. 3.9 Box and whisker plots of the Re_{max} values at the outlets of the simulated vasculature induced over the analysed (5th) cardiac cycle in the common simulated vasculature between the pre- and post-AVF cases. The Remean values are denoted with a straight line within each box.

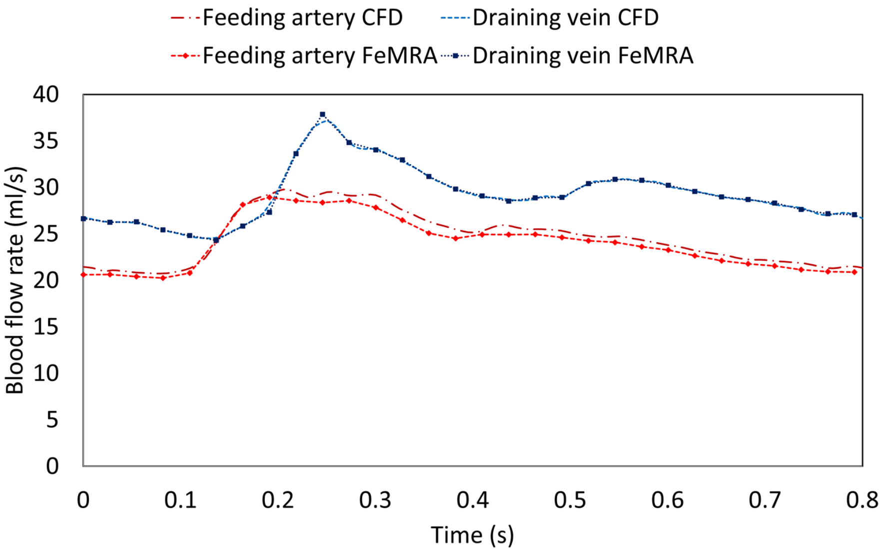

Fig. 3.10 Comparison between the patient-specific phase-contrast FeMRA-obtained volumetric flow rate at the radial (feeding) artery (red dot dash line) and the flow waveform generated computationally in the radial artery (red dash line). The radial artery was assessed at location δ as shown at the inset of Fig. 3.8a. The cephalic vein (blue dot dash line) prescribed waveform at the venous outlet is also presented.

The increased velocity in the left arm vasculature induced by the anastomosis creation resulted in considerably increased TAWSS values throughout the left arm, that is the left subclavian, deep brachial, brachial, radial, ulnar, and interosseous arteries (Fig. 3.11a). The locations of the vasculature with normalised TAWSS (NormTAWSS) exceeding 1.0 include the left subclavian, radial, and ulnar arteries. The most prominent of these regions is the radial artery, where NormTAWSS exceeded the value of 10.0 at the anastomosis location. This is in part due to luminal narrowing. NormTAWSS values exceeded 1.0 also immediately following the AVF anastomosis in both the 'draining artery' and 'draining vein'. Regarding the other regions of the proximal vasculature, the NormTAWSS remained largely unaffected, which is supported by the small change in the localised Re_{max} values (Fig. 3.9). This is due to velocity values impacting WSS magnitudes (as velocity correlates to the shear stress between fluid and vessel wall), in accordance with Equation 3.7.

Furthermore, there are significant changes in the OSI contour plot distribution due to the AVF creation (Fig. 3.11b). Pre-AVF formation, OSI levels of 0.3 were measured in the left subclavian and brachial arteries, with OSI levels of 0.15 in the left radial, ulnar, and interosseous arteries. Following the anastomosis creation, the OSI levels measured in the left arm vasculature are negligible, the only exceptions being the peri-anastomotic region in the draining vessels of the AVF, where OSI is prominent. These results infer that there is minimal directional change in WSS during the cardiac cycle in the left arm vessel proximal to the AVF. However, there are changes in the OSI profiles of the thoracic aorta, with increased OSI levels in various parts of the descending aorta following AVF creation. Lastly, the OSI levels remain similar in magnitude and profile in the common carotid, vertebral, and right subclavian arteries.

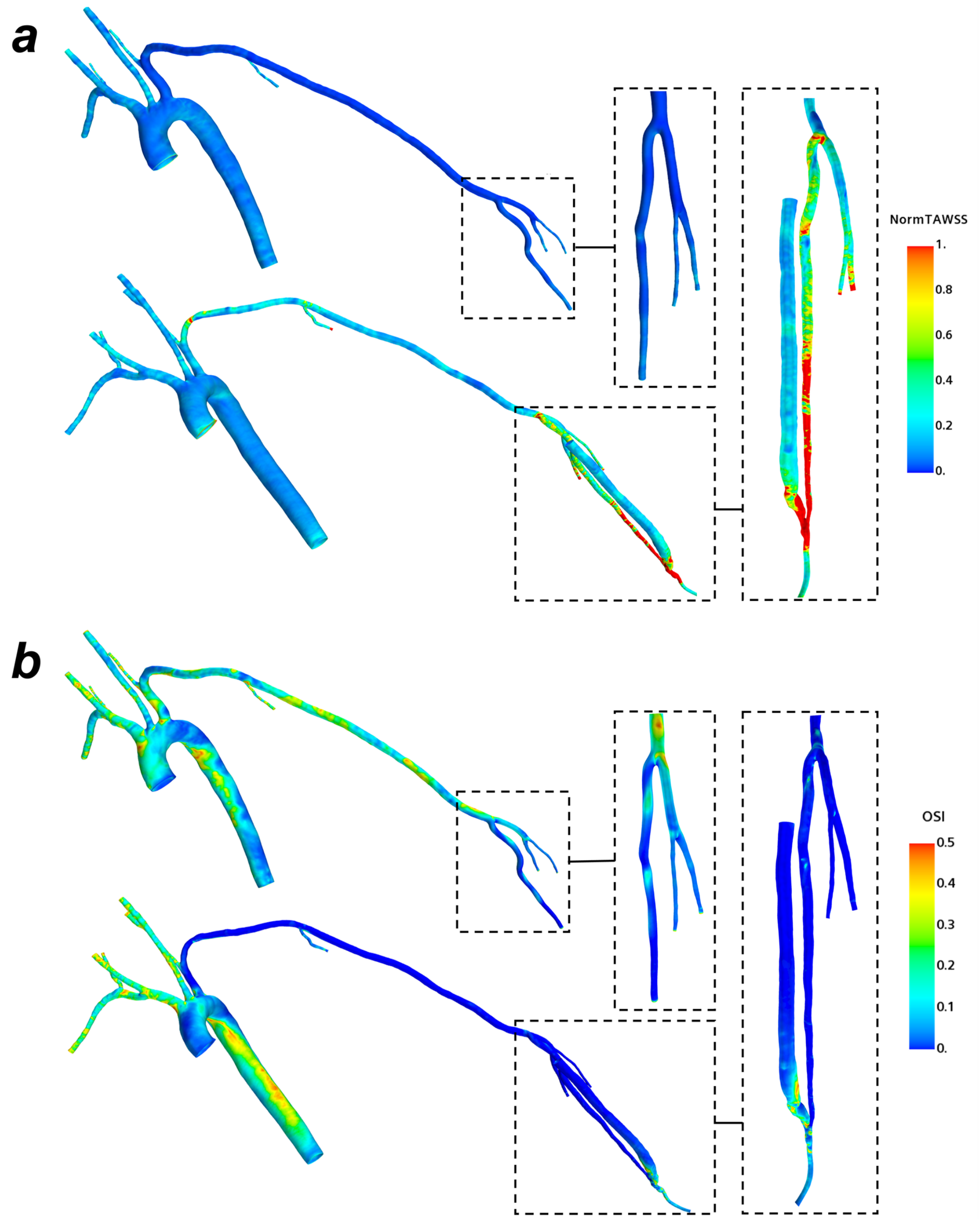

Fig. 3.11 (a) Normalised TAWSS and (b) OSI contour plots prior-to (top) and after (bottom) fistula creation.

3.3.3 Localised haemodynamics at the AVF anastomosis

The non-physiological flow induced by the anastomosis exceeded 4m/s in the left radial artery throughout the cardiac cycle and at the presented time intervals (Fig. 3.12a-c). In the cephalic vein, the velocity streamlines exhibited transitional flow with values below 2m/s, however this equates to a mean flow rate in excess of 1750ml/min, and a maximum flow rate of 2275ml/min (local Remax=3386). Downstream of the fistula in the draining vein, helical flow patterns were characteristically evident throughout the cardiac cycle, which persisted along the entire length of the cephalic vein. Retrograde flow was also observed in the 'draining' (radial) artery at mid-deceleration and peak diastole (Fig. 3.12b-c). Fig. 3.12d-e presents an enlarged view of the normalised TAWSS and OSI distributions shown in Fig. 3.11, respectively, around the localised AVF geometry. It is noted that NormTAWSS is shown in Fig. 3.12d at a different range than in Fig. 3.11a to highlight localised differences. Significantly high NormTAWSS values (>10.0) were observed in the feeding (radial) artery of the AVF, at the apex of the anastomosis, and on the venous side of the anastomosis. This is due to the luminal narrowing of the feeding artery juxta-anastomosis (Fig. 3.7) and the rapid change in flow direction through the AVF. NormTAWSS progressively decreased along the venous and arterial outlet branches to much lower values at short distances from the fistula. The scale of the normalised TAWSS plot was revised to demonstrate the significant normalised WSS values present at the anastomosis location, which greatly exceed the values in the feeding artery. Notably high OSI magnitudes (in the value range of 0.35-0.45) were observed in the distal artery branch of the AVF, in contrast to the negligible OSI values found upstream of the anastomosis (as shown in Fig. 3.11b). High OSI magnitudes were also observed in the venous segment, notably at the apex of the anastomosis and two distal regions where the venous segment has successfully expanded to diameter greater than 6mm.

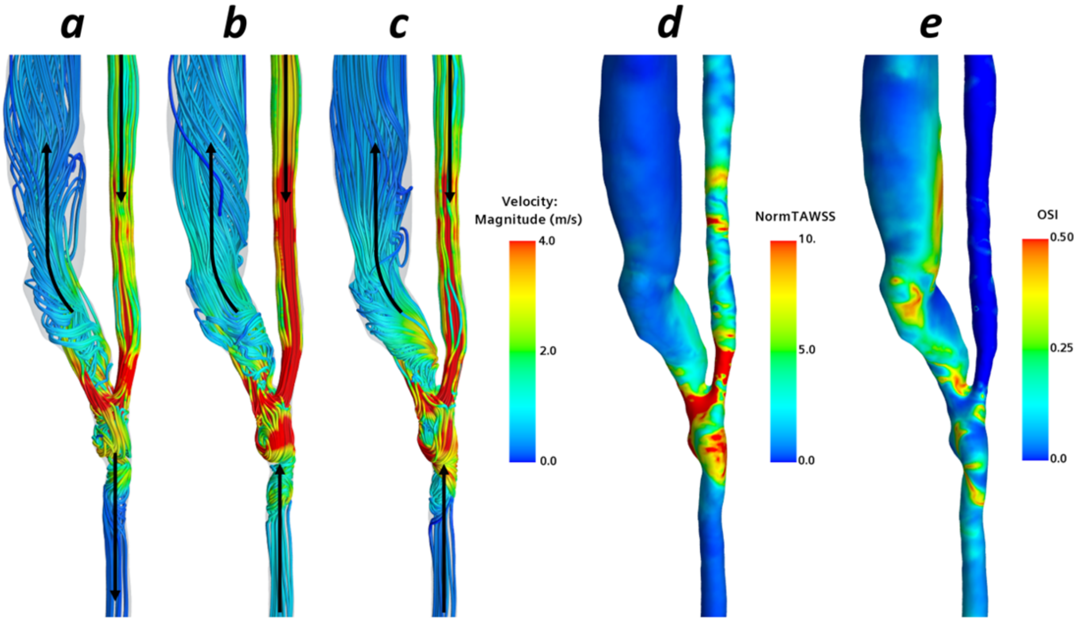

Fig. 3.12 (a-c) Velocity streamlines and flow directions (arrows) in the radiocephalic fistula anastomosis at (a) T1 (peak systole), (b) T2 (mid-deceleration), and (c) T3 (peak diastole). (d) Normalised TAWSS, (e) OSI.

3.4 Discussion

The presented framework of generating a patient-specific geometry from high-resolution FeMRA scans of a young patient with CKD has demonstrated its potential for subsequent patient-specific AVF CFD investigations. This has been an area of difficultly in prior AVF CFD research, where challenges exist in contrast enhancement. Utilising the presented framework can support greater numbers of patient-specific AVF CFD investigations, which can contribute to a previously proposed patient-care centred approach [3]. As such, the principal contribution to knowledge this chapter covers is the workflow of coupling FeMRA to CFD. This workflow has multiple potential uses, in this chapter this workflow was mainly used for elucidating the increased WSS magntitudes (and flow disturbances) induced proximal to a successful AVF, whic can inform surgical procedures for AVF.

The dimensions of the generated domains in this research were validated with respect to the original DICOM stacks. The methods used in the CFD simulations, such as the implementation of 3-element Windkessel models, are standard in computational haemodynamics. The assigning of flow waveforms (from phase-contrast data) to the ‘draining vessels’ of the AVF in the post-AVF case was necessary to produce the correct haemodynamic environment and to account for the retrograde and antegrade flow that is present at the ‘draining artery’ outlet.

The mean percentage difference between the CFD and phase-contrast FeMRA velocity magnitude data (using a surface average of the vessel cross-section) in the radial artery was calculated to be 2.52%, providing a good validation of the CFD results. Replicating the flow conditions in the reconstructed geometry permitted analyses of haemodynamic metrics juxta-anastomosis in addition to analysing the influence of increased cardiac output on the vasculature proximal to the AVF. The key finding from this study was the marked increase in blood flow velocity and TAWSS demonstrated throughout the left subclavian, brachial, and radial arteries unilaterally to the AVF. This is a marker of adaptive arterial remodelling to accommodate the increased flow rates resulting from the surgical anastomosis. In addition, the diameter of the specific reconstructed AVF was suggestive of successful fistula maturation [3]. The localised haemodynamic factors relating to NH and outward remodelling were analysed confirming sufficient AVF flow rates (>600mL/min) and the generation of transitional flow with substantial helical flow patterns in the cephalic vein distal to the anastomosis throughout the cardiac cycle. This arises due to the significant change of direction of the flow entering the vein, which generates complex vortices and secondary flows when flow is exerted on the opposite vessel wall. Our simulation indicated cyclic disturbed flow (OSI 0.42) in the radial artery distal to the anastomosis, and in the vein immediately following the venous swing segment of the AVF. This region of the vein, which experiences low and oscillatory shear stress, corresponds to where luminal reduction may occur due to NH. This hypothesis is reinforced in the findings of Ene-Iordache et al. (2012) [177] and Niemann et al. (2011) [176] in similar AVF configurations. Due to the structure of AVFs, a degree of NH is inevitable and is even observed in functional fistulae. However, further elucidation of the flow mechanisms in AVFs may minimise NH.

3.4.1 Limitations

A limitation in this work was the assumption of rigid walls, however, this is a common approach in computational haemodynamics. The influence of arterial wall deformation on the haemodynamic environment of large vessels is considered relatively small, however, for the juxta-anastomosis environment, wall motion effects may be more pronounced. Fluid-structure interaction (FSI) methodologies can account for this behaviour but FSI modelling is challenging and requires considerable computational expense. For smaller vessels, translational vessel movement may have significant influence on the blood flow profiles within the vessel. A vessel wall motion in a specific direction would shift the maximum velocity of the flow field in the same direction. In order to accurately reflect wall motion observed in the imaging process, a one-way FSI coupling could be established for exerting the wall motion of the fluid. However, due to imaging resolution not being able to capture the vessel walls, the imposing of wall motion in this study would have been a significant assumption. With this assumption, in addition to the vessel wall thickness, imposing vessel wall motion was considered as further work for this study. In future work, with the imaging resolution for vessel walls being limited, a two-way FSI coupling between the fluid and solid will likely be needed. Another key reason for omitting FSI influence from the CFD investigation was the selection of the boundary conditions. Using a prescribed outflow waveform ascertained from phase-contrast data for the AVF draining vessels meant that the flow conditions within the AVF were replicated as closely as possible. The utilisation of a polynomial triphasic aortic inlet waveform calculated using cardiac output data at each visit is also a minor limitation of the CFD study, as the results at peak systole may be slightly different in reality. A triphasic waveform with a higher peak flowrate will induce an increased maximum WSS throughout the domain and vasculature, producing a broader range of WSS metrics thoughout the domain between systole and diastole. However, the deviation between the time-averaged WSS metrics obtained using differing triphasic waveform shape (of the same cardiac output value) would be negligible. Another assumption was that only a single patient was examined in the study. Finally, the selection of Windkessel parameter values can also be considered a limitation due to the resistances and capacitances being estimated as per the ‘Boundary conditions’ subsection. The same Windkessel values were assumed for the terminal arteries in the pre- and post-AVF simulation (apart from the AVF vessels), which is also a potential limitation.

3.4.2 Comparisons to prior work

Prior work has been completed on coupling MRI and CFD [224], and Bozzetto et al. (2016) [155] demonstrated good quality images in a short scan duration when coupling contrast-free MRI and CFD. To our knowledge, this is the first study to couple FeMRA with CFD, particularly to describe AVF dynamics. The majority of CFD studies on AVF haemodynamics focus on the local environment at the site of the anastomosis [225, 226].

For example, Cunnane et al. (2019) [182] studied varying anastomosis angles and their influence on the WSS distribution, while Niemann et al. (2011) [176] examined WSS in six different fistula morphologies. In addition to analysing the local haemodynamics at the anastomosis, our study expands current knowledge by assessing the blood flow dynamics proximal to the fistula, which has not been studied before. Kroon et al. (2012) [227] reviewed the potential use of a patient-specific vascular low-order network model for predicting haemodynamic changes in the network six weeks after AVF creation. However, 3D numerical investigations, such as those presented in this paper, permit a more comprehensive analysis of the haemodynamics than low-order models, despite the inevitably increased computational expense, which is nonetheless lower than FSI simulations.

The use of a CFD simulation in this study is principally due to the question of interest, with there being a requirement to predict the WSS flow fields induced by the generated AVF. Reduced-order models can capture blood flow wave transmission effects and have been successfully applied to the clinical diagnosis of pathological changes in the cardiovascular system [228]. However, the specification of correct values for the parameters within reduced-order models remains an area not sufficiently explored, with inconsistent model parameters being adopted in literature [228]. Additionally, despite the beneficial computational efficiency of reduced-order modelling over CFD and FSI, computation and prediction of WSS flow fields is severely limited. This inferred the use of CFD in this study for the question of interest in this chapter. Reduced-order (1D) models and FSI can both account for the coupling between vascular walls and the blood flow, however the assigning of correct biomechanical wall properties is a cumbersome task due to the complexities within the layers of the vascular walls. With the increased computational runtime and the challenges associated in selecting and defining a hyperelastic vessel wall model, an FSI component was omitted. In part, this omission was also made due to computational runtime being a key consideration behind the use of computational modelling in clinical practice, with ‘benchside’ CFD being an aim of academia and industry. Lastly, the coupling of reduced order models to a 3D CFD (and FSI) model is a potentially viable option for future studies. This option is particularly relevant for study of the WSS metrics in a specific region of the network and incorporating a reduced-order model which approximates the entirety of the vascular network to some extent. In such a scenario acquiring measurements of the flow and or pressure in several areas of the network are highly desirable for informing the values in the reduced order models.

3.4.3 Clinical relevance

The time required for completing this workflow from initial segmentation to CFD post-processing was approximately 6 hours (for an experienced user of the software). The benefit of using CFD in addition to FeMRA is the profiling of haemodynamic metrics that are difficult to measure in-vivo. This is highly relevant for the identification of probable sites of atherosclerotic lesion development proximal to the AVF, and the factors relating to perianastomotic intimal hyperplasia and inadequate outward remodelling at the outflow vein. The current consensus, particularly for adults and older ages, is that atherosclersis usually occurs in arterial regions of low and/or oscillatory WSS [229]. Furthermore, atherosclerotic development typically occurs at wall curvature locations and bifurcations, such as the brachiocephalic trunk, a known location for atherosclerotic lesion development that is also reflected in our results. The atherosclerotic regions identifiable in the TAWSS and OSI contour plots are limited, with low OSI regions in the left arm having high TAWSS values. Conversely, the comparably low TAWSS regions in the aorta, carotid, and vertebral arteries have high OSI values. A small region of potential atherosclerotic development would be a region of left subclavian branch immediately following its bifurcation from the aortic arch, which is due to its comparably low TAWSS values.

In addition to this, the increase in flow velocity and TAWSS at various locations post-AVF indicates likely arterial remodelling [230] proximal to the location of the AVF. These markers were undermined in prior AVF studies, which focused predominately on localised AVF haemodynamics, or in some cases, the AVF's influence on cardiac volume. The impact of arterial remodelling on the arm vessels proximal to the AVF may be detrimental to the patient through increased predisposition to other complications, such as cardiovascular disease and arterial steal syndrome. Further elucidation of important potential complications can be made using more thorough CFD analysis with boundary conditions set by post-AVF patient flow data at several locations in the vasculature. The favourable hypothesis of high TAWSS causing outward remodelling for increased flow rates is also partially considered as a potential factor towards future endothelial damage. Despite the exact pathophysiology not being known, endothelial WSS triggers biomedical and biological events. Evidence suggests perturbed stress and strains disturb the biochemical homeostasis [177] and cause adverse vascular remodelling and potential dysfunction. In addition to endothelial dysfunction, a harbinger of atherosclerosis, low WSS levels have been associated with an increase in neointima formation, and a proclivity toward vein vasoconstriction [231]. However, NH lesions associated with AVFs differ from atherosclerotic lesions. NH occurs due to the proliferation of vascular smooth muscle cells, in addition to neovessels and inflammatory cells. Furthermore, optimal venous endothelial function has been associated with moderate-to-high WSS levels due to the quiescence and alignment of endothelial cells under laminar flow conditions.

The WSS levels modelled by CFD indicate the successful maturation of the AVF. This is identified as the TAWSS values induced in the venous segment (cephalic vein) of the AVF have reduced to baseline levels (<2Pa) following the high WSS levels induced during the creation of the anastomosis. The WSS values correspond to magnitudes reported in prior computational AVF studies [39, 230, 232]. This reflects the desired situation at six weeks post-AVF creation with respect to the 'rule-of-six' [3], where the flow rate exceeds

600mL/min whilst the venous diameter has exceeded 6mm to accommodate the increased flow rate. These conditions are achieved due to the outward remodelling of the cephalic vein, which occurs in conjunction with the maturation of the AVF. The unavoidably high TAWSS and low OSI values at the anastomosis remains an area of potential atherosclerotic and neointimal complications in the successfully matured AVF presented.

3.4.4 Conclusions and further work

This is the first study to demonstrate detailed dynamics of pulsatile blood flow from the aortic root to the distal arm arteries following AVF creation. Moreover, the use of CFD with FeMRA in this study demonstrates the potential for more thorough explanation of the complex haemodynamics associated with patient-specific AVF creation. Haemodynamic changes in the proximal vessels are of clinical importance for AVF maturation, NH and cardiovascular impact, while a central vein (or cephalic arch) stenosis is a common cause of AVF dysfunction and failure. For that purpose, a new methodological framework was presented involving the geometry reconstruction from multiple stacks of FeMRA-obtained medical images of a young patient. This is an important step towards understanding the blood flow development proximal to the arm region where an AVF is created in ESKD patients. The last part of the study involved a detailed haemodynamic analysis of the flow around a patient-specific AVF. This is advantageous in the pre-surgical planning and post-operative evaluation of AVFs, as the arterial blood flow and cross-sectional diameter before AVF formation is known to correlate with its maturation [233]. Additionally, the post-AVF venous blood flow rates relate to AVF maturation, hence analysis of the juxta-anastomosis haemodynamics becomes crucial in relation to success and failure rates. WSS is of high importance in this case, as outward remodelling occurs to reduce the WSS in the AVF over time [27]. The remodelling is associated with the increase in vessel diameter required for the increased flow rates.

An extension to this work will seek to investigate the differing haemodynamic environments in a cohort of patients with varying AVF anastomoses configurations and outcomes (success versus failure). This will include brachiocephalic fistulae in addition to radiocephalic fistulae. Additionally, the arterial wall motion will be accounted for in future numerical simulations of the local AVF haemodynamics by incorporating an FSI element into the investigation.

Chapter 4

Investigating juxta-anastomosis haemodynamics related to AVF success and failure in 6-week post-AVF geometries: a pilot study

4.1 Introduction

The arteriovenous fistula (AVF) is the clinically-preferred vascular access (VA) for commencing and completing regular haemodialysis [234], the most common renal replacement therapy (RRT) for chronic kidney disease (CKD) patients [235]. AVFs have lower mortality and infection risks in comparison to the other VA options, arteriovenous grafts (AVG) and central venous catheters (CVC) [236]. Furthermore, the native AVF is considered the preferential vascular access to initiate patients onto haemodialysis due to its comparably longer survival and lower complication rates [237]. Despite this, the widespread adoption of AVFs is hampered by their wide-ranging and often poor maturation, failure and patency rates (40-80%, 20-70%, 40-70%, respectively) [238–240]. Furthermore, Stoumpos et al. (2019) [95] completed a multicentre obversational cohort study, finding only 37.3% pre-dialysis and 48.3% dialysis patients were using AVFs for haemodialysis one-year after creation. This is notable with the increasing proportion of elderly and frail patients receiving haemodialysis due to end-stage renal disease (ESRD) [241].

The resulting increase in interventions and the number of AVFs failing to mature and the decrease in patency rates is an area of concern [242]. For future AVF planning, a key question in the vascular access research community is whether biometric (age, ethnicity, etc.) or haemodynamic factors are more prominent in the successful development of AVFs. This is the research question this Chapter investigated.

With in-vivo assessments of the AVF haemodynamic environment providing limited information of the flow characteristics in the blood vessels, computational fluid dynamics (CFD) has been previously used for characterising the flow structures within the AVF anatomies [185, 243, 39, 34, 185, 156, 244, 177, 99, 112, 182]. However, a key limitation of prior AVF studies has been the acquisition of patient-specific vessel anatomies. This has synthesised studies using idealised anatomies [40, 245, 181]. The use of FeMRA in this research avoided the contraindicating nature of traditional CT and MRI contrast agents in the ESRD population [138, 246, 132, 247], permitting the acquisition of high-quality images. In addition to the AVF geometry, the imaging protocol enabled the extraction of flow waveforms using phase-contrast MRI (PC-MRI). This permitted patient-specific boundary conditions to be applied to the CFD domains in order to replicate patient-specific flow rates within the computational AVF vessels. Of the 17 patient-specific AVF geometries presented; 8 cases were successful radiocephalic fistulae (RCF), 2 cases were unsuccessful RCF, 4 cases were successful brachiocephalic fistulae (BCF), 2 cases were unsuccessful BCF, and 1 case was a successful BBF.

In addition to addressing the relative impact of biometric and haemodynamic factors on AVF outcome, the other aims of the study were to elucidate desirable flow patterns in successful AVFs, and present how findings from AVF CFD simulations can be used in pre-surgical planning and post-surgical assessment. A ROC (Reciever operating characteristic) analysis was also completed to assess the diagnostic ability of individual vessel characteristics for high AVF venous flowrates ($> 1000 ml/min$).

4.2 Materials and methods

A similar workflow (Fig. 4.1) to the methodology presented in Hyde-Linaker et al. (2022) [246] was applied in all 17 patient geometries used in this study. In brief, after obtaining the high-quality patient images in the form of DICOM stacks, segmentation of the AVF vessels was completed in ITK-SNAP (www.itksnap.org) [215]. Surface (.stl) files were then processed in OpenFlipper (www.openflipper.org) [248] and Paraview (www.paraview.org) [249] before being imported into Simcenter STAR-CCM+ (Siemens Industries Digital

Software) for pre-processing and simulation. Segment v3.0 R7946 [250] was used for extracting the phase-contrast waveforms that were used as boundary conditions. Polyhedral meshes were generated in Simcenter STAR-CCM+ for discretising the domains, utilising mesh characteristics determined in a mesh independence analysis test case (Appendix C.2). This methodology protocol provided an efficient workflow and minimised user error where possible.

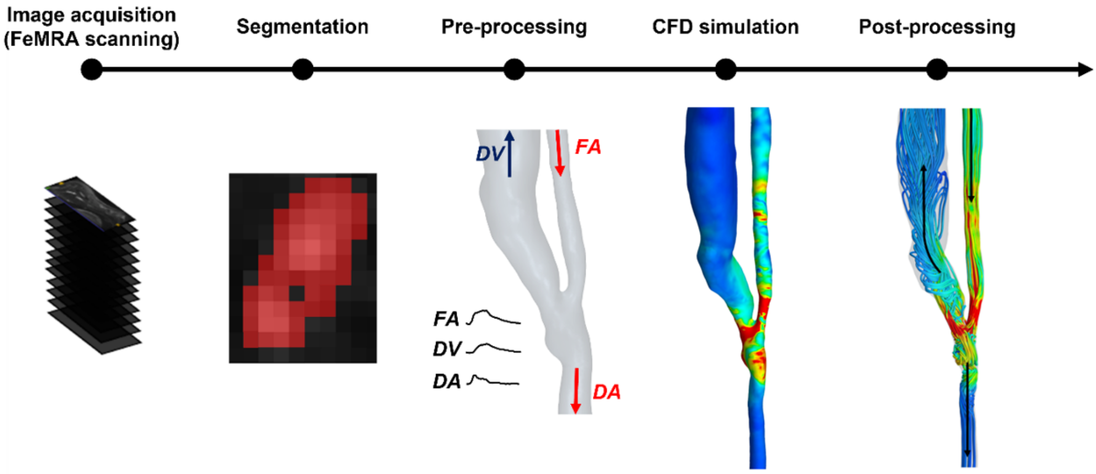

Fig. 4.1 The workflow utilised in this study, from image acquisition to CFD modelling. Where FA: Feeding artery; DV: Draining vein; DA: Distal artery.

4.2.1 Ferumoxytol-enhanced magnetic resonance angiography (FeMRA)

All FeMRA scans were performed on a 3.0T Prisma MRI scanner (Magnetom, Siemens Medical Solutions) with local phased-array imaging coils using a standardised protocol similarly to standard MRA studies with GBCAs (Appendix A.1). All patients were imaged in the supine position [246, 213]. The AVF geometries presented in this study were scanned six weeks after AVF creation, as per the KDOQI guidelines [3], which state that after 6 weeks a successful AVF should have a flow rate in excess of 600mL/min, a venous diameter greater than 6mm, a vein depth less than 6mm, and a cannulation length greater than 6cm.

The details of the CKD population used in this study can be found summarised in Table 4.1.

Table 4.1 Subject population used for the current study (M: Male; F: Female; L: Left arm; R: Right arm; BCF: Brachiochephalic Fistula; RCF: Radiocephalic Fistula; BBF: Brachiobasilic fistula; S: Successful AVF outcome; U: Unsuccessful AVF outcome).

Patient ID	Sex	Age	Ethnicity	BMI	Smoking status	Access side	AVF	Long-term outcome
#45	M	50	White Caucasian	29.8	Ex-smoker	R	BBF	S
#40	M	56	Far East Asian	22.8	Ex-smoker	L	BCF	S
#60	F	41	White Caucasian	22.8	Never	L	BCF	S
#69	F	69	White Caucasian	36.5	Never	L	BCF	S
#71	F	43	White Caucasian	19.3	Current	L	BCF	S
#06	M	75	Far East Asian	31.1	Ex-smoker	L	RCF	S
#18	F	59	White Caucasian	32.0	Never	L	RCF	S
#34	F	68	White Caucasian	30.8	Never	L	RCF	S
57	M	71	White Caucasian	27.8	Ex-smoker	L	RCF	S
#64	M	67	White Caucasian	24.1	Never	L	RCF	S
#65	M	19	White Caucasian	18.1	Never	L	RCF	S
#77	M	78	White Caucasian	29.1	Never	L	RCF	S
#87	M	55	Far East Asian	30.3	Never	L	RCF	S
#44	M	64	White Caucasian	29.5	Ex-smoker	L	BCF	U
#80	F	55	Far East Asian	31.7	Never	R	BCF	U
#72	M	75	White Caucasian	24.8	Never	L	RCF	U
#79	M	41	White Caucasian	27.1	Ex-smoker	L	RCF	U

4.2.2 Conversion of FeMRA images data to three-dimensional computational models

Segmentation

The DICOM stacks acquired from the FeRMA imaging phase (regular Cartesian grids of greyscale data) [149] were processed using ITK-SNAP [215] to segment the vessels of interest (VOI). The ‘snake-evolution’ tool within ITK-SNAP was used (Fig. 4.2) in conjunction with manual segmentation for semi-automatically segmenting the VOI. This permitted the user to focus their manual segmentation time on the regions of interest (ROI). The key ROI in this study was the anastomosis bifurcation of the AVF.

In the segmentation workflow, volume renderings (Appendix A.8) and patient notes aided the identification of the AVF vessels (Fig. 4.2A). This permitted lower and upper greyscale values corresponding to the VOI to be identified. These values specify exclusion regions for the tool (non-blue regions in Fig. 4.2A). The ‘Snake Evolution’ tool was applied at this stage for performing the semi-automatic segmentation step. Seed points are specified in the VOI, and are subsequently expanded within the included (white) regions when the tool is run. The process of this is displayed in Figure 4.2B. Due to the complex haemodynamics and the scan resolution at the anastomosis, a large percentage of the outputs from the semi-automatic tool (in the cohort) excluded the juxta-anastomosis region (Fig. 4.2B). Manual segmentation in these regions was required in these cases in order to complete the segmentation of the VOI (Fig. 4.2C). The resulting segmentation was then inspected and edited to remove any undesired regions prior to export it in .stl format. This segmentation approach was validated through the computation of a DICE score for an aorta and AVF geometry as that described in Chapter 3.

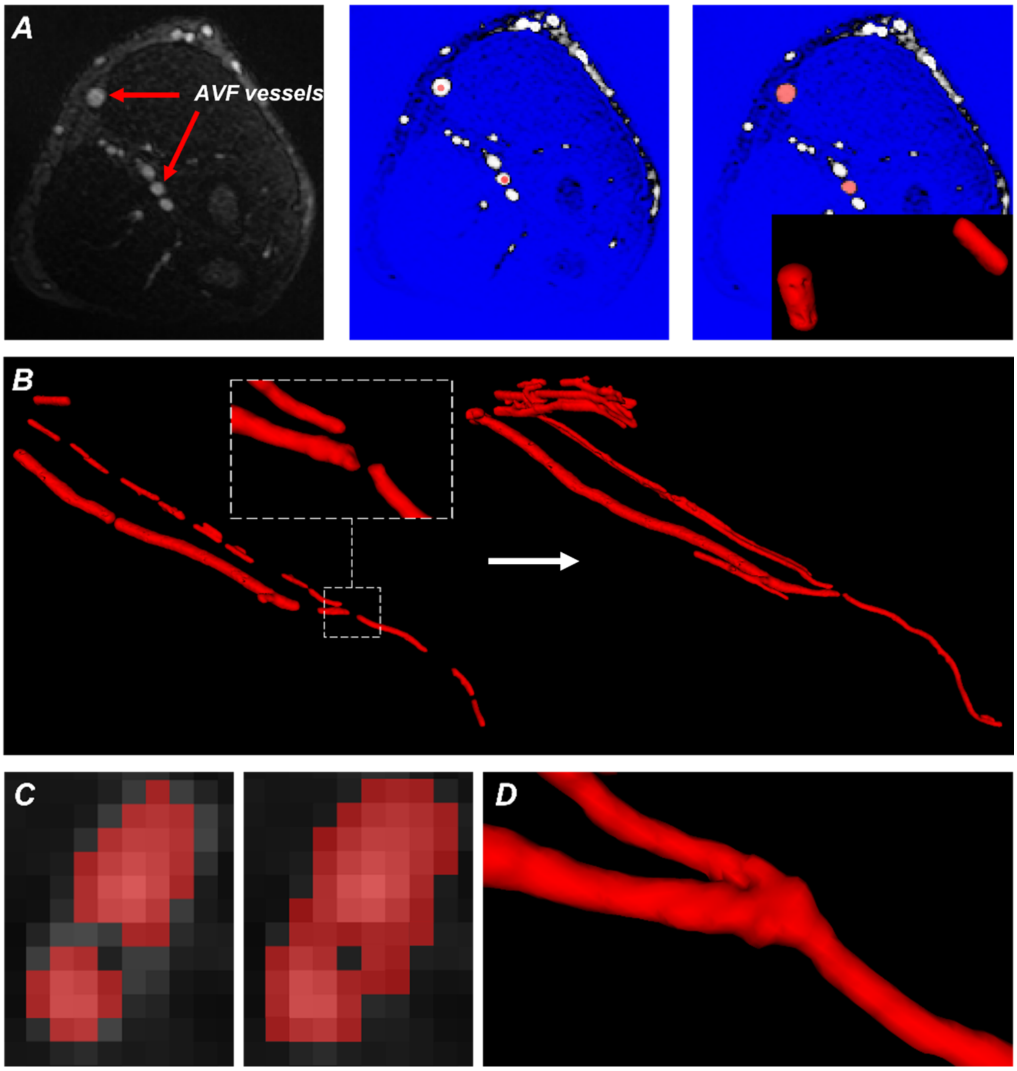

Fig. 4.2 Example AVF vessel segmentation using ITK-SNAP, A) The process of applying the ‘snake-evolution’ tool in the 2D view, where the blue region represents the excluded greyscale values, B) Evolving segmentations using the tool, C) Manual segmentation at the AVF anastomosis, D) Resulting segmentation with gaussian smoothing in ITK-SNAP.

Preparation steps

Following the generation of the surface mesh, remeshing and smoothing filters were iteratively applied to refine the VOI, and refined meshing was also applied at bifurcation

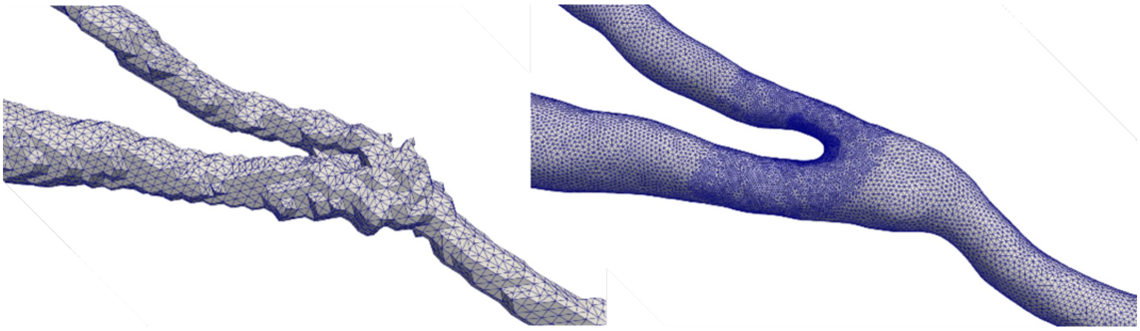

Fig. 4.3 AVF surface file example prior to (left) and following (right) iterative remeshing and smoothing operations with OpenFlipper.

locations (Fig. 4.3). This process is completed by refining the mesh to a higher resolution than the voxel size, ensuring that the smoothing filter does not remove parts of the segmentation. Crucially, this process must generate a smoothed mesh that is valid with respect to the original segmentation (Fig. 4.3). This was verified based on the location of the vessel lumen on the original FeMRA images. Lastly, Paraview was then utilised for clipping the surface file at the locations that the PC-MRI flow waveforms were acquired. Using the DICOM stack to define a reference point within the segmentation process was found to be the easiest way of achieving this. The surface file was clipped normal to the centrelines of the vessel, which were computed using VMTKlab, a GUI-based version of the Vmtk (Vascular modelling toolkit) libraries (www.vmtk.org). The clipped locations are the inlet and outlets of the computational domain in the CFD simulation, as the flow rates are known at these locations.

An extra step specific to this study was to use the clipping tool in Paraview for subdividing the AVF vessels into 1cm segments (Fig. 4.4). It is noted that the anastomosis area is depicted separately in light grey colour. This permitted a thorough breakdown of the localised haemodynamics in each patient.

Extraction of phase contrast data for boundary conditions

The flow at each inlet and outlet patch was specified using waveforms from phase-contrast data (Appendix C.1). The flowrates within the AVF vessels were imaged above and below the location of the anastomosis. This permitted the inlet and outlet waveforms of the computational models to be defined as per the PC-MRI flow waveforms. Segment version 3.0 R7946 [250] was used for acquiring the volumetric flow rates from the PC-MRI (Appendix C.1). The volumetric flow waveforms for use within Simcenter STAR-CCM+. To ensure the conservation of mass and momentum in the simulations, one assumption made was to set the flow rate in the draining artery outflow (Q_{DA}) to equal the feeding

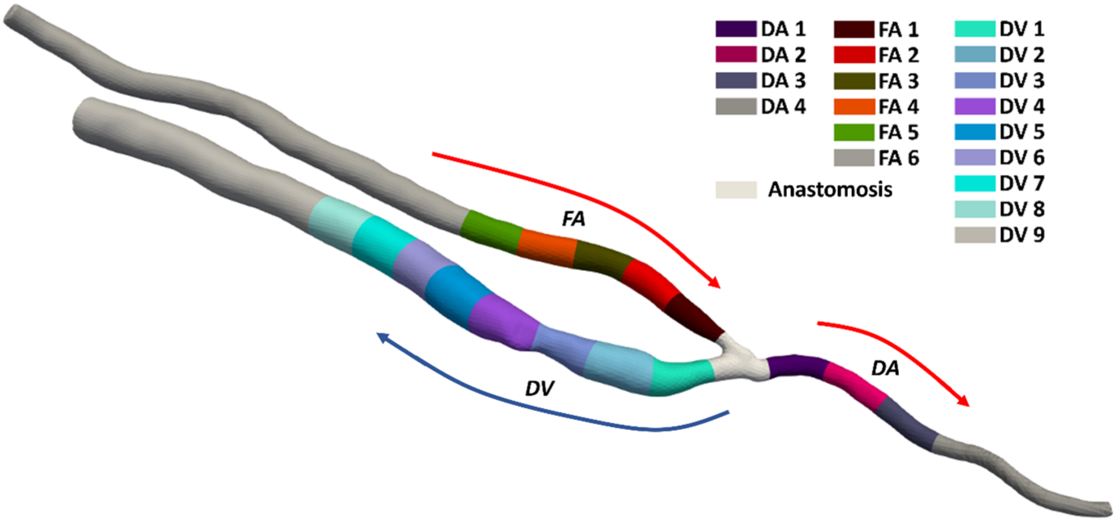

Fig. 4.4 Example of subdivided AVF computational domain (FA: Feeding artery; DV: Draining vein; DA: Distal artery). The number assigned to each 1cm segment corresponds to its distance from the anastomosis, i.e. DA1, FA1, DV1 are the 1cm-segments nearest to the anastomosis, DA2, FA2, DV2 are the second-nearest 1cm-segments to the anastomosis and so on. The final segment of each vessel is not a region analysed (DA4, FA6, DV9). The arrows indicate the direction of blood flow for each artery/vein.

artery flowrate (Q_{FA}) minus the flow rate in the draining vein (Q_{DV}). This assumption was considered logical due to the scan resolution and cross-sectional size of the distal artery (below the anasotmsis) being less reliable than the proximal PC-MRI data.

4.2.3 Model details and haemodynamic metrics

Polyhedral meshes were generated in Simcenter STAR-CCM+ for discretising the domain in each case, utilising mesh characteristics determined in a mesh independence analysis test case (Appendix C.2).

Modelling details

A scale-resolving hybrid turbulence model in STAR-CCM+ was utilised for modelling the blood flow (as described in Chapter 3). This permits the computation of unsteady large-scale turbulence structures whilst having a computational expense similar to a Reynolds-Averaged Navier-Stokes (RANS) model. Duffal et al. (2019) [218] details further information relating to the SRH model utilised in the CFD investigations. The decomposed solution variables from the SRH model are utilised in the Navier-Stokes equations to yield filtered transport equations of mass, momentum, and energy. The governing equations of the flow field, the Navier-Stokes equations are defined by:

$$\nabla . u = 0 \tag{4.1}$$

$$\rho \frac{\partial u}{\partial t} + \rho (u.\nabla) u + \nabla . p = \mu \nabla^2 u \tag{4.2}$$

where u is the velocity vector, p is the pressure, ρ is the fluid density, and μ is the fluid viscosity.

As with Hyde-Linaker et al. 2021 [246], the simulations were completed using a segregated pressure-based flow solver on a finite volume implementation in Star-CCM+ (t=0.001s). A SIMPLE (Semi-Implicit method for pressure-linked equations) pressure-velocity coupling algorithm was used, in addition to an optimised 2nd order temporal discretisation. This reduces the leading-order truncation error by a factor of 2, compared to base-level 2nd-order temporal discretisation [219]. Additionally, a generalised Carreau-Yasuda non-Newtonian model [246, 209] was implemented with values from the literature (Chapter 3, Appendix B.9). This is a preferential assumption over using a Newtonian fluid model which omits the 'shear-thinning' property of blood and manifests at shear rates below $50 - 100s^{-1}$.

4.2.4 Haemodynamic parameter defintions

In computational modelling the continuum assumptions can influence the haemodynamic-induced WSS parameters of interest. To ascertain the influence of the haemodynamics on the arterial and venous vessels, several WSS-related metrics were computed and assessed in post-processing. For a comprehensive description of these metrics, the reader is invited to review Browne et al. (2016) [112]. Time-averaged wall shear stress (TAWSS) is indicative of the force induced on the vessel wall over the entire cardiac cycle [251], whereas the oscillatory shear index (OSI) and transverse WSS (transWSS) metrics seek to characterise the multi-directional nature of WSS in disturbed flows. OSI is a dimensionless metric used for characterising the alignment between the WSS vector and TAWSS during the cardiac cycle. The transWSS metric computes time-averaged WSS elements perpendicular to the mean flow. WSSG, the WSS spatial gradient, is derived from the WSS gradient tensor components parallel and perpendicular to the time-averaged WSS vector. These WSS metrics are defined as per Equations 4.3-4.6.

$$TAWSS = \frac{1}{T} \int_{0}^{T} |\tau_w| \, dt \tag{4.3}$$

$$OSI = \frac{1}{2}\left(\frac{\left|\int_0^T \tau_w dt\right|}{\int_0^T |\tau_w|\, dt}\right) \tag{4.4}$$

$$transWSS = \frac{1}{T}\int_0^T |\vec{\tau_w}.(\vec{n} \times \frac{\int_0^T \vec{\tau_w} dt}{|\int_0^T \vec{\tau_w} dt|})| dt \tag{4.5}$$

$$WSSG = \sqrt{(|\frac{\partial \vec{\tau_w}}{\partial x}|)^2 + (|\frac{\partial \vec{\tau_w}}{\partial y}|)^2 + (|\frac{\partial \vec{\tau_w}}{\partial z}|)^2} \tag{4.6}$$

where $\vec{\tau_w}$ represents the WSS vector and T represents the period of the cardiac cycle.

In addition to the WSS metrics, Localised normalised helicity (LNH) was assessed. LNH [252] is a haemodynamic marker previously suggested to be key in the development of favourable AVF haemodynamics related to successful maturation. LNH is defined as per Equation 4.7. As stated in Morbiducci et al. (2009) [253], LNH is a function of space and time, characterized by a velocity vector V, and it is the local value of the cosine of the angle between the velocity and vorticity vectors [254]. The values for LNH range between -1 and +1, with the sign indicating the direction of rotation [252]. The value of the non-dimensional quantity (LNH) demonstrates when the flow is purely helical (when the absolute value is 1), and zero, where fluid dynamical reflectional symmetry is present [182]. The isosurfaces presented in the thesis have absoulte LNH values greater than or equal to 0.9.

The reader is invited to review Garcia et al. (2017) [252] and Cunnane et al. (2019) [182] for further information regarding the computation of the non-dimensional LNH metric.

$$LNH(x,t) = \frac{V(x,t).\omega(x,t)}{\mid V(x,t) \mid\mid \omega(x,t) \mid} \tag{4.7}$$

where V and ω are the velocity and vorticity vectors [252].

4.2.5 ROC analysis

Along with the CFD component to this investigation, a ROC analysis was used for assessing the diagnostic ability of a binary classifier for discriminating between two patient states. ROC curves are created by plotting the true positive rate (TPR) against false positive rate (FPR). TPR is known as sensitivity (or the probability of detection), FPR is known as $1-$ specificity (or the probability of false alarm). For more information regarding ROC analyses, the reader is referred to Flach (2016) [255].

4.3 Results

The results section of this chapter are subdivided into the following sub-sections; i) vessel characteristics and flow waveforms (including a ROC analysis of vessel characteristics), ii) Biometric factors, and iii) CFD results. The 17 AVF anatomies studied within this Chapter are displayed in Fig. 4.5. With the number of datasets studied and simulated, the cohort was sub-divided into sub-groups based on AVF morphology and outcome (i.e. successful BBF, successful BCF, successful RCF, unsuccessful BCF, and successful RCF).

4.3.1 Vessel characteristics and flow waveforms

The flow rates extracted from the PC-MRI data using Segment v3.0 R7946 [250] (Appendix C.1), and the cross-sectional inscribed diameters of the AVF vessels (feeding artery, draining vein, and draining artery) computed using VMTKlab (Appendix A.3), are given in Figures 4.6-4.7 respectively. A case-by-case breakdown of the vessel waveforms and characteristics are given in Appendix C.5, and the mean feeding artery and draining vein centreline characteristics (observed in the region from the anastomosis up to 10cm along the centreline) are given in Table 4.2.

Flow waveforms

Figure 4.6 presents the mean sub-group flow rate waveforms over a cardiac cycle (normalised with respect to time).

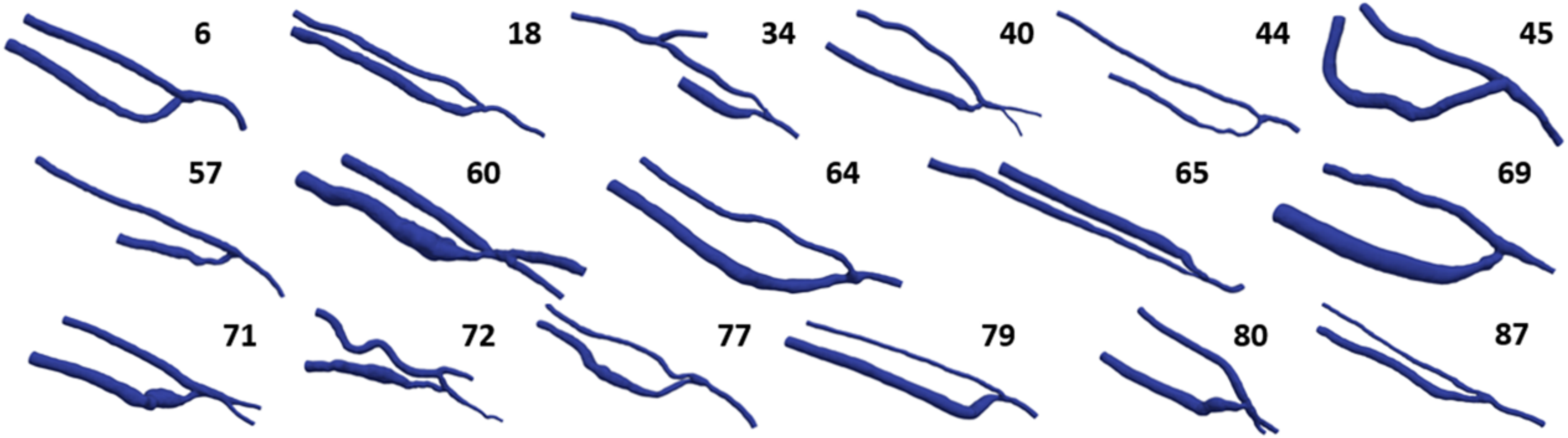

Fig. 4.5 The cohort of AVF anatomies studied within Chapter 4.

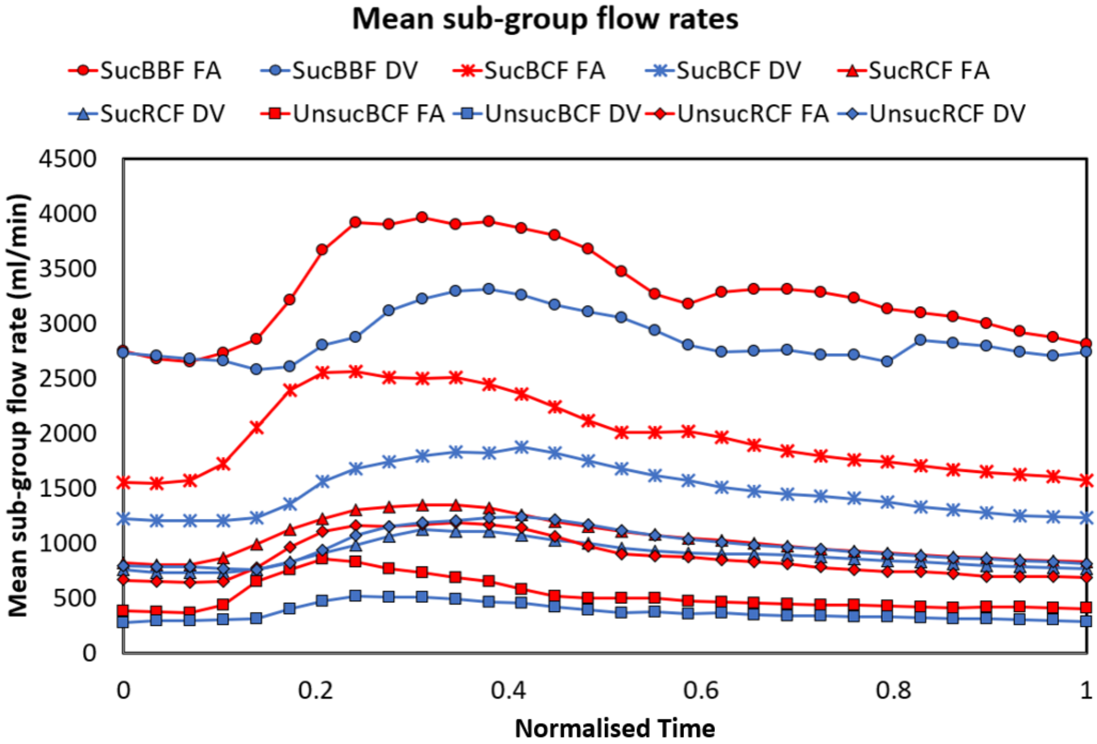

Fig. 4.6 Mean feeding artery (FA) and draining vein (DV) flow-rate (Q_{FA} and Q_{DV}) waveform of each sub-group (defined by success and morphology), normalised with respect to time. A further breakdown of the case-by-case flow waveforms and inscribed diameters (in addition to centerline curvature and torsion) are given in Appendix C.5.

The successful BBF case (n=1) exhibited the greatest feeding artery (FA) and draining vein (DV) flow rates (mean Q_{FA}=3290.1ml/min, mean Q_{DV}=2862.5ml/min), followed by the successful BCF (n=4) sub-group, (mean Q_{FA}=1982.1ml/min, mean Q_{DV}=1481.8ml/min), the successful RCF (n=8) sub-group, (mean Q_{FA}=1035.7ml/min, mean Q_{DV}=892.7ml/min), the unsuccessful RCF (n=2) sub-group, (mean Q_{FA}=871.5ml/min, mean Q_{DV}=972.3ml/min), and the unsuccessful BCF (n=2) sub-group, (mean Q_{FA}=524.3ml/min, mean Q_{DV}=370.8ml/min). A minor phase-shift between the maxima flow rate observed in the feeding artery and the draining vein in all sub-groups, as anticipated.

Vessel characteristics

The cross-sectional inscribed diameters of the AVF vessels (feeding artery, draining vein, and draining artery) computed using VMTKlab (Appendix A.3), are given in Figures 4.7. A case-by-case breakdown of the vessel waveforms and characteristics are given in Appendix C.5, and the mean feeding artery and draining vein centreline characteristics (observed in the region from the anastomosis up to 10cm along the centreline) are given in Table 4.2.

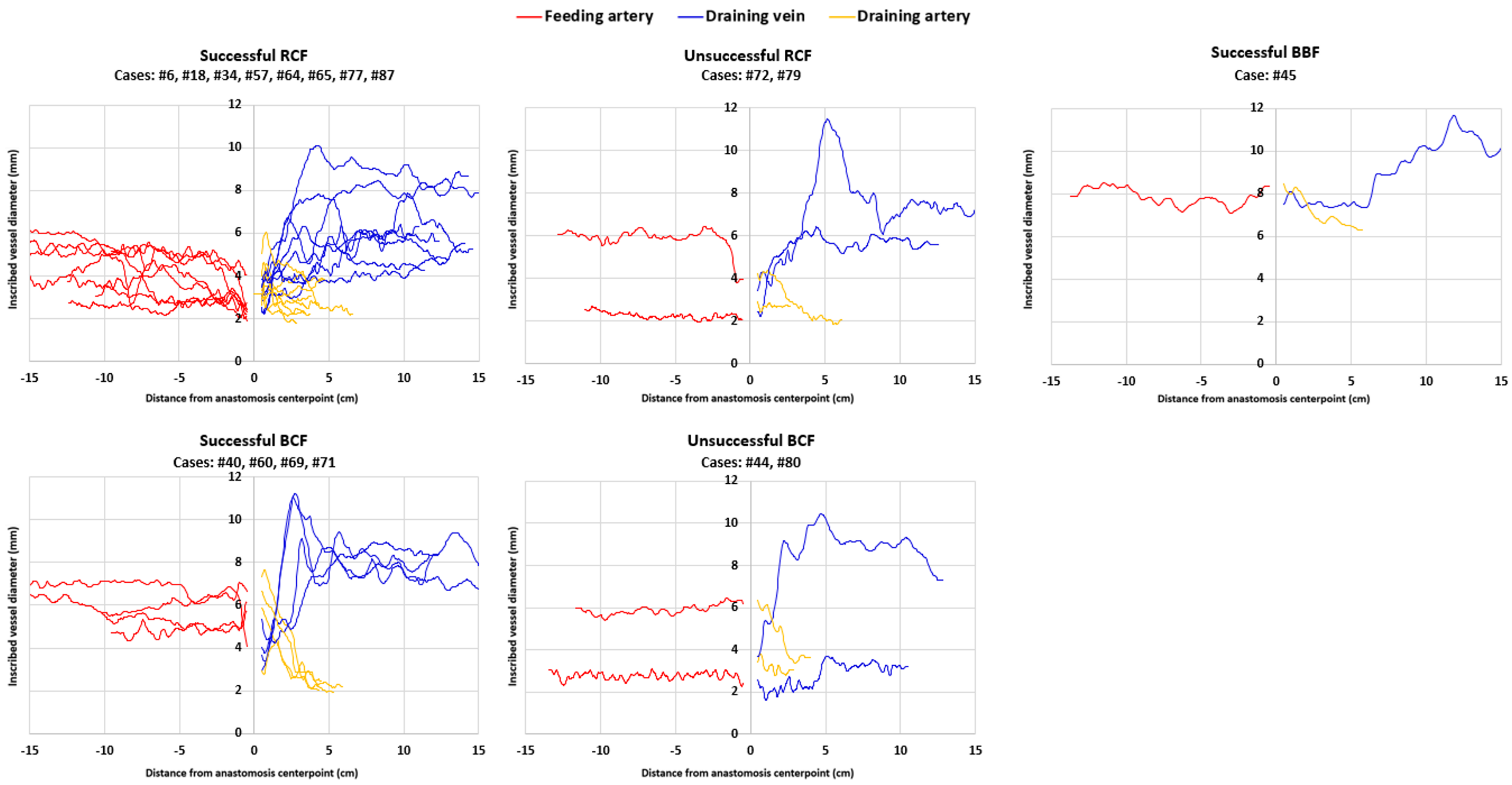

Fig. 4.7 The inscribed diameters along the centrelines of the plotted in sub-groups (defined by success and morphology). Where distance = 0 is the centrepoint of the anastomosis (the centreline intersection point of the anastomosis vessel centrelines), blue lines represent the draining vein, red lines represent the feeding artery, and orange lines represent the draining artery. A further breakdown of the case-by-case flow waveforms and inscribed diameters (in addition to centerline curvature and torsion) are given in Appendix C.5.

Table 4.2 Subject population centreline characteristics (where **mean** feeding artery and draining vein characteristics were evaluated up to 10cm along centreline length, and draining artery characteristics were evaluated up to 5cm along centreline length). Where FA is feeding artery, DV is draining vein, DA is draining artery, S is successful, U is unsuccessful, and D is inscribed diameter.

Sub-group	ID	FA D (mm)	FA Curvature (m^{-1})	FA Torsion (m^{-1})	DV D (mm)	DV Curvature (m^{-1})	DV Torsion (m^{-1})	Anastomosis angle (°)
S RCF	# 6	4.998	0.024	0.391	4.892	0.038	0.107	59.4
S RCF	# 18	4.801	0.025	0.051	6.782	0.042	0.179	61.6
S RCF	# 34	3.723	0.060	0.132	6.239	0.055	0.128	72.9
S RCF	# 57	4.644	0.045	0.176	3.921	0.026	-0.064	60.1
S RCF	# 64	2.922	0.045	-0.245	4.618	0.036	-0.061	72.2
S RCF	# 65	3.841	0.021	-0.153	8.274	0.036	-0.008	26.1
S RCF	# 77	3.108	0.045	-0.030	4.634	0.062	0.075	24
S RCF	# 87	2.641	0.036	0.048	5.511	0.036	0.077	31.5
U RCF	# 72	5.830	0.067	-0.089	7.231	0.055	0.137	80.1
U RCF	# 79	2.226	0.035	-0.015	5.447	0.054	0.195	60
S BCF	# 40	5.230	0.018	-0.158	7.175	0.036	0.096	91.4
S BCF	# 60	6.725	0.014	0.014	7.907	0.035	-0.016	80.4
S BCF	# 69	4.810	0.028	0.177	7.942	0.022	0.186	75.8
S BCF	# 71	6.065	0.013	-0.075	8.059	0.044	-0.125	64.7
U BCF	# 44	2.753	0.046	-0.207	2.832	0.075	0.241	94.9
U BCF	# 80	5.916	0.020	-0.238	8.639	0.037	-0.156	68.2
S BBF	# 45	7.729	0.020	-0.038	8.247	0.029	0.046	81.1

Radiocephalic AVF (#6, #18, #34, #57, #64, #65, #77, #87, #72, #79)

The mean feeding artery inscribed diameter was similar in successful RCF outcomes (3.84mm) when compared to the unsuccessful RCF cases (4.03mm). However, this is largely due to an outlier in unsuccessful RCF sub-group (5.83mm) in sub-group size of 2. The mean draining vein inscribed diameter was higher in the unsuccessful RCF sub-group (6.34mm) when compared to the successful RCF group (5.61mm), this is mainly due to the same outlier case (7.23mm). In this case it is hypothesised that the vein has not become sufficiently arterialised in the weeks following surgery, which resulted in the AVF failing whilst having an increased venous diameter.

The mean curvature of the feeding artery was lower in successful RCF sub-group (successful = 0.038, unsuccessful = 0.051 mm^{-1}), furthermore, the successful RCF cases had a lower mean curvature in the draining vein (successful DV = 0.041, unsuccessful DV = 0.054 mm^{-1}). Lastly, the successful RCF cases (51.0°) had a much lower mean anastomosis angle than the unsuccessful cases (70.1°).

Brachiocephalic AVF (#40, #60, #69, #71, #44, #80)

The feeding artery of the successful BCF sub-group had a higher mean inscribed diameter (5.71mm) and a lower curvature (0.018 mm^{-1}) than the unsuccessful cases (4.33mm, 0.033 mm^{-1}). The mean draining vein inscribed diameter was greater in the successful BCF (7.77mm) and the mean curvature was lower (0.034 mm^{-1}), the unsuccessful mean values were 5.74mm and 0.056 mm^{-1}. The anastomosis angles were comparable in both BCF sub-groups (78.1° and 81.6° in successful and unsuccessful groups respectively).

Successful AVF morphology comparison

The mean inscribed diameters were as anticipated, with the mean BBF diameter being the greatest (7.73mm), followed by BCF (5.71mm), and then RCF (3.84m). The RCF sub-group had the highest feeding artery curvature (0.038 mm^{-1}). The curvature of draining vein in the successful BCF (0.034 mm^{-1}) and RCF sub-groups (0.041 mm^{-1}) was greater than the successful BBF (0.029 mm^{-1}). The draining artery curvatures were comparable across the sub-groups. The successful RCF sub-group had a much lower anastomosis angle, followed by the BCF sub-group, and then the BBF.

ROC analysis of vessel characteristics

The two patient states selected for the ROC analysis was whether the patient presented a venous flow rate less or greater than $1000 ml/min$. This value was set to be greater than the ‘rule-of-six’ criterion, which states a successful AVF should have a venous flow rate greater than $600 ml/min$. The value of $1000 ml/min$ gave 8 patients with a successful (High flow - H) patient state, and 9 patients with an ‘unsuccessful’ patient state (Medium - M or Low - L flow). This breakdown is given in Table 4.3, and the total venous flow rate waveforms are shown in Figure 4.10.

Following the classification of high and low venous flow rates, a ROC analysis was performed in R software version 4.2.3 [256]. Table 4.4 gives the area-under-curve (AUC) for each of the characteristics individually considered in the ROC analysis (Fig. 4.11). The AUC values were obtained using the raw data from the 17 subjects. Due to the limited number of datasets, AUC results obtained using some polynomial interpolation methods in R 4.2.3 [256] are given in the Appendix C.3.

Table 4.3 Classification of venous flowrates for the cohort used in the ROC analysis of the AVF. Where a flowrate greater or equal to 1000 ml/min is considered high (H), a flowrate between 600-1000ml/min is considered medium-low (M-L), and a flowrate less than 600 ml/min is considered low.

Patient	Venous outflow average (ml/min)	Classification	AVF type
#6	1032.9	H	RCF
#40	1360.6	H	BCF
#45	2862.5	H	BBF
#60	1783.3	H	BCF
#65	1753.0	H	RCF
#69	1276.6	H	BCF
#71	1506.6	H	BCF
#72	1368.0	H	RCF
#18	828.6	M (L)	RCF
#34	704.8	M (L)	RCF
#64	906.0	M (L)	RCF
#77	861.8	M (L)	RCF
#80	694.1	M (L)	BCF
#44	46.5	L	BCF
#57	454.3	L	RCF
#79	576.6	L	RCF
#87	599.1	L	RCF

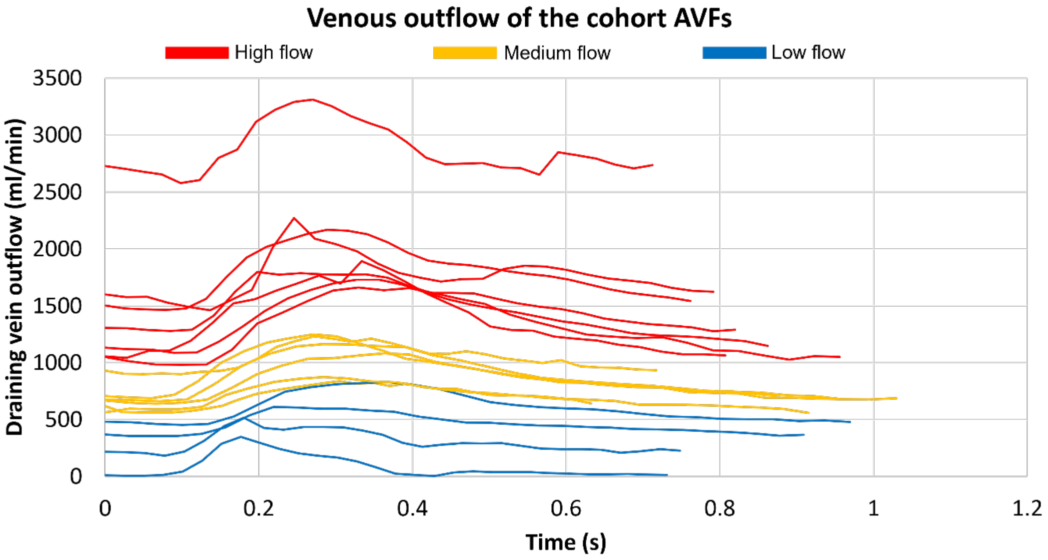

Fig. 4.8 AVF venous outflows of the cohort (classified by venous outflow flowrate). Where flowrates in excess of 1000ml/min are considered high, flowrates between 600-1000ml/min are considered medium, and flowrates below 600ml/min are considered low.

Table 4.4 Area under curve (AUC) values of ROC curves presented in 4.9-4.10

Characteristic	AUC (raw data)
Angle	0.6667
Draining vein curvature	0.4583
Draining artery curvature	0.7014
Feeding artery curvature	0.8194
Draining vein diameter	0.7361
Draining artery diameter	0.7222
Feeding artery diameter	0.7639
Systolic blood pressure	0.6528
Heart rate	0.7014
BMI	0.7083
Age	0.6042

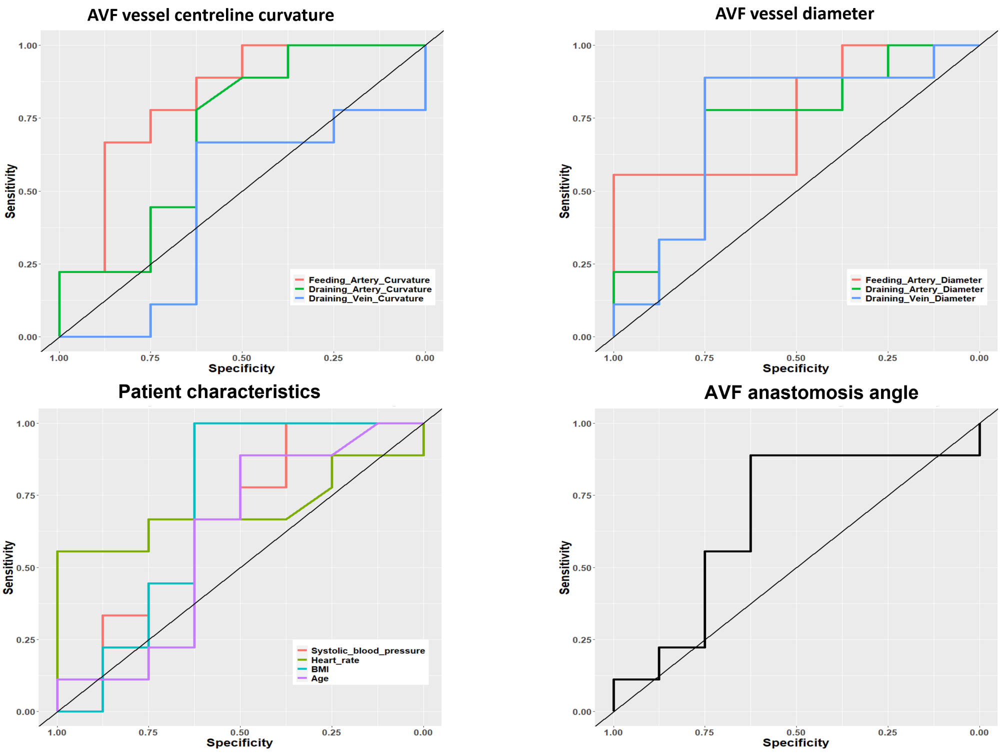

Fig. 4.9 ROC curves for vessel curvature, diameter, patient characteristics, and anastomosis angle using original datasets (n=17). The binary classification between ‘successful’ and ‘unsuccessful’ cases was a venous flow rate greater than or equal to $1000ml/min$.

The closer the AUC value is to 1, the more prominent that factor is in determining AVF ‘high-flow’. However, if the value is almost 1, there may be issues in the setup of the ROC analysis. This was avoided in the ROC analysis presented, and the ROC AUC values were in an acceptable range. An AUC vale of 0.5 (shown by the black lines in Figs. 4.9-4.10) denotes an agnostic indication of high venous flow rate for the metric studied. For example, the draining curvature value was the worse AUC value (0.4583), this infers that is perhaps an inverse relation between high venous flowrates and high draining vein curvature.

The three metrics with the highest AUC values were the feeding artery curvature (0.8194), feeding artery diameter (0.7639), and draining vein diameter (0.7361). An advantageous component of ROC analysis is that the simultaneous impact of multiple factors can be studied. Considering this, a ROC analysis of these three metrics combined was subsequently performed (Fig. 4.10). The AUC value of the combined ROC analysis was **0.830**, indicating a strong correlation between considering all three metrics and AVF success.

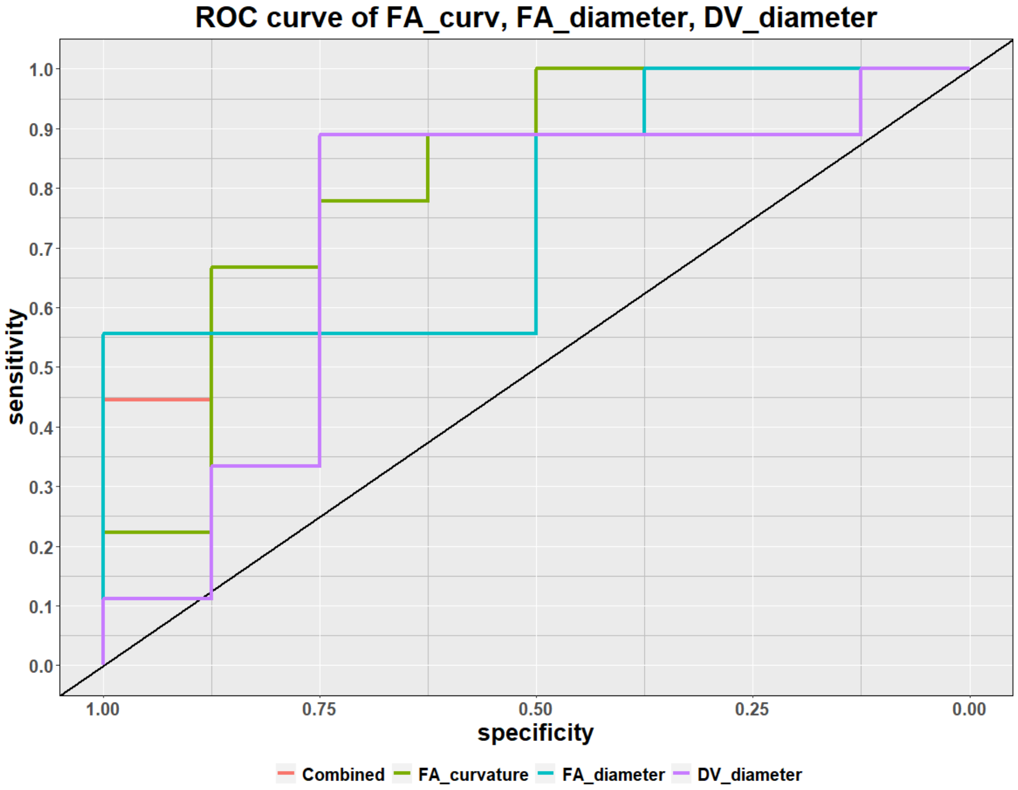

Fig. 4.10 ROC curves for Feeding artery curvature, Feeding artery diameter, Draining vein diameter, and the combined ROC curve of the three aforementioned metrics using original datasets (n=17). The binary classification between ‘successful’ and ‘unsuccessful’ cases was a venous flow rate greater than or equal to $1000ml/min$.

ROC analysis of the vessel characteristics demonstrated that feeding artery curvature (0.8194), feeding artery diameter (0.7639), and draining vein diameter (0.7361) were the most prominent determinants of AVF flow rates in excess of $1000ml/min$. The combined AUC value of these factors combined was 0.830.

These factors indicate that vessel diameter and the arterial curvature (notably the feeding artery curvature) should be the principal focus of vascular mapping sessions, patient-focused AVF planning, and the notable metrics assessed in the 6-week post-surgery follow-up.

4.3.2 Biometric factors

The biometric factors of the cohort are presented in this sub-section, grouped by AVF outcome and morphology. The biometric factors presented include age, BMI, ethnicity, systolic blood pressure, heart rate, and smoking history (Figs. 4.11-4.12).

When looking at the ages and BMI of the cohort, the mean age and BMI were lower in successful BCF when compared to unsuccessful BCF cases (successful BCF: $25.4kg/m^2$ and 52.3 years, unsuccessful BCF: $30.6kg/m^2$ and 59.5 years). Conversely, the mean age and BMI were higher in successful RCF than the unsuccessful RCF cases (successful RCF: $28.0kg/m^2$ and 61.5 years, unsuccessful BCF: $26.0kg/m^2$ and 58.0 years). The age of the successful BBF case (50 years) was comparable to the mean age of the successful BCF cases, while the BMI of the successful BBF ($29.8kg/m^2$) was higher than the mean BMI in both the successful BCF and RCF sub-groups. The composition of the overall cohort and the sub-groups are presented in Table 4.1 and Appendix C.7. The influence of ethnicity, smoking, sex, and pre-AVF status were found to be inconclusive, mainly thought to be due to the size of the cohort.

The successful BCF cases had higher outflow vein mean flow rates (22-30ml/sec) than the unsuccessful BCF cases (12ml/sec, excluding an unsuccessful BCF anomaly). Additionally, all successful BCF cases had a higher heart rate (78-85 bpm pre-AVF, 68-78 bpm post-AVF, Figs. 4.11-4.12) corresponding to a higher AVF flow rate than unsuccessful BCF (58-70 bpm pre-AVF). No differences were observed between successful and unsuccessful BCF cases due to systolic blood pressure, and age did not impact the feeding artery diameter. The vein depth characteristics (Figs. 4.11-4.12) were better in successful BCF cases, as anticipated. There was no clear difference on cannulation length based on outcome. Fig. 4.12 shows a plot of the outflow vein mean flow rate vs the feeding artery mean flow rate, where in combination all successful BCF have clearly higher flow rates (29-38ml/sec in the feeding artery, 20-30ml/sec in the outflow vein).

It was hypothesised that a lower BMI and age are generally more conducive to successful AVF outcome, whereas the RCF results suggest the opposite (Figs. 4.11-4.12). However, this may be due to the sample size of unsuccessful cases (n=2) and a large number of elderly patients in the successful RCF sub-group. With both RCF being the AVF morphology used for initiating patients onto haemodialysis, and the upward trend of elderly patients in the ESRD population, it is natural that this sub-group has an elevated age. Additionally, further inspection of the biometric graphs (Figs. 4.11-4.12) shows no trend in differences between the successful and unsuccessful RCF sub-groups. This is highlighted in the heart rate graphs, where the data points for both RCF outcomes are clustered. This is the same with the BMI-flow rate graphs, where the datapoints are clustered except for a single successful RCF case. Nonetheless, there was a clear cluster of successful RCFs in Fig. 4.12, with most cases having a 15-20 ml/sec flow rate in the feeding artery and

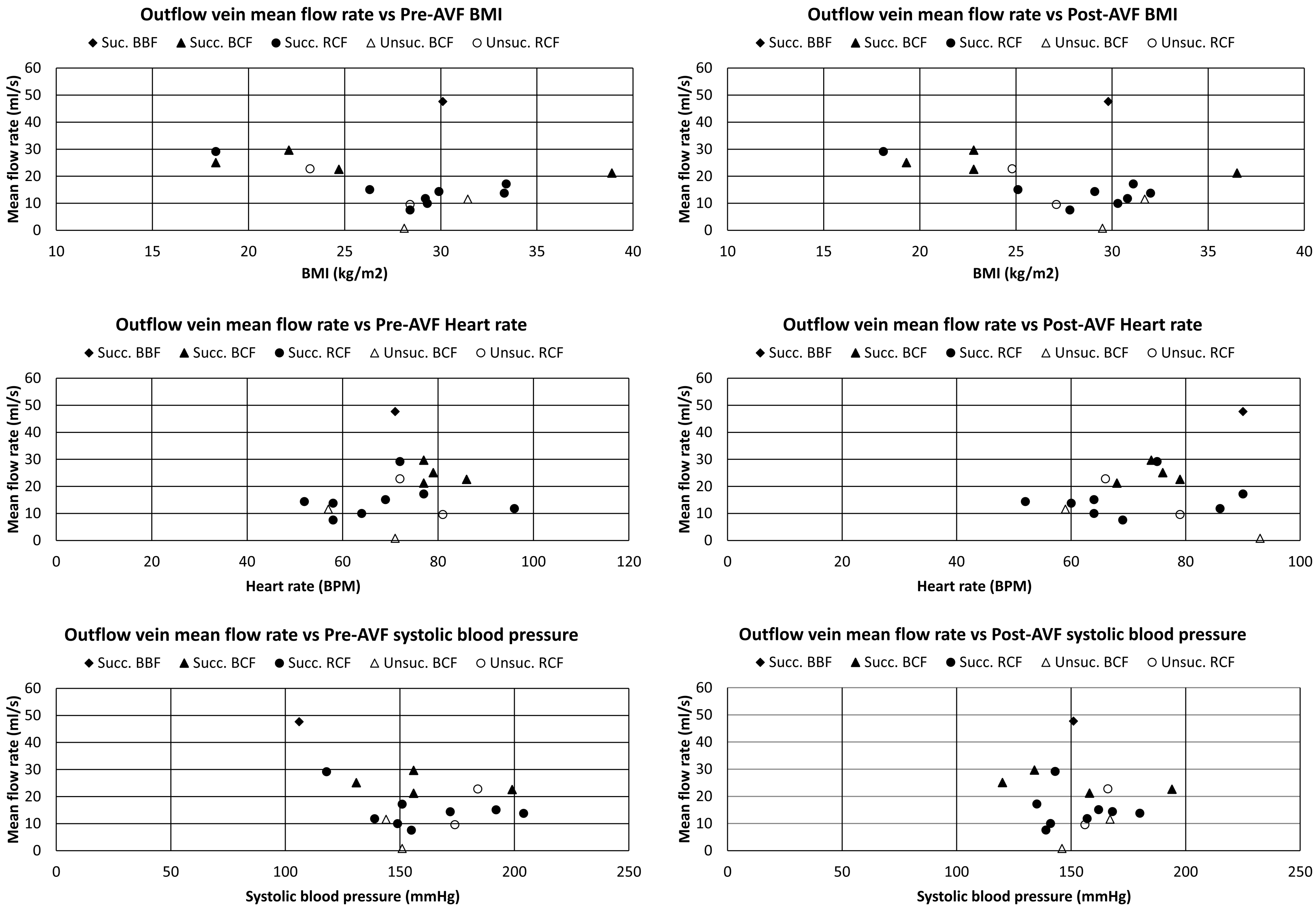

Fig. 4.11 Biometric graphs: Venous (outflow) flow rates against biometric factors measured on the same day as scan.

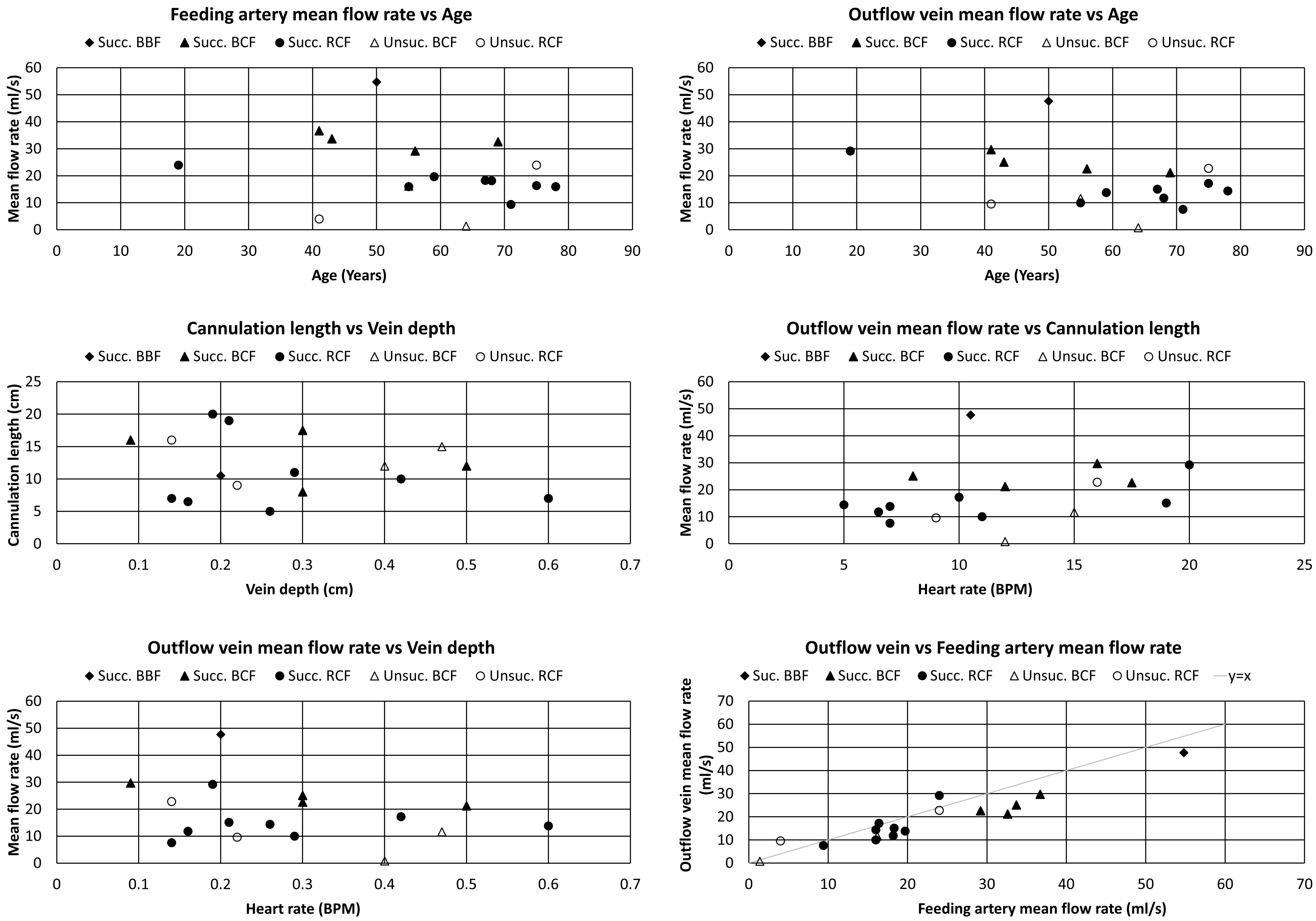

Fig. 4.12 Biometric graphs: Venous flow rates against biometric factors (2). (top row) Feeding artery mean flow rate and outflow flow rate vs age, (middle row) cannulation length vs vein depth and venous flow rate vs cannulation length, and (bottom row) venous flow rate against vein depth and feeding artery flow rate.

10-20ml/sec flow rate in the outflow vein, lower by about 15-18ml/sec and 10 ml/sec, respectively, from the successful BCF cases.

The successful cases had similar heart rates and blood pressures, except for the successful BBF case, which had an elevated heart rate and blood pressure. The successful BCF sub-group had a lower BMI and higher flow than the successful RCF sub-group. Additionally, the successful BCF sub-group had a lower age than the successful RCF sub-group. There was no pattern on the cannulation length or vein depth.

4.3.3 CFD analyses

The results of the CFD analysis are given in this sub-section. The CFD contour plots of TAWSS and WSSG are given alongside the velocity streamline and LNH isosrfuace plots at peak systole in Figs. 4.13-4.17. The LNH isosurfaces are indicative of regions where the absolute LNH value (the local value of the cosine of the angle between the velocity and vorticity vectors) are greater than 0.9. The OSI contour plots are given in the Appendix C.6. Using the results of the simulations, the mean TAWSS, transWSS, WSSG, and OSI values over the cardiac cycle for each 1cm segment of the AVF categories (successful BBF, successful BCF, successful RCF, unsuccessful BCF, unsuccessful RCF) is given in Fig. 4.18. In addition to the 1cm wall segments, the clipping of the domain gives multiple cross-sectional planes (in 1cm intervals) from which the in-plane radial velocity and LNH can be ascertained. These results are presented in Fig. 4.19.

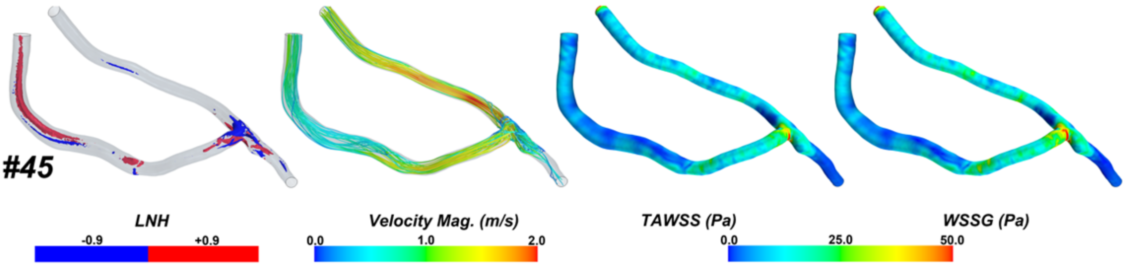

Fig. 4.13 Peak-systole flow (LNH and Velocity Magnitude) and WSS (TAWSS and WSSG) contour plots for the successful brachio-basilic fistulae (BBF) sub-group of the cohort (n=17).

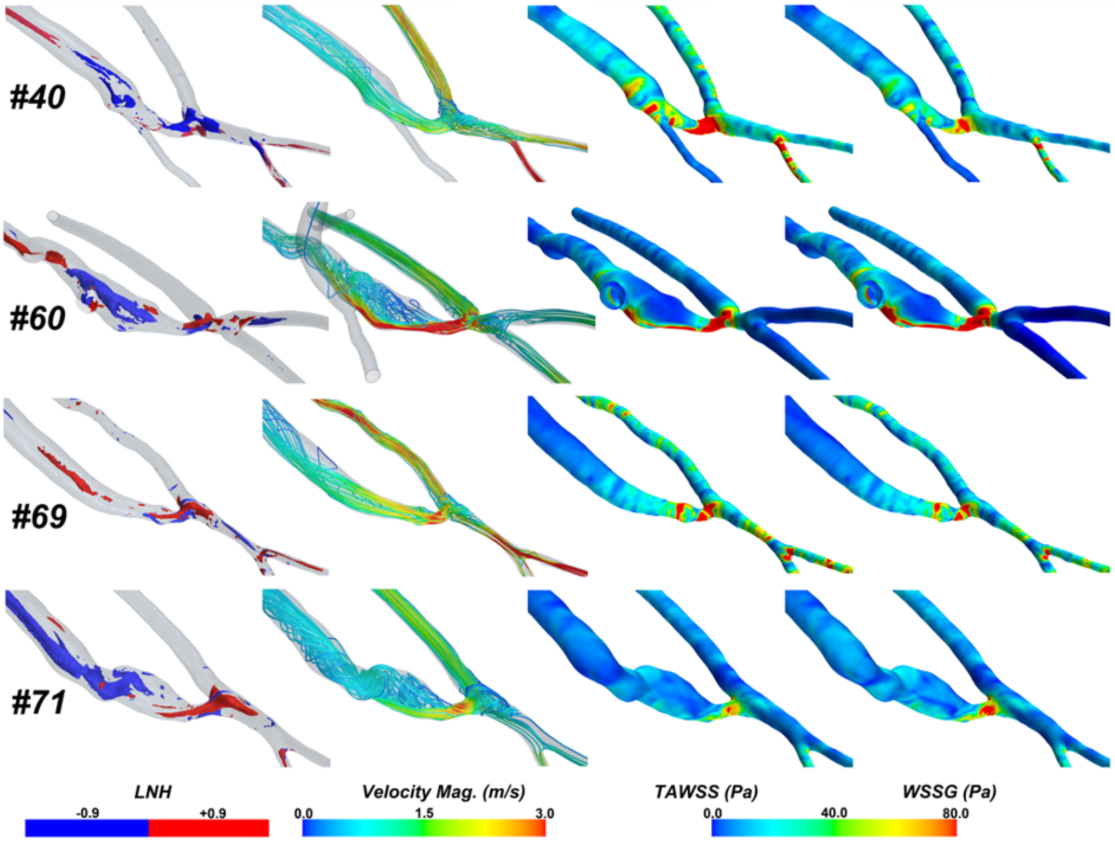

Fig. 4.14 Peak-systole flow (LNH and Velocity Magnitude) and WSS (TAWSS and WSSG) contour plots for the successful brachio-cephalic fistulae (BCF) sub-group of the cohort (n=17).

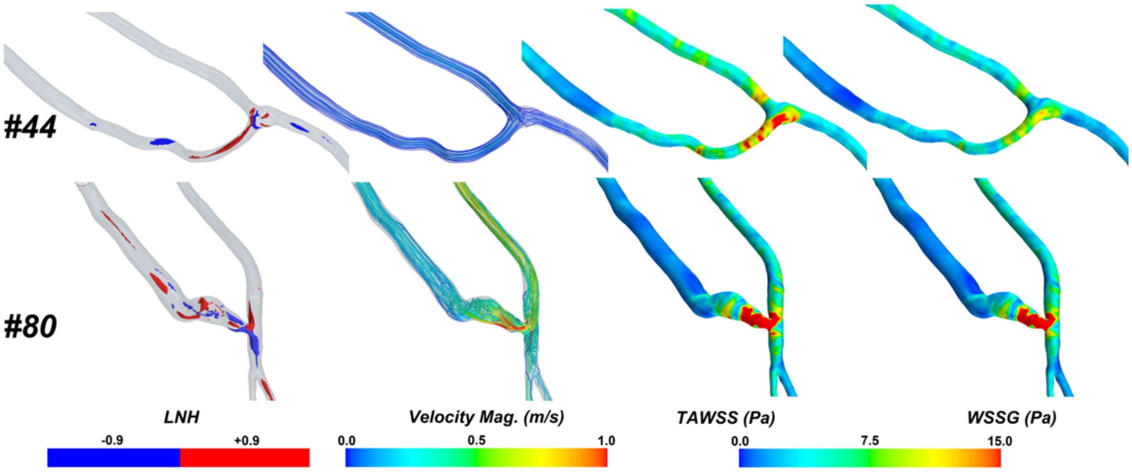

Fig. 4.15 Peak-systole flow (LNH and Velocity Magnitude) and WSS (TAWSS and WSSG) contour plots for the unsuccessful brachio-cephalic fistulae (BCF) sub-group of the cohort (n=17).

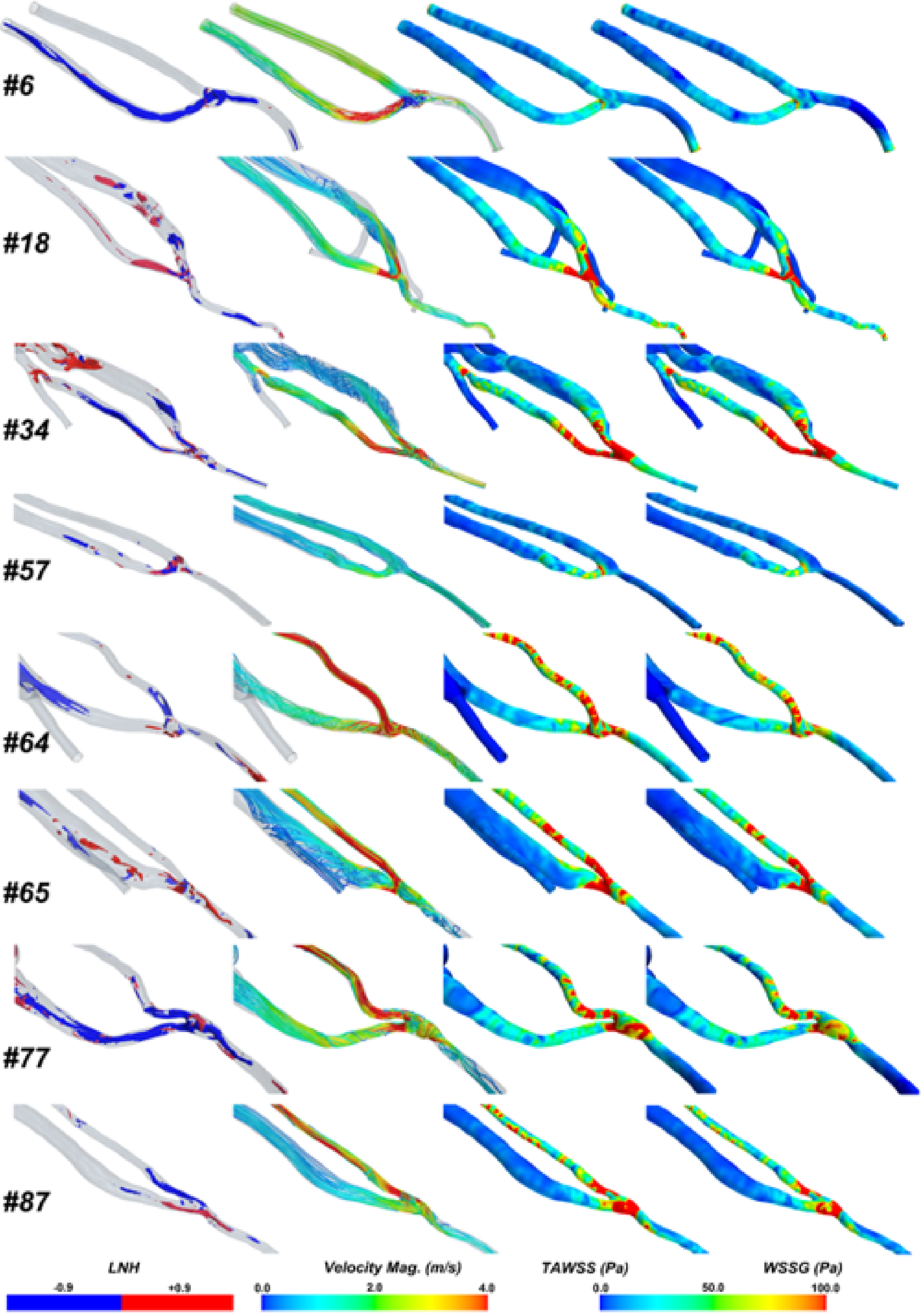

Fig. 4.16 Peak-systole flow (LNH and Velocity Magnitude) and WSS (TAWSS and WSSG) contour plots for the successful radio-cephalic fistulae (RCF) sub-group of the cohort (n=17).

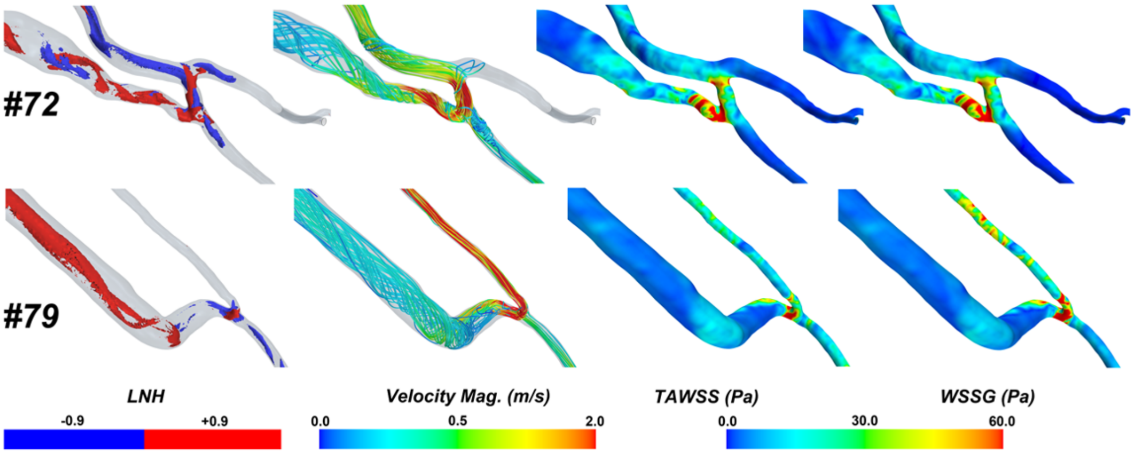

Fig. 4.17 Peak-systole flow (LNH and Velocity Magnitude) and WSS (TAWSS and WSSG) contour plots for the unsuccessful radiocephalic fistulae (RCF) sub-group of the cohort (n=17).

The WSS metrics displayed in Figs. 4.13-4.17 (TAWSS and WSSG) demonstrate an increased surface area on which high WSS is present in the successful sub-groups. Despite the correlations between the successful and unsuccessful outcomes being more difficult to discern looking at the individual contour plots generated by CFD, the plots are useful in visualising the haemodynamic differences within the sub-groups. The radiocephalic AVFs present larger WSS magnitudes due to the smaller vessel cross-sectional areas. Additionally, lower flow rates and less helical flow is induced in the unsuccessful sub-groups (Figs. 4.13-4.17).

Analysis of the WSS metrics over the 1cm segments starting at the feeding artery and finishing at the draining vein demonstrate that each sub-group follows the general trend of increasing WSS in the 1cm segments up to the anastomosis zone, a declining WSS from the anastomosis along the draining vein.

The successful RCF sub-group exhibits the highest TAWSS, transWSS, and WSSG values due to the highest ratio between the induced flowrate and vessel cross-sectional area, resulting in the greatest WSS values. This is followed by the successful BCF and the unsuccessful RCF sub-groups. The successful BBF and unsuccessful BCF sub-groups have the lowest WSS metric magnitudes, largely due to the significantly greater vessel cross-sectional areas (and potentially due to the single BBF dataset within the study).

The OSI metrics follow a similar pattern in all the AVF configurations. The trend demonstrates very low OSI before the anastomosis, which subsequently increases significantly at- and following the anastomosis, this is due to the majority of the flow being pulled into the vein. The low OSI values proximal to the anastomosis indicate laminar and mostly uni-directional flow.

The increased OSI values following the anastomosis describe the turbulent and rotational flow in the venous segment of the AVF. The highest OSI is present in the successful RCF, followed by the successful BCF. Immediately following anastomosis, the successful BBF has the second highest OSI, but this decreases quickly after this datapoint. The OSI in the unsuccessful RCF is very low through the feeding artery and draining vein.

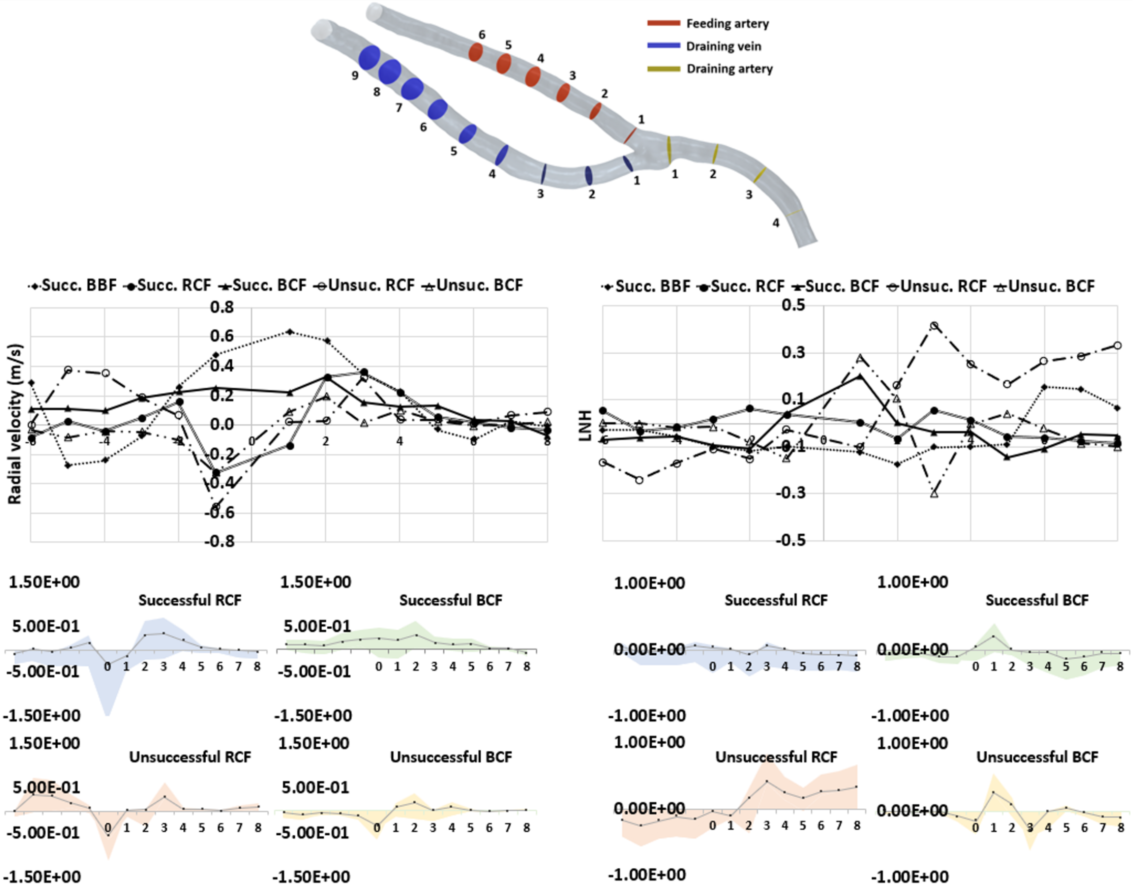

Fig. 4.19 Mean radial velocity and LNH (and error bars (right)) for each sub-group at 1cm cross-sectional plane intervals (n=17). Note that the segments presented follow the segments along the centreline from the feeding artery and draining vein.

Analysis of the LNH and radial velocity values throughout domain along the feeding artery – draining vein flow path demonstrated no discernible differences in rotational component to the flow in the unsuccessful outcomes of the BCF and RCF when compared to the successful outcomes of the same AVF type. This is hypothesised to be due to the sample size of the unsuccessful sub-groups, with prior studies eluding to an elevated rotational component to the flow in successful cases.

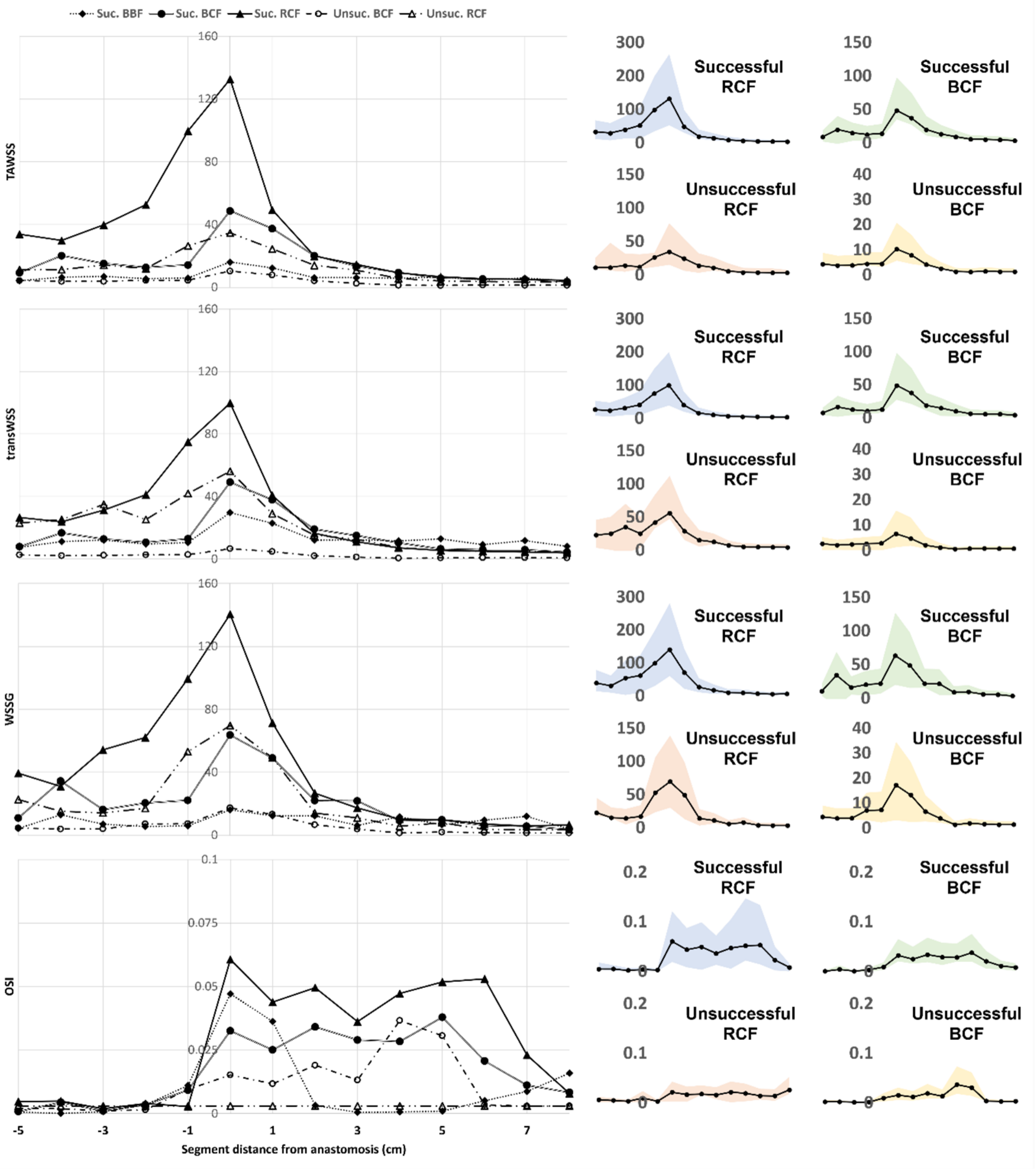

Fig. 4.18 Mean WSS metrics (and error bars (right)) for each sub-group at 1cm segments for the computational AVF domains (n=17). Note that the segments presented follow the segments along the centreline from the feeding artery and draining vein.

4.4 Discussion

4.4.1 Novelty and contribution to knowledge

To the author's knowledge, this is the first study that FeMRA has been coupled with CFD for solely analysing the post-surgical juxta-anastomosis haemodynamic environment of a ESRD cohort. The previous publication by the same group of authors (Hyde-Linaker et al. (2022) [246]) demonstrated that a single patient-specific 3D geometry can be segmented and reconstructed from the high-quality images obtained using the FeMRA protocol. In this study this work has been extended to multiple patients and AVF configurations, focusing on both successful and unsuccessful AVF outcomes.

Comparisons to prior work

Despite this being the first study to couple FeMRA and CFD for simulating the haemodynamic environment juxta-anastomosis, there have been prior studies that have completed CFD studies subsequent to obtaining AVF scan data using image protocols that avoid the contraindicating nature of traditional contrast agents. For example, Bozzetto et al. (2016, 2018) [155, 156] acquired good quality images using contrast-free MRI and CFD and simulated 4 patient-specific geometries 6-weeks post-creation, and Sigovan et al. (2013) [39] used CFD in conjunction with MRI for a longitudinal AVF study. The segmentation effort behind this studies is unknown.

The flow fields generated within the patient-specific simulations in this investigations were similar to those reported prior in idealised geometry simulations [245], with characteristic low and oscillatory WSS in the juxta-anastomotic vein. Similar conclusions relating to the high WSS regions being desirable for initiating positive vessel remodelling [175]. It has previously been reported that smaller anastomosis angle may be more advantageous in AVF success [180]. This was unable to be concluded in this investigation (potentially due to the cohort size), but vessel curvature was described as a key metric behind AVF success. The work completed by Grechy et al. (2017) [225], which used idealised feeding arteries with specified curvatures, demonstrates the varying WSS distributions generated when connecting the anastomosis at either the outer or inner curve of an arterial bend. This demonstrates the influence of the arterial curvature and how it can be leveraged.

4.4.2 Influence of biometric, vessel, and haemodynamics variations on AVF performance

In completing the ROC analysis within this investigation, the vasculature metric found to be the most conducive to AVF success was the feeding artery curvature, followed by the draining vein and feeding artery diameters. With the vessel diameters being an existing component detailed the vascular mapping phase of the pre-surgical planning [3], a greater emphasis on feeding artery vessel curvature is proposed. This requires completing a centreline analysis using either a 3D segmentation (generated using a segmentation strategy similar to that utilised in this investigation), or manually specifying points of a spline on 3D DICOM data in an appropriate software. The segmentation approach is the least prone to human error, and can be completed in an efficient manner by an experienced user of the segmentation software.

The biometric factors that were the most conducive to AVF success were lower age and lower BMI, the influence of ethnicity and sex were found to be negligible with the cohort size. These findings align with the existing reviews within the literature. The principal reasons behind lower age and BMI being more conducive to higher venous AVF flow rates may be due to the ditensibility of the vessels in younger, more elastic vessels. These are key attributes in the vascular remodelling process, where the properties of the ECM adjust during the ‘arterialisation’ (outward redmodelling) phase of AVF maturation. This is hypothesised in the findings in this study, due to the in-vivo assessment of vessel properties being unfeasible.

The CFD analyses demonstrated that higher TAWSS, transWSS, and WSSG values correspond to improved AVF outcome (in relation to venous flow rate). This is anticipated due to the higher (successful) flow rates inducing a higher frictional force on the vessel walls and therefore higher WSS magnitudes. However, it can also be noted that the presence of elevated WSS can trigger a cascade of biochemical factors which cause arterialisation of the vessel(s), which is desirable in the case of the AVF. Therefore, the selection of AVF site and morphology should be selected to maximise uniform and high TAWSS in the vessel. Minimising the curvature of the draining vein was also found to be desirable in the ROC analysis completed (Table 4.4), in large part due to the desirable flow conditions described. In other words, the lower curvature in the draining vein is interlinked with desirable the TAWSS and OSI distributions that are desirable for vascular remodelling process, and this is evident in the simulated flow-field when viewed in conjunction with the superior vessel characteristics determined through the ROC analysis. As with prior studies and reviews [38], the turbulent flow within the venous segment is hypothesised to induce increased endothelial cell (EC) turnover and poor EC alignment. The abnormal WSS distributions within the venous segment result in low WSS regions and the excitation of NH pathways [38, 257]. This is supported by studies such as Jia et al. (2015) [258], which have demonstrated that flow patterns are key, and that NH have a strong inverse correlation with WSS levels in AVF creation.

4.4.3 Clinical relevance and limitations

Question of interest and clinical relevance

The question of interest for the simulations was to elucidate whether biometric or haemodynamic factors were more prevalent in the outcome of the AVF. By determining the relative impacts, it was hoped the decisions relating to patient-specific AVFs can be better informed.

With regard to biometric factors, lower BMI and patient age were found to be the most desirable patient characteristics for AVF success. This is hypothesised to be in large part due to the traditional increased distensibility and elasticity in the vessels of younger patients. Further work is required to validate this. The vessel characteristics found to be the most conducive for presenting the environment for desirable flow field were minimised curvature in the feeding artery and the draining vein, and increased cross-sectional areas of the feeding artery and draining vein. Despite the vessel selection criterion implemented clinically, where arterial vessels in excess of 2mm diameter are considered for AVF generation ([3, 258]), the findings of the analyses within this investigation demonstrate that the curvature of the vessels is as prominent (if not more so,) than the vessel diameters (particularly considering their diameters pre-AVF generation. This is key information for informing the AVF site and morphology selection, a process largely determined by surgeon experience and preference.

The ROC analysis completed demonstrated that despite the clear correlation between lower BMI and age with high venous flow rates ($>1000 ml/min$), with AUC values of 0.7083 and 0.6042 respectively, the vessel characteristics are more prominent in the cohort studied (feeding artery curvature AUC=0.8194).

As anticipated, the haemodynamic CFD analyses reflected that the increased flow rates induced by the successful AVFs generated significantly higher WSS values juxta-anastomosis, with the mean maxima of each WSS metrics being observed at the anastomosis segment of the sub-divided computational domain. Notably, the mean transWSS and WSSG values observed within the unsuccessful RCF sub-group were greater than the successful BCF and BBF sub-groups. This is in large part to the sample size of the unsuccessful RCF sub-group, the smaller vessel cross-sectional diameter in an RCF case, and a potentially anamolus result. A key difference between the successful and unsuccessful sub-groups was the mean OSI observed in the anastomosis and venous segments, with markedly higher values being observed in the successful cases. This is indicative of both the turbulent and disturbed flow patterns within this region generating patches of low and oscillatory WSS, but also the conditions which can infer locations of neointimal hyperplasia, a key complication in the AVF and vascular access community.

Context of use

The use of the CFD element in this study was to investigate the flow-patterns juxta-anastomosis. This was achieved by imposing the known flow waveforms (from PC-MRI) at the inlet and outlets of the domain. On a patient-specific level, the utilisation of CFD for generating the flow-fields and examining the flow patterns can be vital in predictions potential sources of future complications, such as the onset of neointimal hyperplasia in low and oscillatory WSS regions highlighted within the OSI contour plots (Appednix C.6). Particular attention should be paid to locations of chronic WSS adjacent to low/oscillatory WSS regions, as this can be a notable location for re-interventions to prevent potential thrombosis.

Considering these points, the workflow's future context of use may be to inform future AVF planning, whether it be when initiating a new patient onto haemodialysis using an AVF, creating a subsequent AVF in a patient, or to perform interventions to improve an existing AVF.

4.4.4 Limitations

Omission of the influence of the fluid-structure interaction (FSI) was an assumption made in this investigation. The rationale behind this was due to the scope and context of use behind the simulations. The principal aim for the study was to replicate the flow conditions observed using PC-MRI, this inferred the use of prescribed waveforms at the inlet and outlets. This approach does not generate representative pressures within the domain, and as such, the pressures exerted on the wall model (if present) would not be physiologically representative. Additionally, generating representative pressures within AVF with the correct flowrate is very challenging due to the 'non-physiological' flow within the AVF. This creates a difficulty in the selection of appropriate values for coupled pressure systems (such as the Windkessel model). Lastly, the selection of an appropriate hyperelastic wall model, whether it be a single wall model or a 'layered-approach', and the values selected for the model, are an assumption when not being based on patient-specific data, which wasn't feasible in this investigation.

Other limitations on the workflow include the resolution of the scan data (for generating the 3D vessels) and the PC-MRI data (for extracting the flow waveform data). The segmentation of the vessels is a potential source of human error, but this was minimised through the computation of a DICE score in a prior paper by the same group of authors [246] (Chapter 3).

The main limitation of the findings within this study was the cohort size, and the number of patients in each sub-group. With the drastically different flow-rates and vessel characteristics, it is important to consider the differing morphologies separately. Ultimately, due to the cohort size, further work is required to clarify the initial conclusions in this pilot study.

4.4.5 Future work

To further this work and support the findings of this paper, many additional datasets will require segmentation and analysis. Two options exist for generating these datasets; repeating the scanning, segmentation, and CFD workflow presented for the necessary number of patients, or complete the workflow for a representative sample of the ESRD population and perform a shape modelling workflow to interpolate and generate many datasets and geometries based the limited number of datasets available and acquired. A minimum of approximately 10-20 datasets per AVF sub-group is required for the shape modelling approach. This may be much more achievable per institution, particularly with the nature of differing AVF locations, morphologies, and outcomes. Specifically on the datasets studied in this research, further work may evolve from this study in the form of fluid-structure interaction (FSI) simulations, however, the designation of the vessel wall material properties becomes very difficult when assessing the venous vessel. Additionally, the vessel wall is usually not visible on the scans due to resolution in most cases. Lastly, one patient (the successful RCF anomaly) demonstrated retrograde flow. Due to the noticeable differences of this case with the others, the likelihood of retrograde flow in young CKD patients may be a research question in the future. Further studies indicating this would be required in the interim however.

Chapter 5

Computational aortic haemodynamics in relation to the influence of AVF on CVD risk

5.1 Introduction

Chronic kidney disease (CKD), the declination of kidney function to a glomerular filtration rate of $< 60\ mL/min/1.73m^2$ for more than 3 months, often progresses to end-stage renal disease (ESRD) levels (a glomerular filtration rate of $< 15\ mL/min/1.73m^2$). The primary causations of ESRD are diabetes and hypertension, and ESRD patients have a high prevalence of concomitant cardiovascular disease (CVD) [38, 259]. CVD is the primary morbidity and mortality cause in the ESRD population [259].

Arteriovenous fistulae (AVF) are the preferential vascular access for initiating patients onto haemodialysis [3] despite the complications that result in the poor maturation and patency rates. Successful AVFs provide consistently high ('non-physiolgical') flow rates for haemodialysis due to the AVF altering the resistances of the vascular network in its proximity. One neglected area of research is the impact of successful AVF on the haemodynamics in the aorta region of CKD and ESRD patients. This is of particular interest as the CKD population is exposed to an elevated cardiovascular risk in addition to the renal-associated mortality risks.

In early CKD stages (1-3) patients, CVD death rates are greater than the general populous [260]. In ESRD cases and advanced CKD stages, the CVD risk is 10-20 times greater than the general population [261]. This is demonstrated by cardiovascular complications being the leading cause of death in ESRD patients (stage 5) [261]. The manifestations of CVD include coronary artery disease and heart failure.

The correlation between CVD and CKD is somewhat explainable by the common risk factors, such as hypertension and type 2 diabetes. However, it is hypothesised that maladaptive cardiovascular remodelling may occur due to CKD inducing a systemic proinflammatory state [262]. The resulting vascular remodeling in CKD (particularly cases with an AVF) promotes atherosclerosis, calcifications, and heart-based complications. CKD may also release hormone and enzymes in response to kidney injury that induces cardiac damage due to haemodynamic alterations [263]. The investigation in this chapter focuses on examining the aortic haemodynamics induced by the presence of the AVF, the resulting WSS distribution, and how this information can be used for in the pre-surgical and post-operative patient-specific planning.

The cohort studied included subjects with successful and unsuccessful AVF cases from varying AVF morphologies. This is key as vascular access selection influences and contributes to the overall morbidity and mortality of the patient [264].

The scope of the study was to recognise the prognostic capabilities of CFD with respect to future cardiovascular complications in CKD patients following the surgical creation of an AVF. A key area of interest was the subclavian arteries of each subject, an often neglected area. By computing the ratio between the magnitudes of the WSS metrics induced in the subclavian artery proximal to the AVF with that of the WSS induced in the subject's opposite subclavian artery, a patient-specific assessment of the AVF's influence can be obtained.

The identification of potentially detrimental haemodynamics is particularly necessary with the potentially long usage of AVFs, which can have a long lifespan despite the aging CKD population. Analysis of the simulated flow patterns and WSS distributions may permit the long-term prediction of cardiovascular complications should the AVF be successful and provide a long-term vascular access. As such, the question of interest in this investigation is; can the influence of the AVF on the proximal haemodynamics be quantified with WSS and OSI metrics? The context of use of the workflow used in the simulations is to elucidate the haemodynamic environment in and adjacent to the aorta when a successful AVF has been generated.

5.2 Materials and methodologies

The pipeline used in pre-processing all 24 anatomies of this Chapter was similar to that of Chapters 3 and 4 [246]. These geometries were then used for computational fluid dynamics (CFD) within STAR-CCM+, using triphasic inlet waveforms with known cardiac outputs. The image data, cardiac output, and AVF flowrate information was obtained 6-weeks following the creation of the AVF.

High-quality images of the patient's chest region in the form of DICOM stacks was ascertained from FeMRA. The visible systemic vessels were then segmented using ITK-SNAP (www.itksnap.org) [215]. Surface (.stl) files of the ITK-SNAP segmentations were then processed in OpenFlipper (www.openflipper.org) [248] and Paraview (www.paraview.org) (Chapters 3-4) before being imported into Simcenter STAR-CCM+ for pre-processing and simulation (numerical modelling).

The inlet of all the anatomies was located at the ascending aorta, and each simulation had 7 outlets; the right subclavian, right vertebral, right common carotid, left common carotid, left vertebral, left subclavian, and descending aorta arteries (Fig. 5.1). Each patient's cardiac output and cardiac cycle period was known. These cardiac outputs and periods were applied to a generic triphasic waveform to match the patient's blood flow characteristics at the ascending aorta. This was due to the precise waveform shapes being unknown.

Flow splits were applied to the outlets of the domain (all the vessels, excluding the ascending aorta) using a combination of designated flow splits and the known phase-contrast waveform data in the arm of the AVF. Segment v3.0 R7946 [250] was used for extracting the phase-contrast waveform (Chapter 4, Appendix C.1) that was used for calculating the boundary condition in the subclavian artery of the AVF-arm in each case. Polyhedral meshes were generated in Simcenter STAR-CCM+ (Siemens Industries Digital Software) for discretising the computational domains, utilising mesh characteristics determined in a mesh independence analysis test case (Appendix D.2). This repeatable pipeline provided an efficient workflow and minimised user error where possible.

5.2.1 Extraction of phase contrast data and boundary conditions

Cardiac output, phase contrast data, and idealised waveforms

The cardiac output of the subject was acquired in the post-operative imaging process 6-weeks following AVF creation (Table 5.1). Additionally, localised imaging in the AVF-arm

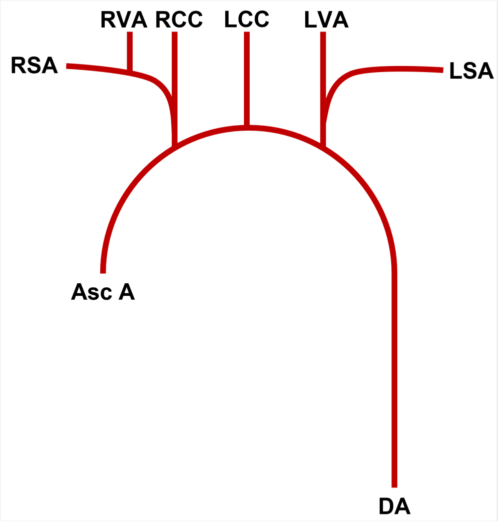

Fig. 5.1 Schematic of computational domain of the vasculature (red) studied within the investigation of this chapter. Where Asc A is the ascending aorta, DA is the descending aorta, RSA is the right subclavian artery, RVA is the right vertebral artery, RCC is the right common carotid artery, LCC is the left common carotid artery, LVA is the left vertebral artery, and LSA is the left subclavian artery.

of the subjects was completed at this time. Phase-contrast MRI (PC-MRI) data (Chapter 4) was acquired for these vessels (in the majority of cases). The averaged flow rate in the proximal vessel of the AVF was then used for determining the flow-split percentage to the subclavian artery in the same arm as the AVF. Assumed initial flow split percentages were required for the other outlets in this pilot study (carotids, vertebral, descending aorta, and non-AVF arm subclavian) due to the lack of flowrate data available for the other vessels.

The known cardiac outputs and periods were applied to a generic triphasic waveform (sourced from haemod.uk) to match the patient's blood flow characteristics at the ascending aorta (Fig. 5.2). These values were used in conjunction with baseline flow splits (Fig. 5.3), these values were; 0.68 (descending aorta), 0.06 (right and left subclavian), 0.05 (carotids), 0.02 (vertebrals). These baseline values were selected based on flow splits previously reported in literature [211, 265, 266]. These baseline flow divisions were then modified in each patient by incorporating the known flow rate in the subclavian of the AVF-arm. The process used for this is demonstrated in Figure 5.3. After establishing the flow split of the cardiac output in the AVF-arm subclavian outlet, the original flow divisions assigned to the other vessels were reduced in accordance with their original flow split value. This established that the sum of the flow split outlets was equal to 1 (Fig. 5.3). This ensured the conservation of mass and momentum in the simulations. The flow splits of each case are presented in the Table 5.1.

Of the 24 simulations completed, 6 did not have phase contrast waveform data in the arm of the AVF. The flow splits of these datasets were calculated by averaging the flow splits percentages in the same AVF morphology and outcome sub-group (i.e. for a successful BCF subject without flowrate data in the arm, the averaged flow-splits from the successful BCF cases with flowrate data was used). Datasets in Table 5.1 denoted by A in their classification had PC-MRI flowrate data in the AVF-arm, those denoted by B did not. For example, $SucBCF_A$ is a successful BCF type with PC-MRI data, and $SucBCF_B$ successful BCF type without PC-MRI data.

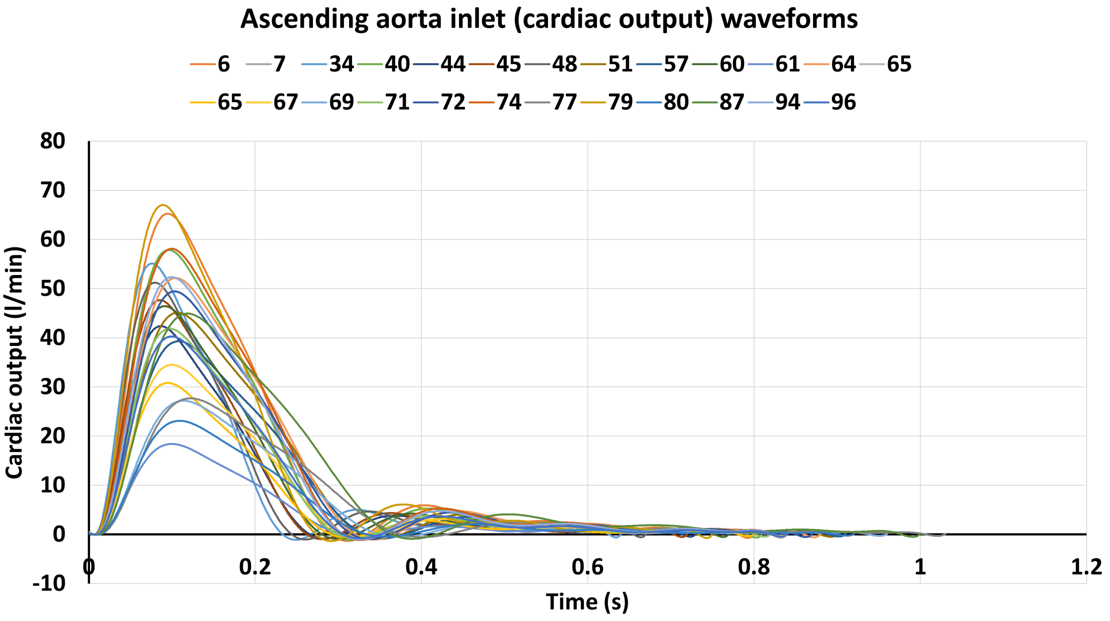

Fig. 5.2 Inlet (ascending aorta) waveforms for each patient within the cohort studied in Chapter 5. Each waveform was calculated using patient-specific cardiac output values.

5.3 Flow-splitting methodology

Figure 5.3 demonstrates the ‘flow-spitting’ methodology used in this study. With the absence of flow data in the other outlet arteries, and the created AVF generating high ‘non-physiological’ flow, flow-split outlets were determined to be the most suitable approach for replicating the haemodynamics in the AVF-arm subclavian artery. There exists several ‘flow-splitting’ methodologies documented in literature, such as Murray’s ‘cube’ law and Chnafa et al. (2018) [222]. These approaches calculate flow splits in each branch of the network using the diameter ratio of the daughter vessels, and apply this to the flow. The

Table 5.1 The CKD cohort classification of inlet (cardiac output) information and the calculated flow splits for each case.

Patient ID	Cardiac output (l/min)	Period (s)	AVF arm	Classification	DA (%)	RSA (%)	LCC (%)	RCC (%)	LVA (%)	RVA (%)	LSA (%)
#45	7.1	0.72	R	$SucBBF_A$	41.9	43.3	3.7	3.7	1.2	1.2	4.9
#40	9.7	0.81	L	$SucBCF_A$	61.2	7.2	5.4	5.4	1.8	1.8	17.2
#60	7.4	0.77	L	$SucBCF_A$	53.2	5.3	4.7	4.7	1.6	1.6	28.0
#69	5.4	0.96	L	$SucBCF_A$	48.8	5.7	4.3	4.3	1.4	1.4	34.0
#71	7.1	0.82	L	$SucBCF_A$	54.1	5.4	4.8	4.8	1.6	1.6	25.8
#48	7.1	0.67	L	$SucBCF_B$	60.4	7.1	5.3	5.3	1.8	1.8	18.3
#6	10.8	0.72	L	$SucRCF_A$	65.1	5.4	5.0	5.0	1.7	1.7	15.1
#18	5.7	0.96	L	$SucRCF_A$	54.7	3.7	3.3	3.3	1.1	1.1	32.9
#34	7.3	0.64	L	$SucRCF_A$	59.9	5.0	4.1	4.1	1.4	1.4	24.0
#57	7.4	0.91	L	$SucRCF_A$	65.8	5.6	5.1	5.1	1.7	1.7	13.9
#64	9.5	0.88	L	$SucRCF_A$	62.9	5.8	4.7	4.7	1.6	1.6	18.9
#65	5.1	0.80	L	$SucRCF_A$	48.0	1.9	2.1	2.1	0.7	0.7	44.4
#77	5.9	1.03	L	$SucRCF_A$	58.7	4.7	3.9	3.9	1.3	1.3	25.2
#87	9.3	1.00	L	$SucRCF_A$	64.0	5.1	4.8	4.8	1.6	1.6	17.0
#44	5.4	0.73	L	$UnsucBCF_A$	63.5	7.5	5.6	5.6	1.9	1.9	14.2
#80	4.4	0.92	R	$UnsucBCF_A$	58.5	20.8	5.2	5.2	1.7	1.7	5.9
#51	8.4	0.90	L	$UnsucBCF_A$	64.8	7.6	5.7	5.7	1.9	1.9	12.4
#67	5.0	0.84	L	$UnsucBCF_B$	67.6	8.0	5.0	5.0	2.0	2.0	8.6
#74	10.1	0.84	L	$UnsucBCF_B$	65.5	7.7	5.8	5.8	1.9	1.9	11.4
#94	9.1	0.84	L	$UnsucBCF_B$	65.9	7.8	5.8	5.8	1.9	1.9	10.9
#72	8.9	0.87	L	$UnsucRCF_A$	62.4	7.3	5.5	5.5	1.8	1.8	15.6
#79	10.4	0.75	L	$UnsucRCF_A$	64.5	7.6	5.7	5.7	1.9	1.9	12.7
#61	3.2	0.84	L	$UnsucRCF_B$	54.9	5.5	4.9	4.9	1.6	1.6	25.7
#96	7.0	0.84	L	$UnsucRCF_B$	65.0	7.6	5.7	5.7	1.9	1.9	12.1

flow-splits leading to outlets are then summed to yield the overall flow-split to each outlet (Appendix B.5). However, such an approach in this case would not generate the correct flow-split that is known from the PC-MRI data. In order to generate the flow-splits for each anatomy, a modified flow-splitting method was generated in this Chapter (Fig. 5.3), and applied to each case. The relationship between the resulting flow-splits of each case and cardiac output are given previously in Table 5.1, and Figs. 5.4-5.5.

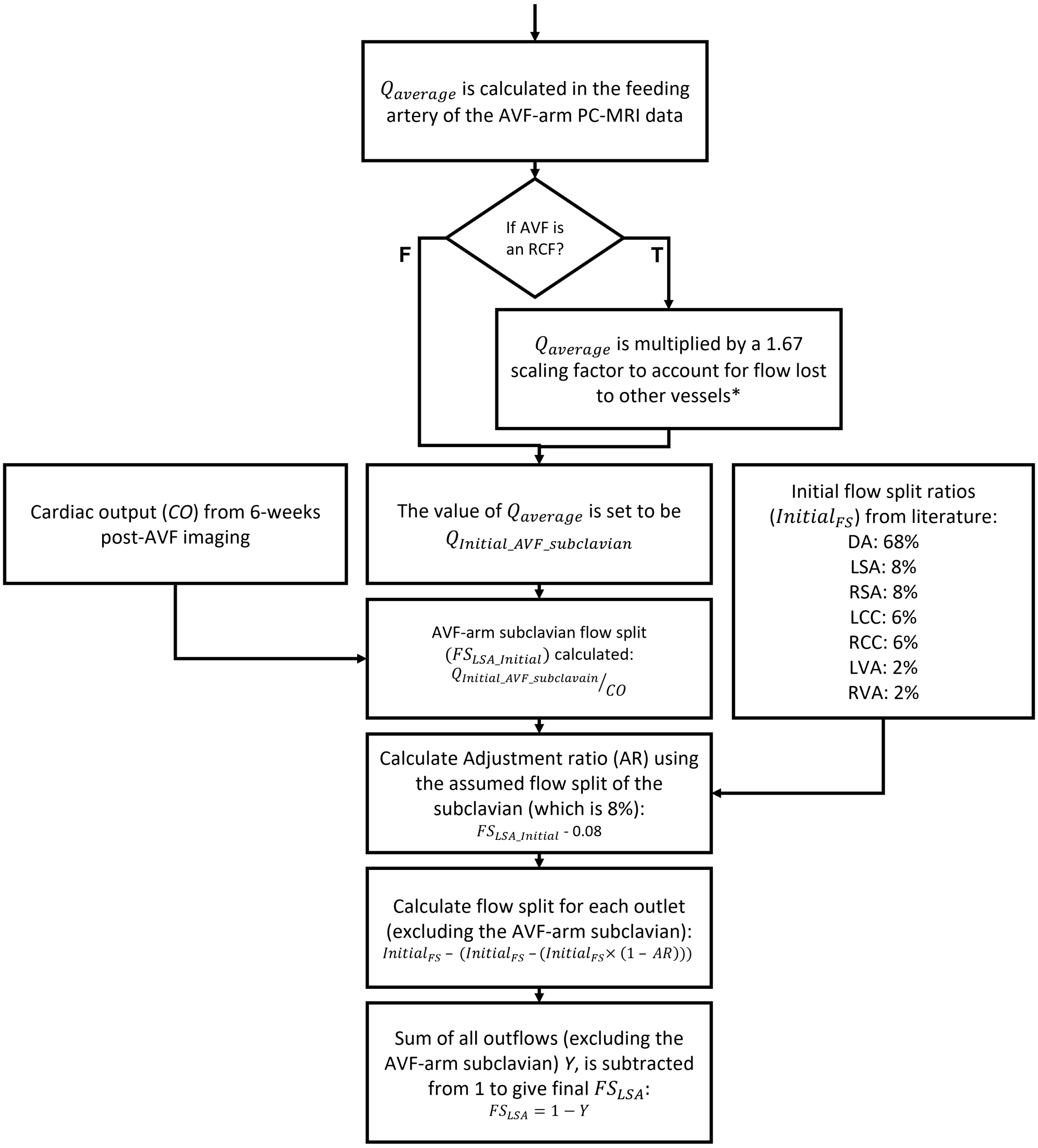

Fig. 5.3 Flow chart used for assigning the flow split percentages for the boundary conditions of the geometries in this Chapter.

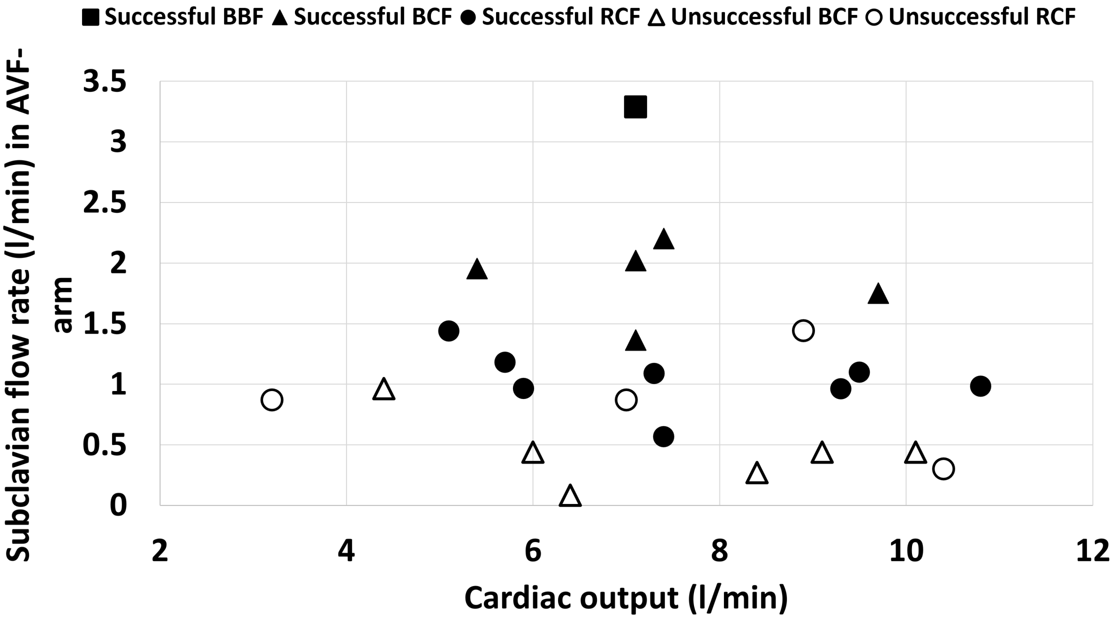

Fig. 5.4 Flow rate in each AVF-arm subclavian against cardiac output for each case studied in Chapter 5. Each case is plotted according to the sub-group.

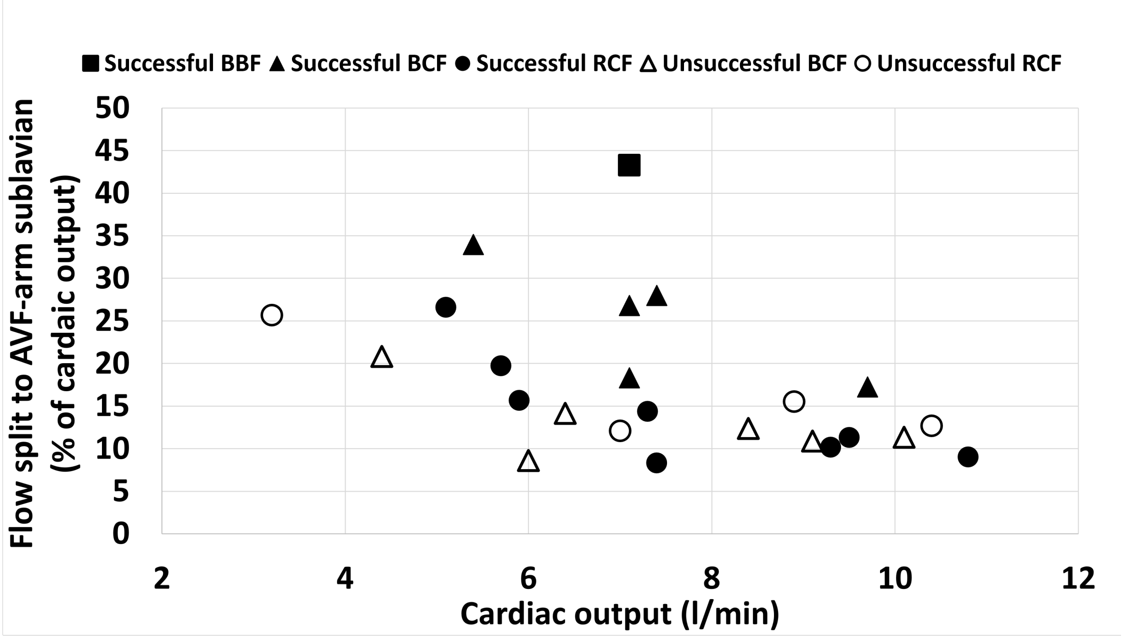

Fig. 5.5 Flow split percentage in each AVF-arm subclavian against cardiac output for each case studied in Chapter 5. Each case is plotted according to the sub-group.

5.4 Model details and haemodynamic metrics

5.4.1 Modelling details

The CFD modelling techniques utilised in this study are covered in greater depth in Chapter 3 and Hyde-Linaker et al. 2022 [246], with the approaches utilised in this study (Appendix A) being discussed concisely herein.

A scale-resolving hybrid turbulence model in STAR-CCM+ (Chapter 3-4) was utilised for modelling the blood flow. This permits the computation of unsteady large-scale turbulence structures whilst having a computational expense similar to a Reynolds-Averaged Navier-Stokes (RANS) model. Duffal et al. (2019) [218] details further information relating to the SRH model utilised in the CFD investigations. The decomposed solution variables from the SRH model are utilised in the Navier-Stokes equations to yield filtered transport equations of mass, momentum, and energy. The governing equations of the flow field, the Navier-Stokes equations, are defined by:

$$\nabla.u = 0 \tag{5.1}$$

$$\rho\frac{\partial u}{\partial t} + \rho(u.\nabla)u + \nabla.p = \mu\nabla^2 u \tag{5.2}$$

where u is the velocity vector, p is the pressure, ρ is the fluid density, and μ is the fluid viscosity.

The simulations were completed using a segregated pressure-based flow solver on a finite volume implementation in Star-CCM+ ($\Delta t = 0.001s$) (Chapter 3)[246]. A SIMPLE (Semi-Implicit method for pressure-linked equations) pressure-velocity coupling algorithm was used, in addition to optimised 2nd-order temporal discretisation. This reduces the leading-order truncation error by a factor of 2, compared to base-level 2nd-order temporal discretisation [219].

Additionally, a generalised Carreau-Yasuda non-Newtonian model was implemented with values from literature (Chapter 3). This is a key assumption in the modelling process, as prior studies have implemented a Newtonian fluid model for approximating the rheology of blood. However, the Newtonian rheology assumption omits the ‘shear-thinning’ property of blood, which manifests at shear rates below $50 - 100s^{-1}$. This makes the selection of the non-Newtonian model superior to a Newtonaian fluid assumption.

The haemodynamic metrics assessed in this Chapter include TAWSS, transWSS, WSSG, and OSI (Chapter 4, Appendix A.7) [112, 246].

5.4.2 CFD post-processing

In order to obtain the WSS and OSI metric information in the right and left subclavian arteries, the computational domain (in .stl format) was clipped within Paraview [249] to the extents of the subclavian arteries demonstrated in Figure 5.6. Following the acquisition of the surface meshes for each of the subclavian arteries, the files were imported into STAR-CCM+ (Fig. 5.6 left). Arbitrary probe derived parts were then generated within STAR-CCM+ (Fig. 5.6 right) by specifying the wall of the computational domain and the clipped .stl representing the relevant subclavian artery (Fig. 5.6).

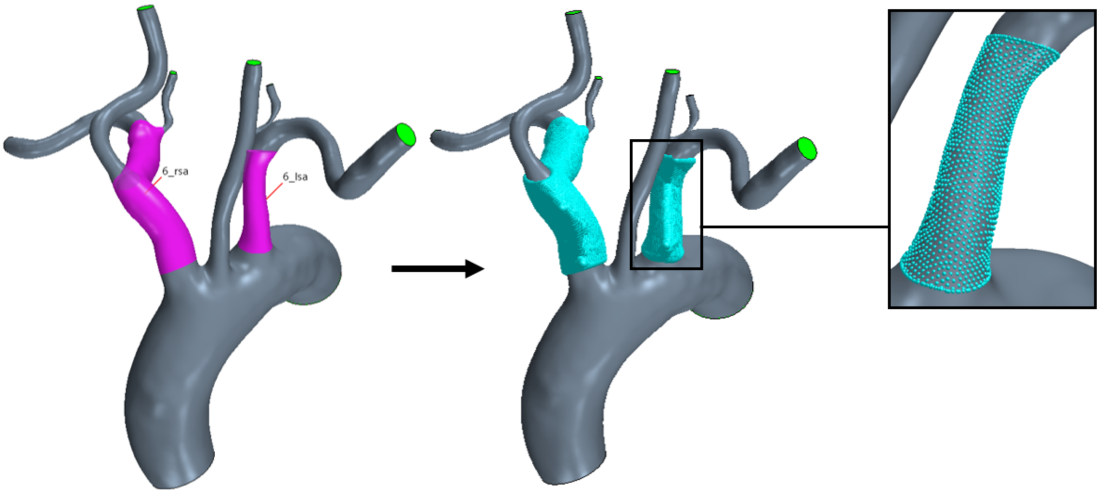

Fig. 5.6 Configuring the arbitrary probe derived parts for each case (example shown is case #6). Where lilac shaded regions represent the clipped .stl files used for defining the subclavian artery regions, and the blue points represent the points of the arbitrary probes generated.

5.5 Results

The results of the investigation are presented into the following sub-sections; i) CFD contour plots of the TAWSS, OSI, and transWSS metrics, and ii) analysis of the WSS induced in the subclavian artery of AVF-arm compared to the non-AVF-arm subclavian. Further results in the form of velocity streamline contour plots at peak systole, mid-deceleration, and peak diastole are given in Appendix D.3, and the normalised pressure contour plots at peak systole are given in Appendix D.4.

The contour plots of the WSS (TAWSS and transWSS) and OSI metrics obtained in the simulations of this Chapter are demonstrated in Figures 5.7-5.14 (and the Appendix D.3-D.4).

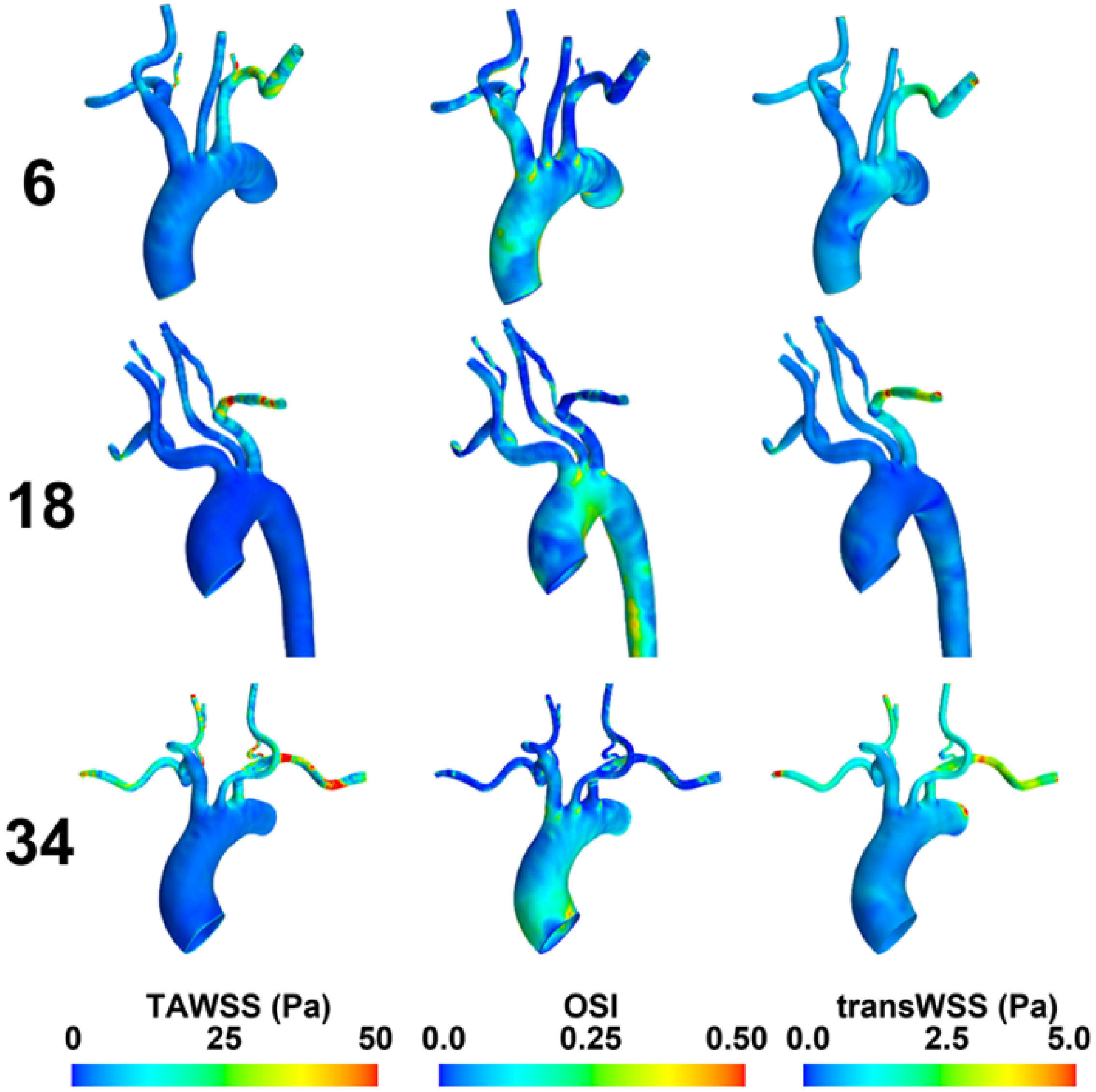

Fig. 5.7 TAWSS, OSI and transWSS contour plots plotted on the wall of each computational for subject IDs 6, 18, and 34.

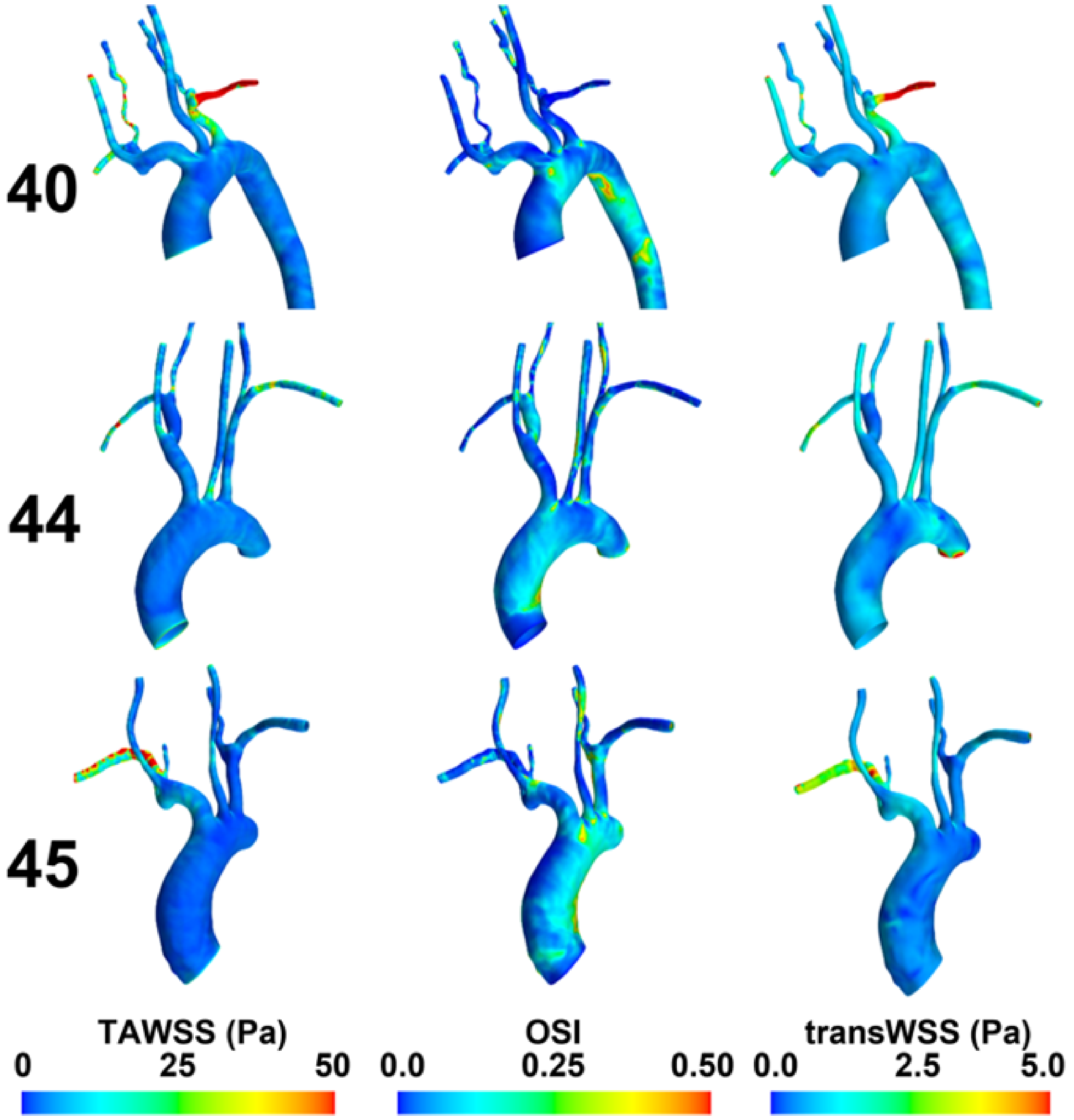

Fig. 5.8 TAWSS, OSI and transWSS contour plotted on the wall of each computational for subject IDs 40, 44, and 45.

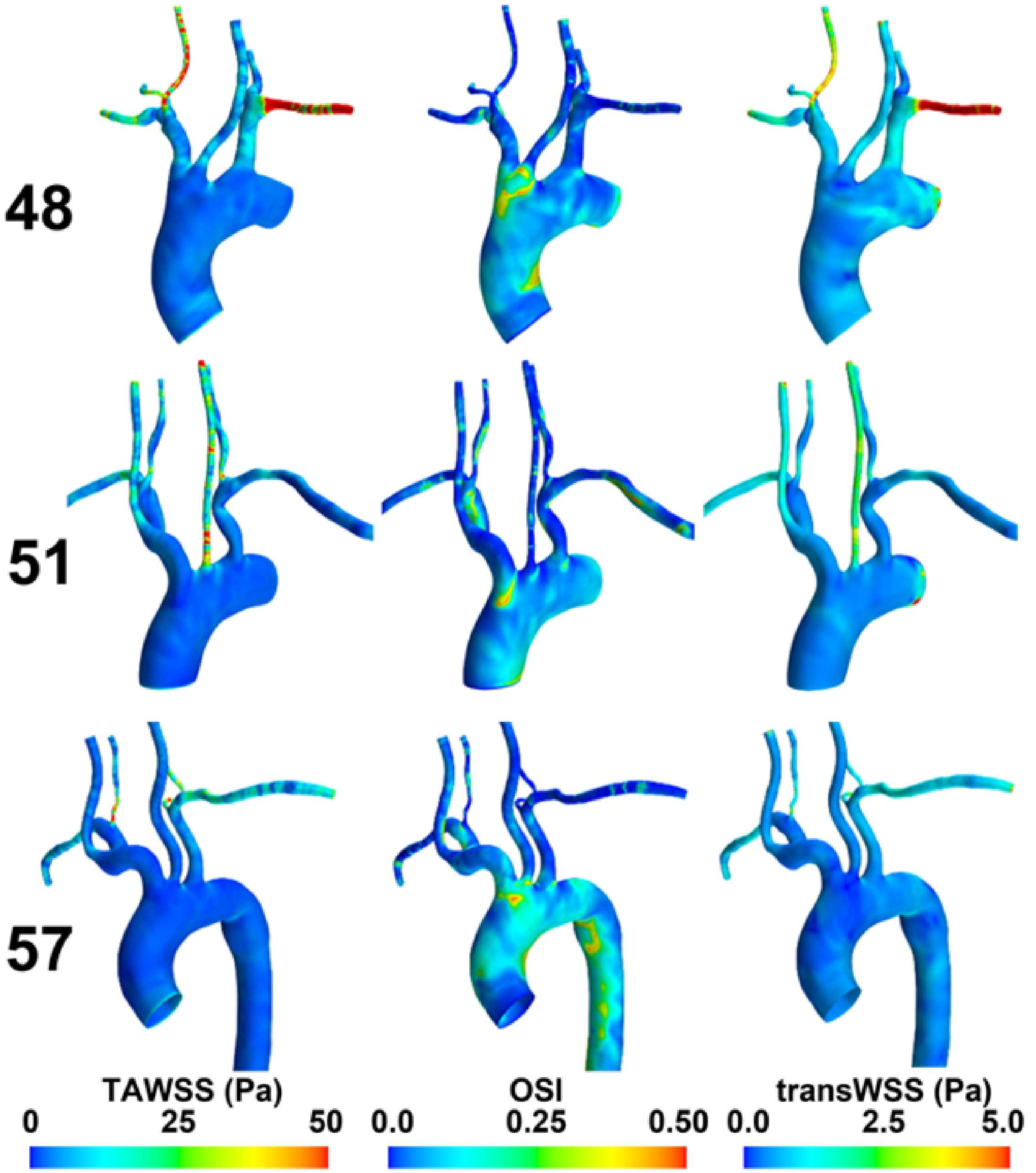

Fig. 5.9 TAWSS, OSI and transWSS contour plotted on the wall of each computational for subject IDs 48, 51, and 57.

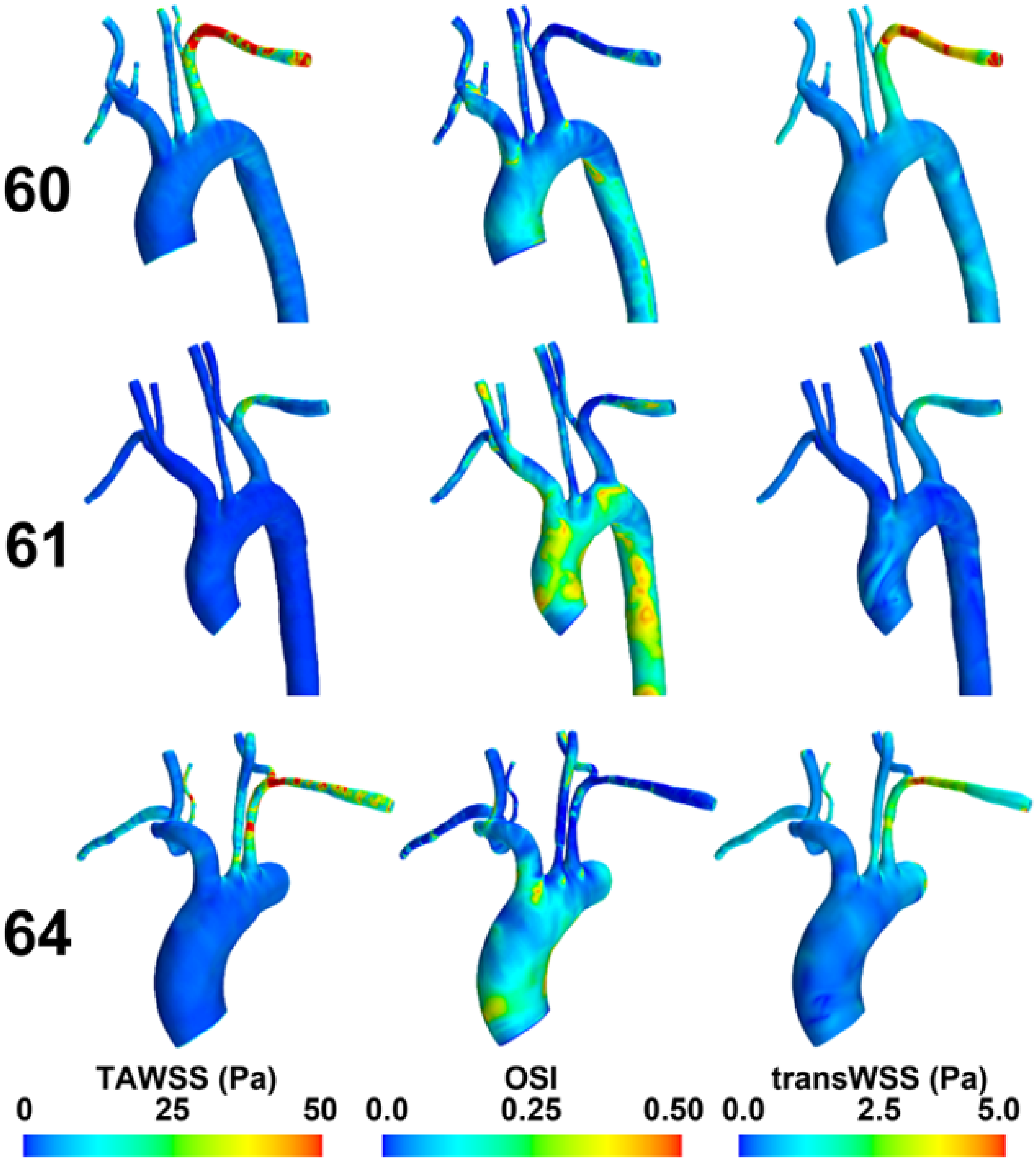

Fig. 5.10 TAWSS, OSI and transWSS contour plotted on the wall of each computational for subject IDs 60, 61, and 64.

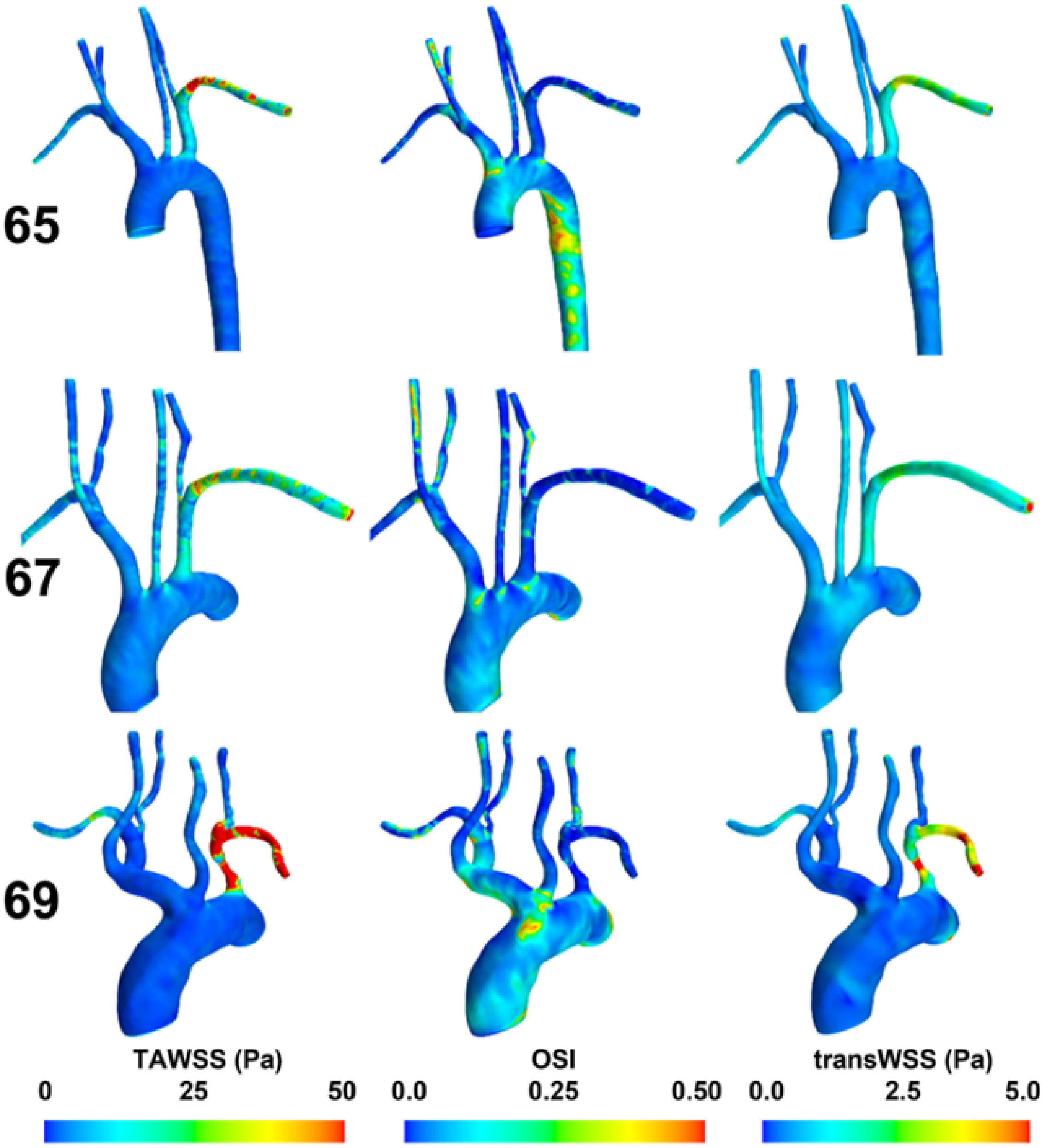

Fig. 5.11 TAWSS, OSI and transWSS contour plotted on the wall of each computational for subject IDs 65, 67, and 69.

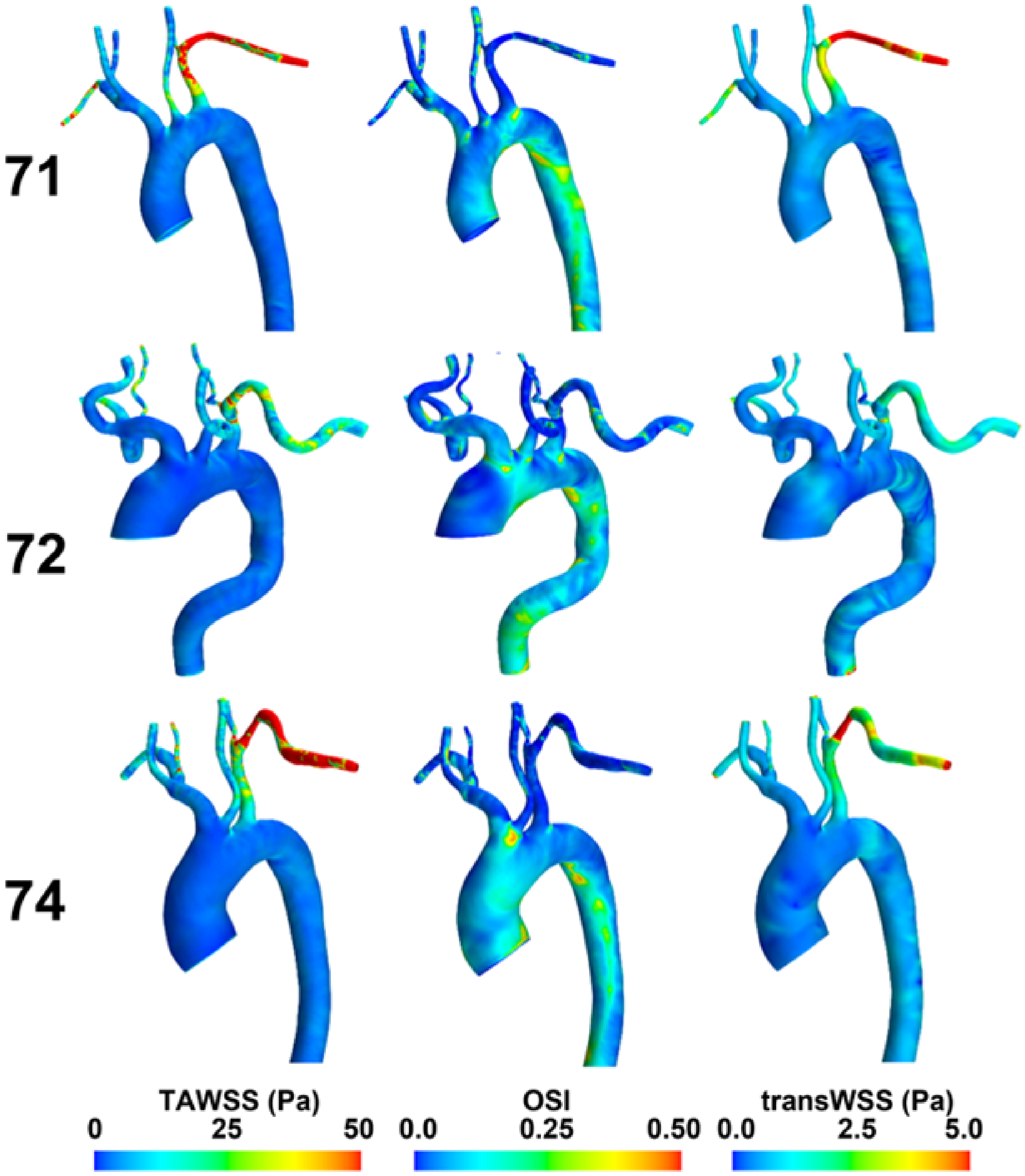

Fig. 5.12 TAWSS, OSI and transWSS contour plotted on the wall of each computational for subject IDs 71, 72, and 74.

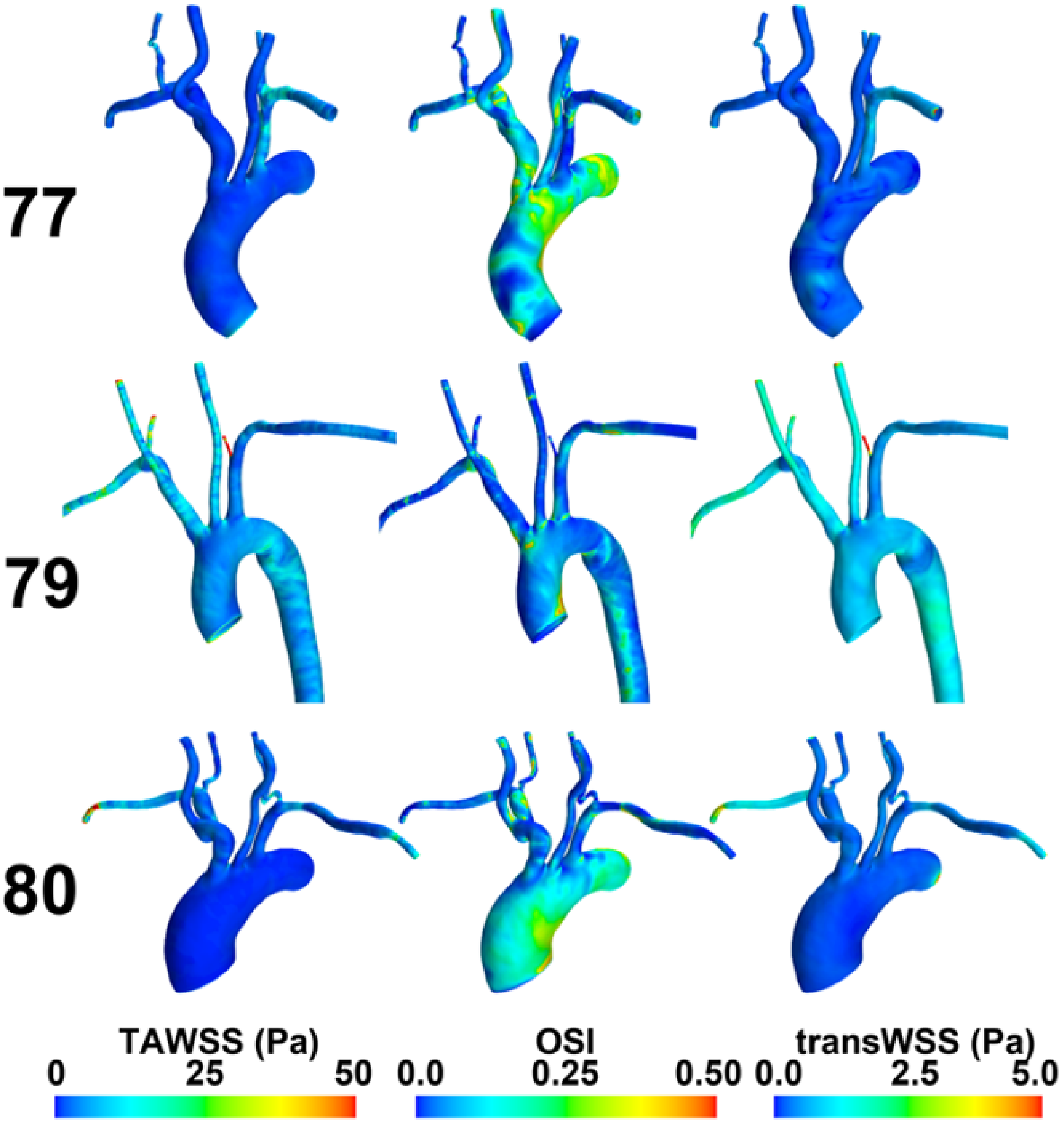

Fig. 5.13 TAWSS, OSI and transWSS contour plotted on the wall of each computational for subject IDs 77, 79, and 80.

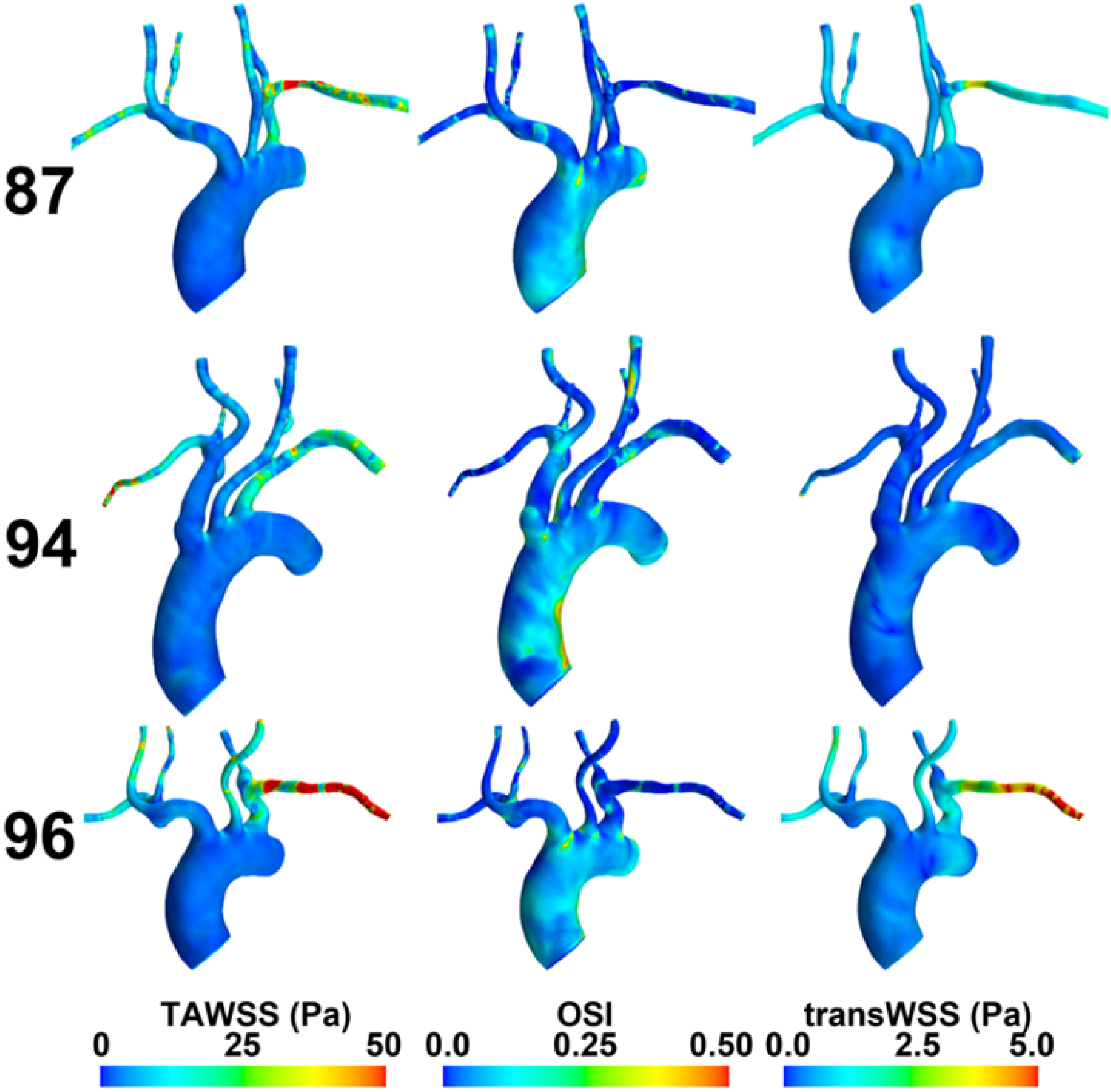

Fig. 5.14 TAWSS, OSI and transWSS contour plotted on the wall of each computational for subject IDs 87, 94, and 96.

The successful AVF cases (#6, #18, #34, #40, #45, #48, #57, #60, #64, #65, #69, #71, #77, #87) (Figs. 5.7-5.13) exhibit elevated TAWSS and transWSS levels in the subclavian artery of the AVF-arm over the other vessels within the computational domain(s). The subclavian artery of the AVF-arm in unsuccessful AVF cases (#44, #51, #61, #67, #72, #74, #79, #80, #94, #96) (Figs. 5.8-5.14) demonstrate similar WSS levels to the other vessels. Variations exist in the WSS and OSI distributions of the successful and unsuccessful cases. The AVF-arm subclavian artery in several successful cases (e.g. #40, #45, #48, #60, #64,, #65, #69, #71) is dominated by high TAWSS and transWSS at the outer curvature of the artery, particularly following the left vertebral artery bifurcation. This is also notable in some unsuccessful cases (#74, #96), where failure AVF has occured following the 6-week scan. Conversely, several successful cases (#6, #18, #57) demonstrate only moderately higher TAWSS and transWSS levels (than the rest of the domain), in accordance with the increased flow rates to the AVF-arm due to the decreased vascular resistance downstream. High OSI magnitudes are induced in the inner curvature of the aortic arch in the majority of cases. Other noteworthy high OSI locations include the bifurcation junctions in both successful and unsuccessful cases, with the highest OSI magnitudes being visible at the brachiocephalic trunk of the bovine aortae (#48, #57, #69, #74). The OSI levels induced in the AVF-arm subclavian artery of successful cases is lower than the unsuccessful cases.

Upon creating the AVF anastomosis, a shunt is established between the high pressure (low capacitance) arterial vessel and the low pressure (high capacitance) venous vessel. This triggers multiple biochemical chains, two of which are key for the haemodynamics. Firstly, an increase in cardiac output occurs [267]. This is due to reduced systemic vascular resistance, increased venous return, and the maintenance of peripheral perfusion. In turn this often results in increased myocardial contractility, and an increased stroke volume and heart rate [128]. The increased myocardial contractility is incurred primarily due to the prolonged increase in CO [204, 268, 269]. One potential reason for this phenomenon reported in animal [270] and clinical studies [271] is the increased myocardial oxygen demand and perfusion requirements (leading to the increased CO) due to the presence of the AVF [204].

Secondly, the shunt modifies the resistances in the vascular network in the arm of the AVF. With the greatly reduced vascular resistances in the AVF arm, more flow is diverted to this location. The increased flow to the AVF location results in an increased force exerted by the fluid on the vessel wall in the vessel proximal to the AVF. This is evident in the subclavian artery of the AVF-arm in the successful AVF cases. With the varying flow rates induced by the AVF, (due to AVF type, patient characteristics, etc.) there is a distribution in the WSS and OSI observed in the AVF-arm subclavian artery.

The mean TAWSS, OSI, and transWSS metrics in the subclavian artery proximal to the AVF are plotted against cardiac output in Fig. 5.15. Additionally, the mean TAWSS, OSI, and transWSS metrics in the subclavian artery proximal to the AVF are plotted against AVF-arm subclavian artery flow rate in Fig. 5.16. Using the results plotted in Fig. 5.16, a Pearson correlation coefficient (r) was computed for each of the WSS metrics in each of the cohort sub-groups (against the AVF-arm flow rate), and the cohort as whole (Table 5.2). Due to the limited size of the cohort, limited correlations were indicated with respect to the AVF-arm flowrate. Treating the cohort as a whole, a moderately positive correlation was observed between TAWSS and transWSS (0.392 and 0.477 respectively) and AVF-arm subclavian flowrate, and moderately negative correlation was observed between OSI and

AVF-arm subclavian flowrate (-0.370). By analysing the sub-groups, the strong positive correlations were the TAWSS and transWSS r values for the Unsuccessful RCF group. The strong negative correlation was the OSI r value for the Successful BCF group (-0.823). The Unsuccessful BCF group demonstrated the weak correlations for each metric (TAWSS: -0.074, transWSS: -0.157, OSI: 0.173), however, this is largely due to the group size (n=2).

Table 5.2 Pearson correlation coefficient (r) for WSS metrics in the subclavian artery of each subgroup (presented in Fig. 5.16).

Group	TAWSS r value	transWSS r value	OSI r value
Successful BCF (sub-group)	0.364	0.653	-0.823
Successful RCF (sub-group)	0.214	0.339	-0.371
Unsuccessful BCF	-0.074	-0.157	0.173
Unsuccessful RCF	0.766	0.967	-0.591
Combined (all cohort)	0.392	0.477	-0.370

With increased flow rates generally inducing greater WSS levels, Figs 5.15-5.16 demonstrate successful AVFs induce greater WSS levels in the AVF-arm subclavian artery. A linear relationship between subclavian artery flow rate and the mean WSS metrics can be observed in Fig. 5.16. The unsuccessful AVF cases also also follow this trend. The only outlier to the linear relationship described is the successful BBF case, which is an outlier with respect to the other AVF morphologies, but also potentially to the flow-splitting methodology used in this investigation. In addition to the linear relationship between WSS and flow rate, an inverse linear relationship can be observed between mean OSI and subclavian artery flowrate (Fig. 5.16). There are two clear clusters of data, grouped by the successful cases (with high flowrate and lower mean OSI) and unsuccessful case (with lower flowrate and higher mean OSI). The successful BBF case is an outlier. Figure 5.15 demonstrates the cardiac output as a single measure is not an indication of the WSS and OSI magnitude induced in the subclavian artery of the AVF-arm 6-weeks following AVF creation.

The raw data of the mean WSS and OSI metrics and mean AVF-arm subclavian flow rate data is given in Table 5.2.

In addition to establishing that cardiac output cannot be used at the only measure of the haemodynamic flow conditions within the AVF-arm subclavian artery, this investigation sought to establish the ratio between the WSS metric values observed in the subclavian artery in the AVF arm and the WSS metric values observed in the non-AVF arm (Tables 5.2-5.3, Fig. 5.17-5.18).

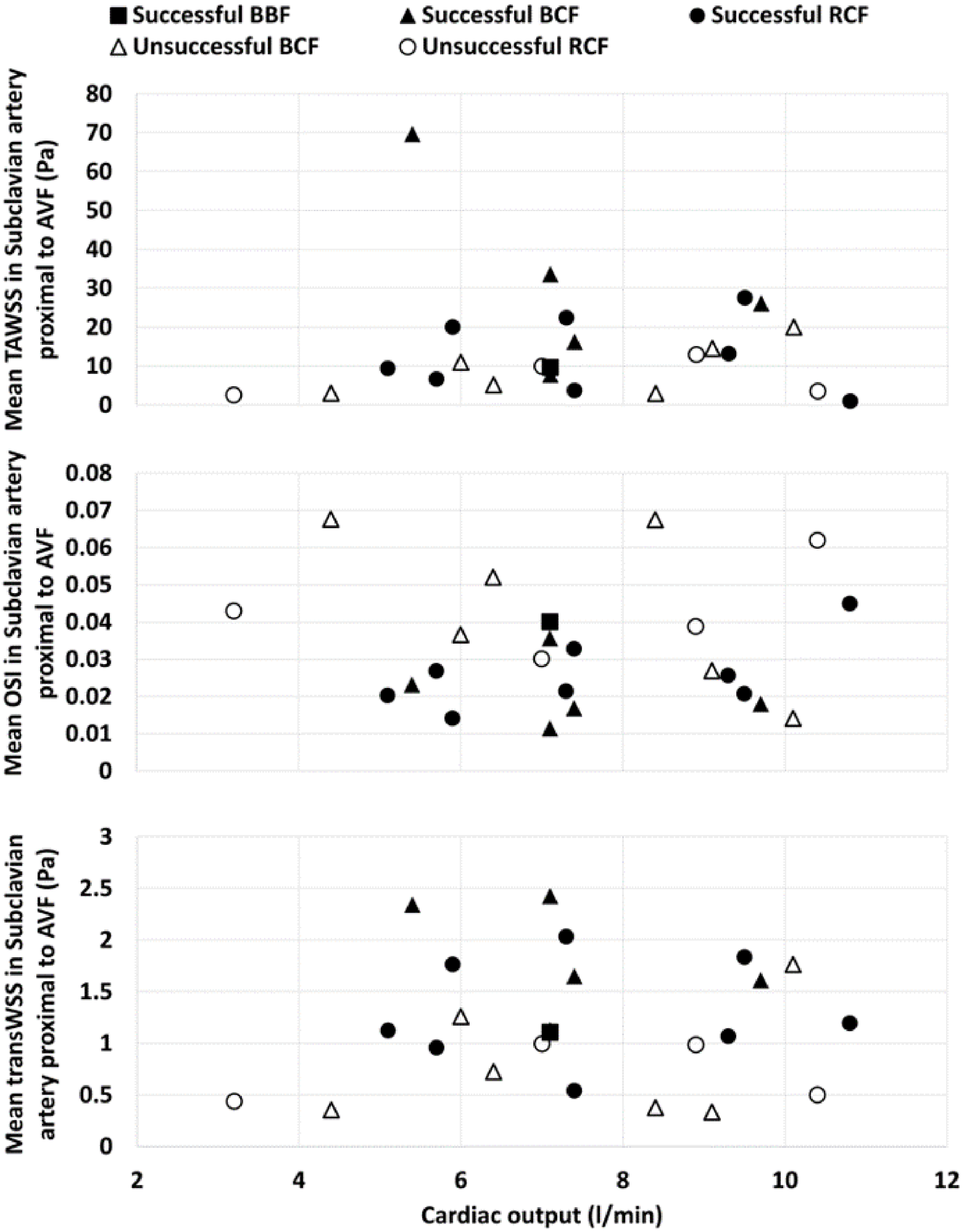

Fig. 5.15 Mean TAWSS, OSI, and transWSS metrics in the subclavian artery (in AVF-arm) plotted against cardiac output measured and prescribed at the ascending aorta (inlet).

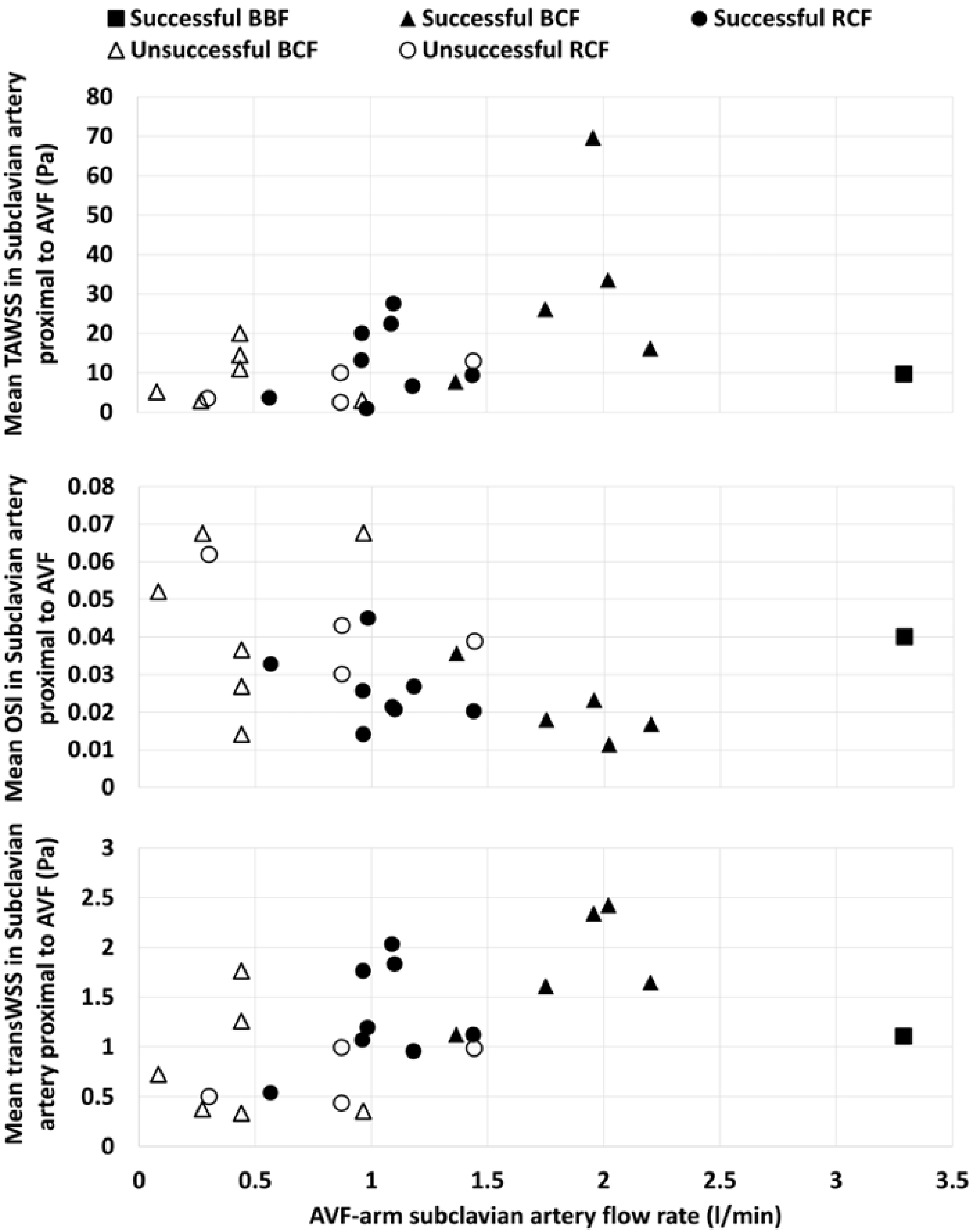

Fig. 5.16 Mean TAWSS, OSI, and transWSS metrics in the subclavian artery (in AVF-arm) plotted against mean flowrate within the AVF-arm subclavian artery.

Table 5.3 Mean flow rate, TAWSS, OSI, and transWSS metrics induced in the subclavian artery of the arm proximal to the AVF.

Subject	Mean AVF-arm subclavian flow rate (l/min)	Mean TAWSS (Pa)	Mean transWSS (Pa)	Mean WSSG	Mean OSI
45	3.290	9.705	1.105	9.18	0.04
40	1.751	26.141	1.611	25.638	0.018
60	2.201	16.302	1.65	14.859	0.017
69	1.956	69.669	2.34	50.269	0.023
71	2.020	33.605	2.425	29.045	0.011
48	1.365	7.79	1.125	7.33	0.036
6	0.984	1.015	1.194	8.66	0.045
18	1.181	6.686	0.957	6.446	0.027
34	1.089	22.479	2.033	21.926	0.021
57	0.567	3.753	0.54	3.551	0.033
64	1.100	27.623	1.835	22.095	0.021
65	1.439	9.443	1.123	8.203	0.02
77	0.964	20.1	1.764	16.854	0.014
87	0.962	13.261	1.069	9.263	0.026
44	0.083	5.223	0.725	4.905	0.052
80	0.965	3.082	0.354	2.786	0.068
51	0.273	3.019	0.377	2.794	0.068
67	0.440	11.061	1.26	9.072	0.037
74	0.440	20.1	1.764	16.854	0.014
94	0.440	14.596	0.335	14.118	0.027
72	1.442	13.012	0.987	12.511	0.039
79	0.301	3.59	0.501	3.086	0.062
61	0.872	2.64	0.439	2.457	0.043
96	0.872	10.049	0.996	8.268	0.03

Table 5.4 Ratio of mean flow rate, TAWSS, transWSS, WSSG, and OSI metrics induced in the subclavian artery of the arm proximal to the AVF compared to the values induced in the subclavian artery of the non-AVF arm.

Subject	Flow rate ratio	Mean TAWSS ratio	Mean transWSS ratio	Mean WSSG ratio	Mean OSI ratio
45	8.84	5.161	3.273	5.595	0.416
40	2.39	5.249	3.074	5.880	0.275
60	5.28	5.267	3.933	5.829	0.206
69	5.96	49.150	15.480	60.561	0.198
71	4.78	8.229	4.893	8.885	0.168
48	2.58	1.134	1.173	1.128	0.861
6	2.80	2.708	2.963	3.044	0.456
18	8.89	4.294	3.337	4.752	0.380
34	4.80	4.075	2.820	4.279	0.413
57	2.48	2.035	1.989	2.220	0.449
64	3.26	8.355	4.437	9.152	0.307
65	23.4	3.814	3.091	4.242	0.235
77	5.36	5.988	4.076	7.617	0.401
87	3.33	4.295	2.422	4.667	0.411
44	1.89	1.491	1.596	1.559	0.711
80	3.53	2.101	1.217	2.092	0.917
51	1.63	0.746	0.797	0.749	1.203
67	1.08	3.043	2.393	3.190	0.615
74	1.48	3.952	3.263	4.103	0.365
94	1.40	4.295	2.422	4.667	0.411
72	2.14	3.122	0.347	2.717	0.085
79	1.67	0.494	0.524	0.486	0.778
61	4.67	4.056	3.136	5.117	0.322
96	1.59	2.661	2.409	2.786	0.577

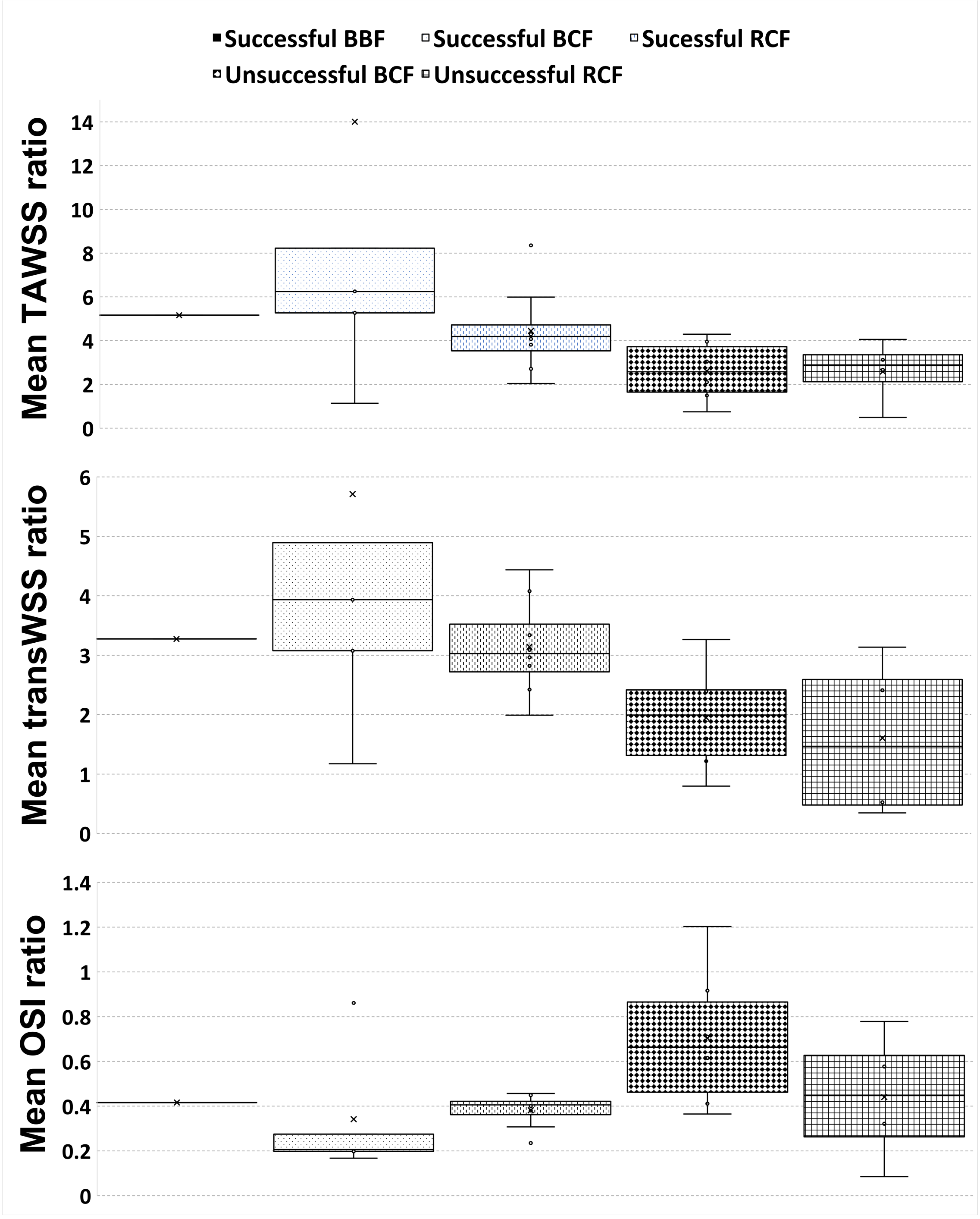

Fig. 5.17 Box plots of the ratio of WSS and OSI metrics (Table 5.2) between the subclavian arteries of the AVF and non-AVF arms.

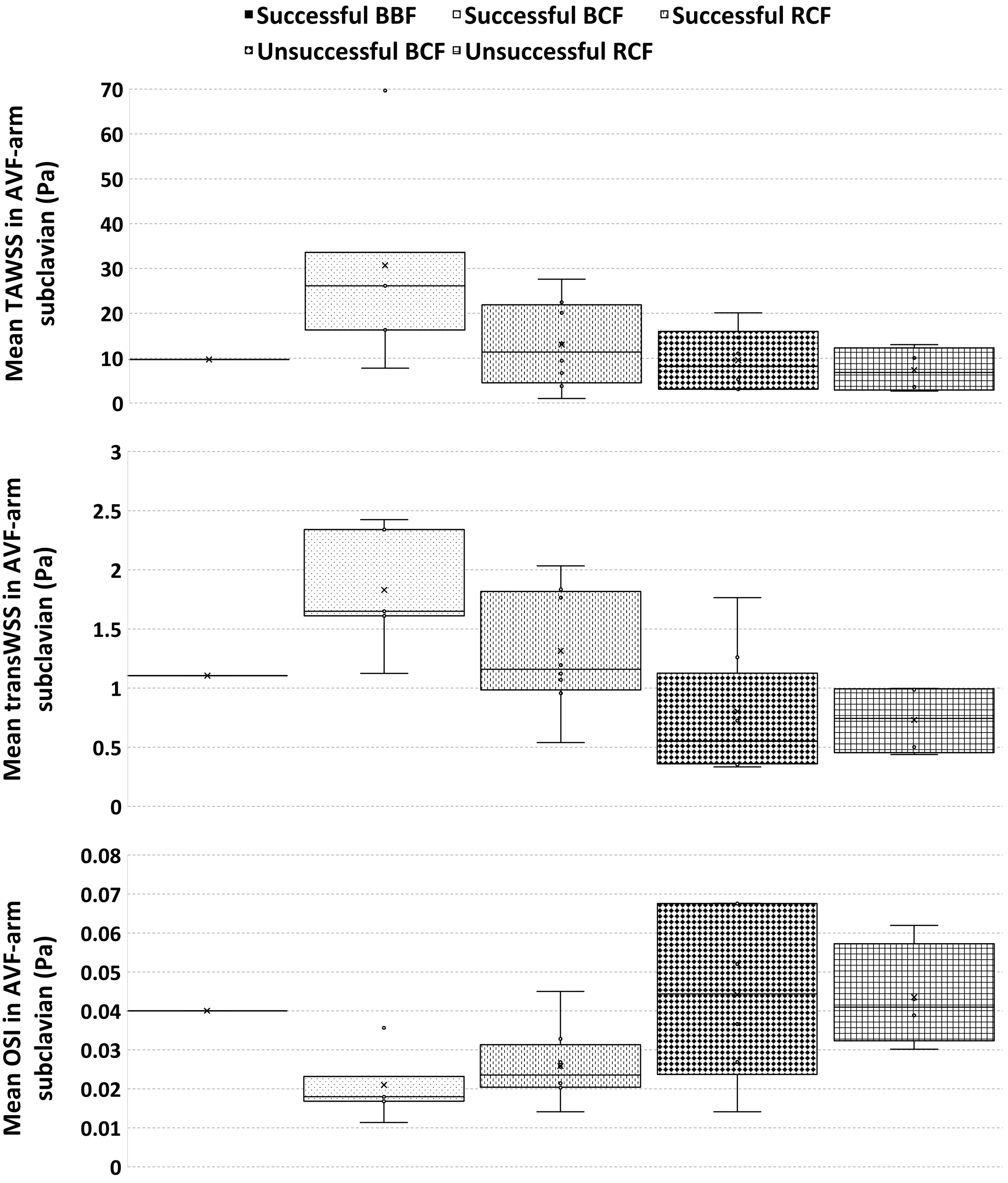

Fig. 5.18 Mean WSS and OSI metrics in the AVF-arm subclavian sub-groups within the cohort.

The presence of a successful AVF inferred increased TAWSS, transWSS, and WSSG levels in the AVF-arm subclavian (Fig. 5.18). The mean TAWSS levels were higher in all successful sub-groups (BBF = 9.71Pa, BCF = 30.70Pa, RCF = 13.04Pa) when compared to the unsuccessful sub-groups (BCF = 9.51Pa, RCF = 7.32Pa). This is also reflected in the mean transWSS sub-group values, where the successful cases (BBF = 1.11Pa, BCF = 1.83Pa, RCF = 1.31Pa) experienced greater transWSS than the unsuccessful cases (BCF

= 0.80Pa, RCF = 0.73Pa). Lastly, the mean OSI values induced within the successful groups (BBF = 0.040, BCF = 0.021, RCF = 0.026) was lower than that of the unsuccessful sub-groups (BCF = 0.044, RCF = 0.044). The ratio between the flow induced mean flowrates induced in the subclavian artery of the AVF-arm was markedly higher than the subclavian of the opposite arm (8.84 in the successful BBF, 4.20 in the successful BCF, 6.79 in the successful RCF, 1.83 in the unsuccessful BCF, and 2.52 in the unsuccessful RCF). This is demonstrated in Fig. 5.17.

5.6 Discussion and conclusions

5.6.1 Novelty and contribution

Despite the breadth of research and studies utilising CFD for assessing the haemodynamic environment of a patient or cohort [272–277], this study represents the first time that the aortic haemodynamics of ESRD cohort (with the influence of an AVF) has been specifically studied. The novelty of the previous publication by the same group of authors [246] studied the influence of the proximal haemodynamics on a single CKD patient with a successful RCF, and this investigation has extended this work to establish the WSS induced in the subclavian artery of the AVF-arm. Additionally, this study has furthered the confidence in the coupling between FeMRA and CFD.

Comparisons to prior work

Hyde-Linaker et al. (2022) [246] demonstrated that the presence of an AVF can trigger a 2.13 factor increase in the maximum Reynolds number (Chapter 3) observed in the subclavian artery of the AVF-arm. The increase in the maximum Reynolds number in other locations sampled within the AVF-arm ranged by a factor of 2.13-2.47. With the Reynolds number being a dimensionless value obtained using the velocity of the flow field, and Reynolds number being directly proportional to flow rate, the values of the ratio between AVF-arm subclavian flow and non-AVF arm subclavian were anticipated to be in the same range. With several cases exhibiting markedly higher ratios, the median ratio in the cohort was calculated to be 3.03. This difference is hypothesised to be largely due to the inclusion of other AVF types.

With the absence of other papers in literature utilising CFD for investigating the influence of the AVF on the aortic haemodynamics, comparisons can be made to flow fields simulated in the aortae of prior CFD research [211], or lumped parameter (zero-D or 1D) approaches utilised previously for estimating cardiac response and vascular access planning [278, 279, 227]. The flow fields within this investigation are similar to those simulated in the literature prior, excluding the increased flow rate and WSS values in the subclavian of the AVF-arm [275].

Regarding the lumped parameter approaches utilised in literature previously for assessing post-operative flow conditions associated with an AVF, Kroon et al. (2012) [227] implemented a 1D pulse wave propagation model of the arterial network to capture the long-term structural modelling. Additionally, Bode et al. (2012) [279] demonstrated the use of patient-specific pulse wave propagation models for predicting post-operative flow. Despite not being similar in methodology, such research and Huberts et al. (2012) [278] demonstrates the applicability of the predicting or gaining insight into the resulting haemodynamics following AVF creation. The major benefit of CFD over the pulse wave propagation model methods is the acquisition of the WSS distributions, which account for 3D anatomical variations. The localised WSS metrics obtained by CFD are crucial to the development of pathological conditions such as neointimal hyperplasia and atherosclerosis. Due to this, the acquisition of the flow fields (using CFD) over the entire cardiac cycle are of key importance for the surgical planning of the AVF anastomosis. The added advantage of using CFD for the proximal haemodynamics is that the magnitude and distributions of WSS metrics induced in the bifurcations near the aortae can be obtained, these WSS values are unobtainable or have many assumptions when considered in 1D. In other words, 1D simulations are limited in cases of localised complex haemodynamics, and are more suited to simulating the haemodynamics on a ‘network-sized’ or ‘multi-bifurcation’ scale. The selection over using 1D or 3D for a simulation in a given study comes down to the question of interest. In the cases explored in the this chapter, the extraction of the WSS levels induced in the AVF-arm and the non-AVF arm (for the purposes of computing a ratio), negated the use of 1D simulations. Furthermore, the outlet conditions utilised in the study were total flow percentages, which would have complicated the outlet definitions in the available 1D methodologies should they have been applied. Howver, the use of a CFD simulation in this study is principally due to the question of interest, and should the question be flow-related only, a 1D simulation may suffice. In this scenario, an upside to having the segmentation would be the more refined prescription of cross-sectional areas used in the 1D network definition, as opposed to assumed values. Lastly, a coupled 1D-3D approach may be the most suitable approach (with regards to computational expense) in other cases where the extraction of WSS values in a specific 3D region in required, but where 1D methods can approximate the proximal and distal haemodynamics.

5.6.2 Limitations

One key limitation of the investigation in this chapter is the scan region (and resulting segmentation) in several of the geometries, with the majority of the descending aorta being excluded in these cases. However, the use of flow split outlets (as opposed to pressure outlets) reduced the impact of this factor. Additionally, the descending aorta was not the region of interest. Another limitation in several of the cases was the lack of PC-MRI data from which a known flow split could be calculated. This limitation was reduced as much as possible by utilising the flow splits calculated in the rest of that sub-group for which the flow-split was known. These cases utilised known cardiac outputs for the ascending aorta inlet information.

The scan resolution and the resulting segmentation methodology are key determinants of the precision and accuracy of the resulting computational domain used in the investigation. A DICE score was completed in a prior investigation to demonstrate the validation of the segmentation approach (Chapter 3). Additionally, a mesh independence study (including the calculation of Richardson extrapolation and grid convergence index) was calculated to ensure the mesh density and characteristics were suitable (Appendix D.2).

The flow-splitting methodology and the initial assumed flow split values were also a source of limitation. Despite the initial flow split values used being sourced from literature [211], there is a negation of the ‘true’ patient-specific flow splits when applying the assumed literature values across a cohort. This was deemed suitable in this investigation due to the lack of patient-specific flow data in the non-AVF vessels. However, the acquisition and use of patient-specific flow data in the rest of the vessels would be a first step in furthering the research in this chapter. The last noteworthy limitation of this investigation is that the study is not longitudinal, i.e. information and simulations relating to the patients pre-AVF condition, and follow-up post-AVF condition (after the 6-week scan mark) is not known or simulated.

5.6.3 Clinical relevance

The time required for segmenting aorta and the secondary vessels in the FeMRA datasets is less than that of the smaller AVF vessels presented in Chapter 4. This is in large part due to the vessels being more visible, and the higher flow rates making the aorta and the secondary vessels sharp within the image data. The time required for an experienced user of a segmentation software to accurately extract the vessels of interest is less than 1 hour. The follow pre-processing steps prior to simulation also require 1-2 hours of work. The simulations (depending on mesh resolution, time step, solution storage intervals, and computational resource) can take multiple hours or multiple days. The requirement for a quick turnaround from scan to simulation post-processing is somewhat avoided in this investigation due to the proposed context of use. In a clinical setting, the simulations used for assessing the aortic haemodynamics would be for long-term planning and study long-term detrimental haemodynamics. The detrimental haemodynamics would be manifested in cardiovascular complications, which although despite being the greatest cause of mortality in the ESRD population, may not be the most immediate area of concern due to haemodialysis being required 3-4 times a week.

With the creation of the AVF altering downstream resistances in vascular network, the aortic haemodynamics (notably at the subclavian artery proximal to the AVF) are significantly altered. This modified flow-field persists while an AVF remains successful or is in the process of maturing. Cardiovascular complications and atherosclerosis are predisposed to bifurcations and vessel curvatures, where complex haemodynamics arises. Low and oscillatory WSS has been linked with atherogenesis, the process of atherosclerotic plaque formation. Plaque development can modify the local WSS topography over time and lead to vessel geometrical irregularities, or narrowed arteries. Such outcomes can impair endothelial function and lead to the formation of atherosclerotic plaques. The low and oscillatory WSS regions can promote the accumulation of lipids and platelets, hallmarks of atherosclerosis. Issues such as luminal narrowing can lead to increased WSS levels, which may further plaque progression. Additionally, high WSS can be associated with the formation of vulnerable plaque phenotype [280]. High WSS regions are typically associated as a key regulator in the vascular network, with vasodilatory substances being excreted and the endothelium being maintained. However, chronic high WSS has been stated to stimulate aneurysm formation and atherosclerotic plaque destabilisation in vessels with stenoses [281], case 69 in Fig. 5.11 is a potential example of this.

Considering the above, it is proposed that high TAWSS and transWSS observed distal the vertebral artery (in the AVF-arm) should not be a major area of concern due to the unavoidable increase in observed WSS and the mostly low OSI observed in this region. However, particular attention should be given to the WSS and OSI distributions in the subclavian artery (in the AVF-arm) proximal to the vertebral artery (the regions evaluated within this investigation, Fig. 5.6).

5.6.4 Conclusions and further work

This investigation has demonstrated the workflow and FeMRA-CFD coupling first implemented in Hyde-Linaker et al. (2022) [246] can be applied to multiple chest scans from a cohort of ESRD patients for the propose of evaluating the influence of a AVF on the proximal haemodynamics. The question of interest was *"can the influence of a successful AVF be quantified by using WSS and OSI metrics?"*. Through sub-dividing the cohort into sub-groups based on AVF outcome and morphology, it was observed that the subclavian artery of the AVF-arm experiences TAWSS and transWSS in greatly increased magnitudes should the AVF be successful (Fig. 5.18). Additionally this is reflected in the ratio between the WSS levels in the subclavian arteries of the successful and unsuccessful sub-groups (Fig. 5.17). Lastly, the mean OSI levels induced in successful cases were found to be less than the unsuccessful cases (Fig. 5.16, Table 5.2).

There exists several routes forward for this research. The most immediate extension to this work would be to apply the same workflow to a patient cohort with phase-contrast waveform data at several of the vessel outlets. This would eliminate the use of the assumed intial flow split values, one of the key assumptions in this investigation. Incorporating an FSI element to the simulations would also be an extension to this work. However, the definition of appropriate patient-specific parameters in hyperelastic wall models can be challenging, and measuring wall distensibility in-vivo is often infeasible.

Another extension to this work would be to complete a pre-AVF and post-AVF comparison (similarly to the investigation in Chapter 3). This would permit the user to analyse the relative increase in the subclavian artery proximal to the AVF following its creation. Chapter 3 demonstrates a three-fold increase in WSS for a single-patient, and analysis of multiple patients may elucidate this further. In addition to studying the fluid dynamics following AVF creation (such as the increased cardiac output), analysis of changes in vessel characteristics would be possible.

Lastly, further work to this investigation could come in the form of simulating the haemodynamics on a larger cohort of data. Generating large repositories of data has the potential of being crucial for considering cases where the proximal haemodynamic implications contraindicate AVF as a vascular access, or when the resulting haemodynamics from the AVF require frequent monitoring.

Considering these points, WSSG may be the most appropriate measure of determining potentially problematic haemodynamics. This is due to plaques occurring in low/oscillatory WSS regions initiating atherosclerotic regions. With plaques potentially modifying flow characteristics, high WSS profiles may be generated in this region subsequently. This can initiate cardiovascular and atherosclerotic complications. For example, when atherosclerosis is exposed to high WSS regions, biochemical reactions can cause thinning, erosion, and rupture of plaque caps [282].

Through analyses of the WSS metrics and contour plots, it can be established that an elevated risk of cardiovascular complications (e.g. aneurysms) is induced in successful AVF cases, in particular BCF cases. A likely location of the complications (aneurysms etc.) is the choatic and disturbed flow location juxta-to the subclavian artery of the AVF-arm. Longer-term follow-up simulations should be completed in order to assess the impact of increased cardiac output over time, and modified flow-rates in the subclavian artery induced due to the AVF. Sustained elevated WSS levels in the subclavian should be considered by practitioners.

Chapter 6

Discussion

6.1 Key results, novelty, and contribution

6.1.1 Key results

The research questions of this thesis (as stated in Chapter 1) were as follows:

- can a 'scan-to-simulation' workflow be established for patient-specific AVF from FeMRA? Can this be used for a patient-care focused AVF planning approach?
- can this workflow be used to study the influence of an AVF on the proximal haemodynamic environment?
- can vessel and or fluid flow markers in a cohort of AVF cases establish whether biological or haemodynamic flow factors are more crucial to AVF success?
- what is the influence of the AVF on the wall shear stress (WSS) metrics in the proximal subclavian artery? How does the WSS values compare to the opposite subclavian vessel?

The aim behind addressing these research questions was to contribute to the existing vascular access literature, and the AVF CFD studies in particular. The outcomes of this research and subsequent investigations are hoped to lead to superior patient-centred care (a focus of the KDOQI guidelines [3]) and improved patient quality-of-life.

The key results of this research were:

- FeMRA was coupled with CFD in order to generate patient-specific AVF models for analysis of each haemodynamic environment.

- The FeMRA-CFD coupled workflow was used with a dataset registration workflow for generating a patient-specific model (of a 19-year-old RCF case) from the ascending aorta to the draining vein.
  - The pre- and post-AVF haemodynamics demonstrated a significant 2-3-fold increase in blood flow rate was induced downstream of the left subclavian artery.
- Through a combination of ROC and CFD analysis, the feeding artery curvature was found to be the most prominent factor influencing AVF success in the jxta-anastomosis pilot study
  - Lower patient age and BMI were the biological factors that could be linked with higher AVF flow rates
  - Successful AVF cases exhibit greater WSS magnitudes and greater OSI values in the venous AVF segment than the unsuccessful AVF cases
- The presence of a successful AVF 6-weeks post-creation causes the subclavian artery of the AVF-arm to exhibit greater flow than the non-AVF-arm by factor of 4.20-8.83 (depending on morphology

Novelty and contribution

Prior work has been completed on coupling MRI and CFD for AVF studies [224], and Bozzetto et al. (2018) [156] demonstrated good quality images in a short scan duration when coupling contrast-free MRI and CFD (for studying AVF). However, the segmentation difficulty of these studies is unknown. To the author's knowledge, this is the first research to couple FeMRA with CFD, particularly for describing AVF dynamics. This coupled approach can be implemented clinically and in in-silico trial workflows. The segmentation and pre-processing workflow created within this research can be used for this. One component to this workflow in Chapter 3 was the novel approach for a dataset registration workflow where three segmentations were combined into a single geometry for CFD analysis. Despite DICOM tags of the scanned data giving the anatomy's position with respect to the other vessels in the other scans, a registration was required to align them due to deviations in patient alignment. Although being a time-intensive process which may not be applicable on a larger-scale, this workflow has demonstrated a way to combine multiple patient-specific segmentations for separate scans without combining the scans at the DICOM level. Within Chapter 5, traditional flow-splitting techniques such as Murray's law and Chnafa et al. (2018) [222] were not applicable due to the 'non-physiological' flow-rates induced by the presence of the AVF. In order to establish suitable flow-splits in each of the cases, a new flow-split workflow (for when flow-rate data is known for one outlet) was implemented. The methodology adjusted the other outlet splits whilst giving the precise flow-split (in successful cases) to the subclavian outlet (in the AVF-arm).

6.2 Workflows and limitations

6.2.1 Limitations

The resolution of the images obtained through the FeMRA imaging protocol used for segmentation, meshing, and simulation is a minor limitation of the simulations. Moreover, the segmentation of the vessel structures from the images is a source of human error (particular with a large number of datasets). However, this error was minimised through the computation of a DICE score (Chapter 3). A limitation of the CFD investigations was the assumption of rigid walls, however, this is a common approach in computational haemodynamics. The influence of arterial wall deformation on the haemodynamic environment of large vessels is considered relatively small, however, for the juxta-anastomosis environment, wall motion effects may be more pronounced. Fluid-structure interaction (FSI) methodologies can account for this behaviour but FSI modelling is challenging and requires considerable computational expense. This makes FSI less applicable when considering running patient-specific simulations in a clinical setting, despite the varying reports of the influence of FSI [283, 284]. When considering FSI, significant attention is required for selecting the most appropriate material properties of the wall, and the treatment of the wall model as either elastic or hyperelastic. When treating the arterial wall as hyperelastic (as it is in reality), the definition of the model parameters requires significant attention, and can lead to multiple wall definitions being used per patient. This is due to the varying properties across the layers of the arterial (and venous) walls, and the patient variability in the elasticity and compliance the vessel walls. Completing in-vivo assessments of patient-specific vessel wall compliance is challenging, and often leads to assumptions on the wall properties when included. Due to the scope of this research and the research questions being considered, FSI was omitted from the investigations in this research.

Another key reason for omitting the FSI influence from the CFD investigation was the selection of the boundary conditions. Using a prescribed outflow waveform ascertained from phase-contrast data for the AVF draining vessels meant that the flow conditions within the AVF were replicated as closely as possible. Utilisation of a polynomial triphasic aortic inlet waveform calculated using cardiac output data at each visit is also a minor limitation of the CFD study in Chapter 5, as the results at peak systole may be slightly different in reality. Finally, the specification of the boundary conditions is usually a source of limitation in CFD studies. The use of phase-contrast waveforms in Chapter 4 was used for replicating flow-conditions, and limitations are therefore minimal. Windkessel parameter values (Chapter 3) can also be considered a limitation due to the resistances and capacitances being estimated for each case using assumed values for vessel resistance, capacitance, and compliance. The same Windkessel values were assumed for the terminal arteries in the pre- and post-AVF simulation (apart from the AVF vessels), which is also a potential limitation. Lastly, the flow-split values used within Chapter 5 were based on a workflow that used initial estimates for the flow-splits. However, the workflow permitted the configuration of flow-splits to correspond to the known cardiac output and the AVF-arm flowrate data, which was the main aim of the flow-splitting workflow.

Of particular pertinence to boundary conditions, the question of ‘can a single flow-rate and or cardiac output be utilised for accurately predicting the various states of a patient?’ arises. This is due to the varying patient states (physical activity, rest, caffeine) inducing differing cardiac outputs and therefore differing boundary conditions. Using a single sample of flow waveform data is therefore somewhat of an assumption and a limitation. However, this is a frequent approach in literature due to availability of patient waveform data and feasibility of acquiring multiple waveforms per patient. This use of the patient waveform data permits the assessment of anatomical variations on the flow waveforms with known flowrates at a patient’s resting state.

6.2.2 Verification and validation

Chapters 4 and 5 sought to replicate flow conditions acquired through the computational extraction of flow waveforms from PC-MRI. The flow waveforms and split imposed at the outlets minimises potential sources of error (for the VOI in the flow-split case), and can be said to validate the haemodynamics generated within the computational domain. Chapter 3 utilised lumped Windkessel models for predicting physiological pressure thoughout the domain. Validation of the pressures simulated (with estimate R, C, Z values) can be achieved through blood pressure measurement techniques. This was not feasible in that study, however, the flow waveforms induced were validated with respect to PC-MRI flow waveform.

Aside from the initial flow-rate acquisition and specification of the boundary conditions, the modelling practices used in the model generation and CFD phases minimised potential sources of error where possible and permitted the verification and validation of the modelling with respect to the question of interest and context of use that they were intended (ASME V & V 40). Techniques such as computation of DICE scores, and producing surface mesh resolutions finer than the original segmentation meant that the model generated workflow produced a mesh that was limited only by the original scan resolution. Iterative remeshing with low-level smoothing factors was used so as not to distort the generated domain of the vasculature.

The CFD modelling practices used followed accepted academic and industry validation methods, with mesh independence studies (Appendix C.2, D.2) being computed for each investigation presented. Grid convergence index and Richardson extrapolation ensured that the mesh characteristics used within the investigations of each cohort were of sufficient resolution. Prism layer meshing and computation of accurate y+ values ensured near-wall flow-phenomena were captured.

6.2.3 Computational resource

In Chapter 3 it is noted that despite 1D network simulations providing a rapid computation, 3D numerical investigations permit a more comprehensive analysis of the haemodynamics than low-order models, despite the inevitably increased computational expense.

One potential issue with the wide adoption of CFD in clinical practice is the time required for segmentation and simulations, where the ideal clinical use case is to have a ’bedside simulation’. Several barriers such as cloud-based resources have progressed the feasibility of this. However, items requiring user input, such as the segmentation, remain barriers. Additionally, initialisation of the computational domain in haemodynamic studies often requires 4-5 cardiac cycles, which greatly increases computational expense and limits the current clinical use of CFD. This may shift academic and industry haemodynamic CFD to focus more on the surgical planning and device ‘testing’ cases, where timescales on the *critical path* are longer and CFD time-frames are more feasible.

6.3 Discussion related to the investigations within this research

6.3.1 Computational haemodynamic conclusions

Proximal haemodynamics to the AVF

Chapter 3 investigated the proximal haemodynamics to an AVF in a 19-year-old CKD patient with a successful RCF (in the left arm). The question of interest of this investigation was whether a workflow could be establish for unifying three segmentations from a single patient? And if so, what is the influence of the AVF on the proximal haemodynamics? Following the construction of the workflow, the key finding from this study was the marked increase in blood flow velocity and TAWSS demonstrated throughout the left subclavian, brachial, and radial arteries unilaterally to the AVF. This is a marker of adaptive arterial remodelling to accommodate the increased flow rates resulting from the surgical anastomosis. In addition, the diameter of the specific reconstructed AVF was suggestive of successful fistula maturation [3]. The localised haemodynamic factors relating to NH and outward remodelling were analysed confirming sufficient AVF flow rates (>600mL/min) and the generation of transitional flow with substantial helical flow patterns in the cephalic vein distal to the anastomosis throughout the cardiac cycle. This arises due to the significant change of direction of the flow entering the vein, which generates complex vortices and secondary flows when flow is exerted on the opposite vessel wall. Our simulation indicated cyclic disturbed flow (OSI 0.42) in the radial artery distal to the anastomosis, and in the vein immediately following the venous swing segment of the AVF. This region of the vein, which experiences low and oscillatory shear stress, corresponds to where luminal reduction may occur due to NH. The context of use of the workflow is to investigate proximal haemodynamics in a post-operative analysis.

Juxta-anastomsis patient-specific haemodynamics 6-weeks following AVF creation

The question of interest in this investigation (in Chapter 4) was; are biological factors, vessel characteristics, or haemodynamic factors more prominent in determining the long-term outcome of an AVF? And what factors may be the most prominent? The context of use for the simulations was to examine the vessel characteristics and WSS profiles to examine whether AVF long-term outcomes can be determined at the 6-weeks post-AVF creation imaging follow-up.

By performing a ROC analysis of the vessel characteristics to and from the AVF anatomosis, feeding artery curvature, feeding artery diameter, and draining vein diameter were found to be the best prognostic factors of superior venous flow rate and dialysis procedure speeds. Additionally, combining these parameters into a single ROC analysis was found to yield an area-under-curve value of 0.83. Factors such as anastomosis angle were found to be not as prominent. However, this may be due to the study size. Analysis of the WSS and OSI metrics in the 1cm segment sub-divisions within the cohort demonstrated an increase in WSS leading up the anastomosis, with the maxima WSS being observed in the anastomosis segment. The WSS then decreased with each distal 1cm segment. OSI values in both successful and unsuccessful cases indicated mostly uni-directional flow in the feeding artery, which then increased in the venous segment by a small amount in unsuccessful cases and by a large amount in successful AVFs. This indicated disturbed and oscillatory flow in the venous segment, indicative of outward remodelling and conditions for potential neointimal hyperplasia. Analysis of the LNH and radial velocity values throughout the domain along the feeding artery-draining vein flow path shows there is an elevated rotational component to the flow in the unsuccessful outcomes of the BCF and RCF when compared to the successful outcomes of the same AVF type.

Aortic haemodynamics post-AVF creation

The question of interest for the simulations completed in Chapter 5 were; can the influence of the AVF on the haemodynamic environment in the aortic region (notably in the subclavian arteries) be quantified? The context of use of the simulations was to obtain WSS and OSI metrics within the subclavian arteries. This allowed the ratio of the WSS and OSI between the AVF-subclavian and the opposite subclavian to be established. Markedly elevated WSS values were observed in the AVF-arm subclavian in successful cases over the unsuccessful subjects (e.g. the mean TAWSS in the subclavian AVF-arm were 9.7 in the successful BBF, 30.7 in the successful BCF, 13.0 in the successful RCF, 9.5 in the unsuccessful BCF, and 7.3 in the unsuccessful RCF). Despite the high WSS values being linked to endothelial health, chronic high WSS is linked with atherosclerotic complications, notably the rupturing of plaques. This is somewhat unavoidable due to the 'non-physiological' flow induced by the AVF. As such, it is proposed that subjects with low/oscillatory WSS juxta-to chronic high WSS regions (e.g. AVF-arm subclavian arteries with a higher degree of curvature) be investigated more throughly prior to AVF-creation. The presence of pre-existing plaques should be a noteworthy finding.

6.4 Future outlook of AVF computational haemodynamics for clinical AVF generation

6.4.1 Summary of current state of AVFs

CKD has an increasing worldwide incidence [8]. Currently CKD accounts for approximately 16% of the global disease burden [285]. The increasing number of elderly patients constitutes the fastest growing element of the ESRD population, and the increasing prevalence of ESRD infers the continued need for RRT [8]. The RRT strategies include peritoneal dialysis (6.4%), renal transplant (29.3%), and hemodialysis (HD) (64.2%) [8, 286, 287]. Kidney transplantation waiting times mean that despite it being the preferential RRT strategy, a majority of the CKD population require routine HD treatments. This infers the use of a vascular access in the form of an AVF, AVG, or a CVC.

The KDOQI guidelines [3] state that the AVF is the optimal VA for HD due to less complications, superior patency rates, and lower associated costs. Lower infection and mortality has also been proposed in support for AVFs [83]. Despite this, the high primary maturation failure rate of AVFs (up to 60% of AVFs not being suitable for HD 5 months post-creation) [89, 28, 288] and the patency rates (60% 1-year primary patency and 71% 1-year secondary patency) [96] demonstrate clear issues in AVFs being a permanent and widely-implemented solution. The hypothesised impact of the haemodynamics of these maturation and patency rates infers that elucidation of AVF haemodynamics will be key in improving these rates, as well as the implementation and adoption of AVFs in clinical practice.

6.4.2 AVFs in in-silico trials

Computational haemodynamics investigating AVF performance and configuration can be classed under in-silico trials, an individualised computer simulation used in the development or regulatory evidence of a medical product, device, or intervention [289]. With the clinical trial cost estimates being in the 10s of million dollars, and the time being approximately 5 years, in-silico trials offer the opportunity to reduce costs, follow up times, and time to market.

With FeMRA circumventing the historic blocker to the generation of 3D patient-specific models, a new look can be given to compiling databases of longitudinally scanned AVF geometries. This can inform desirable AVF characteristics across a much larger (and international) cross-section of the ESRD population. Statistical shape modelling (SSM) may be also used for generating more geometries whilst FeMRA becomes gradually adopted.

These geometry databases can be used for studying several questions of interest at a time, with the context of use varying depending on the user's application or research area. Furthermore, being able to simulate patient-specific anatomy with respect to anatomic variations and differing boundary conditions infers the generation of many datasets. Performing in-silico trials on this magnitude infers large volumes of simulation data (Fig. 6.1), which will need robust management, retrieval and archival of data.

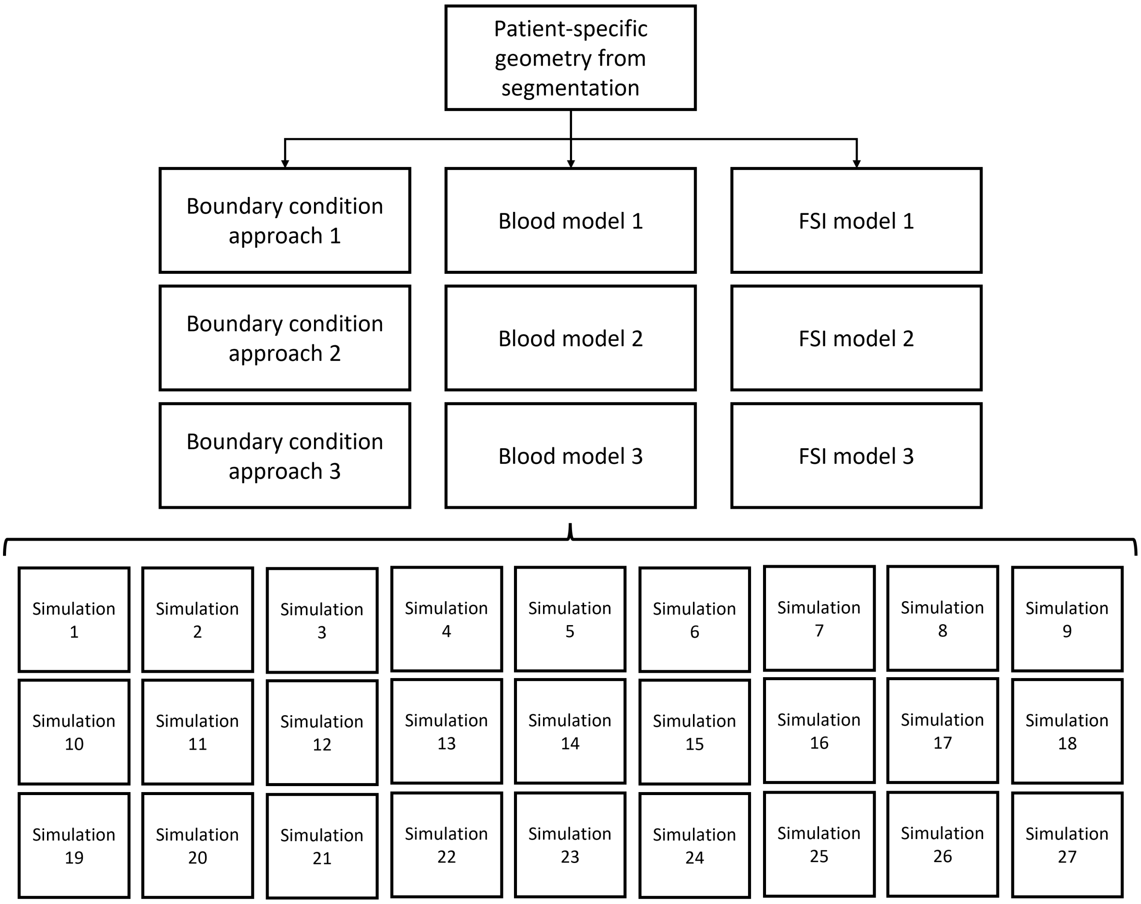

Fig. 6.1 Example figure of the quantity of cases generated in an in-silico trial workflow when considering multiple boundary condition, blood model, and FSI model approaches.

6.4.3 Simulation of AVF in current and future research

The segmentation of the geometries from the FeMRA scans was easier to complete in successful cases, particularly in those with larger vessel cross-sections (such as the Successful BBF and BCF cases). The unsuccessful RCF cases were the most challenging due to the lower flow rates (which makes the vessels less visible due to the contrast not being as visible), and the smaller vessel cross-sections. However, Chapter 4 of this research demonstrated that the visualisation and segmentation of non-matured AVF vessels is possible. The segmentation time per case ranged from 30 minutes to 200 minutes. The preparation steps (smooth, clipping, computing centrelines) was 1-2 hours per case, largely due to the number of packages and software utilised in the workflow. This could be reduced in a commercial image processing software.

Despite the information acquired within the simulations of this research, the methodology and pipeline may remain a blocker to the wide implementation of such an approach within the clinical environment on a patient-specific level if rapid turnaround time from scan to simulation result is required. This is mainly due to the time required to generate the patient-specific AVF models. Despite the greatly enhanced visualisation of the arm vessels with the use of FEMRA, the time and costs of the segmentation ‘user-hours’ may infer that the approach does not become scalable on an individual patient level. This will be largely due to the resources available to the surgeon and hospital. However, with the amount of flow and WSS data generated using CFD, and an individualised patient focus being a major aspect of clinical vascular access guidelines [3], the use of CFD for re-intervention planning may be the most immediate solution for informing the AVF location and morphology. This is particularly the case in challenging patients (elderly, frail, etc.). With the use of FeMRA overcoming the imaging (and vessel visualisation) issues, and despite the segmentation and CFD workflow producing large amounts of data, there may remain instances where more rapid workflows exist for acquiring the baseline information required for the surgeon.

The quickest approach which obtains the least information is the 2-dimensional analyses of the patient-specific vessel diameters and flow magnitudes in the haemodynamic environment proximal and distal to the anastomosis. The main advantage of this approach is that is does not require further investment in most hospitals, which have access to 2D phase-contrast software. However, as demonstrated within Chapters 3, 4, and 5 of this research, the 3-dimensional flow conditions greatly influence the haemodynamic WSS metrics hypothesised to influence the development of the AVF. This 2D approach does not permit simulation or study of the pre-operative and post-surgical haemodynamic and WSS environment, and should therefore only be considered the baseline requirement.

A second approach which can be considered is to utilise the current segmentation methodology for constructing a virtual population, otherwise known as a virtual dataset. Despite this being a workload-heavy approach on the front-end, once the segmentations are complete, a virtual AVF corresponding to the patient’s characteristics can be generated by varying some pre-defined parameters (e.g. vessel diameter, patient age). This AVF can then be used in-place of a model generated from a patient-specific reconstruction. The advantage of this method is the rapid turnaround from completing the imaging protocol to acquiring a patient 'focused' model, which can be used for pre-surgical planning and post-operative evaluation. This is one of the major proponents to 'in-silico trials', and should be explored where possible. The historical blockers to such an approach have been the imaging limitations (which are resolved using FeMRA) and the acquisition of a suitable database of scans. An ideal database would have a plentiful number of scans and have wide variability within the cohort(s). Limited variability would constrain the 'patient-specific' details of the virtual AVFs, which is a crucial factor of this approach. This approach does limit the patient-applicability of the subsequent findings, but is an improvement on solely using 2D analysis. The last drawback to mention is the aforementioned segmentation time upfront.

Another approach which can be considered is the creation of a AI-based tool which can automatically segment datasets, in this case, FeMRA-acquired DICOM stacks. Such a tool can export the segmentation ready for simulation pre-processing. Synopsys Simpleware's Knee MRI 'auto-segmentation' tool is a good example of this. This approach is highly desirable as this avoids the constraint behind deploying the workflows presented in research into clinical practice. In order to create the AI-based tool, a significant number of ground-truth segmentations are required in order to 'train' the model. Several challenges exist in training such a model for the AVF datasets in this research however. Firstly, the location of the anastomosis differs across the patient cohort. As well as the subdivision of brachiocephalic and radiocephalic fistulae, many of the radiocehpalic fistulae were situated near the hand as opposed to the mid-forearm. These minor differences in fistulae location could infer the creation of numerous models and tools trained for differing AVF locations. Additionally, the differing AVF morphologies (Chapter 3) make the task of training the tool more complicated and may constrain the use of any such tool. Moreover, the differences that may exist between differing MRI-based imaging protocols (e.g. intra-hospital) may limit the tool further. The time-required for completing the ground-truth segmentations is also a consideration with the aforementioned differing AVF locations and morphologies. As such, such a tool may only prove useful for rapid in-house 3D segmentation of AVF datasets with common location, morphology, and imaging protocol.

Lastly, the use of 4D MRI may provide a suitable solution for purely performing a post-operative evaluation of the vessel's haemodynamics. Software such as *Circle cvi42* (https://www.circlecvi.com/) has the capability of quantifying and visualising flow over the cardiac cycle. This can serve the pre-operative AVF vascular screening process. The main advantage of 4D MRI over CFD is that the simulation run-time required for CFD is avoided completely. Secondly, the influence of boundary conditions, even with specified flow rate from 2D phase-contrast data, is avoided. Finally, the segmentation time and potential segmentation errors (human or algorithm) are also avoided. The drawbacks of the 4D flow analysis technique are fairly standard items, such as resolution and human-error during software-usage. However, being able to complete the entire AVF vascular screening and post-surgical analysis with flow visualisation within one software is advantageous on a clinical level.

The focus within future computational AVF haemodynamic studies should be to contribute to digital evidence and conclusions for informing clinical practice on AVF creation and intervention. FeMRA represents an effective way of generating contrast-enhanced vessels in the DICOM for subsequent segmentation and CFD analysis. The use of FeMRA and CFD for compiling a library of reference CFD and geometry data is proposed to be the next immediate step of the research questions addressed in this thesis.

References

[1] The structure of the kidney and nephron (national institute of diabetes and digestive and kidney diseases, national institutes of health). https://www.niddk.nih.gov/health-information/kidney-disease/nephrotic-syndrome-adults. Last accessed: 25/02/2023.

[2] Lesley A Inker, Hiddo J Lambers Heerspink, Hasi Mondal, Christopher H Schmid, Hocine Tighiouart, Farzad Noubary, Josef Coresh, Tom Greene, and Andrew S Levey. Gfr decline as an alternative end point to kidney failure in clinical trials: a meta-analysis of treatment effects from 37 randomized trials. *American journal of kidney diseases*, 64(6):848–859, 2014.

[3] Charmaine E Lok, Thomas S Huber, Timmy Lee, Surendra Shenoy, Alexander S Yevzlin, Kenneth Abreo, Michael Allon, Arif Asif, Brad C Astor, Marc H Glickman, et al. Kdoqi clinical practice guideline for vascular access: 2019 update. *American Journal of Kidney Diseases*, 75(4):S1–S164, 2020.

[4] Schematic diagram of haemodialysis procedure. https://www.niddk.nih.gov/health-information/kidney-disease/kidney-failure/hemodialysis. Last accessed: 25/02/2023.

[5] Vascular access options for haemodialysis: Central venous catheter (cvc), arteriovenous fistula (avf), and arteriovenous graft (avg)). https://suryakidneycare.in/av. Last aaccessed: 25/02/2023.

[6] The differing avf classifications (radiology key website. https://radiologykey.com/arteriovenous-fistulas/. Last accessed: 25/02/2023.

[7] The differing avf anastomoses (radiology key website. https://radiologykey.com/arteriovenous-fistulas/. Last accessed: 25/02/2023.

[8] Haidi Hu, Sandeep Patel, Jesse J Hanisch, Jeans M Santana, Takuya Hashimoto, Hualong Bai, Tambudzai Kudze, Trenton R Foster, Jianming Guo, Bogdan Yatsula, et al. Future research directions to improve fistula maturation and reduce access failure. In *Seminars in vascular surgery*, volume 29, pages 153–171. Elsevier, 2016.

[9] Anton N Sidawy, Richard Gray, Anatole Besarab, Mitchell Henry, Enrico Ascher, Michael Silva Jr, Arnold Miller, Larry Scher, Scott Trerotola, Roger T Gregory, et al. Recommended standards for reports dealing with arteriovenous hemodialysis accesses. *Journal of vascular surgery*, 35(3):603–610, 2002.

[10] Tonia C Rothuizen, ChunYu Wong, Paul HA Quax, Anton Jan van Zonneveld, Ton J Rabelink, and Joris I Rotmans. Arteriovenous access failure: more than just intimal hyperplasia? *Nephrology Dialysis Transplantation*, 28(5):1085–1092, 2013.

[11] Yutaka Matsubara, Gathe Kiwan, Arash Fereydooni, John Langford, and Alan Dardik. Distinct subsets of t cells and macrophages impact venous remodeling during arteriovenous fistula maturation. *JVS-Vascular Science*, 1:207–218, 2020.

[12] Gautier Bideault, Anthony Scaccia, Thomas Zahel, Robert W Landertinger, and Chathuri Daluwatte. Verification and validation of computational models used in biopharmaceutical manufacturing: potential application of the asme verification and validation 40 standard and fda proposed ai/ml model life cycle management framework. *Journal of Pharmaceutical Sciences*, 110(4):1540–1544, 2021.

[13] MF Hashmi, O Benjamin, and SL Lappin. *End-Stage Renal Disease*. StatPearls Publishing, Treasure Island, FL, 2022.

[14] Robert A Wolfe, Valarie B Ashby, Edgar L Milford, Akinlolu O Ojo, Robert E Ettenger, Lawrence YC Agodoa, Philip J Held, and Friedrich K Port. Comparison of mortality in all patients on dialysis, patients on dialysis awaiting transplantation, and recipients of a first cadaveric transplant. *New England journal of medicine*, 341(23):1725–1730, 1999.

[15] Roger W Evans, Diane L Manninen, Louis P Garrison Jr, L Gary Hart, Christopher R Blagg, Robert A Gutman, Alan R Hull, and Edmund G Lowrie. The quality of life of patients with end-stage renal disease. *New England journal of medicine*, 312(9):553–559, 1985.

[16] Andreas Laupacis, Paul Keown, Nancy Pus, Hans Krueger, Beryl Ferguson, Cindy Wong, and Norman Muirhead. A study of the quality of life and cost-utility of renal transplantation. *Kidney international*, 50(1):235–242, 1996.

[17] Juliana Feiman Sapiertein Silva, Gustavo Fernandes Ferreira, Marcelo Perosa, Hong Si Nga, and Luis Gustavo Modelli de Andrade. A machine learning prediction model for waiting time to kidney transplant. *Plos one*, 16(5):e0252069, 2021.

[18] Ji Hyeon Park, Hayne Cho Park, Do Hyoung Kim, Young-Ki Lee, and AJin Cho. Mortality and risk factors in very elderly patients who start hemodialysis: Korean renal data system (kords), 2016-2020. 2022.

[19] Domenico Santoro, Filippo Benedetto, Placido Mondello, Narayana Pipitò, David Barillà, Francesco Spinelli, Carlo Alberto Ricciardi, Valeria Cernaro, and Michele Buemi. Vascular access for hemodialysis: current perspectives. *International journal of nephrology and renovascular disease*, 7:281–294, Jul 2014. 25045278[pmid].

[20] Charmaine E Lok and Matthew J Oliver. Overcoming barriers to arteriovenous fistula creation and use. In *Seminars in dialysis*, volume 16, pages 189–196. Wiley Online Library, 2003.

[21] Adrian Sequeira, Mihran Naljayan, and Tushar J. Vachharajani. Vascular access guidelines: Summary, rationale, and controversies. *Techniques in Vascular and Interventional Radiology*, 20(1):2–8, 2017. SI: Dialysis Access.

[22] Klaus Konner, Barbara Nonnast-Daniel, and Eberhard Ritz. The arteriovenous fistula. *Journal of the American Society of Nephrology*, 14(6):1669–1680, 2003.

[23] Christoph Georg Radosa, Julia Caroline Radosa, Norbert Weiss, Christine Schmidt, Sebastian Werth, Thomas Hofmockel, Verena Plodeck, Christian Gatzweiler, Michael Laniado, and Ralf-Thorsten Hoffmann. Endovascular creation of an arteriovenous fistula (endoavf) for hemodialysis access: first results. *CardioVascular and Interventional Radiology*, 40:1545–1551, 2017.

[24] Stephen B Leapman, Michael Boyle, Mark D Pescovitz, Martin L Milgrom, Rahul M Jindal, and Ronald S Filo. The arteriovenous fistula for hemodialysis access: gold standard or archaic relic? *The American Surgeon*, 62(8):652–6, 1996.

[25] Siddharth Pandey, Manoj Kumar, Manav Agrawal, Manmeet Singh, Ajay Aggarwal, Gaurav Garg, Samarth Agarwal, and Satyanarayan Sankhwar. The effects of preoperative blood pressure on early failure rate of distal arteriovenous fistulas for hemodialysis access. *Hemodialysis International*, 23, 05 2019.

[26] Charmaine Lok. Fistula interventions: Less is more. *Journal of the American Society of Nephrology*, 30:ASN.2019090952, 10 2019.

[27] Joana Gameiro and Jose Ibeas. Factors affecting arteriovenous fistula dysfunction: a narrative review. *The journal of vascular access*, 21(2):134–147, 2020.

[28] Prabir Roy-Chaudhury, Lois Arend, Jianhua Zhang, Mahesh Krishnamoorthy, Yang Wang, Rupak Banerjee, Antoine Samaha, and Rino Munda. Neointimal hyperplasia in early arteriovenous fistula failure. *American Journal of Kidney Diseases*, 50(5):782–790, 2007.

[29] C.Y. Wong, T.C. Rothuizen, M.R. de Vries, T.J. Rabelink, J.F. Hamming, A.J. van Zonneveld, P.H.A. Quax, and J.I. Rotmans. Elastin is a key regulator of outward remodeling in arteriovenous fistulas. *European Journal of Vascular and Endovascular Surgery*, 49(4):480–486, 2015.

[30] Michael R Ward, Gerard Pasterkamp, Alan C Yeung, and Cornelius Borst. Arterial remodeling: mechanisms and clinical implications. *Circulation*, 102(10):1186–1191, 2000.

[31] Max LA Ebert, Vanessa F Schmidt, Lena Pfaff, Anne von Thaden, Melanie A Kimm, and Moritz Wildgruber. Animal models of neointimal hyperplasia and restenosis: species-specific differences and implications for translational research. *Basic to Translational Science*, 6(11):900–917, 2021.

[32] Timmy Lee and Naveed Ul Haq. New developments in our understanding of neointimal hyperplasia. *Advances in chronic kidney disease*, 22(6):431–437, 2015.

[33] Lan Jia, Lihua Wang, Fang Wei, Haibo Yu, Hongye Dong, Bo Wang, Zhi Lu, Guijiang Sun, Haiyan Chen, Jia Meng, et al. Effects of wall shear stress in venous neointimal hyperplasia of arteriovenous fistulae. *Nephrology*, 20(5):335–342, 2015.

[34] Daniel Pike, Yan-Ting Shiu, Maheshika Somarathna, Lingling Guo, Tatyana Isayeva, John Totenhagen, and Timmy Lee. High resolution hemodynamic profiling of murine arteriovenous fistula using magnetic resonance imaging and computational fluid dynamics. *Theoretical Biology and Medical Modelling*, 14(1):1–17, 2017.

[35] John E Carroll, Eamonn S Colley, Shannon D Thomas, Ramon L Varcoe, Anne Simmons, and Tracie J Barber. Tracking geometric and hemodynamic alterations of an arteriovenous fistula through patient-specific modelling. *Computer methods and programs in biomedicine*, 186:105203, 2020.

[36] Eamonn Colley, Anne Simmons, Ramon Varcoe, Shannon Thomas, and Tracie Barber. Arteriovenous fistula maturation and the influence of fluid dynamics. *Proceedings of the Institution of Mechanical Engineers, Part H: Journal of Engineering in Medicine*, 234(11):1197–1208, 2020.

[37] Tambudzai Kudze, Shun Ono, Arash Fereydooni, Luis Gonzalez, Toshihiko Isaji, Haidi Hu, Bogdan Yatsula, Ryosuke Taniguchi, Jun Koizumi, Toshiya Nishibe, and Alan Dardik. Altered hemodynamics during arteriovenous fistula remodeling leads to reduced fistula patency in female mice. *JVS-vascular science*, 1:42–56, 2020. 32754721[pmid].

[38] Mary Hammes. Hemodynamic and biologic determinates of arteriovenous fistula outcomes in renal failure patients. *BioMed research international*, 2015:171674–171674, 2015. 26495286[pmid].

[39] Monica Sigovan, Vitaliy Rayz, Warren Gasper, Hugh F Alley, Christopher D Owens, and David Saloner. Vascular remodeling in autogenous arterio-venous fistulas by mri and cfd. *Annals of biomedical engineering*, 41(4):657–668, 2013.

[40] Jeffrey E Hull, Boris V Balakin, Brad M Kellerman, and David K Wrolstad. Computational fluid dynamic evaluation of the side-to-side anastomosis for arteriovenous fistula. *Journal of vascular surgery*, 58(1):187–193, 2013.

[41] Michael Allon, Michelle L Robbin, Carlton J Young, Mark H Deierhoi, Jeremy Goodman, Michael Hanaway, Mark E Lockhart, and Silvio Litovsky. Preoperative venous intimal hyperplasia, postoperative arteriovenous fistula stenosis, and clinical fistula outcomes. *Clinical Journal of the American Society of Nephrology*, 8(10):1750–1755, 2013.

[42] Juan C Duque, Marwan Tabbara, Laisel Martinez, Angela Paez, Guillermo Selman, Loay H Salman, Omaida C Velazquez, and Roberto I Vazquez-Padron. Similar degree of intimal hyperplasia in surgically detected stenotic and nonstenotic arteriovenous fistula segments: a preliminary report. *Surgery*, 163(4):866–869, 2018.

[43] Mark D Solomonson, Michael E Johnson, and Duane Ilstrup. Risk factors in patients having surgery to create an arteriovenous fistula. *Anesthesia & Analgesia*, 79(4):694–700, 1994.

[44] Jennifer M MacRae, Sanjay Pandeya, Dennis P Humen, Nikolai Krivitski, and Robert M Lindsay. Arteriovenous fistula-associated high-output cardiac failure: a review of mechanisms. *American Journal of Kidney Diseases*, 43(5):e21–1, 2004.

[45] Jennifer M MacRae, Adeera Levin, and Israel Belenkie. The cardiovascular effects of arteriovenous fistulas in chronic kidney disease: a cause for concern? In *Seminars in dialysis*, volume 19, pages 349–352. Wiley Online Library, 2006.

[46] George Hyde-Linaker, Pauline Hall Barrientos, Sokratis Stoumpos, David Brian Kingsmore, and Asimina Kazakidi. Patient-specific computational haemodynamics associated with the surgical creation of an arteriovenous fistula. *Medical Engineering Physics*, 105:103814, 2022.

[47] Andrew S Levey and Josef Coresh. Chronic kidney disease. *The lancet*, 379(9811):165–180, 2012.

[48] Andrew P McMahon. Development of the mammalian kidney. *Current topics in developmental biology*, 117:31–64, 2016.

[49] Kamyar Kalantar-Zadeh, Tazeen H Jafar, Dorothea Nitsch, Brendon L Neuen, and Vlado Perkovic. Chronic kidney disease. *The lancet*, 398(10302):786–802, 2021.

[50] S Pirola, Z Cheng, OA Jarral, DP O'Regan, JR Pepper, T Athanasiou, and XY Xu. On the choice of outlet boundary conditions for patient-specific analysis of aortic flow using computational fluid dynamics. *Journal of biomechanics*, 60:15–21, 2017.

[51] Manuel Praga and Enrique Morales. The fatty kidney: obesity and renal disease. *Nephron*, 136(4):273–276, 2017.

[52] Adam Whaley-Connell, Michael G Shlipak, Lesley A Inker, Manjula Kurella Tamura, Andrew S Bomback, Georges Saab, Susanna M Szpunar, Samy I McFarlane, Suying Li, Shu-Cheng Chen, et al. Awareness of kidney disease and relationship to end-stage renal disease and mortality. *The American journal of medicine*, 125(7):661–669, 2012.

[53] Paola Romagnani, Giuseppe Remuzzi, Richard Glassock, Adeera Levin, Kitty J Jager, Marcello Tonelli, Ziad Massy, Christoph Wanner, and Hans-Joachim Anders. Chronic kidney disease. *Nature reviews Disease primers*, 3(1):1–24, 2017.

[54] Dimitrios J Tsakiris, Vianda S Stel, Patrik Finne, Emily Fraser, James Heaf, Johan De Meester, Sabine Schmaldienst, Friedo Dekker, Enrico Verrina, and Kitty J Jager. Incidence and outcome of patients starting renal replacement therapy for end-stage renal disease due to multiple myeloma or light-chain deposit disease: an era-edta registry study. *Nephrology Dialysis Transplantation*, 25(4):1200–1206, 2010.

[55] Chi-yuan Hsu, Glenn M Chertow, Charles E McCulloch, Dongjie Fan, Juan D Ordoñez, and Alan S Go. Nonrecovery of kidney function and death after acute on chronic renal failure. *Clinical Journal of the American Society of Nephrology*, 4(5):891–898, 2009.

[56] Valerie A Luyckx, David ZI Cherney, and Aminu K Bello. Preventing ckd in developed countries. *Kidney international reports*, 5(3):263–277, 2020.

[57] Matthew Snelson, Rachel E Clarke, and Melinda T Coughlan. Stirring the pot: can dietary modification alleviate the burden of ckd? *Nutrients*, 9(3):265, 2017.

[58] Andrew S Levey, Silvia M Titan, Neil R Powe, Josef Coresh, and Lesley A Inker. Kidney disease, race, and gfr estimation. *Clinical Journal of the American Society of Nephrology*, 15(8):1203–1212, 2020.

[59] Hiddo J Lambers Heerspink, Misghina Weldegiorgis, Lesley A Inker, Ron Gansevoort, Hans-Henrik Parving, Jamie P Dwyer, Hasi Mondal, Josef Coresh, Tom Greene, Andrew S Levey, et al. Estimated gfr decline as a surrogate end point for kidney failure: A post hoc analysis from the reduction of end points in non–insulin-dependent diabetes with the angiotensin ii antagonist losartan (renaal) study and irbesartan diabetic nephropathy trial (idnt). *American journal of kidney diseases*, 63(2):244–250, 2014.

[60] Marion Kerr, Benjamin Bray, James Medcalf, Donal J O'Donoghue, and Beverley Matthews. Estimating the financial cost of chronic kidney disease to the nhs in england. *Nephrology Dialysis Transplantation*, 27(suppl_3):iii73–iii80, 2012.

[61] Chronic kidney disease. early identification and management of chronic kidney disease in adults in primary and secondary care (2015). National Institute for Health and Care Excellence. http://www.nice.org.uk. Last accessed: 22/02/2023.

[62] M Tonelli, N Wiebe, G Knoll, A Bello, S Browne, D Jadhav, S Klarenbach, and J Gill. Systematic review: kidney transplantation compared with dialysis in clinically relevant outcomes. *American journal of transplantation*, 11(10):2093–2109, 2011.

[63] Alex Goldfarb-Rumyantzev, John F Hurdle, John Scandling, Zhi Wang, Bradley Baird, Lev Barenbaum, and Alfred K Cheung. Duration of end-stage renal disease and kidney transplant outcome. *Nephrology Dialysis Transplantation*, 20(1):167–175, 2005.

[64] Muhammad Sohaib Karim, Prabesh Aryal, Ali Gardezi, Dana F Clark, Fahad Aziz, and Sandesh Parajuli. Vascular access in kidney transplant recipients. *Transplantation Reviews*, 34(3):100544, 2020.

[65] Winnie Chan, Jos A Bosch, David Jones, Philip G McTernan, Anna C Phillips, and Richard Borrows. Obesity in kidney transplantation. *Journal of Renal Nutrition*, 24(1):1–12, 2014.

[66] Neeraj Sharma, Arnav Mahajan, and Yasir A Qazi. Marginal kidney transplantation: the road less traveled. *Current opinion in organ transplantation*, 24(1):92–96, 2019.

[67] Suphamai Bunnapradist and Gabriel M Danovitch. Evaluation of adult kidney transplant candidates. *American journal of kidney diseases*, 50(5):890–898, 2007.

[68] Kidney research uk: Our position on organ donation. National Institute for Health and Care Excellence. https://www.kidneyresearchuk.org/about-us/position-statements/statement-on-organ-donation/. Last accessed: 22/02/2023.

[69] Daljit K Hothi, Lynsey Stronach, and Elizabeth Harvey. Home haemodialysis. *Pediatric Nephrology*, 28:721–730, 2013.

[70] National kidney federation's call to action on home dialysis postcode poverty. National Kidney federation website. https://www.kidney.org.uk/news/national-kidney-federations-call-to-action-on-home-dialysis-postcode-poverty. Last accessed: 22/02/2023.

[71] Aminu K Bello, Ikechi G Okpechi, Mohamed A Osman, Yeoungjee Cho, Htay Htay, Vivekanand Jha, Marina Wainstein, and David W Johnson. Epidemiology of haemodialysis outcomes. *Nature Reviews Nephrology*, 18(6):378–395, 2022.

[72] GS Georgiadis, KM Kantartzi, VA Vargemezis, and MK Lazarides. The history of vascular access in hemodialysis patients: From the early days of willem j. kolff to the present. *ARCHIVES OF HELLENIC MEDICINE*, 24(4):389–397, 2007.

[73] Mario Cozzolino, Lorenza Magagnoli, Paola Ciceri, Ferruccio Conte, and Andrea Galassi. Effects of a medium cut-off (theranova®) dialyser on haemodialysis patients: a prospective, cross-over study. *Clinical Kidney Journal*, 14(1):382–389, 2021.

[74] Hans-Dietrich Polaschegg. Red blood cell damage from extracorporeal circulation in hemodialysis. In *Seminars in dialysis*, volume 22, pages 524–531. Wiley Online Library, 2009.

[75] Pang-Yen Fan and SJ Schwab. Vascular access: concepts for the 1990s. *Journal of the American Society of nephrology*, 3(1):1–11, 1992.

[76] FHN Trial Group. In-center hemodialysis six times per week versus three times per week. *New England Journal of Medicine*, 363(24):2287–2300, 2010.

[77] Steve J Schwab. Vascular access for hemodialysis. *Kidney international*, 55(5):2078–2090, 1999.

[78] Michael Allon. Vascular access for hemodialysis patients: New data should guide decision making. *Clinical Journal of the American Society of Nephrology*, 14(6):954–961, 2019.

[79] Surendra Shenoy. Surgical anatomy of upper arm: what is needed for avf planning. *The Journal of Vascular Access*, 10(4):223–232, 2009.

[80] Donald D Bell and John J Rosental. Arteriovenous graft life in chronic hemodialysis: A need for prolongation. *Archives of Surgery*, 123(9):1169–1172, 1988.

[81] Luis Coentrão, Carla Santos-Araújo, Claudia Dias, Ricardo Neto, and Manuel Pestana. Effects of starting hemodialysis with an arteriovenous fistula or central venous catheter compared with peritoneal dialysis: a retrospective cohort study. *BMC nephrology*, 13(1):1–7, 2012.

[82] Citations. *American Journal of Kidney Diseases*, 46:2–3, Oct 2005.

[83] Jehad Almasri, Mouaz Alsawas, Maria Mainou, Reem A Mustafa, Zhen Wang, Karen Woo, David L Cull, and M Hassan Murad. Outcomes of vascular access for hemodialysis: A systematic review and meta-analysis. *Journal of vascular surgery*, 64(1):236–243, 2016.

[84] Ivan D Maya and Michael Allon. Core curriculum in nephrology-vascular access: Core curriculum 2008. *American Journal of Kidney Diseases*, 51(4):702–708, 2008.

[85] Sean Kalloo, Peter G Blake, and Jay Wish. A patient-centered approach to hemodialysis vascular access in the era of fistula first. In *Seminars in dialysis*, volume 29, pages 148–157. Wiley Online Library, 2016.

[86] Michael B Silva Jr, Robert W Hobson II, Peter J Pappas, Zafar Jamil, Clifford T Araki, Mark C Goldberg, Gary Gwertzman, and Frank T Padberg Jr. A strategy for increasing use of autogenous hemodialysis access procedures: impact of preoperative noninvasive evaluation. *Journal of vascular surgery*, 27(2):302–308, 1998.

[87] S. Stoumpos et al. Ferumoxytol-enhanced magnetic resonance angiography for the assessment of potential kidney transplant recipients. *Eur Radiol*, 28, 2018.

[88] Joke van der Linden, Thomas W Lameris, Anton H van den Meiracker, André AEA de Smet, Peter J Blankestijn, and Marinus A van den Dorpel. Forearm venous distensibility predicts successful arteriovenous fistula. *American journal of kidney diseases*, 47(6):1013–1019, 2006.

[89] BS Dixon. Why don't fistulas mature? *Kidney international*, 70(8):1413–1422, 2006.

[90] Martin Ferring, John Henderson, and Teun Wilmink. Accuracy of early postoperative clinical and ultrasound examination of arteriovenous fistulae to predict dialysis use. *The journal of vascular access*, 15(4):291–297, 2014.

[91] Nikola Gjorgjievski, Pavlina Dzekova-Vidimliski, Vesna Gerasimovska, Svetlana Pavleska-Kuzmanovska, Julija Gjorgievska, Petar Dejanov, Aleksandar Sikole, and Ninoslav Ivanovski. Primary failure of the arteriovenous fistula in patients with chronic kidney disease stage 4/5. *Open Access Macedonian Journal of Medical Sciences*, 7(11):1782, 2019.

[92] BD Bray, J Boyd, C Daly, K Donaldson, A Doyle, JG Fox, A Innes, I Khan, RK Peel, A Severn, et al. Vascular access type and risk of mortality in a national prospective cohort of haemodialysis patients. *QJM: An International Journal of Medicine*, 105(11):1097–1103, 2012.

[93] Carrie A Schinstock, Robert C Albright, Amy W Williams, John J Dillon, Eric J Bergstralh, Bernice M Jenson, James T McCarthy, and Karl A Nath. Outcomes of arteriovenous fistula creation after the fistula first initiative. *Clinical Journal of the American Society of Nephrology*, 6(8):1996–2002, 2011.

[94] Henricus JT Huijbregts, Michiel L Bots, Cees HA Wittens, Yvonne C Schrama, Frans L Moll, Peter J Blankestijn, et al. Hemodialysis arteriovenous fistula patency revisited: results of a prospective, multicenter initiative. *Clinical journal of the American Society of Nephrology*, 3(3):714–719, 2008.

[95] Sokratis Stoumpos, Jamie P Traynor, Wendy Metcalfe, Ram Kasthuri, Karen Stevenson, Patrick B Mark, David B Kingsmore, and Peter C Thomson. A national study of autogenous arteriovenous access use and patency in a contemporary hemodialysis population. *Journal of Vascular Surgery*, 69(6):1889–1898, 2019.

[96] Ahmed A Al-Jaishi, Matthew J Oliver, Sonia M Thomas, Charmaine E Lok, Joyce C Zhang, Amit X Garg, Sarah D Kosa, Robert R Quinn, and Louise M Moist. Patency rates of the arteriovenous fistula for hemodialysis: a systematic review and meta-analysis. *American Journal of Kidney Diseases*, 63(3):464–478, 2014.

[97] LC Bylsma, SM Gage, H Reichert, SLM Dahl, and JH Lawson. Arteriovenous fistulae for haemodialysis: a systematic review and meta-analysis of efficacy and safety outcomes. *European journal of vascular and endovascular surgery*, 54(4):513–522, 2017.

[98] Olurotimi J Badero, Moro O Salifu, Haimanot Wasse, and Jack Work. Frequency of swing-segment stenosis in referred dialysis patients with angiographically documented lesions. *American journal of kidney diseases*, 51(1):93–98, 2008.

[99] Leonard D. Browne, Khalid Bashar, Philip Griffin, Eamon G. Kavanagh, Stewart R. Walsh, and Michael T. Walsh. The role of shear stress in arteriovenous fistula maturation and failure: A systematic review. *PloS one*, 10(12):e0145795–e0145795, Dec 2015. 26716840[pmid].

[100] Jeng-Jiann Chiu and Shu Chien. Effects of disturbed flow on vascular endothelium: pathophysiological basis and clinical perspectives. *Physiological reviews*, 91(1):327–387, 2011.

[101] Guohao Dai, Mohammad R Kaazempur-Mofrad, Sripriya Natarajan, Yuzhi Zhang, Saran Vaughn, Brett R Blackman, Roger D Kamm, Guillermo García-Cardeña, and Michael A Gimbrone Jr. Distinct endothelial phenotypes evoked by arterial waveforms derived from atherosclerosis-susceptible and-resistant regions of human vasculature. *Proceedings of the National Academy of Sciences*, 101(41):14871–14876, 2004.

[102] Bogdan Ene-Iordache, Luca Cattaneo, Gabriele Dubini, and Andrea Remuzzi. Effect of anastomosis angle on the localization of disturbed flow in ‘side-to-end’fistulae for haemodialysis access. *Nephrology Dialysis Transplantation*, 28(4):997–1005, 2013.

[103] Nirvana Sadaghianloo, Julie Contenti, Alan Dardik, and Nathalie M Mazure. Role of hypoxia and metabolism in the development of neointimal hyperplasia in arteriovenous fistulas. *International journal of molecular sciences*, 20(21):5387, 2019.

[104] Mark G. MacAskill, David G. Watson, Marie-Ann Ewart, Roger Wadsworth, Andrew Jackson, Emma Aitken, Graeme MacKenzie, David Kingsmore, Susan Currie, and Paul Coats. Improving arteriovenous fistula patency: Transdermal delivery of diclofenac reduces cannulation-dependent neointimal hyperplasia via ampk activation. *Vascular Pharmacology*, 71:108–115, 2015.

[105] Akihito Muto, Lynn Model, Kenneth Ziegler, Sammy DD Eghbalieh, and Alan Dardik. Mechanisms of vein graft adaptation to the arterial circulation–insights into the neointimal algorithm and management strategies–. *Circulation Journal*, 74(8):1501–1512, 2010.

[106] Theodore H Spaet, Michael B Stemerman, Frank J Veith, and I Lejnieks. Intimal injury and regrowth in the rabbit aorta; medial smooth muscle cells as a source of neointima. *Circulation research*, 36(1):58–70, 1975.

[107] Prabir Roy-Chaudhury, Yang Wang, Mahesh Krishnamoorthy, Jianhua Zhang, Rupak Banerjee, Rino Munda, Sue Heffelfinger, and Lois Arend. Cellular phenotypes in human stenotic lesions from haemodialysis vascular access. *Nephrology Dialysis Transplantation*, 24(9):2786–2791, 2009.

[108] Joan HF Drosopoulos, Rosemary Kraemer, Hao Shen, Rita K Upmacis, Aaron J Marcus, and Elgilda Musi. Human solcd39 inhibits injury-induced development of neointimal hyperplasia. *Thrombosis and haemostasis*, 103(2):426, 2010.

[109] Andre Biuckians, Eric C Scott, George H Meier, Jean M Panneton, and Marc H Glickman. The natural history of autologous fistulas as first-time dialysis access in the kdoqi era. *Journal of vascular surgery*, 47(2):415–421, 2008.

[110] Bradley S Dixon, Lisa Novak, and Jerry Fangman. Hemodialysis vascular access survival: upper-arm native arteriovenous fistula. *American journal of kidney diseases*, 39(1):92–101, 2002.

[111] Abigail Falk. Maintenance and salvage of arteriovenous fistulas. *Journal of Vascular and Interventional Radiology*, 17(5):807–813, 2006.

[112] Leonard D. Browne, Khalid Bashar, Philip Griffin, Eamon G. Kavanagh, Stewart R. Walsh, and Michael T. Walsh. The role of shear stress in arteriovenous fistula maturation and failure: A systematic review. *PLOS ONE*, 10(12):1–24, 12 2016.

[113] Dean Y Li, Gilles Faury, Douglas G Taylor, Elaine C Davis, Walter A Boyle, Robert P Mecham, Peter Stenzel, Beth Boak, Mark T Keating, et al. Novel arterial pathology in mice and humans hemizygous for elastin. *The Journal of clinical investigation*, 102(10):1783–1787, 1998.

[114] Michael Allon, Silvio Litovsky, Carlton J Young, Mark H Deierhoi, Jeremy Goodman, Michael Hanaway, Mark E Lockhart, and Michelle L Robbin. Medial fibrosis, vascular calcification, intimal hyperplasia, and arteriovenous fistula maturation. *American journal of kidney diseases*, 58(3):437–443, 2011.

[115] Jean-Marc Corpataux, Erik Haesler, Paolo Silacci, Hans Beat Ris, and Daniel Hayoz. Low-pressure environment and remodelling of the forearm vein in brescia–cimino haemodialysis access. *Nephrology Dialysis Transplantation*, 17(6):1057–1062, 2002.

[116] Keith B Quencer and Tamir Friedman. Declotting the thrombosed access. *Techniques in Vascular and Interventional Radiology*, 20(1):38–47, 2017.

[117] PPGM Rooijens, JHM Tordoir, Theo Stijnen, JPJ Burgmans, TI Yo, et al. Radiocephalic wrist arteriovenous fistula for hemodialysis: meta-analysis indicates a high primary failure rate. *European journal of vascular and endovascular surgery*, 28(6):583–589, 2004.

[118] A Falk, V Teodorescu, WY Lou, J Uribarri, and JA Vassalotti. Treatment of" swing point stenoses" in hemodialysis arteriovenous fistulae. *Clinical nephrology*, 60(1):35–41, 2003.

[119] Kaveh Kian and Arif Asif. Cephalic arch stenosis. In *Seminars in dialysis*, volume 21, pages 78–82. Wiley Online Library, 2008.

[120] Arif Asif, Gautam Cherla, Donna Merrill, Cristian D Cipleu, Patricia Briones, and Phillip Pennell. Conversion of tunneled hemodialysis catheter–consigned patients to arteriovenous fistula. *Kidney international*, 67(6):2399–2406, 2005.

[121] George M Nassar, Binh Nguyen, Edward Rhee, and Katafan Achkar. Endovascular treatment of the “failing to mature” arteriovenous fistula. *Clinical Journal of the American Society of Nephrology*, 1(2):275–280, 2006.

[122] Aleksandar Jankovic, Tatjana Damjanovic, Zivka Djuric, Jelena Marinkovic, Georg Schlieper, Jelena Tosic-Dragovic, Petar Djuric, Jovan Popovic, Juergen Floege, and Nada Dimkovic. Impact of vascular calcifications on arteriovenous fistula survival in hemodialysis patients: a five-year follow-up. *Nephron*, 129(4):247–252, 2015.

[123] Su Jin Choi, Hye Eun Yoon, Young Soo Kim, Sun Ae Yoon, Chul Woo Yang, Yong-Soo Kim, Sun Cheol Park, and Young Ok Kim. Pre-existing arterial micro-calcification predicts primary unassisted arteriovenous fistula failure in incident hemodialysis patients. In *Seminars in dialysis*, volume 28, pages 665–669. Wiley Online Library, 2015.

[124] Sokratis Stoumpos, Alan G Jardine, and Patrick B Mark. Cardiovascular morbidity and mortality after kidney transplantation. *Transplant International*, 28(1):10–21, 2015.

[125] Jennifer M MacRae. Vascular access and cardiac disease: is there a relationship? *Current opinion in nephrology and hypertension*, 15(6):577–582, 2006.

[126] Joëlle Cridlig, Christine Selton-Suty, François Alla, Anne Chodek, Alice Pruna, Michele Kessler, and Luc Frimat. Cardiac impact of the arteriovenous fistula after kidney transplantation: a case-controlled, match-paired study. *Transplant International*, 21(10):948–954, 2008.

[127] Shoshana H Ballew and Kunihiro Matsushita. Cardiovascular risk prediction in ckd. In *Seminars in Nephrology*, volume 38, pages 208–216. Elsevier, 2018.

[128] Arthur C Guyton and Kiichi Sagawa. Compensations of cardiac output and other circulatory functions in areflex dogs with large av fistulas. *American Journal of Physiology-Legacy Content*, 200(6):1157–1163, 1961.

[129] Colin G Caro. Discovery of the role of wall shear in atherosclerosis. *Arteriosclerosis, thrombosis, and vascular biology*, 29(2):158–161, 2009.

[130] Gökhan Íİlhan, Ertap Esi, Şahin Bozok, Íİsmail Yürekli, Berkan Özpak, Ahmet Özelçi, Buğra Destan, and Ali Gürbüz. The clinical utility of vascular mapping with doppler ultrasound prior to arteriovenous fistula construction for hemodialysis access. *The journal of vascular access*, 14(1):83–88, 2013.

[131] Rajiv Saran, Ronald L Pisoni, and William F Weitzel. Epidemiology of vascular access for hemodialysis and related practice patterns. *Contributions to Nephrology*, 142:14–28, 2004.

[132] Ali K Abu-Alfa. Nephrogenic systemic fibrosis and gadolinium-based contrast agents. *Advances in chronic kidney disease*, 18(3):188–198, 2011.

[133] Andrew Davenport. Changing the hemodialysis prescription for hemodialysis patients with subdural and intracranial hemorrhage. *Hemodialysis International*, 17:S22–S27, 2013.

[134] Andrew Davenport. The rationale for the use of low molecular weight heparin for hemodialysis treatments. *Hemodialysis International*, 17:S28–S32, 2013.

[135] AS Bode, RN Planken, MAG Merkx, FM Van der Sande, L Geerts, JHM Tordoir, and T Leiner. Feasibility of non-contrast-enhanced magnetic resonance angiography for imaging upper extremity vasculature prior to vascular access creation. *European Journal of Vascular and Endovascular Surgery*, 43(1):88–94, 2012.

[136] RN Planken, T Leiner, RJ Nijenhuis, LE Duijm, PW Cuypers, P Douwes-Draaijer, FM Van Der Sande, AG Kessels, and JH Tordoir. Contrast-enhanced magnetic resonance angiography findings prior to hemodialysis vascular access creation: a prospective analysis. *The journal of vascular access*, 9(4):269–277, 2008.

[137] David W Windus. Permanent vascular access: a nephrologist's view. *American journal of kidney diseases*, 21(5):457–471, 1993.

[138] S. Stoumpos et al. Ferumoxytol mr angiography versus duplex us for vascular mapping before arteriovenous fistula surgery for hemodialysis. *Radiology*, 297, 2020.

[139] VS Balakrishnan, M Rao, AT Kausz, L Brenner, BJG Pereira, TB Frigo, and JM Lewis. Physicochemical properties of ferumoxytol, a new intravenous iron preparation. *European journal of clinical investigation*, 39(6):489–496, 2009.

[140] David M Hasan, Matthew Amans, Tarik Tihan, Christopher Hess, Yi Guo, Soonmee Cha, Hua Su, Alastair J Martin, Michael T Lawton, Edward A Neuwelt, et al. Ferumoxytol-enhanced mri to image inflammation within human brain arteriovenous malformations: a pilot investigation. *Translational stroke research*, 3:166–173, 2012.

[141] Mustafa R Bashir, Lubna Bhatti, Daniele Marin, and Rendon C Nelson. Emerging applications for ferumoxytol as a contrast agent in mri. *Journal of Magnetic Resonance Imaging*, 41(4):884–898, 2015.

[142] Joy P Walker, Emily Nosova, Monica Sigovan, Joseph Rapp, Marlene S Grenon, Christopher D Owens, Warren J Gasper, and David A Saloner. Ferumoxytol-enhanced magnetic resonance angiography is a feasible method for the clinical evaluation of lower extremity arterial disease. *Annals of vascular surgery*, 29(1):63–68, 2015.

[143] Gesine Knobloch, Timothy Colgan, Curtis N Wiens, Xiaoke Wang, Tilman Schubert, Diego Hernando, Samir D Sharma, and Scott Reeder. Relaxivity of ferumoxytol at 1.5 t and 3.0 t. *Investigative radiology*, 53(5):257, 2018.

[144] Robert Landry, Paula M Jacobs, Robert Davis, Magdy Shenouda, and W Kline Bolton. Pharmacokinetic study of ferumoxytol: a new iron replacement therapy in normal subjects and hemodialysis patients. *American journal of nephrology*, 25(4):400–410, 2005.

[145] Pippa Storey, Ruth P Lim, Hersh Chandarana, Andrew B Rosenkrantz, Daniel Kim, David R Stoffel, and Vivian S Lee. Mri assessment of hepatic iron clearance rates after uspio administration in healthy adults. *Investigative radiology*, 47(12):717–724, 2012.

[146] Ghaneh Fananapazir, Daniele Marin, Paul V Suhocki, Charles Y Kim, and Mustafa R Bashir. Vascular artifact mimicking thrombosis on mr imaging using ferumoxytol as a contrast agent in abdominal vascular assessment. *Journal of Vascular and Interventional Radiology*, 25(6):969–976, 2014.

[147] J.P. Finn, K.-L. Nguyen, F. Han, Z. Zhou, I. Salusky, I. Ayad, and P. Hu. Cardiovascular mri with ferumoxytol. *Clinical Radiology*, 71(8):796–806, 2016. Special Issue: Spotlight on Cardiovascular Imaging.

[148] Luca Antiga, Bogdan Ene-Iordache, Lionello Caverni, Gian Paolo Cornalba, and Andrea Remuzzi. Geometric reconstruction for computational mesh generation of arterial bifurcations from ct angiography. *Computerized Medical Imaging and Graphics*, 26(4):227–235, 2002.

[149] PG Young, TBH Beresford-West, SRL Coward, B Notarberardino, B Walker, and A Abdul-Aziz. An efficient approach to converting three-dimensional image data into highly accurate computational models. *Philosophical Transactions of the Royal Society A: Mathematical, Physical and Engineering Sciences*, 366(1878):3155–3173, 2008.

[150] James Albert Sethian. *Level set methods and fast marching methods: evolving interfaces in computational geometry, fluid mechanics, computer vision, and materials science*, volume 3. Cambridge university press, 1999.

[151] Nathan Wilson, Kenneth Wang, Robert W Dutton, and Charles Taylor. A software framework for creating patient specific geometric models from medical imaging data for simulation based medical planning of vascular surgery. In *Medical Image Computing and Computer-Assisted Intervention–MICCAI 2001: 4th International Conference Utrecht, The Netherlands, October 14–17, 2001 Proceedings 4*, pages 449–456. Springer, 2001.

[152] Adam Updegrove, Nathan M Wilson, Jameson Merkow, Hongzhi Lan, Alison L Marsden, and Shawn C Shadden. Simvascular: an open source pipeline for cardiovascular simulation. *Annals of biomedical engineering*, 45:525–541, 2017.

[153] P. Yushkevich et al. Itk-snap: An interactive tool for semi-automatic segmentation of multi-modality biomedical images, 2016. IEEE Engineering in Medicine and Biology Society Conference.

[154] Ryan P. O'Hara, Arpita Chand, Sowmya Vidiyala, Stacie M. Arechavala, Dimitrios Mitsouras, Stephen Rudin, and Ciprian N. Ionita. Advanced 3d mesh manipulation in stereolithographic files and post-print processing for the manufacturing of patient-specific vascular flow phantoms. *Proceedings of SPIE–the International Society for Optical Engineering*, 9789:978909, Feb 2016. 28649165[pmid].

[155] Michela Bozzetto, Bogdan Ene-Iordache, and Andrea Remuzzi. Transitional flow in the venous side of patient-specific arteriovenous fistulae for hemodialysis. *Annals of Biomedical Engineering*, 44:2388–401, 08 2016.

[156] M. Bozzetto et al. Toward longitudinal studies of hemodynamically induced vessel wall remodeling. *Int J Artif Organs*, 41, 2018.

[157] Zaher Kharboutly, Marianne Fenech, J.M. Treutenaere, Isabelle Claude, and Cecile Legallais. Blood flow simulation in an arteriovenous fistula. 01 2005.

[158] Zaher Kharboutly, J.M. Treutenaere, Marianne Fenech, T. Chambon, Isabelle Claude, and Cecile Legallais. Numerical simulation of blood flow in a side-to-end fistula for hemodialysis. *Journal of Biomechanics*, 39, 07 2006.

[159] Zaher Kharboutly, Marianne Fenech, J Treutenaere, Isabelle Claude, and Cecile Legallais. Investigations into the relationship between hemodynamics and vascular alterations in an established arteriovenous fistula. *Medical engineering physics*, 29:999–1007, 12 2007.

[160] Zaher Kharboutly, Valerie Deplano, Éric Bertrand, and Cecile Legallais. Numerical and experimental study of blood flow through a patient-specific arteriovenous fistula used for hemodialysis. *Medical engineering and physics*, 32:111–8, 12 2009.

[161] Zaher Kharboutly, J. Treutenaere, and Cecile Legallais. Arteriovenous fistula: A realistic numerical blood flow simulation with a compliant wall. *The International journal of artificial organs*, 32:393–393, 07 2009.

[162] Zaher Kharboutly, J. Treutenaere, and Cecile Legallais. Improving hemodialysis adequacy outcomes through cannulation planning by numerical simulation. *The International journal of artificial organs*, 34:626–626, 08 2011.

[163] G. T. Carroll, T. M. McGloughlin, P. E. Burke, M. Egan, F. Wallis, and M. T. Walsh. Wall Shear Stresses Remain Elevated in Mature Arteriovenous Fistulas: A Case Study. *Journal of Biomechanical Engineering*, 133(2), 01 2011. 021003.

[164] Rym. Mehri, Catherine. Mavriplis, and Marianne Fenech. Red blood cell aggregates and their effect on non-newtonian blood viscosity at low hematocrit in a two-fluid low shear rate microfluidic system. *PLOS ONE*, 13(7):e0199911, Jul 2018.

[165] S. O'Callaghan, M. Walsh, and T. McGloughlin. Numerical modelling of newtonian and nonnewtonian representation of blood in a distal end-to-side vascular bypass graft anastomosis. *Medical engineering and physics, 28(1), 70–74.*, 2006.

[166] Hernan Morales, Ignacio Larrabide, Arjan Geers, Martha Aguilar, and Alejandro Frangi. Newtonian and non-newtonian blood flow in coiled cerebral aneurysms. *Journal of biomechanics*, 46, 07 2013.

[167] Carolyn Fisher and Jenn Rossmann. Effect of non-newtonian behavior on hemodynamics of cerebral aneurysms. *Journal of biomechanical engineering*, 131:091004, 10 2009.

[168] Syamantak Haldar, Swati Mukhopadhyay, and GC Layek. Flow and heat transfer of casson fluid over an exponentially shrinking permeable sheet in presence of exponentially moving free stream with convective boundary condition. *Mechanics of Advanced Materials and Structures*, 26(17):1498–1504, 2019.

[169] M. Van Doormaal et al. Haemodynamics in the mouse aortic arch computed from mri-derived velocities at the aortic root. *J R Soc Interface*, 9, 2012.

[170] Peter D. Weinberg. Disease patterns at arterial branches and their relation to flow. *Biorheology*, 39:533–537, 2002. 3,4.

[171] A. Kazakidi et al. Effect of reynolds number and flow division on patterns of haemodynamic wall shear stress near branch points in the descending thoracic aorta. *J R Soc Interface*, 6, 2008.

[172] A. Kazakidi et al. Effect of reverse flow on the pattern of wall shear stress near arterial branches. *J R Soc Interface*, 8, 2011.

[173] Ryan M. Pedrigi, Vikram V. Mehta, Sandra M. Bovens, Zahra Mohri, Christian Bo Poulsen, Willy Gsell, Jordi L. Tremoleda, Leila Towhidi, Ranil de Silva, Enrico Petretto, and Rob Krams. Influence of shear stress magnitude and direction on atherosclerotic plaque composition. *Royal Society Open Science*, 3(10):160588, 2016.

[174] Ulf Krueger, Juergen Zanow, and Hans Scholz. Computational fluid dynamics and vascular access. *Artificial Organs*, 26(7):571–575, 2002.

[175] Jeffrey E. Hull, Boris V. Balakin, Brad M. Kellerman, and David K. Wrolstad. Computational fluid dynamic evaluation of the side-to-side anastomosis for arteriovenous fistula. *Journal of Vascular Surgery*, 58(1):187 – 193.e1, 2013.

[176] A. Niemann et al. Computational fluid dynamics simulation of a-v fistulas: From mri and ultrasound scans to numeric evaluation of hemodynamics. *J Vasc Access*, 13, 2011.

[177] Bogdan Ene-Iordache and Andrea Remuzzi. Disturbed flow in radial-cephalic arteriovenous fistulae for haemodialysis: Low and oscillating shear stress locates the sites of stenosis. *Nephrology, dialysis, transplantation : official publication of the European Dialysis and Transplant Association - European Renal Association*, 27:358–68, 01 2012.

[178] Bogdan Ene-Iordache, Lidia Mosconi, Giuseppe Remuzzi, and Andrea Remuzzi. Computational fluid dynamics of a vascular access case for hemodialysis. *Journal of Biomechanical Engineering*, 123:284–92, 07 2001.

[179] Andrea Remuzzi and Bogdan Ene-Iordache. Novel paradigms for dialysis vascular access: upstream hemodynamics and vascular remodeling in dialysis access stenosis. *Clinical journal of the American Society of Nephrology*, 8(12):2186–2193, 2013.

[180] Bogdan Ene-Iordache, Luca Cattaneo, Gabriele Dubini, and Andrea Remuzzi. Effect of anastomosis angle on the localization of disturbed flow in ‚Äòside-to-end‚Äô fistulae for haemodialysis access. *Nephrology Dialysis Transplantation*, 28(4):997–1005, 07 2012.

[181] F Iori, L Grechy, RW Corbett, W Gedroyc, N Duncan, CG Caro, and PE Vincent. The effect of in-plane arterial curvature on blood flow and oxygen transport in arterio-venous fistulae. *Physics of Fluids*, 27(3):031903, 2015.

[182] C. V. Cunnane et al. The presence of helical flow can suppress areas of disturbed shear in parameterised models of an arteriovenous fistula. *Int J Numer Method Biomed Eng*, 35, 2019.

[183] Andrea Remuzzi and Bogdan Ene-Iordache. Novel paradigms for dialysis vascular access: upstream hemodynamics and vascular remodeling in dialysis access stenosis. *Clinical journal of the American Society of Nephrology : CJASN*, 8(12):2186–2193, Dec 2013. 23990161[pmid].

[184] Olivia Ng, Sanjiv D Gunasekera, Shannon D Thomas, Ramon L Varcoe, and Tracie J Barber. The effect of assumed boundary conditions on the accuracy of patient-specific cfd arteriovenous fistula model. *Computer Methods in Biomechanics and Biomedical Engineering: Imaging & Visualization*, pages 1–13, 2022.

[185] Andrea Remuzzi and Michela Bozzetto. Biological and physical factors involved in the maturation of arteriovenous fistula for hemodialysis. *Cardiovascular engineering and technology*, 8(3):273–279, 2017.

[186] Patrick M McGah, Daniel F Leotta, Kirk W Beach, and Alberto Aliseda. Effects of wall distensibility in hemodynamic simulations of an arteriovenous fistula. *Biomechanics and modeling in mechanobiology*, 13(3):679–695, 2014.

[187] Iolanda Decorato, Zaher Kharboutly, Tommaso Vassallo, Justin Penrose, Cécile Legallais, and Anne-Virginie Salsac. Numerical simulation of the fluid structure interactions in a compliant patient-specific arteriovenous fistula. *International journal for numerical methods in biomedical engineering*, 30(2):143–159, 2014.

[188] E Colley, J Carroll, S Thomas, A Simmons, and T Barber. Development of a patient-specific fsi model of an arteriovenous fistula. *Development*, 5(8), 2016.

[189] C. Caro, T. Pedley, R. Schroter, and W. Seed. *The Mechanics of theCirculation (2nd ed.)*. Cambridge, UK: Cambridge Univ. Press.

[190] Veronique Peiffer, Spencer J Sherwin, and Peter D Weinberg. Does low and oscillatory wall shear stress correlate spatially with early atherosclerosis? a systematic review. *Cardiovascular research*, 99(2):242–250, 2013.

[191] Véronique Peiffer, Spencer J Sherwin, and Peter D Weinberg. Computation in the rabbit aorta of a new metric–the transverse wall shear stress–to quantify the multidirectional character of disturbed blood flow. *Journal of biomechanics*, 46(15):2651–2658, 2013.

[192] A. Caroli et al. Validation of a patient-specific hemodynamic computational model for surgical planning of vascular access in hemodialysis patients. *Kidney Int*, 84, 2013.

[193] Yogesh N. V. Reddy, Masaru Obokata, Patrick G. Dean, Vojtech Melenovsky, Karl A. Nath, and Barry A. Borlaug. Long-term cardiovascular changes following creation of arteriovenous fistula in patients with end stage renal disease. *European Heart Journal*, 38(24):1913–1923, 03 2017.

[194] P. Cockwell and L. Fisher. The global burden of chronic kidney disease. *The Lancet*, 395, 2020.

[195] S. Okada and S. Shenoy. Arteriovenous access for hemodialysis: Preoperative assessment and planning. *J Vasc Access*, 15, 2014.

[196] M. J. Brescia et al. Chronic hemodialysis using venipuncture and a surgically created arteriovenous fistula. *N Engl J Med*, 275, 1966.

[197] A. C. Guyton and K. Sagawa. Compensations of cardiac output and other circulatory functions in areflex dogs with large a-v fistulas. *Am. J. Physiol.-Legacy Content*, 200, 1961.

[198] M. L. Robbin et al. Arteriovenous fistula development in the first 6 weeks after creation. *Radiology*, 279, 2016.

[199] H. I. Feldman et al. Hemodialysis vascular access morbidity. *Journal of the American Society of Nephrology*, 7, 1996.

[200] K. R. Polkinghorne et al. Vascular access and all-cause mortality: A propensity score analysis. *Clin J Am Soc Nephrol*, 15, 2004.

[201] C.Y. Wong et al. Vascular remodeling and intimal hyperplasia in a novel murine model of arteriovenous fistula failure. *J Vasc Surg*, 59, 2013.

[202] Adam B Stern and Philip J Klemmer. High-output heart failure secondary to arteriovenous fistula. *Hemodialysis International*, 15(1):104–107, 2011.

[203] Rachel S Chang, Jiun-Ruey Hu, Joshua A Beckman, Rachel C Forbes, Saed H Shawar, and Beatrice P Concepcion. High output heart failure associated with arteriovenous fistula in the setting of kidney transplantation. *Kidney International Reports*, 6(2):544–551, 2021.

[204] Kevin Ingle, Linh Pham, Viangkaeo Lee, Lingling Guo, Tatyana Isayeva-Waldrop, Maheshika Somarathna, and Timmy Lee. Cardiac changes following arteriovenous fistula creation in a mouse model. *The journal of vascular access*, 24(1):124–132, 2023.

[205] A. Kumar et al. Radio-median cubital / radiocephalic arteriovenous fistula at elbow to prevent vascular steal syndrome associated with brachiocephalic fistula: Review of 320 cases. *Indian J Urol.*, 23, 2007.

[206] P. Roy-Chaudhury et al. Predicting dialysis vascular access blood flow and diameter: too much, too little, or just right. *Kidney Int.*, 84, 2013.

[207] Y. Zhu et al. Clinical validation and assessment of aortic hemodynamics using computational fluid dynamics simulations from computed tomography angiography. *Biomed. Eng. Online*, 17, 2018.

[208] L. Johnston et al. Hemodynamic abnormalities in the aorta of turner syndrome girls. *Front. cardiovasc. med.*, 8, 2021.

[209] Maria Boumpouli, Mark HD Danton, Terence Gourlay, and Asimina Kazakidi. Blood flow simulations in the pulmonary bifurcation in relation to adult patients with repaired tetralogy of fallot. *Medical Engineering & Physics*, 85:123–138, 2020.

[210] Maria Boumpouli, Emilie L Sauvage, Claudio Capelli, Silvia Schievano, and Asimina Kazakidi. Characterization of flow dynamics in the pulmonary bifurcation of patients with repaired tetralogy of fallot: a computational approach. *Frontiers in Cardiovascular Medicine*, 8:703717, 2021.

[211] Lauren Johnston, Ruth Allen, Pauline Hall Barrientos, Avril Mason, and Asimina Kazakidi. Hemodynamic abnormalities in the aorta of turner syndrome girls. *Frontiers in Cardiovascular Medicine*, 8:670841, 2021.

[212] Mark A Van Doormaal, Asimina Kazakidi, Marzena Wylezinska, Anthony Hunt, Jordi L Tremoleda, Andrea Protti, Yvette Bohraus, Willy Gsell, Peter D Weinberg, and C Ross Ethier. Haemodynamics in the mouse aortic arch computed from mri-derived velocities at the aortic root. *Journal of The Royal Society Interface*, 9(76):2834–2844, 2012.

[213] Sokratis Stoumpos, Martin Hennessy, Alex T Vesey, Aleksandra Radjenovic, Ram Kasthuri, David B Kingsmore, Patrick B Mark, and Giles Roditi. Ferumoxytol-enhanced magnetic resonance angiography for the assessment of potential kidney transplant recipients. *European radiology*, 28(1):115–123, 2018.

[214] David T. Wymer, Kunal P. Patel, William F. Burke, and Vinay K. Bhatia. Phase-contrast mri: Physics, techniques, and clinical applications. *RadioGraphics*, 40(1):122–140, 2020. PMID: 31917664.

[215] Paul A. Yushkevich, Joseph Piven, Heather Cody Hazlett, Rachel Gimpel Smith, Sean Ho, James C. Gee, and Guido Gerig. User-guided 3D active contour segmentation of anatomical structures: Significantly improved efficiency and reliability. *Neuroimage*, 31(3):1116–1128, 2006.

[216] Federico Greco and Carlo Augusto Mallio. Artificial intelligence and abdominal adipose tissue analysis: a literature review. *Quantitative Imaging in Medicine and Surgery*, 11(10):4461, 2021.

[217] B. L. Broadhead et al. Sensitivity- and uncertainty-based criticality safety validation techniques. *Nucl Sci Eng*, 146, 2004.

[218] Vladimir Duffal, Benoît de Laage de Meux, and Rémi Manceau. Development and validation of a hybrid rans-les approach based on temporal filtering. In *Fluids Engineering Division Summer Meeting*, volume 59032, page V002T02A053. American Society of Mechanical Engineers, 2019.

[219] Veer Vatsa, Mark Carpenter, and David Lockard. Re-evaluation of an optimized second order backward difference (bdf2opt) scheme for unsteady flow applications. In *48th AIAA aerospace sciences meeting including the new horizons forum and aerospace exposition*, page 122, 2010.

[220] Nicolaas Westerhof, Nikos Stergiopulos, Mark IM Noble, Berend E Westerhof, et al. *Snapshots of hemodynamics: an aid for clinical research and graduate education*, volume 7. Springer, 2010.

[221] S Pirola, Z. Cheng, O.A. Jarral, D.P O'Regan, J.R. Pepper, T. Athanasiou, and X.Y. Xu. On the choice of outlet boundary conditions for patient-specific analysis of aortic flow using computational fluid dynamics. *J Biomech. 2017 Jul 26;60:15-21.*, 2017.

[222] C. Chnafa et al. Better than nothing: A rational approach for minimizing the impact of outflow strategy on cerebrovascular simulations. *Am J Neuroradiol.*, 39, 2018.

[223] J. Alastruey Arimon. *Numerical modelling of pulse wave propagation in the cardiovascular system : development, validation and clinical applications*. PhD thesis, Imperial College London, 2006.

[224] H. Ha et al. Fluid-dynamic optimal design of helical vascular graft for stenotic disturbed flow. *PLOS ONE*, 9, 2014.

[225] L. Grechy et al. Suppressing unsteady flow in arterio-venous fistulae. *Phys. Fluids*, 29, 2017.

[226] C. Yang et al. The anastomotic angle of hemodialysis arteriovenous fistula is associated with flow disturbance at the venous stenosis location on angiography. *Front. Bioeng. Biotechnol.*, 8, 2020.

[227] Wilco Kroon, Marielle Bosboom, Wouter Huberts, Jan Tordoir, and Frans van de Vosse. Computational model for estimating the short-and long-term cardiac response to arteriovenous fistula creation for hemodialysis. *Medical & biological engineering & computing*, 50:1289–1298, 2012.

[228] Yubing Shi, Patricia Lawford, and Rodney Hose. Review of zero-d and 1-d models of blood flow in the cardiovascular system. *Biomedical engineering online*, 10:33–33, Apr 2011. 21521508[pmid].

[229] J. R. A. Mitchell and C. J. Schwartz. *Arterial disease*. Blackwell Scientific Publications, 1965.

[230] M. K. Krishnamoorthy et al. Hemodynamic wall shear stress profiles influence the magnitude and pattern of stenosis in a pig av fistula. *Kidney Int.*, 74, 2008.

[231] S. Lehoux et al. Molecular mechanisms of the vascular responses to haemodynamic forces. *J. Intern. Med.*, 259, 2006.

[232] Etienne Roux, Pauline Bougaran, Pascale Dufourcq, and Thierry Couffinhal. Fluid shear stress sensing by the endothelial layer. *Frontiers in Physiology*, 11:861, 2020.

[233] A. Oprea et al. Correlation between preoperative vein and artery diameters and arteriovenous fistula outcome in patients with end-stage renal disease. *Clujul Med*, 91, 2018.

[234] Edmund YM Chung, Debbie Knagge, Simone Cheung, Jessica Sun, Lauren Heath, Hayden McColl, Henry Guo, Lauren Gray, Tarini Srivastava, Joshua Sandy, et al. Factors associated with functional arteriovenous fistula at hemodialysis start and arteriovenous fistula non-use in a single-center cohort. *The Journal of Vascular Access*, 23(4):558–566, 2022.

[235] Ru Yu Tan and Chieh Suai Tan. Brief introduction of hemodialysis and vascular access. In *Dialysis Access Management*, pages 1–3. Springer, 2021.

[236] Teófilo Yan, Joana Gameiro, João Grilo, Rui Filipe, and Ernesto Rocha. Hemodialysis vascular access in elderly patients: A comprehensive review. *The Journal of Vascular Access*, page 11297298221097233, 2022.

[237] Patrick Sowa and Matthew Blecha. Predictors of mortality within 24 months of initial arteriovenous access creation. *Annals of Vascular Surgery*, 81:258–266, 2022.

[238] Siddharth Venkat Ramanan, Ravindra Attur Prabhu, Indu Ramachandra Rao, Arun Chawla, Srinivas Vinayak Shenoy, Shankar Prasad Nagaraju, and Mohan V Bhojaraja. Outcomes and predictors of failure of arteriovenous fistulae for hemodialysis. *International Urology and Nephrology*, 54(1):185–192, 2022.

[239] Jay B Wish and Sharon M Moe. Moving beyond the assumed: Improving fistula success rates, 2017.

[240] Carney Chan, Christian J Ochoa, and Steven G Katz. Prognostic factors for arteriovenous fistula maturation. *Annals of vascular surgery*, 49:273–276, 2018.

[241] Bruno Fraga Dias, João Fernandes, Inês Sala, Joana Freitas, Josefina Santos Lascasas, Jorge Malheiro, and António Cabrita. Mo838: Urgent-start haemodialysis in the elderly patients: Patterns and predictors of 1-year mortality. *Nephrology Dialysis Transplantation*, 37(Supplement_3):gfac083–020, 2022.

[242] Peiyun Liu, Suh Chien Pang, Huihua Li, Ru Yu Tan, Ren Kwang Alvin Tng, Shien Wen Sheryl Gan, Hui Lin Lina Choong, Tze Tec Chong, and Chieh Suai Tan. Outcomes of arteriovenous fistula in elderly patients on maintenance haemodialysis. *International Urology and Nephrology*, 53(9):1923–1931, 2021.

[243] Yong He, Christi M Terry, Cuong Nguyen, Scott A Berceli, Yan-Ting E Shiu, and Alfred K Cheung. Serial analysis of lumen geometry and hemodynamics in human arteriovenous fistula for hemodialysis using magnetic resonance imaging and computational fluid dynamics. *Journal of biomechanics*, 46(1):165–169, 2013.

[244] Bogdan Ene-Iordache and Andrea Remuzzi. Disturbed flow in radial-cephalic arteriovenous fistulae for haemodialysis: low and oscillating shear stress locates the sites of stenosis. *Nephrology Dialysis Transplantation*, 27(1):358–368, 07 2011.

[245] Bogdan Ene-Iordache and Andrea Remuzzi. Disturbed flow in radial-cephalic arteriovenous fistulae for haemodialysis: low and oscillating shear stress locates the sites of stenosis. *Nephrology Dialysis Transplantation*, 27(1):358–368, 2012.

[246] George Hyde-Linaker, Pauline Hall Barrientos, Sokratis Stoumpos, David Brian Kingsmore, and Asimina Kazakidi. Patient-specific computational haemodynamics associated with the surgical creation of an arteriovenous fistula. *Medical Engineering & Physics*, 105:103814, 2022.

[247] O Clement, N Faye, L Fournier, N Siauve, and G Frija. Kidney and iodinated and gadolinium-based contrast agents. *Journal de Radiologie*, 92(4):291–298, 2011.

[248] Jan Möbius and Leif Kobbelt. Openflipper: An open source geometry processing and rendering framework. In *Proceedings of the 7th International Conference on Curves and Surfaces*, page 488–500, Berlin, Heidelberg, 2010. Springer-Verlag.

[249] James Ahrens, Berk Geveci, and Charles Law. Paraview: An end-user tool for large data visualization. *The visualization handbook*, 717(8), 2005.

[250] Einar Heiberg, Jane Sjögren, Martin Ugander, Marcus Carlsson, Henrik Engblom, and Håkan Arheden. Design and validation of segment - a freely available software for cardiovascular image analysis. *BMC medical imaging*, 10:1, 01 2010.

[251] Luisa Sousa, Catarina Castro, Carlos Conceição António, Joao Tavares, André Santos, Rosa Santos, Pedro Castro, and Elsa Azevedo. Simulated hemodynamics in human carotid bifurcation based on doppler ultrasound data. *International Journal of Clinical Neurosciences and Mental Health*, Issue 1 (2014) – Supplement 1:7 pag., 05 2014.

[252] Julio Garcia, Alex J. Barker, Jeremy D. Collins, James C. Carr, and Michael Markl. Volumetric quantification of absolute local normalized helicity in patients with bicuspid aortic valve and aortic dilatation. *Magnetic resonance in medicine*, 78(2):689–701, Aug 2017. 27539068[pmid].

[253] Umberto Morbiducci, Raffaele Ponzini, Giovanna Rizzo, Marcello Cadioli, Antonio Esposito, Francesco De Cobelli, Alessandro Del Maschio, Franco Maria Montevecchi, and Alberto Redaelli. In vivo quantification of helical blood flow in human aorta by time-resolved three-dimensional cine phase contrast magnetic resonance imaging. *Annals of biomedical engineering*, 37:516–531, 2009.

[254] Henry Keith Moffatt and Arkady Tsinober. Helicity in laminar and turbulent flow. *Annual review of fluid mechanics*, 24(1):281–312, 1992.

[255] Peter A Flach. Roc analysis. In *Encyclopedia of machine learning and data mining*, pages 1–8. Springer, 2016.

[256] R Core Team. *R: A Language and Environment for Statistical Computing*. R Foundation for Statistical Computing, Vienna, Austria, 2021.

[257] George E Smith, Risha Gohil, and Ian C Chetter. Factors affecting the patency of arteriovenous fistulas for dialysis access. *Journal of vascular surgery*, 55(3):849–855, 2012.

[258] Lan Jia, Lihua Wang, Fang Wei, Haibo Yu, Hongye Dong, Bo Wang, Zhi Lu, Guijiang Sun, Haiyan Chen, Jia Meng, et al. Effects of wall shear stress in venous neointimal hyperplasia of arteriovenous fistulae. *Nephrology*, 20(5):335–342, 2015.

[259] Kirsten L Johansen, Glenn M Chertow, Robert N Foley, David T Gilbertson, Charles A Herzog, Areef Ishani, Ajay K Israni, Elaine Ku, Manjula Kurella Tamura, Shuling Li, et al. Us renal data system 2020 annual data report: epidemiology of kidney disease in the united states. *American journal of kidney diseases*, 77(4):A7–A8, 2021.

[260] Jessica Kendrick and Michel B Chonchol. Nontraditional risk factors for cardiovascular disease in patients with chronic kidney disease. *Nature clinical practice Nephrology*, 4(12):672–681, 2008.

[261] Daniel E Weiner and Mark J Sarnak. Cardiac function and cardiovascular disease in chronic kidney disease. In *National Kidney Foundation Primer on Kidney Diseases*, pages 506–514. Elsevier, 2018.

[262] Nikayla Patel, Muhammad Magdi Yaqoob, and Dunja Aksentijevic. Cardiac metabolic remodelling in chronic kidney disease. *Nature Reviews Nephrology*, 18(8):524–537, 2022.

[263] Donald E Wesson, Jerry M Buysse, and David A Bushinsky. Mechanisms of metabolic acidosis–induced kidney injury in chronic kidney disease. *Journal of the American Society of Nephrology*, 31(3):469–482, 2020.

[264] Ronald L Pisoni, Lindsay Zepel, Friedrich K Port, and Bruce M Robinson. Trends in us vascular access use, patient preferences, and related practices: an update from the us dopps practice monitor with international comparisons. *American Journal of Kidney Diseases*, 65(6):905–915, 2015.

[265] S Pirola, Z Cheng, OA Jarral, DP O'Regan, JR Pepper, T Athanasiou, and XY Xu. On the choice of outlet boundary conditions for patient-specific analysis of aortic flow using computational fluid dynamics. *Journal of biomechanics*, 60:15–21, 2017.

[266] Ning Yang, Steven Deutsch, Eric G Paterson, and Keefe B Manning. Comparative study of continuous and pulsatile left ventricular assist devices on hemodynamics of a pediatric end-to-side anastomotic graft. *Cardiovascular engineering and technology*, 1:88–103, 2010.

[267] M Tessa Savage, Charles J Ferro, Antonio Sassano, and Charles RV Tomson. The impact of arteriovenous fistula formation on central hemodynamic pressures in chronic renal failure patients: a prospective study. *American journal of kidney diseases*, 40(4):753–759, 2002.

[268] Y Ori, A Korzets, M Katz, Y Perek, I Zahavi, and U Gafter. Haemodialysis arteriovenous access—a prospective haemodynamic evaluation. *Nephrology Dialysis Transplantation*, 11(1):94–97, 1996.

[269] Emile Holman. Abnormal arteriovenous communications: Great variability of effects with particular reference to delayed development of cardiac failure. *Circulation*, 32(6):1001–1009, 1965.

[270] Gerald D Buckberg, David E Fixler, Joseph P Archie, and Julien IE Hoffman. Experimental subendocardial ischemia in dogs with normal coronary arteries. *Circulation research*, 30(1):67–81, 1972.

[271] Steven D Crowley, David W Butterly, Robert H Peter, and Steve J Schwab. Coronary steal from a left internal mammary artery coronary bypass graft by a left upper extremity arteriovenous hemodialysis fistula. *American journal of kidney diseases*, 40(4):852–855, 2002.

[272] Keisuke Kojima, Takafumi Hiro, Yutaka Koyama, Akihito Ohgaku, Hidesato Fujito, Yasunari Ebuchi, Riku Arai, Masaki Monden, Suguru Migita, Tomoyuki Morikawa, et al. High wall shear stress is related to atherosclerotic plaque rupture in the aortic arch of patients with cardiovascular disease: a study with computational fluid dynamics model and non-obstructive general angioscopy. *Journal of Atherosclerosis and Thrombosis*, 28(7):742–753, 2021.

[273] Andrea S Les, Shawn C Shadden, C Alberto Figueroa, Jinha M Park, Maureen M Tedesco, Robert J Herfkens, Ronald L Dalman, and Charles A Taylor. Quantification of hemodynamics in abdominal aortic aneurysms during rest and exercise using magnetic resonance imaging and computational fluid dynamics. *Annals of biomedical engineering*, 38:1288–1313, 2010.

[274] Armin Leuprecht, Sebastian Kozerke, Peter Boesiger, and Karl Perktold. Blood flow in the human ascending aorta: a combined mri and cfd study. *Journal of engineering mathematics*, 47:387–404, 2003.

[275] Rodrigo M Romarowski, Adrien Lefieux, Simone Morganti, Alessandro Veneziani, and Ferdinando Auricchio. Patient-specific cfd modelling in the thoracic aorta with pc-mri–based boundary conditions: A least-square three-element windkessel approach. *International journal for numerical methods in biomedical engineering*, 34(11):e3134, 2018.

[276] Satoshi Numata, Keiichi Itatani, Keiichi Kanda, Kiyoshi Doi, Sachiko Yamazaki, Kazuki Morimoto, Kaichiro Manabe, Koki Ikemoto, and Hitoshi Yaku. Blood flow analysis of the aortic arch using computational fluid dynamics. *European Journal of Cardio-Thoracic Surgery*, 49(6):1578–1585, 2016.

[277] Chi Wei Ong, Ian Wee, Nicholas Syn, Sheryl Ng, Hwa Liang Leo, Arthur Mark Richards, and Andrew MTL Choong. Computational fluid dynamics modeling of hemodynamic parameters in the human diseased aorta: A systematic review. *Annals of Vascular Surgery*, 63:336–381, 2020.

[278] W Huberts, AS Bode, W Kroon, RN Planken, JHM Tordoir, FN Van de Vosse, and EMH Bosboom. A pulse wave propagation model to support decision-making in vascular access planning in the clinic. *Medical engineering & physics*, 34(2):233–248, 2012.

[279] Aron S Bode, Wouter Huberts, E Marielle H Bosboom, Wilco Kroon, Wim PM Van der Linden, R Nils Planken, Frans N Van de Vosse, and Jan HM Tordoir. Patient-specific computational modeling of upper extremity arteriovenous fistula creation: its feasibility to support clinical decision-making. *PloS one*, 7(4):e34491, 2012.

[280] Manli Zhou, Yunfeng Yu, Ruiyi Chen, Xingci Liu, Yilei Hu, Zhiyan Ma, Lingwei Gao, Weixiong Jian, and Liping Wang. Wall shear stress and its role in atherosclerosis. *Frontiers in Cardiovascular Medicine*, 10, 2023.

[281] Jennifer M Dolan, John Kolega, and Hui Meng. High wall shear stress and spatial gradients in vascular pathology: a review. *Annals of biomedical engineering*, 41:1411–1427, 2013.

[282] Joseph J Boyle, Peter L Weissberg, and Martin R Bennett. Human macrophage-induced vascular smooth muscle cell apoptosis requires no enhancement of fas/fas-l interactions. *Arteriosclerosis, thrombosis, and vascular biology*, 22(10):1624–1630, 2002.

[283] Mei Yan Chong, Boram Gu, Bee Ting Chan, Zhi Chao Ong, Xiao Yun Xu, and Einly Lim. Effect of intimal flap motion on flow in acute type b aortic dissection by using fluid-structure interaction. *International journal for numerical methods in biomedical engineering*, 36(12):e3399, 2020.

[284] M Malvè, A García, J Ohayon, and MA Martínez. Unsteady blood flow and mass transfer of a human left coronary artery bifurcation: Fsi vs. cfd. *International communications in heat and mass transfer*, 39(6):745–751, 2012.

[285] Vivekanand Jha, Guillermo Garcia-Garcia, Kunitoshi Iseki, Zuo Li, Saraladevi Naicker, Brett Plattner, Rajiv Saran, Angela Yee-Moon Wang, and Chih-Wei Yang. Chronic kidney disease: global dimension and perspectives. *The Lancet*, 382(9888):260–272, 2013.

[286] Pietro Ravani, Suetonia C Palmer, Matthew J Oliver, Robert R Quinn, Jennifer M MacRae, Davina J Tai, Neesh I Pannu, Chandra Thomas, Brenda R Hemmelgarn, Jonathan C Craig, et al. Associations between hemodialysis access type and clinical outcomes: a systematic review. *Journal of the American Society of Nephrology*, 24(3):465–473, 2013.

[287] Charmaine E Lok and Robert Foley. Vascular access morbidity and mortality: trends of the last decade. *Clinical Journal of the American Society of Nephrology*, 8(7):1213–1219, 2013.

[288] Laura M Dember, Gerald J Beck, Michael Allon, James A Delmez, Bradley S Dixon, Arthur Greenberg, Jonathan Himmelfarb, Miguel A Vazquez, Jennifer J Gassman, Tom Greene, et al. Effect of clopidogrel on early failure of arteriovenous fistulas for hemodialysis: a randomized controlled trial. *Jama*, 299(18):2164–2171, 2008.

[289] Jeff Bodner and Vikas Kaul. A framework for in silico clinical trials for medical devices using concepts from model verification, validation, and uncertainty quantification (vvuq). In *Verification and Validation*, volume 84782, page V001T02A001. American Society of Mechanical Engineers, 2021.

[290] Paula Martins, Samuel Silva, Catarina Oliveira, Carlos Ferreira, António Teixeira, and Augusto Silva. Investigating the differences between european portuguese sounds: An approach using polygonal mesh comparison. 06 2011.

[291] Vicent Caselles, Ron Kimmel, and Guillermo Sapiro. Geodesic active contours. *International Journal of Computer Vision*, 22:61–79, 02 1997.

[292] Song Chun Zhu and A. Yuille. Region competition: unifying snakes, region growing, and bayes/mdl for multiband image segmentation. *IEEE Transactions on Pattern Analysis and Machine Intelligence*, 18(9):884–900, 1996.

[293] Adam Updegrove, Nathan Wilson, Jameson Merkow, Hongzhi Lan, Alison Marsden, and Shawn Shadden. Simvascular: An open source pipeline for cardiovascular simulation. *Annals of Biomedical Engineering*, 45, 12 2016.

[294] Richard Izzo, David Steinman, Simone Manini, and Luca Antiga. The vascular modeling toolkit: a python library for the analysis of tubular structures in medical images. *Journal of Open Source Software*, 3(25):745, 2018.

[295] Pierre J. Carreau. Rheological equations from molecular network theories. *Transactions of the Society of Rheology*, 16(1):99–127, 1972.

[296] Kenji Yasuda. Investigation of the analogies between viscometric and linear viscoelastic properties of polystyrene fluids /. 08 2005.

[297] Marcin Sosnowski, Jaroslaw Krzywanski, and Renata Gnatowska. Polyhedral meshing as an innovative approach to computational domain discretization of a cyclone in a fluidized bed clc unit. *E3S Web of Conferences*, 14:01027, 01 2017.

[298] A. Arzani. Accounting for residence-time in blood rheology models: Do we really need non-newtonian blood flow modelling in large arteries? *Journal of The Royal Society Interface*, 15:20180486, 09 2018.

[299] G. Carty, S. Chatpun, and D.M. Espino. Modeling blood flow through intracranial aneurysms: A comparison of newtonian and non-newtonian viscosity. *J. Med. Biol. Eng.*, 36, 396–409, 2016.

[300] Yacine Addad, Ulka Gaitonde, Dominique Laurence, and Stefano Rolfo. Optimal unstructured meshing for large eddy simulations. *Quality and Reliability of Large-Eddy Simulations*, 12, 01 2008.

[301] Lewis Fry Richardson and Richard Tetley Glazebrook. Ix. the approximate arithmetical solution by finite differences of physical problems involving differential equations, with an application to the stresses in a masonry dam. *Philosophical Transactions of the Royal Society of London. Series A, Containing Papers of a Mathematical or Physical Character*, 210(459-470):307–357, 1911.

[302] Lewis Fry Richardson and J. Arthur Gaunt. Viii. the deferred approach to the limit. *Philosophical Transactions of the Royal Society of London. Series A, Containing Papers of a Mathematical or Physical Character*, 226(636-646):299–361, 1927.

[303] Joseph Katz. *Introductory fluid mechanics*. Cambridge University Press, 2010.

[304] C Steffen, r, D Reddy, and KBMQ Zaman. Analysis of flowfield from a rectangular nozzle with delta tabs. In *Fluid Dynamics Conference*, page 2146, 1995.

[305] Zeinab Pouransari, Luc Vervisch, and Arne V Johansson. Reynolds number effects on statistics and structure of an isothermal reacting turbulent wall-jet. *Flow, turbulence and combustion*, 92:931–945, 2014.

[306] G. L. Papageorgiou and N. B. Jones. Wave reflection and hydraulic impedance in the healthy arterial system: a controversial subject. *Med Biol Eng Comput.*, 26, 1988.

[307] AP Avolio. Multi-branched model of the human arterial system. *Medical amp; biological engineering amp; computing*, 18(6):709—718, November 1980.

[308] N Suwa, T Niwa, H Fukasawa, and Y Sasaki. Estimation of intravascular blood pressure gradient by mathematical analysis of arterial casts. *The Tohoku journal of experimental medicine*, 79:168—198, March 1963.

Appendix A

Materials and methods pertaining to all investigation chapters

This section details the methodologies implemented in the investigations of this research, in addition to the materials and theory. Section A.1 details the imaging protocol utilised for acquiring the datasets used in this research, section A.2 details further details regarding the segmentation and model generation methodologies not presented in the main body of the thesis, section A.3 details the geometry characterisation methods, section A.4 discusses numerical modelling theory, such as the finite-volume method and the governing equations, section A.5 discusses the mesh generation pipeline used for discretising the computational domains, section A.6 details the boundary conditions assigned to the models, and section A.7 describes the parameters analysed in the investigations of this research.

A.1 Ferumoxytol-enhanced MRA (FeMRA)

As aforementioned in Chapter 2, traditional contrast agents used in magnetic resonance angiography (MRA) are avoided in patients with advanced renal failure due to the associated risks. Gadolinium-based contrast agents (GBCA) are not utilised due to the potential risk of nephrogenic systemic fibrosis, whereas iodinated contrast agents can precipitate significant decline in renal functionality, leading to earlier-than-expected dialysis.

Ferumoxytol has been utilised as a contrast agent in prior investigations, notably in Stoumpos et al. (2020) [138]. The reader is invited to review Stoumpos et al. (2020) [138] for further details regarding the FeMRA protocols.
The protocol utilised for the scans in this research is similar to that of standard GBCA-MRA protocols, aside from the contrast agent. All scans generated for this use in this research

were performed on a 3.0T Prisma MRI scanner (Magnetom, Siemens Medical Solutions, Erlangan, Germany) with local phased-array imaging coils using a standardised protocol similar to that of standard MRA studies. All patients were imaged in the supine position. The outcome of the scanning phase of the research were multiple FeMRA-obtained DICOM stacks for the chest, upper arm, and lower arm regions of a subject. Scans of the aortic arch and AVF vessels were obtained for each patient.

Additionally, 2D time-resolved phase-contrast MRI (PC-MRI) data was obtained proximal and distal to the AVF anastomosis in the majority of the subjects within this research. The vessels of the PC-MRI waveform data varied between datasets due to differing AVF morphologies. The PC-MRI data was acquired for a single cardiac cycle and the scans were oriented axially to the patient's arm. Through plane flow metrics were computed using Segment version 3.0 R7946.

The FeMRA imaging details of the research are given in the Table A.1.

Table A.1 FeMRA imaging details

Scan	VENC (cm/s)	TE (ms)	TR (ms)	Slice thickness (mm)	FOV (mm)	Resolution (pixels per mm)	WL	WW
Chest	-	1.03	2.86	3	325x400	0.96	138	348
Upper Arm	-	1.53	4.5	3	300x480	1.40	139	379
Lower Arm	-	1.64	4.7	3	175x400	1.68	112	319
PC Proximal*	150	2.47	A5 5∼s	3	340x234	0.565	157	394
PC Distal*	150	2.47	A5 5∼s	3	340x234	0.565	158	391

*where PC represents Phase-Contrast, VENC is velocity encoding, TE is the echo time, TR is the repetition time, FOV is the field-of-view, WL is the window level, and WW is the window width

A.2 Segmentation and model generation

A.2.1 Segmentation and reconstruction

With the implementation of FeMRA, there exists a significant variation in the maxima DICOM greyscale values in the patient population. As detailed previously (Chapter 2), automatic segmentation techniques have a very limited application window in the scope of this research due to the number of datasets required for training ML- and AI-based segmentation tools. Additionally, despite manual segmentation permitting clinical experts to have full control of the segmentation, this necessitates significant user input (time and effort) and can still be prone to human error.

Considering these points, semi-automatic segmentation techniques offer the best compromise. This approach involves the user specifying various parameters to produce a segmentation or ‘mask’, which then has to be edited manually to remove undesired voxels included in the segmentation produced from automatic algorithms. In this research, ITK-SNAP [215] was used as the predominant segmentation software.

ITK-SNAP theory

ITK-SNAP is an open-source application for active contour segmentation. SNAP is a end-user application bundled with the Insight Toolkit (ITK), a libarary of image analysis algorithms. Yushkevich et al. (2006) [215] gives an overview of the methods implemented in SNAP, the functionality of ITK-SNAP, and a validation study of the tool. The validation of this software has been completed previously using MRI caudate nucleas segmentation [290].

In order to segment the arterial and venous vessels of interest, each voxel in the structure must be assigned a label. Upon import, each voxel is assigned a ‘Clear’ value, meaning the pixel hasn’t been segmented thus far. The semi-automatic segmentation method in ITK-SNAP uses a ‘region growing’ method that implement active contour segmentation.

SNAP implements two 3D active contour segmentation methods, these being the Geodesic Active Contours by Caselles et al. (1997) [291] and Region Competition by Zhu and Yuille (1996) [292]. Both methodologies evolve the estimate VOI using one or more contours. The evolving contour is a closed surface $C(u,v;t)$ parameterised by variables u,v and by the time variable t. The VOI is sought to be bounded by the contour.

The evolution of the contour is given by Equation A.1.

$$\frac{\partial}{\partial t}C(t,u,v) = F\overrightarrow{N} \tag{A.1}$$

where $\overrightarrow{N}$ is the contour normal, and F is the sum of forces normal to the contour.

The forces normal to the contour can be subdivided into internal and external forces. Internal forces are derived from the contour geometry and impose constraints on the contour shape. External forces incorporate information derived from the image data. Active contour methods have differing definitions of internal and external forces. Caselles et al. (1997) [291] ascertain external forces from gradient magnitude image intensity, Zhu and

Yuille (1996) [292] use voxel probability maps. In both of these studies mean curvature, C, is used for defining internal forces.

Caselles et al. uses Equation A.2 for the force acting on the contour.

$$F = \alpha g_I + \beta k g_I + \Gamma(g_I.\overrightarrow{N}) \tag{A.2}$$

where g_I is the speed function derive from the gradient magnitude of the image I, k is the mean curvature of the contour, α,β,γ are weights for modulating the three components of F.

The speed function is defined so that the value is near 0 at the edges of intensity in the input image, whereas at near constant intensity regions the value is 1. The speed function in SNAP is defined as per:

$$g_I(x) = \frac{1}{1 + (NGM_I(x)/v)^{\Lambda}} \tag{A.3}$$

where v is a user-supplied parameter for determining shape of monotonic mapping, and NGM_I is the normalized gradient magnitude of I, defined as per Equation A.5.

$$NGM_I(x) = \frac{||\nabla(G_\sigma I)||}{max_I||\nabla(G_\sigma I)||} \tag{A.4}$$

where the $G_\sigma I$ parameter denotes convolution of I with the isotropic Gaussian kernel with aperture σ, and ∇ is a user-supplied parameters that determine the shape of the monotonic mapping between the normalized gradient magnitude and the speed function.

Due to the speed function being non-negative, the αg_I acts outwards causing the contour to expand. The outward force is countered by an inwards advection force $\Gamma(g_I.\overrightarrow{N})$ when the contour approaches an edge of intensity.
In Zhu and Yuille (1996) [292], the external force is computed by estimating the likelihood of a voxel belonging to the VOI. SNAP uses thresholds to achieve this. In SNAP the total force is given by:

$$F = \alpha(P_obj - P_bg) + \beta k \tag{A.5}$$

This differs to Zhu and Yuille (1996) [292], where the external force is computed by the difference between logarithms of two probabilities. Yushkevich et al. (2006) [215] further details these points.

ITK-SNAP usage

Segmentation within ITK-SNAP was performed using the steps discussed in Chapters 3-5, these steps can explicitly be stated in the following points:

- DICOM stack acquired from FeMRA was imported into ITK-SNAP.
- Lower and upper greyscale threshold values were specified for defining the extents of the vessels of interest (VOI). These values varied between datasets, and sometimes localised (low greyscale) regions of vessels may not be captured.
- The region-growing 'snake-evolution' tool within ITK-SNAP was implemented. This involved specifying 'bubbles' at various intervals along the VOI (every 1-2cm). These bubbles were then expanded iteratively over 300 iterations to fill the specified greyscale range.
- The resulting segmentation was then reviewed to identify any regions of the VOI that were missed are over-segmented.
- Manual segmentation (using the paint tool) was then completed at the regions omitted from the region-growing tool, in addition to over-segmented locations. This stage also permitted undesired vessels (and similar greyscale tissues) to be removed from the segmentation.
- After completing these steps, the resulting stepped geometry was smoothed with a low-level gaussian filter and exported in an STL format for further processing.

Particular tidy up was required in datasets where inconsistent voxel greyscale levels were observed at the location of the anastomosis. This is a known area of potential problems due to the complex haemodynamics at this bifurcation. In these circumstances, the voxels at each slice were manually segmented (Figure 5.2 in Chapter 5 demonstrates this).

A.2.2 Intra-software segmentation validation

To ensure that the segmentation produced by the user using ITK-SNAP was independent of the software, an aorta and AVF dataset was segmented within ITK-SNAP and Simvascular [293]. In order to compare the two segmentations, the DICE score (coefficient) between the segmentations was computed. This coefficient can be used for ascertaining the 'pixel-wise' agreement between two segmentations. The DICE coefficient is calculated by the double of the segmentation overlap being divided by the total number of pixels in both the images.

The DICE score comparison for this research was completed in Chapter 4.

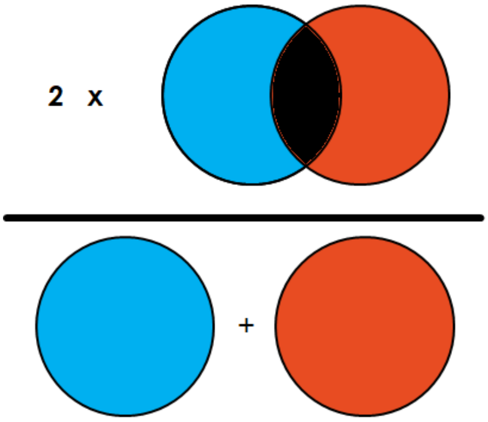

Fig. A.1 Computation of the DICE score. Where the DICE score is equal to 2 × the number of intersecting voxels divided by the sum of the voxels in both segmentations

A.2.3 Iterative smoothing and remeshing

OpenFlipper, an application and framework for processing geometric data, was used for iteratively smoothing and remeshing the segmented geometries. After importing the STL of the segmentation into OpenFlipper, the geometry was remeshed uniformly using a value (in mm) more refined than original segmentation. For example, if the resolution of the image data was 0.8mm, an edge length value less than 0.8mm was used in the remeshing process. Following remeshing, the geometry was then smoothed using a smoothing factor of 3. This remeshing followed by smoothing process was iterated twice to remove any problematic mesh regions whilst not distorting the geometry. Lastly, the resulting STL was imported into Meshmixer, a state-of-the-art software for working with triangle meshes, and the triangulation was refined at the bifurcations of the domain. This was completed to aid the Surface wrapping mesh generation techniques within the mesh generation pipeline. In several tests a copy of the original segmentation from ITK-SNAP was also imported so visual checks can be made on the distortion of smoothing factors on the geometry in this process.

A.3 Geometry characterisation

A key aspect of computational haemodynamics is the characterisation of patient-specific vasculature. The computation of vessel centrelines is a key characteristic, as the centrelines are used for ascertaining the vessel cross-sectional area, curvature, and torsion. Concisely put, the centerlines are determined as weighted shortest paths traced between two specified extremal points. VMTKLab, an application for processing 3D medical images, was used in this research for generating vessel centrelines. VMTKLab incorporates a number of state-of-the-art algorithms, particularly from the Vascular Modelling Toolkit (VMTK) libraries. This is documented in prior work [294].

In order to generate centrelines within VMTKLab, the inlets and outlets of the geometry are specified using points, which snap to the nearest vertex (Fig. A.2). The centrelines are then generated and exported in .csv format for processing. In this research, the inscribed vessel diameter was used in the geometry characterisation workflows.

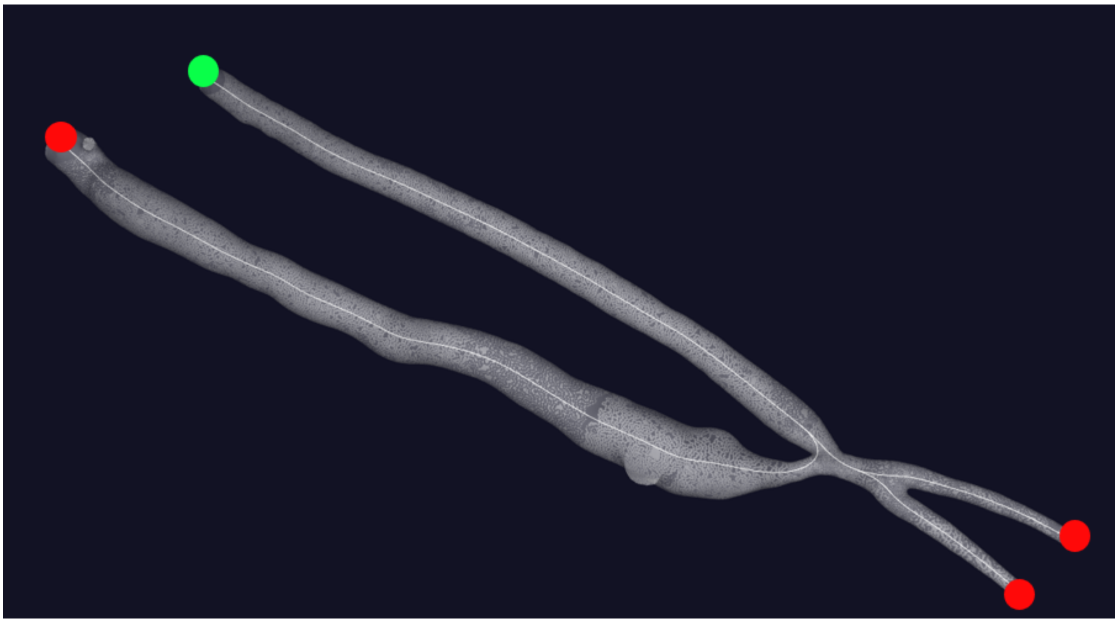

Fig. A.2 Centreline generated in VMTKlab, where the green point represents the inlet seed point, and the red point represents the outlet seed points. The example shown is case 60 in Chapter 4.

A.4 Computational fluids modelling theory

This section details the theory behind the use of computational haemodynamic modelling for the investigations in this research. The equations presented in this section are sourced from the STAR-CCM+ User Guide v15.06 (Simcenter STAR-CCM+, Siemens Industries Digital Software), which the reader is invited to review for further details behind the equations and algorithms implemented within Simcenter STAR-CCM+.

A.4.1 Fundamental laws and governing equations

With the length-scales of blood vessels considered in this research greatly exceeding inter-atomic distances, the structure of the fluid (and solids) can be considered as continua.

The physics of the continua are governed by mathematical models that are derived from fundamental laws of conservation. These are the Navier-Stokes equations. These conservation laws of mass, linear momentum, angular momentum, and energy, are expressed in Equations A.6-A.10 in differential form.
Conservation of mass:

$$\frac{\partial \rho}{\partial t} + \nabla(\rho v) = 0 \tag{A.6}$$

where ρ is density, and v is the continuum velocity.

Conservation of linear momentum:

$$\frac{\partial(\rho v)}{\partial t} + \nabla(\rho v \otimes v) = \nabla.\sigma + f_b \tag{A.7}$$

where $\otimes$ denotes outer product, f_b is resultant of body forces per unit volume, σ is stress tensor. The fluid stress tensor is written as the sum of normal and shear stress $\sigma = -pI + T$, where p denotes pressure, and T is viscous stress tensor. This yields Equation A.8.

$$\frac{\partial(\rho v)}{\partial t} + \nabla(\rho v \otimes v) = -\nabla.(pI) + \nabla.T + f_b \tag{A.8}$$

Conservation of angular momentum:

$$\sigma = \sigma^T \tag{A.9}$$

Conservation of energy:

$$\frac{\partial \rho E}{\partial t} + \nabla(\rho E v) = f_b.v + \nabla.(v.\sigma) - \nabla.q + S_E \tag{A.10}$$

where E is the total energy per unit mass, q is the heat flux, and S_E is an energy source per unit volume.

For the investigations of this research (and the majority of fluid flow cases), the partial differential equations are not a closed set, meaning the number of unknowns is greater than the number of equations. Therefore, additional equations are added to the mathematical model so as to give closure to the equation set. The additional equations are termed constitutive laws and vary depending on the fluid or solid properties being modelled.

Discretisation, the division of a continuous domain into a finite number of subdomains (cells/elements), is used for converting the continuous system of equations into a set of algebraic equations that can be solved numerically. This is made possible by i) unknowns being stored at positions within the mesh such as vertices or edges, and ii) an integral form of the differential equations being employed for spatial discretisation. Subsequently, the time derivative is discretised, meaning that a nonlinear coupled system of algebraic equations can be solved for each time step specified within the pre-processing phase. In this research, the discretisation of the continuous equations was achieved using the Finite Volume Method (FVM).

In accordance with discretisation, Equations A.6-A.10 can be integrated over a finite volume. This produces the fluid flow governing equations (Equations A.11-A.13).

Continuity equation:

$$\frac{d}{dt}\int_V \rho dV + \oint_A \rho \mathbf{v}.d\mathbf{a} = \int_V S_u dV \tag{A.11}$$

Momentum equation:

$$\frac{d}{dt}\int_V \rho v dV + \oint_A \rho \mathbf{v} \otimes v.da = -\oint_A pI.da + \oint_A T.da + \int_V f_b dV + \int_V s_u dV \tag{A.12}$$

Energy equation:

$$\frac{d}{dt}\int_V \rho E dV + \oint_A \rho H v.da = -\oint_A q.da + \oint_A T.vda + \int_V f_b.vdV + \int_V S_u dV \tag{A.13}$$

where S_u and su are user source terms.

A.4.2 Numerical solutions of fluid flow

To solve the momentum equations for the velocity field of the fluid, closure is required between the stress tensor and fluid velocity field. This is possible using constitutive equations and relations. Many constitutive equations exist that include different fluid (and material) properties, such as viscosity and the normal stress coefficients. Moreover, equations of state (constitutive relations) are used for closing the system of equations.

Equations of state are constitutive relations describing the relation between density and internal energy to pressure and temperature (the two basic thermodynamic variables). The approach utilised in STAR-CCM+ for the investigations in this research was the constant fluid density assumption, i.e. $\rho = \rho_0$.

Rheology model

With blood being a non-Newtonian fluid, i.e. not a linearly viscous fluid, a model must be used to account for the properties of blood under varying forces. The viscoelastic nature of blood means that the fluid undergoes viscous and elastic behaviour when undergoing deformation. The stresses are dependant on the current motion of the fluid and the recent history of motion. The ‘relaxation time’ of the fluid quantifies this effect. Additionally, the viscoelastic non-Newtonian properties give a constitutive equation to resolve the stress tensor T. In this research a generalised Carreau-Yasuda non-Newtonian model [295, 296] was used when considering blood to be non-Newtonian. Considering a blood to be non-Newtonian is a prerequiste to the AVF simulation due to the shear rates that would stretch the Newtonian rheology assumption. The isothermal assumption is made in this research. The non-Newtonian generalised Carreau-Yasuda model defines the properties of blood; as per:

$$\mu(\dot{\gamma}) = \mu_\infty + (\mu_0 - \mu_\infty)(1 + (\lambda\dot{\gamma})^a)^{(n-1)/a} \tag{A.14}$$

where a is the a shear-thinning control parameter, λ is the relaxation time, μ_0 is the zero shear viscosity, μ_∞ is the infinite shear viscosity, n is the power constant, and $\dot{\gamma}$ is the shear rate. The parameters used in the simulations are defined as per [295]:

- infinite shear viscosity $\mu_{\text{inf}} = 0.00345 Pa.s$
- viscosity at zero shear rate $\mu_0 = 0.056 Pa.s$
- relaxation time constant $\lambda = 3.313s$
- $n = 0.357$
- $a = 0.5$

The properties of the fluid continua (blood) were defined in STAR-CCM+ in the pre-processing phase of the CFD simulation.

Finite volume method

With the FVM, the computational domain is subdivided into a finite number of small control volumes. These are the cells of the computational mesh. Discrete integral forms of the conservation equations (Equations A.10-A.13) are applied to each volume. This seeks to ascertain a system of linear algebraic equations, which can be used for resolving the unknowns. In STAR-CCM+ variable values are stored at cell centers using a co-located variable agreement.

The transformation of the mathematical model to algebraic equations requires discretising the governing equations in space and time. The algebraic equations are then solved using a algebraic multi-grid solver. In transient simulations, physical time is sub-divided into specified time-steps.

The introduction of the constitutive relations into the conservation equations results in a closed set of equations. Integration of the generic transport equation over a control volume V and the application of Gauss's divergence theorem results in the integral form of the transport equation (Equation A.15).

$$\frac{d}{dt}\oint_V \rho\phi dV + \oint_A \rho\mathbf{v}\phi.d\mathbf{a} = \oint_A \Gamma\nabla\phi d\mathbf{a} + \oint_V S_\phi dV \tag{A.15}$$

where ϕ is the transport of a scalar, A is the surface area of control volume, $d\mathbf{a}$ is the surface vector, Γ is the diffusion coefficient, the components of the equation are the transient, convective, diffusive, and source terms respectively.

The surface integrals in Equation A.15 are evaluated using quadratic approximations. The integral is expressed in terms of variable values at a location of the cell face. Within *Simcenter STAR-CCM+* a second-order midpoint rule is used, meaning the integral is evaluated as the product of the values for both the cell face center and cell face area, as per:

$$\oint_A \mathbf{J}^\phi.d\mathbf{a} \approx \Sigma_f \mathbf{J}^\phi_f.\mathbf{a}_f \tag{A.16}$$

where $\mathbf{J}^\phi$ is the convective/diffusive flux of the fluid property ϕ, a_f is the surface area vector of the cell face (f), and Σ_f is the sum over all cell faces of the cell.

The values at each cell face center are unknown and approximated through interpolation of cell center values and calculated with discretisation schemes.

The source term in the general transport equation involves the integration over the cell volume. *Simcenter STAR-CCM+* approximates the volume integral through the product of the source term mean value at the cell center and cell volume as per:

$$\oint_V S_\phi dV \approx S_{\phi_0} V_0 \tag{A.17}$$

This approximation is second-order accurate, where the cell face center is the area weight center and cell center is the volume center. Applying the integration approximation gives the semi-discrete transport equation (Equation A.18).

$$\frac{d}{dt}(\rho\phi V)_0 + \Sigma_f[\rho\phi(\mathbf{v}.\mathbf{a})]_f = \Sigma_f(\Gamma\nabla\phi.\mathbf{a})_f + (S_\phi V)_0 \tag{A.18}$$

In transient cases, such as the unsteady and pulsatile cases in this research, time is considered an additional coordinate, which is discretised in addition to spatial discretisation. This is achieved, as stated prior, by using time-steps. For solving the flow at time-steps, the solution of the governing equations is ascertained at each time-step where the solution at time t requires the solutions from prior time-steps. Differing time-integration schemes can be employed for integrating the fluxes and sources.

Implicit time integration is used in this research in the form of a Euler implicit scheme. This uses the solution at the current time step (n+1) in addition to the previous time step (n). A first-order temporal scheme is given in Equation A.19.

$$\frac{d}{dt}(\rho\phi V)_0 = \frac{(\rho\phi V)_0^{n+1} - (\rho\phi V)_0^n}{\delta t} \tag{A.19}$$

Segregated flow solver

In this research, the segregated flow solver within STAR-CCM+ was utilised. This solver sequentially solves the integral mass and momentum conservation equations to obtain the solution variables such as velocity and pressure. The segregated flow solver uses a pressure-velocity coupling algorithm, while mass conservation is maintained on the velocity field by solving a pressure-correction equation. This equation is constructed using the continuity and momentum equations, and the predicted velocity field fulfils the continuity equation through pressure correction.

The SIMPLE (Semi-Implicit Method for Pressure-Linked Equations) pressure-velocity coupling algorithm was employed for the segregated flow solver in this research. The widely implemented SIMPLE algorithm can be summarised as follows:

1. Set boundary conditions
2. Compute reconstruction gradients of velocity and pressure
3. Compute the velocity and pressure gradients
4. Solve discretised momentum equation, which yields intermediate velocity field
5. Compute uncorrected mass fluxes at faces $\dot{m}_f*$
6. Solve pressure correction equation, producing pressure correction p’
7. Update pressure field ($p^{n+1} = p^n + \omega p'$) where ω is the under-relaxation factor for pressure
8. Update boundary pressure correction p'_b

9. Correct face mass fluxes ($\dot{m}_f^{n+1} = \dot{m}_f * + \dot{m}'_f$
10. Correct cell velocities ($v_p^{n+1} = v_p * - \frac{V \nabla p'}{{a'_p}^{v}}$, where $\nabla p'$ is gradient of pressure correctors, ${a'_p}^{v}$ is vector of central coefficients for discretised velocity equation, and V is the cell volume
11. Update density due to pressure changes
12. Free temporary storage

The discrete pressure correction equation is written in coefficient form, and is described as per Equation A.20.

$$p'_p + \sum_n a_n p'_n = r \tag{A.20}$$

where the residual r is the net mass flow into a cell ($r = -\sum_n \dot{m}_f *$).

A.4.3 Turbulence and transition

Turbulence, chaotic and disturbed flow, occurs when convective force in the flow overcome the viscous forces. The ratio between convective and viscous forces, the Reynolds number (Re) (Equation A.21), is a non-dimensional quantity used for classifying laminar, transitional, and turbulent flow. A Re value of 2300 typically represents the presence of transitional and turbulent flow.

$$Re = \rho u L / \mu \tag{A.21}$$

where u is the flow speed (e.g. peak systolic inlet velocity), L is a characteristic linear dimension, e.g. the inlet diameter, and ρ and μ are physiologically relevant blood values for the dynamic viscosity and density. When assumed in this research, these values were $0.0035 Pa.s$ and $1060 kg/m^3$ respectively.

Resolving the exact solution for the governing equations of turbulent flows is achievable using Direct Numerical Simulation (DNS). However, this is often impractical due to the computational cost and resources required. Instead, irregular fluctuating flow quantities at small scales are often solved as averaged or filtered quantities. Turbulence models offer differing methods for modelling these structures. Turbulence models can be classified into Reynolds-averaged Navier-Stokes turbulence (RANS) models and scale-resolving simulations. With existing turbulence models all providing approximate turbulent flow distributions, the selection of the most appropriate model is based predominantly on experience.

RANS modelling

Each RANS turbulence model gives closure relations for the RANS equations, which govern transport of mean flow quantities. Each variable (ϕ) in the instantaneous Navier-Stokes equations is decomposed into its mean $\overline{\phi}$ and its fluctuating component ϕ' as per:

$$\phi = \overline{\phi} + \phi' \tag{A.22}$$

where ϕ is representative of velocity, pressure and energy. Considering steady-state simulations, the averaging process is time-averaging. This is opposed to ensemble averaging in transient cases.

The Navier-Stokes equations (given previously) include a stress tensor (Equation A.23) in RANS modelling.

$$T_{RANS} = -\rho \begin{pmatrix} \overline{u}'u' & \overline{u}'v' & \overline{u}'w' \\ \overline{u}'v' & \overline{v}'v' & \overline{v}'w' \\ \overline{u}'w' & \overline{v}'w' & \overline{w}'w' \end{pmatrix} + \frac{2}{3}\rho k I \tag{A.23}$$

where ρ is density. u, v, and w are the velocity components, k is the turbulent kinetic energy, and I is the identity tensor.

The differing approaches used for modelling T_{RANS} (and giving closure to the governing equations) are denoted by the equations of the model used (k-epsilon, k-omega, etc.). The RANS simulations completed within this research utilsed the k-epsilon model, which solves for turbulent kinetic energy, k, and turbulent dissipation rate, ε.

The transport equations of kinetic energy k and turbulent dissipation rate ε are defined as per:

$$\frac{\partial}{\partial t}(\rho k) + \nabla.(\rho k \overline{v}) = \nabla.[(\mu + \frac{\mu_t}{\sigma_k})\nabla k] + P_k - \rho(\varepsilon - \varepsilon_0) + S_k \tag{A.24}$$

$$\frac{\partial}{\partial t}(\rho \varepsilon) + \nabla.(\rho \varepsilon \overline{v}) = \nabla.[(\mu + \frac{\mu_t}{\sigma_\varepsilon})\nabla \varepsilon] + \frac{1}{T_e} C_{\varepsilon 1} P_\varepsilon - C_{\varepsilon 2} f_2 \rho (\frac{\varepsilon}{T_e} - \frac{\varepsilon_0}{T_0}) + S\varepsilon \tag{A.25}$$

where $\overline{v}$ is mean velocity, μ is dynamic viscosity, $\sigma_k, \sigma_\varepsilon, C_{\varepsilon 1}, C_{\varepsilon 2}$ are model coefficients, f_2 is a damping function, S_k S_ε are user-specified source terms, and P_k and P_ε are production terms, defined in the Appendix.

Scale-Resolving Hybrid model

Scale-resolving simulations resolve large scales of turbulence and model small-scale motions. These simulations include large eddy simulation (LES) and detached eddy simulation (DES). Despite some limited computational haemodynamic studies using LES previously, LES was deemed not appropriate for the investigations in this research due to the meshing requirements of LES and the length-scale being considered. DES is a hybrid LES-RANS approach for resolving turbulent structures in the core flow and covers the wall boundary layers using a RANS model. As such, DES omits the expensive mesh requirements of LES, whilst being able to fully resolve larger scale flow (unlike RANS modelling). With these considerations, the scale-resolving hybrid (SRH) model in STAR-CCM+ was used for the majority of simulations within the research.

The SRH filtering results in transport equations being equivalent to the RANS equations for a large filter time-width, and LES equations for a short filter-width. Between these time scales, time step and mesh size is used for determining turbulent structure resolution [218].

The equations solved in the SRH model are ascertained using a spatial-temporal filtering, i.e. each variable φ is decomposed into a filtered $\overline{\tilde{\varphi}}$ and a subfiltered value φ' as per:

$$\varphi = \overline{\tilde{\varphi}} + \varphi' \tag{A.26}$$

where ϕ is representative of quantities such as velocity components, pressure, and energy.

This results in the momentum equations for RANS averaged velocity ($\overline{v}$) and the LES filtered velocity ($\overline{v}$) being defined as per Equations A.27-A.28.

$$\frac{\partial}{\partial t}(\rho\overline{v}) + \nabla.(\rho\overline{v}\otimes\overline{v}) = -\nabla.\overline{p}I + \nabla.(\overline{T} + T_{RANS}) + f_b \tag{A.27}$$

$$\frac{\partial}{\partial t}(\rho\overline{v}) + \nabla.(\rho\overline{v}\otimes\overline{v}) = -\nabla.\overline{p}I + \nabla.(\overline{T} + T_{SGS}) + f_b \tag{A.28}$$

Duffal et al. (2019) [218] details further information relating to the SRH model utilised in the CFD investigations.

A.4.4 Wall treatment

Walls are a source of vorticity and accurate prediction of the flow across the wall boundary layer is essential for both laminar and turbulent boundary layers. The turbulent boundary layer is comprised of an outer and inner layer. The inner layer can be further subdivided into the viscous, log, and buffer layer. Each of the sub-layers is modeled using different empirical approaches, with the wall functions being defined in terms of non-dimensional quantities. This makes the algebraic approximations independent of the Reynolds number of the flow. For the turbulence models in Simcenter STAR-CCM+ used in this research, the all-y+ wall treatment was used. This uses blended wall functions and provides valid boundary conditions for flow, energy, and turbulence quantities for a wide range of near-wall mesh densities. The value of y+ relates to prism layer meshing of the computational domain as is defined as per Equation A.29.

$$y+ = \frac{y\rho u_T}{\mu} \tag{A.29}$$

where $y+$ is a non-dimensional distance to describe mesh resolution near domain walls (in this study $y+ = 1$), u_T is the friction velocity, μ is the fluid viscosity, and y is the height of the first prism layer.

A.5 Mesh generation pipeline

This section details the mesh generation techniques, rationale, and methodologies. The high-order mesh generation protocols for the subsequent CFD simulations were completed within Simcenter STAR-CCM+.

A.5.1 Surface mesh import and region assignment

After generating the STL file of the vasculature in each case (Chapter 3), the ‘boundaries’ (inlets and outlets) of the computational domain were clipped from the STL file (normal to the centreline of the domain) using Paraview [249]. This is useful for the following steps within STAR-CCM+.

The model preparation steps of the geometry within STAR-CCM+ were as follows:

1. The ‘open’ shell STL of the vasculature was imported into STAR-CCM+ (with correct scaling)
2. The open boundaries of the STL surface mesh were filled using the *Fill Holes* tool
3. The ‘Filled Holes’ surfaces were then split (using the *Split by angle* tool). The resulting surfaces were then renamed to the appropraite inlet/outlet patch name.

4. Lastly, the surfaces of the vessel wall segmentation and inlet and outlet patches were grouped into a single geometry using the *Extract Volume* tool. This produces a consistently valid and 'watertight' triangulated surface mesh to be subsequently meshed (Fig. A.3).

Prior to mesh generation, the continua for the fluid domain is defined. Additionally, the Extract Volume surface mesh is assigned as a region, with each surface being allocated as a boundary (inlet, outlet, or wall). It is important to do this at this stage as the mesh generation (with prism-layer meshing) is dependent on the specification of inlets and outlets. Following this, the physics of the region is defined as the continua, which has the description of blood. The non-Newtonian blood model is incorporated at this stage. These steps permit a region-based meshing (RBM) approach to be implemented, allowing a robust, efficient, and repeatable meshing protocol.

A.5.2 Mesh element composition

Simcenter STAR-CCM+ enables automatic volume mesh generation with optimised cell quality. Within STAR-CCM+ there are several options regarding the composition of the mesh. Polyhedral meshing and prism layer meshers were used in STAR-CCM+ for the mesh discretisation of the computational domains in this research. The meshes were generated in parallel, which speeds up volume mesh generation.

Polyhedral meshes require no more surface preparation than tetrahedral meshes, whilst containing approximately five times fewer cells than the equivalent tetrahedral mesh. Polyhedral meshes are also less sensitive to stretching [297] and due to having many neighbours, polyhedral meshes give a superior approximation to gradients. Additionally, prism layers reduce numerical diffusion adjacent to the wall and capture the viscous effects.

Prior to the core mesh generation a subsurface is generated using the specified prism layer thickness. The core mesh is subsequently generated from this subsurface, with the prism layer mesh being generated by extruding the cell faces from the resultant core mesh and the original domain surface. When generating a polyhedral mesh, an initial tetrahedral mesh is generated for the input surface. A dualization scheme is then used to mark the center of the tetrahedral cells and midpoint on boundary edges. This enables polyhedral cells (typically of 14 cell faces) to be generated from the boundary edge inwards. Volume cell sizes grow from the surface or custom cell size to the core mesh at a rate specified using the Volume Growth Rate. The custom cell sizes referred to are determined by the prism layers.

Prism layer meshing In the cases considered within this research, the near-wall haemodynamics are crucial to capture due to the impact of blood flow on the wall shear stress metrics that are of key interest. In order to accurately compute the flow in the inner boundary sub-layers, a fine mesh resolution is used adjacent to the walls. This infers the use of prism layer meshing.

Prism layers permit the CFD solver to resolve near wall flows accurately, and enhance the solver's prediction of forces on the domain walls and flow separation. Prediction of flow features requires resolving velocity gradient adjacent to the wall. Applying a prism layer mesh allows the resolution of viscous sublayer directly if the turbulence model supports it, i.e. where $y+ \leq 1$. The prism layer mesh properties (thickness, number of layers) is defined by the turbulence modelling technique and the underlying physics of the simulation. In addition to the advantageous near-wall mesh density offered by prism layer meshes, they also allow high-aspect-ratio cells to be used. The use of prism layers also reduce numerical diffusion (discretisation error that smears discontinuities and steep gradients in a finite volume advection scheme) near the wall. The use of prism layers minimises numerical diffusion due to flow aligning with the mesh.

The dimensions of the prism layer mesh elements are specified using the non-dimensional wall distance $y+$ (A.29). The thickness of the prism layer was calculated using a y+ value of 1, based on prior haemodynamic studies [298, 299].

Based on the y+ and the fluid properties, the frictional velocity (U_T), WSS (τ_w), and the skin friction coefficient (C_f) can be calculated according to Equations A.30-A.32, from which a initial estimation of first cell height Δy_1 can be determined for the construction of the mesh.

$$U_T = \sqrt{\frac{\tau_w}{\rho}} \tag{A.30}$$

$$\tau_w = \frac{1}{2}.C_f.\rho.U^2 \tag{A.31}$$

$$C_f = [2log_{10}(Re_x) - 0.65]^{-2.3} \tag{A.32}$$

A.5.3 Meshing parameters and validation

The use of polyhedral and prism layer meshing within STAR=CCM+ permits the specification of numerous meshing parameters. Within this research most of the parameters were kept consistent between the differing cases (Table A.2) as the parameters were found to capture the initial geometry edges accurately

.

Table A.2 Mesh characteristics consistent between different cases.

Target surface size	100
Minimum surface size	10
Surface curvature	360
Surface growth rate	1.3
Volume growth rate	1.2
Maximum tet size	100 % of base size

The meshing parameters modified for the mesh refinement study between investigations were i) the base size of the core (polyhedral) mesher, and ii) the number of prism layers. Additionally, changing the number of prism layers in the mesh generation changes the prism layer stretching ratio. The prism layer total thickness was set to be equal to the absolute size calculated from using a y+ value of 1.

The various meshing configuration for each of the Chapters of this research were informed using a precursor steady-state RANS (k-epsilon) simulation. The inlet specified in these cases used a constant-uniform peak systolic inlet. This permitted an *a posteriori* approach for predicting the turbulence characteristics prior to the simulations, which further informs the mesh characteristics. The parameters assessed within the precursor CFD simulations were the wall y+, Taylor Mirco Scale, and Kolmogorov length scale values [300]. These values are commonly used for ascertaining an appropriate base size for large-eddy simulations (LES) which resolve turbulence characteristics. An insufficient grid resolution would result in the LES subgrid scale (SGS) model being utilised for inappropriate length scales.

In each precursor steady-state RANS simulation, the height of the first prism layer (y) was ascertained by first calculating the Reynolds number (Re) (Equation A.27). Following this, a 'safety factor' of 2 ($y+ = 0.5$) was incorporated and of the value y was computed using Re. Following the initial y calculation, a mesh independence analysis was completed. The base mesh size was varied and the number of prism layers varied with a constant prism layer total thickness (using y+) and a prism layer stretching of 1.35. This established the most suitable mesh density that had the best trade-off between computational expense and accuracy (Appendix).

A.5.4 Grid convergence

Establishing grid convergence is a prerequisite for numerical studies. This verifies the equations are being solved correctly independent of grid resolution. A minimum of 3 simulations (with a constant refinement ratio, r, between them) is required to establish grid convergence. Velocity magnitude was the parameter of interest selected for analysis across several cross-sections throughout the domain(s) across the investigations.

Firstly, the order of convergence (p) is computed, as per:

$$p = ln(\frac{(f_3 - f_2)}{(f_2 - f_1)})/ln(r) \tag{A.33}$$

where f_3 is the result with the finest mesh, f_2 is the result with the medium mesh, f_1 is the result with the coarsest mesh.

Secondly, a Richardson extrapolation was performed to predict the value at $h = 0$, as per:

$$f_{h=0} = f_{fine} + \frac{(f_1 - f_2)}{r^p - 1} \tag{A.34}$$

The grid convergence index (GCI) is then computed for each mesh resolution, as per:

$$GCI = \frac{F_s|\varepsilon|}{r^P - 1} \tag{A.35}$$

where F_s is the prescribed safety factor.

Lastly, the grid resolution is checked to be in the asymptotic convergence range, as per:

$$\frac{GCI_{2,3}}{r^P \times GCI_{1,2}} \approx 1 \tag{A.36}$$

where P is the order of convergence, $GCI_{2,3}$ is the GCI between the meshes with the 2nd and 3rd most dense meshes, $GCI_{1,2}$ is the GCI between the meshes with the most and 2nd most coarse meshes, and r is the ratio between the elements in the most and 2nd most dense meshes.

In order to establish grid convergence in the investigations of this research, the velocity magnitude values at several cross-sections across a representative computational domain in each of the investigations was analysed. The order of convergence between coarse, medium and fine mesh densities was computed in order to perform a Richardson extrapolation [301, 302]. This permitted the grid convergence index (GCI) [217] to be calculated for the increasing mesh densities (Appendix B, C, D). The grids were checked to be in the asymptotic range of convergence as per Equation A.35.

A.6 Boundary conditions

The boundary conditions of the model, as the name suggests, define how flow enters and leaves the computational domain, with flow being confined by the presence of a wall boundary.

In this research differing patch definitions were applied between studies. Velocity and mass flow inlets were used as inflow conditions, where the flow distribution and fluid properties are known and assigned. The velocity inlet condition specifies the velocity (m/s), inflow direction, and temperature variables, whereas the mass flow condition specifies mass flow rate (kg/s). The inflow direction specified in the investigations of this research using the both inlet conditions were normal to the inlet surface, the temperature was defined as isothermal. Uniform profiles were utilised due to entrance lengths being accounted for the model setup (Appendix B, C, D). The velocity and mass flow inlet conditions were used for prescribing cardiac waveforms obtained using cardiac outputs and or phase-constrast MRI flow data.

The outflow conditions utilised within the research were pressure outlets, prescribed flow splits (as a percentage of the inlet waveform), and prescribed flow waveforms. The pressure outlets considered in this research were three-element windkessel models, as opposed to zero-pressure outlets which have limited physiological relevance. These approaches are discussed in Appendices B, C, and D.

A.7 Haemodynamic parameter defintions

In computational modelling the continuum assumptions can influence the haemodynamic-induced WSS parameters of interest. To ascertain the influence of the haemodynamics on the arterial and venous vessels, several WSS-related metrics were computed and assessed in post-processing. For a comprehensive description of these metrics, the reader is invited to review Browne et al. (2016) [112]. Time-averaged wall shear stress (TAWSS) is indicative of the force induced on the vessel wall over the entire cardiac cycle [251], whereas the oscillatory shear index (OSI) and transverse WSS (transWSS) metrics seek to characterise the multi-directional nature of WSS in disturbed flows. OSI is a dimensionless metric used for characterising the alignment between the WSS vector and TAWSS during the cardiac cycle. The transWSS metric computes time-averaged WSS elements perpendicular to the mean flow. WSSG, the WSS spatial gradient, is derived from the WSS gradient tensor components parallel and perpendicular to the time-averaged WSS vector. These WSS metrics are defined as per Equations A.37-A.40.

$$TAWSS = \frac{1}{T}\int_{0}^{T} |\tau_w|\, dt \tag{A.37}$$

$$OSI = \frac{1}{2}\left(\frac{\left|\int_0^T \tau_w dt\right|}{\int_0^T |\tau_w|\, dt}\right) \tag{A.38}$$

$$transWSS = \frac{1}{T}\int_0^T |\vec{\tau}_w.(\vec{n} \times \frac{\int_0^T \vec{\tau}_w dt}{|\int_0^T \vec{\tau}_w dt|})|dt \tag{A.39}$$

$$WSSG = \sqrt{(|\frac{\partial \vec{\tau}_w}{\partial x}|)^2 + (|\frac{\partial \vec{\tau}_w}{\partial y}|)^2 + (|\frac{\partial \vec{\tau}_w}{\partial z}|)^2} \tag{A.40}$$

where $\vec{\tau}_w$ represents the WSS vector and T represents the period of the cardiac cycle.

In addition the WSS metrics, Localised normalised helicity (LNH) was assessed. LNH [252] is a haemodynamic marker previously suggested to be key in the development of favourable AVF haemodynamics related to successful maturation. LNH is defined as per Equation A.41.

$$LNH = \frac{u.\omega}{|\, u \,||\, \omega \,|} \tag{A.41}$$

where u is velocity and ω is vorticity.

A.8 Volume renderings of DICOM data

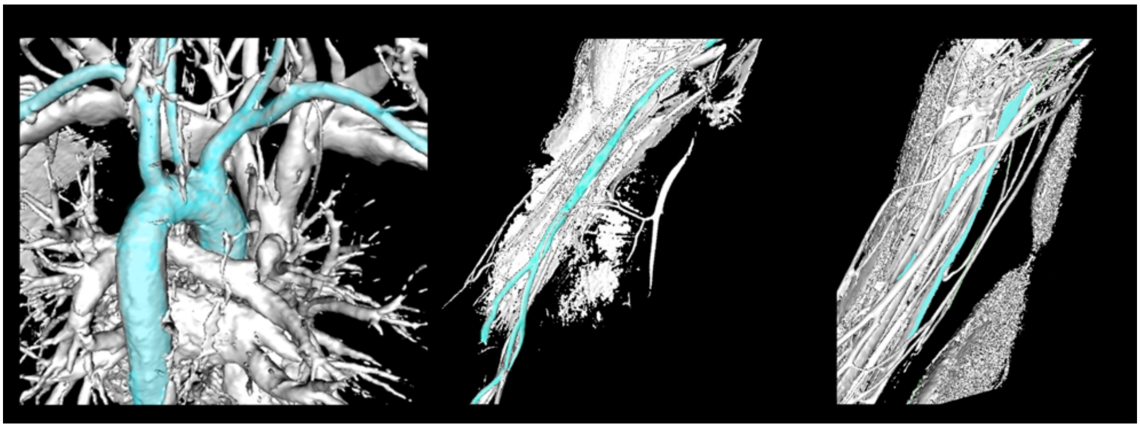

Fig. A.3 Example volume renderings (in Osirix, www.osirix-viewer.com) of vessels of interest within chest (left), upper arm (middle), and lower arm (right) DICOM stack obtained using FeMRA.

A.9 Turbulence model comparison

In order to compare the suitability of a scale-resolving hybrid turbulence model over a laminar model, comparison study was completed on the geometry presented in Chapter 3. The maximum cross-sectional flow rates induced at 15 locations was analysed, in addition to the normalised TAWSS mean value across the domain.

Figures A.4-A.5 demonstrate the differing cross-section velocity magnitudes throughout the computational domain, Table A.3 gives minimum, mean, medium, and maximum percentage differences obtained using a laminar model as opposed to the adopted scale-resolving hybrid turbulence model.

Figure A.6 gives the normalised TAWSS contour plots obtained using a laminar model and a scale-resolving hybrid turbulence model. The normalisation was computed using the normalisation method documented in Appendix B (Section B.1). The mean Normalised TAWSS values in the laminar model and the scale-resolving hybrid turbulence model were 0.41 and 0.45 respectively.

The Reynolds numbers observed in Chapter 3 determine that turbulence modelling should be implemented.

Table A.3 Percentage difference between the maximum velocity induced through computational domain using laminar and scale-resolving hybrid turbulence model

Minimum percentage difference	1.82
Mean percentage difference	5.23
Median percentage difference	5.19
Maximum percentage difference	11.14

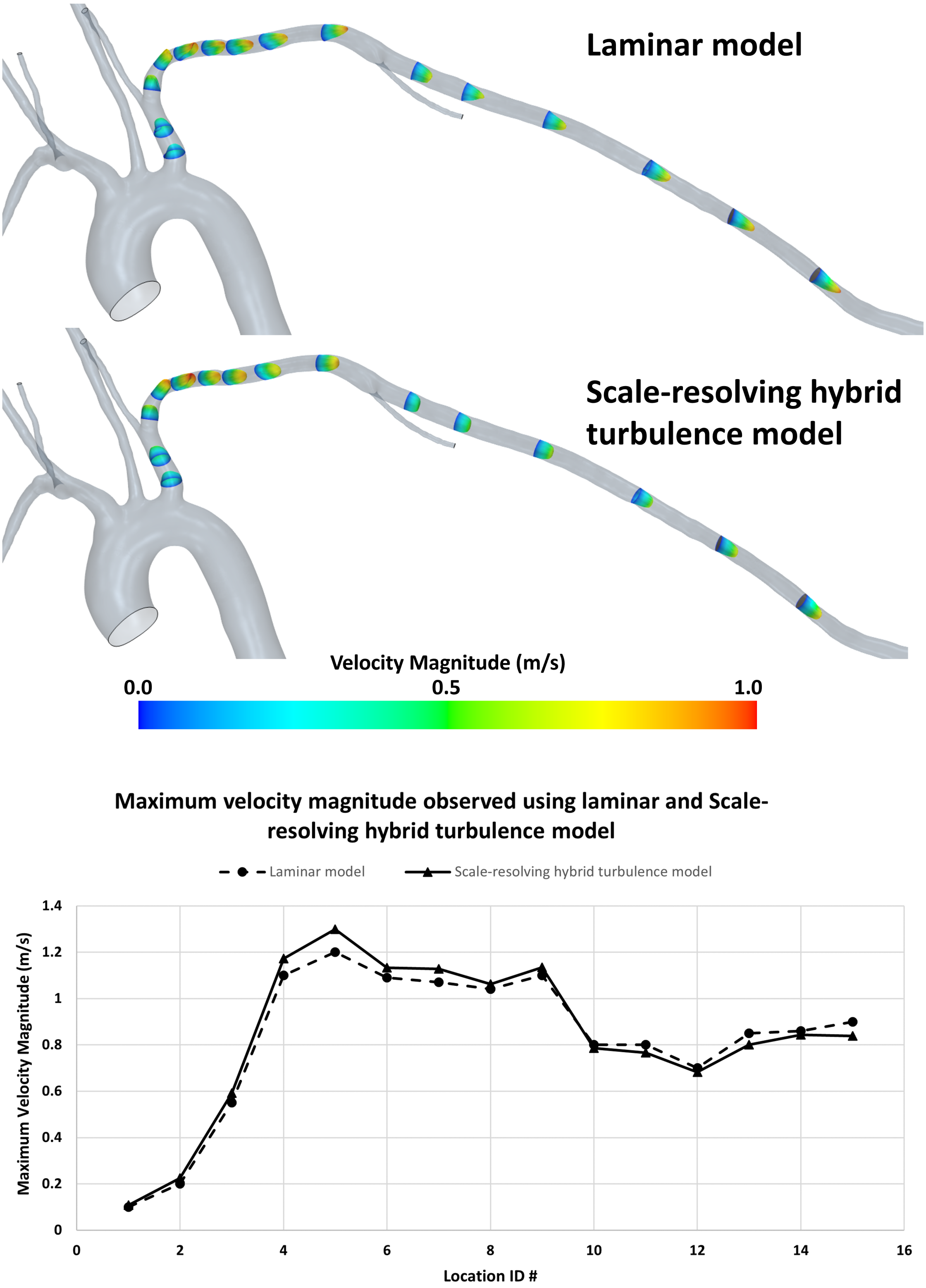

Fig. A.4 Comparison of maximum velocity magnitude observed using laminar and Scale-resolving hybrid turbulence model in 19-year-old RCF case studied in Chapter 3.

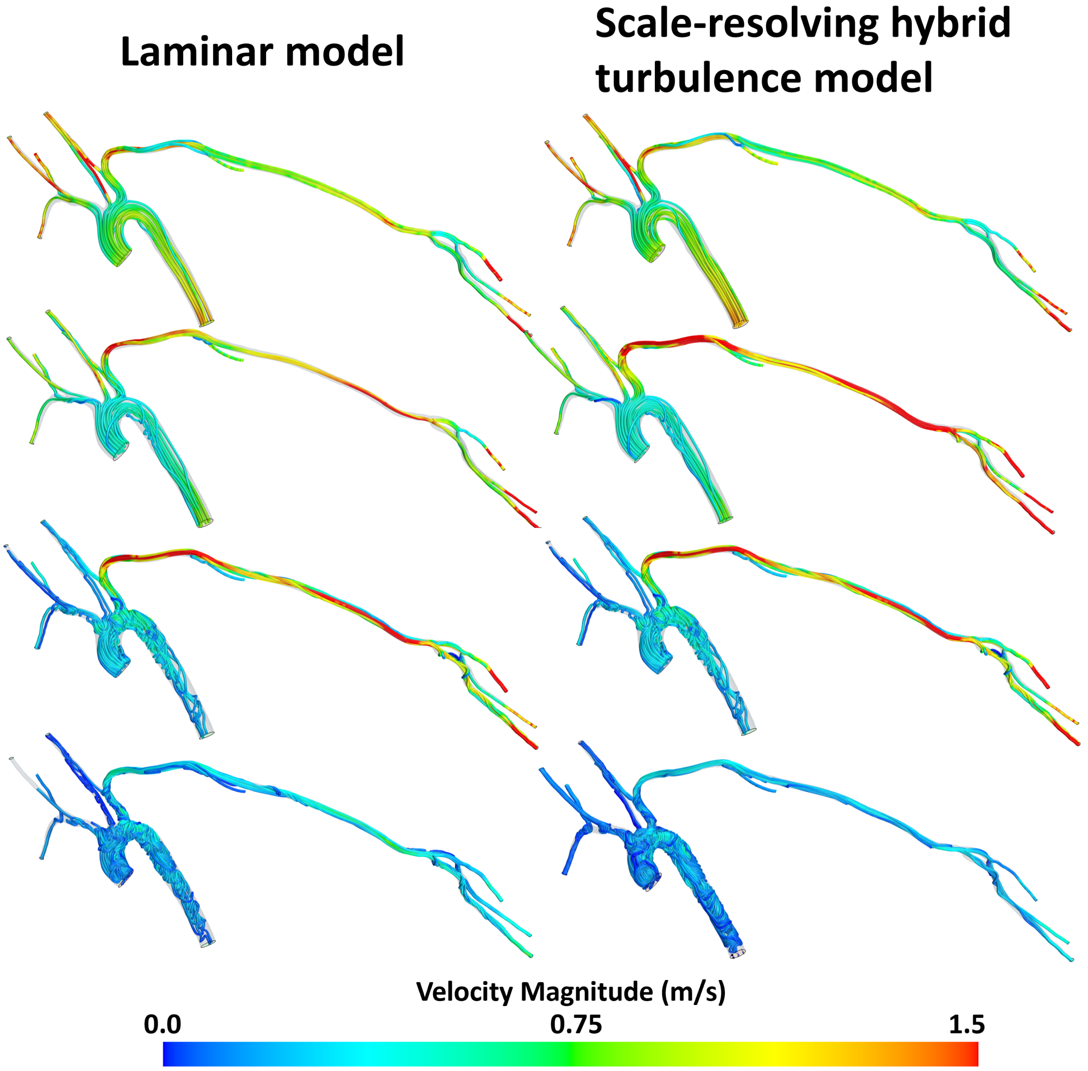

Fig. A.5 Velocity streamline contour plots at A) Peak systole, B) Mid deceleration, C) Peak diastole, and D) Mid-late diastole using laminar and Scale-resolving hybrid turbulence model in 19-year-old RCF case studied in Chapter 3.

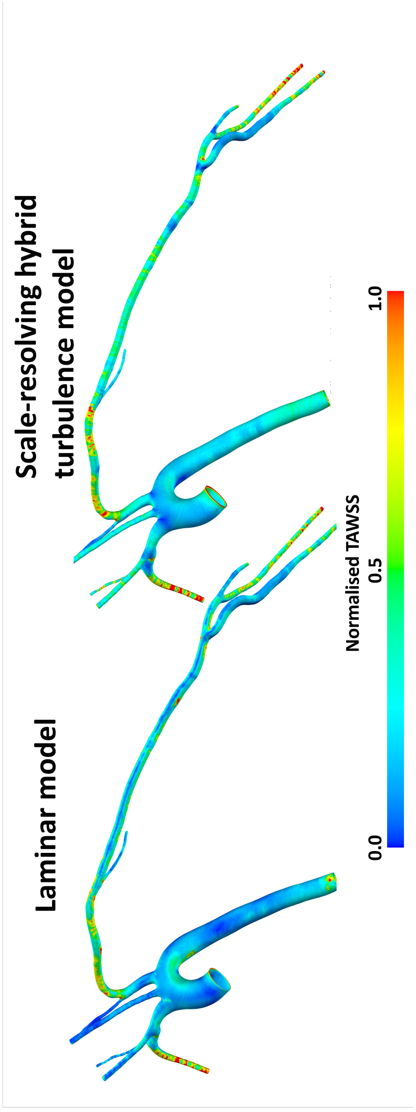

Fig. A.6 Normalised TAWSS contour plots generated using laminar and Scale-resolving hybrid turbulence model in 19-year-old RCF case studied in Chapter 3.

Appendix B

Supplementary material for Chapter 3

B.1 Wall shear stress estimation at inlet computation

The equation for wall shear stress (WSS) is defined as per:

$$\tau = \mu \frac{du}{dy} \tag{B.1}$$

where μ is the viscosity of the fluid, u is the velocity of the fluid, y is the normal distance from the wall.

The velocity profile at the inlet of the domain is defined as being normal to the inlet plane. The profile is assumed to be parabolic, much like flow between two parallel plates, the velocity profile for such a flow (Fig. B1) is defined as per:

$$\frac{u}{u_{max}} = 1 - (\frac{2y}{h})^2 \tag{B.2}$$

where u is the velocity at a given location in the flow, u_{max} is the maximum velocity of the parabolic velocity profile, h is the distance between the assumed plates, and y is the vertical distance from a plate surface.

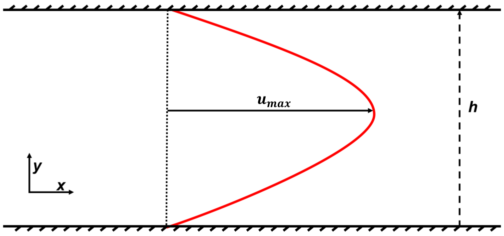

Fig. B.1 Parabolic flow profile between two plates.

In order to input the velocity parameter from Equation B2 into Equation B1, Equation B2 must be differentiated with respect to y. The differential of Equation B2 yields the following:

$$\frac{du}{dy} = \frac{-8u_{max}y}{h^2} \tag{B.3}$$

Substituting Equation B3 into Equation B1 gives the WSS equation (Equation B4) to be used for estimating the WSS at the inlet:

$$\tau = \frac{-8\mu u_{max}y}{h^2} \tag{B.4}$$

Equation B4 is cited in the manuscript, with $y = \frac{h}{2}$ being used for assessing shear stress with regard to maximum flow velocities experienced at peak systole. Background information on this can be found in Katz [303].

B.2 Calculation of initial prism layer height

Based on the desired y+ and the fluid properties, the frictional velocity (u_T), WSS (τ_w), and the skin friction coefficient (C_f) were calculated as per Equations A.30-A.32 for estimating the first prism cell height of the mesh, similarly to Johnston et al. [211] The values computed through the use of Equations A.30-A.32 are given in Table B1.

Table B.1 Values used for the initial hybrid mesh generation

Aortic D (m)	Re (No units)	C_f (No units)	τ_w (Pa)	u_T (m/s)	y (m)
0.0253	4291	0.0130	2.15	0.0451	7.323E-05

B.3 Grid convergence calculation equations

The calculation of the grid convergence index (GCI) between three mesh densities, further elaborated on in Steffen et al.[304], was calculated in this study using Equations A.33-A.36.

The grid convergence study establish a minima of 2 million elements was required for the computational study. The mean convergence value across the 12 locations in the vasculature in each of the cases ranged from 0.978 – 1.01, which was deemed appropriate for the study.
The final mesh characteristics selected for each investigation was validated for the simulations through the computation of the maximum wall y+, Taylor Mirco-, and Kolmogorov length scales for the steady-state RANS simulation (Section B.4).

In all cases, due to the base size of the mesh being less than the Kolmogorov and Taylor scales computed by the RANS simulation, the base size was appropriate. Typically, the Kolmogorov scale gives an over-refinement which could be appropriate for direct numerical simulation (DNS), whereas a base size exceeding the Taylor scale indicates an inappropriate cell size for an SGS model (in LES) to contribute substantially.

B.4 Mesh base size validation

Further to the grid convergence study, the Kolmogorov and Taylor Micro scales [305] were used for ascertaining a reference for the necessary mesh resolution for this study. A precursor RANS steady-state simulation using a uniform peak systole inlet was completed for the pre-AVF study. The calculated base size adhered to the necessary specification determined by the calculation of the Kolmogorov and Taylor mirco scales (Figure B2, Table B2).

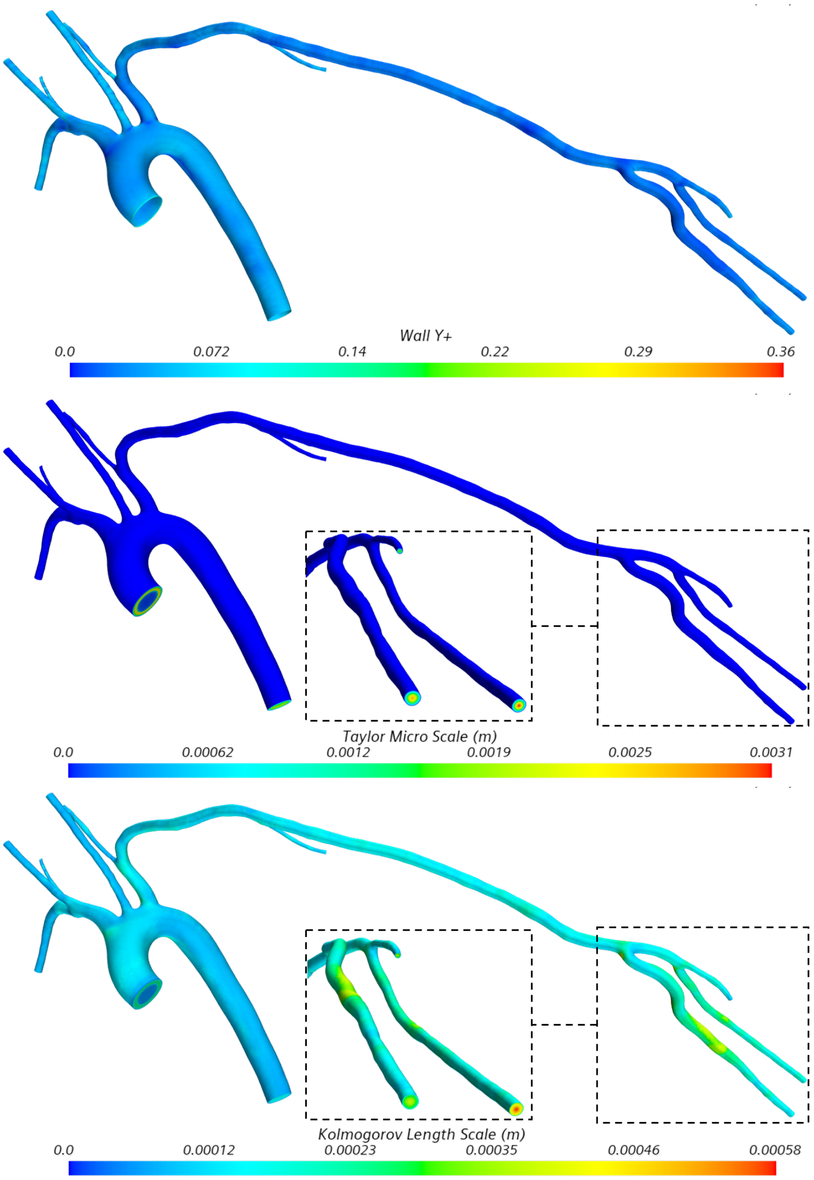

Fig. B.2 Wall Y+, Taylor Mirco scale, and Kolmogorov length scale of the pre-AVF geometry.

Table B.2 Maximum length scale values ascertained from a steady-state RANS simulation using the mesh calculated from performing GCI calculations.

Wall y+	Kolmogorov length scale (m)	Taylor Mirco Scale (m)
0.36	0.00058	0.0031

The calculated and implemented base size of the mesh (3.8E-4m) was considered appropriate, due to the value being less than the maximum Kolmogorov and Taylor mirco scale values. Typically, the Kolmogorov scale gives a mesh refinement appropriate for direct numerical simulation (DNS). The Taylor micro scale gives an upper limit for cell size, where the cell size is inappropriate for the subgrid-scale model.

An example of a selected mesh utilised for the CFD investigations in this paper can be visualised in Figure B3, this example shows the mesh used for the post-AVF simulation.

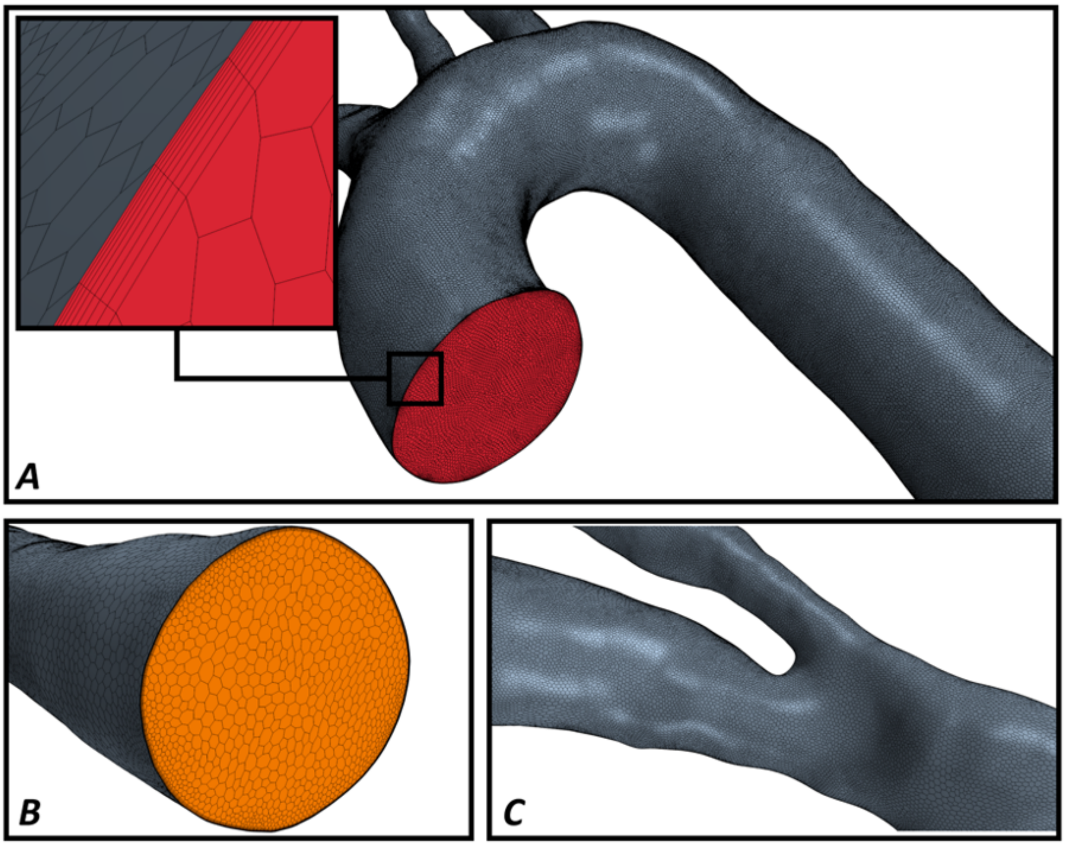

Fig. B.3 Mesh configuration for the post-AVF simulation, where (A) shows the mesh density in the aortic region and at the ascending aorta inlet patch (red), (B) shows the mesh density at the cephalic vein outlet (orange), and (C) shows the mesh density at the anastomosis.

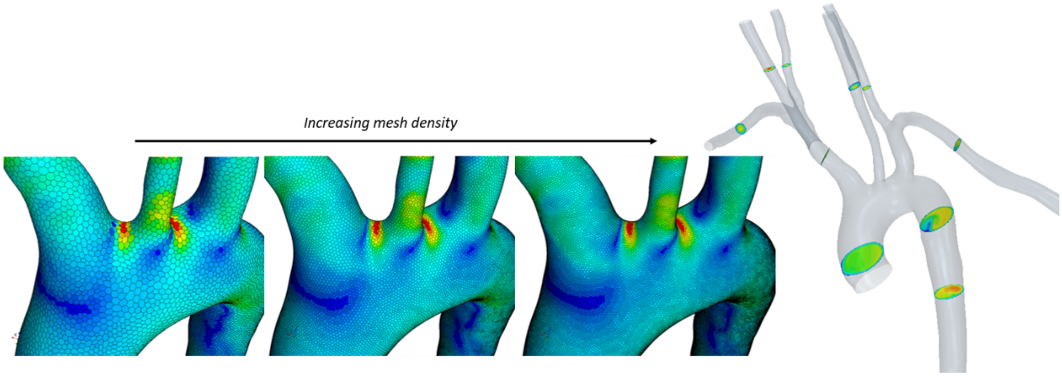

Fig. B.4 Example of increasing mesh density using base size characteristics of the mesh.

B.5 Calculated physiological flow-splits using the ‘splitting method’

The ‘splitting method’ described in Chnafa et al. [222] was used in the pre-AVF study as a comparison for the three-element Windkessel models, which were used for assigning pressure outlet boundary conditions.

The method works by comparing the diameters of daughter vessel branches immediately following a bifurcation. The percentage flow splits of each bifurcation are subsequently summed along each centreline leading to an outlet. Figure B4 demonstrates an example of the cross-sectional areas used for calculating the averaged diameters of each branch, which were then used for generating the ‘flow split’ percentages given in Table B3.

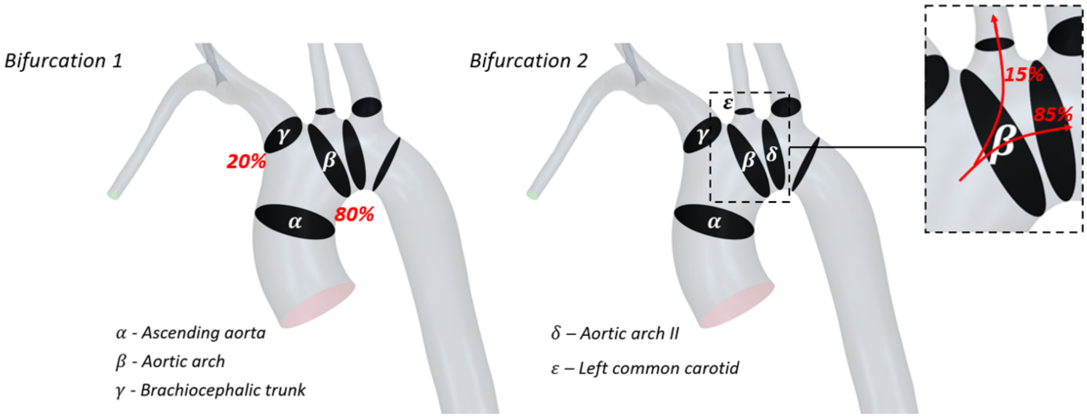

Fig. B.5 Flow-splitting methodology example using daughter vessel bifurcation workflows.

Table B.3 Calculated physiological flow-splits for the pre-AVF case

Outlet	Flow split (% of cardiac input)
Descending aorta (DA)	71.9
Right subclavian (RSA)	6.4
Right vertebral (RVA)	1.8
Right common carotid (RCC)	5.7
Left common carotid (LCC)	5.9
Left vertebral (LVA)	1.8
Left deep brachial (DBA)	0.4
Left radial (LRA)	3.2
Left interosseous (LIA)	1.1
Left ulnar (LUA)	1.8

B.6 Windkessel model information

Windkessel models have been utilised extensively in prior haemodynamic studies. The three-element Windkessel model was proposed in Westerhof et al. (2018) [220], which the reader is advised to refer to for further information.

The information presented herein in this subsection is sourced from Alastruey et al.[223] (2006), which the reader is advised to refer to for further information.

Using the technique described in Alastreuy Arimon (2006), the fluid inertia and resistance, and the wall compliance of the omitted vessels is estimated using scaling laws. The critical assumptions of the method are that the radii and lengths of the neglected vessels remain constant, in addition to the downstream vessels being arranged in a bifurcating tree.

The radii and lengths of successive bifurcation generations are approximated using a geometric series as per:

$$R_1 = \phi R_0 \tag{B.5}$$

$$l_1 = \lambda l_0 \tag{B.6}$$

where R_0 is the terminal vessel radius, l_0 is the terminal artery length, R_1 is the daughter vessel radii, l_1 is the length of the two daughter vessels, and ϕ and λ are scaling factors.

Generalising for an n^{th} bifurcation, we can say:

$$R_n = \phi R_{n-1} \tag{B.7}$$

$$l_n = \lambda l_{n-1} \tag{B.8}$$

where R_n and l_n are the radius and length of each 2^n vessels after n^{th} bifurcation. This results in the following:

$$R_n = \phi^n R_0 \tag{B.9}$$

$$l_n = \lambda^n l_0 \tag{B.10}$$

The value of ϕ and λ can be ascertained by assuming the following conditions:

- Radius of each vessel decreases after each bifurcation ($\phi < 1$)
- Length of each vessel decreases after each bifurcation ($\lambda < 1$)
- Total cross-sectional area increases after each bifurcation up to capillaries ($2\phi^2 > 1$)
- Total volume decreases after each bifurcation ($2\lambda\phi^2 < 1$)
- Total lateral surface increases after each bifurcation ($2\lambda\phi > 1$)

The last two conditions seek to provide perfusion with a small vessel volume and large lateral surface. Figure B5 shows these conditions plotted with respect to ϕ and λ. The shaded section contains the valid ϕ and λ values that satisfy all constraints. This is useful for ascertaining a prediction of λ as the value of $\phi = \sqrt{0.6}$. The values that satisfy a pair of ϕ and λ are therefore bounded by:

$$\frac{1}{2\phi} < \lambda < \frac{1}{2\phi^2} \tag{B.11}$$

The value of used was 0.7, slightly on the higher specified limit. This is specified as a defined value due to the difficultly in changing the value.

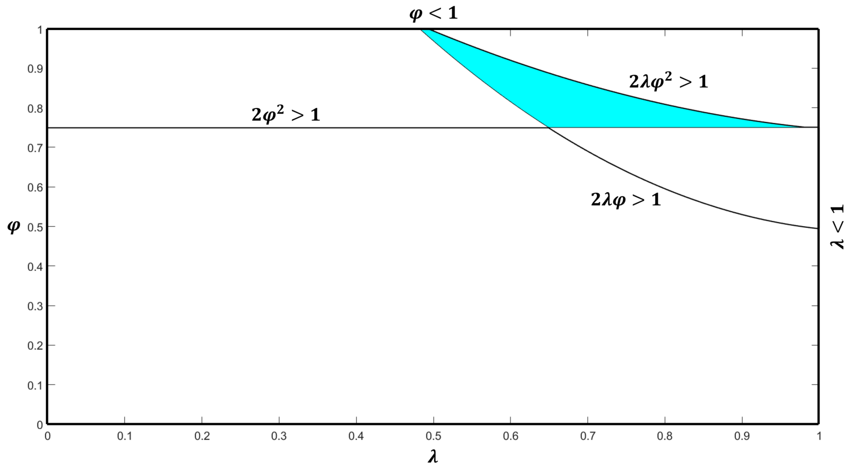

Fig. B.6 Bounds for φ and λ that satisfy the estimation of windkessel parameters methodology documented in Alastruey Arimon (2006).

Resistance

Assuming Poiseuille's flow, pressure gradient in each vessel after n^{th} bifurcation (Δp_n), is related to the flow rate (Q_n) as per:

$$\Delta p_n = \frac{8\mu l_n}{\pi(R_n)^4} Q_n \tag{B.12}$$

With Poiseuille's flow approximating the pulsatile flow, an assumption is made that the flow rate is the same in each of the 2^n vessels, meaning that $Q_n = \frac{Q_0}{2}$, where Q_0 is the mean flow at the outlet of the terminal artery. Through substitution, the value of Δp_n can be ascertained as per:

$$\Delta p_n = (\frac{\lambda}{2\phi^4})^n \frac{8\mu l_n}{\pi(R_n)^4} Q_n = (\frac{\lambda}{2\phi^4})^n \Delta p_0 \tag{B.13}$$

with Δp_0 is the mean pressure gradient at the terminal artery.

We can then ascertain an estimate for the the distal resistance of a vessel. This is due to pressure being proportional to the resistance ($R = \frac{\Delta p}{Q}$), and assuming $\frac{\lambda}{2\phi^4})^n < 1$, we can state:

$$R = (\frac{\lambda}{2\phi^4 - \lambda})R_0 \tag{B.14}$$

The values of R_0 used for each terminal artery were calculated as per:

$$R_0 = \frac{\rho l_0}{A_0} \tag{B.15}$$

where ρ is fluid density, l_0 is the length of the terminal artery, and A_0 is the terminal cross-sectional area.

Compliance

The assumption of c_n (pulse wave velocity) being proportional to $A_n^{-1/4}$ (where A is area) is made. As such:

$$c_n = \phi^{-n/2} c_0 \tag{B.16}$$

The compliance of the vessel after n^{th} bifurcation is given by:

$$C_n = \frac{A_n l_n}{\rho (c_n)^2} \tag{B.17}$$

where C is compliance, A is cross-sectional area, l is vessel length, and c is pulse wave velocity.

Though substitution we can obtain:

$$C_n = (\lambda \phi^3)^n C_0 \tag{B.18}$$

As $C_0 = \frac{A_0 l_0}{\rho (c_0)^2}$, and since $\phi < 1$, $2\phi^2 < 1$, then $2\phi^3 < 1$, and C_T converges to:

$$C = \frac{2\phi^3}{1 - 2\phi^3} C_0 \tag{B.19}$$

Initial C_0 values were inferred from literature.

B.6.1 Windkessel models

In order to prescribe realistic network pressures to the outlets of the arterial system in Chapter 4, zero-dimensional windkessel models were coupled to the pressure outlets of the CFD simulation. Despite characteristically overestimating compliance, the widely-used three-element windkessel model (Equation X) was implemented. The capacitive (C) and resistance (R) parameters in this model account for the compliance of the terminal artery and the peripheral resistance downstream of the terminal branch respectively, the characteristic impedance element (Z) represents the resistance of the terminal branch where it is located.

$$\frac{\partial p_d}{\partial t} + \frac{p_d}{RC} = \frac{Q}{C} \tag{B.20}$$

Due to the windkessel models being frequently used for time-discretised CFD studies, it is advantageous to also discretise windkessel models in the time-domain (Equations X-x). The implicit time discretisation of the three-element windkessel gives the formation of an equation for pressure at the following timestep (Equation X).

$$\frac{p^{n+1} - p}{\Delta t} + \frac{p^{n+1}}{RC} = \frac{f(Q)}{C} \tag{B.21}$$

In order to simplify the discretisation, the term f(Q) (Equation X) is introduced for the right hand side of the equation.

$$f(Q) = Q(1 + \frac{Z_C}{R}) + Z_C C \frac{dQ}{dt} \tag{B.22}$$

Using this term, and letting $\beta = \frac{RC}{\Delta t}$, we can define and use the 3-element Windkessel model as per Equation X.

$$p^{n+1} = \frac{\beta p^n + Q^{n+1}(R + Z(1+\beta)) - Z\beta Q^n}{1+\beta} \tag{B.23}$$

Where τ=RC, p is pressure at the current timestep, p^{n+1} is pressure at the next timestep, Q is volumetric flowrate at the current timestep, Δt is the timestep, R is the characteristic resistance, C is the characteristic capacitance, Z_C is the characteristics impedence.

The discretisation of the 3-element windkessel model (Equation X) was verified through comparing the pressure waveform generated using velocity waveforms in the Haemod virtual patient database (haemod.uk). Moreover, the implementation of the discretisation was assessed in three software; Mircosoft Excel, Simcenter AMESim (a 0D and 1D modelling software), and Simcenter STAR-CCM+. The CFD simulation in STAR-CCM+ used a straight cylindrical tube of the same diameter as the Haemod virtual dataset. The maximum percentage difference between the differing implementations and the Haemod data was 0.1% after 3 cardiac cycles. This test also established that a minima of three cardiac cycles was required to initialise the computational domain to the desired arterial pressures before results of the 'actual' CFD simulation could be gathered. As such, the fifth cardiac cycle computed was the cycle analysed in Windkessel-based simulations, as this ensured the windkessel models produced correct values.

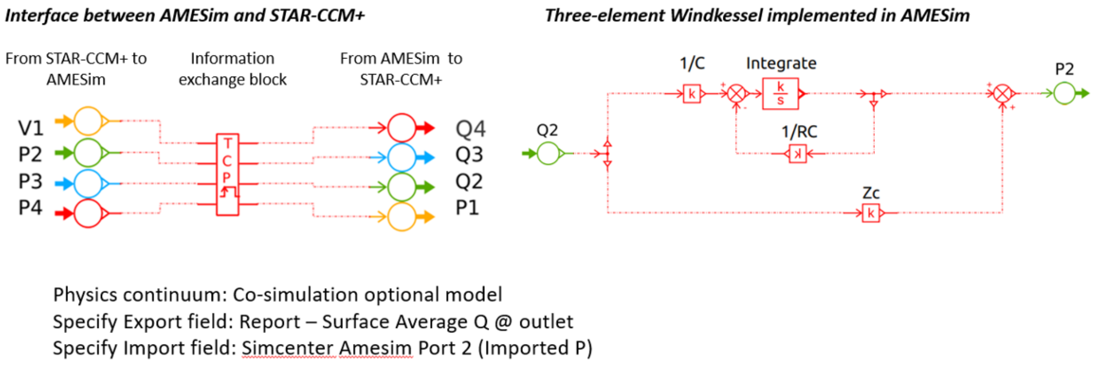

Physics continuum: Co-simulation optional model
Specify Export field: Report – Surface Average Q @ outlet
Specify Import field: Simcenter Amesim Port 2 (Imported P)

Fig. B.7 Implementation of windkessel model in Simcenter Amesim.

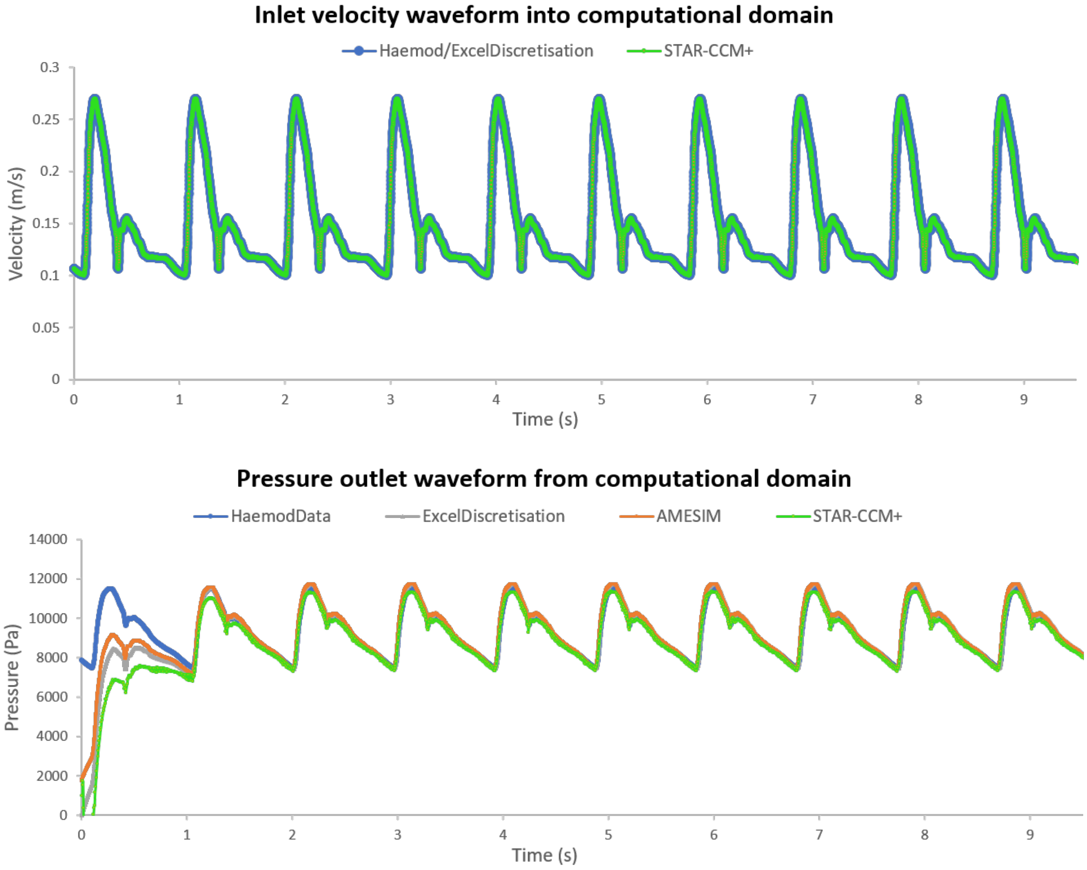

Fig. B.8 Pressure waveforms over cardiac cycles for cylindrical tube simulation for validating windkessel discretisation in Simcenter Amesim and STAR-CCM+

A crucial assumption made regarding the implementation of windkessel models as boundary conditions are the values given to the impedance, capacitance and resistive elements. These values are dependent on the artery's characteristics in addition to the downstream vasculature. The values used in this study are obtained through predictions of the pulse wave velocity in various parts of the vasculature network.

Estimation of windkessel parameters

The methodology utilised in this research for estimating windkessel parameters is sourced from Alastruey Arimon (2006) [223], using Equations B.24-B.27.
The characteristic impedance Z and capacitance C_0 of each terminal artery is ascertained using Equations B.24-B.25 respectively.

$$Z = \frac{\rho_f c_d}{A_d} \tag{B.24}$$

$$C_0 = \frac{A_d L}{\rho \left(c_d\right)^2} \tag{B.25}$$

where L, c_d, and A_d are the vessel length, pulse wave velocity (PWV) and vessel area at diastolic pressure, respectively.

The values of C_0 and Z are both used in the calculation of R and C, as per Equations B.26-B.27.

$$R = \left(\frac{1}{1-\frac{\lambda}{2\varphi^4}} - 1\right) Z = \left(\frac{\lambda}{2\varphi^4 - \lambda}\right) Z \tag{B.26}$$

$$C = \sum C_{T_n} = \left(\frac{1}{1-2\lambda\varphi^3} - 1\right) C_0 = \left(\frac{2\lambda\varphi^3}{1-2\lambda\varphi^3}\right) C_0 \tag{B.27}$$

where λ and φ are constants. The value of φ has been proposed to be $\sqrt{0.6}$ [306], based on the data of Avolio (1980) [307] and Suwa et al. (1963) [308]. The value of λ selected for this study was 0.7, slightly on the lower side of the criterion specified for this method [223]:

$$\frac{1}{2\varphi} < \lambda < \frac{1}{2\varphi^2} \tag{B.28}$$

B.7 Calculated windkessel values in proximal-to-fistula study

The values calculated for the Windkessel models in the pre- and post-AVF haemodynamic study (Table B4) were calculated using the methodology proposed in Alastruey et al.[223] (2006). These values are the same for pre- and post-AVF, the only exception being the radial artery outlet in the post-AVF case, where a flow waveform was assigned using phase-contrast data. The use of these windkessel parameters is demonstrated in the contour plots of normalised pressure ($\frac{P}{0.5\rho}$) at peak systole (Figure B7), where P is pressure and ρ is fluid density.

Table B.4 Calculated Windkessel values for proximal-to-fistula case

Outlet	R $*10^{10}$ $(Pa.s.m^{-}3)$	C $*10^{-10}$ $(m^3.Pa^{-}1)$	Z $*10^{9}$ $(Pa.s.m^{-}3)$
Descending aorta (DA)	0.02	5.040	0.03
Right subclavian (RSA)	0.24	0.256	0.41
Right vertebral (RVA)	0.85	0.205	1.45
Right common carotid (RCC)	0.30	0.523	5.13
Left common carotid (LCC)	0.23	0.978	4.01
Left vertebral (LVA)	0.85	0.204	1.45
Left deep brachial (DBA)	2.22	0.044	3.81
Left radial (LRA)*	0.45	0.602	0.77
Left interosseous (LIA)	1.73	0.057	2.97
Left ulnar (LUA)	1.00	0.215	1.71

* modified in the post-AVF simulation as described in the paper and in following section.

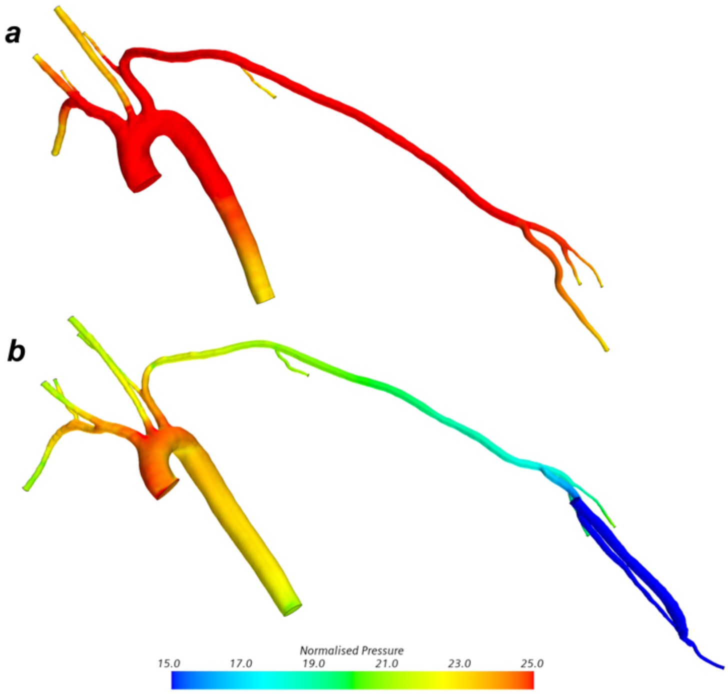

Fig. B.9 Normalised pressure figure at peak-systole for (a) pre- and (b) post-AVF case, where normalised pressure is calculated through dividing pressure by half of the fluid density ($\frac{P}{0.5\rho}$).

B.8 Phase-contrast waveforms assigned to draining vessels in the post-AVF case

Fig. B8 displays an annotated version of the post-AVF domain for reference. The pre-AVF case omits the cephalic vein and the distal parts of the radial artery (as per Figure 1 in the paper).

In the post-AVF simulation, phase-contrast flow waveforms were applied at the radial artery and cephalic vein outlets. These are displayed in Figure B9 as ‘Draining artery FeMRA’ and ‘Draining vein FeMRA’ respectively.

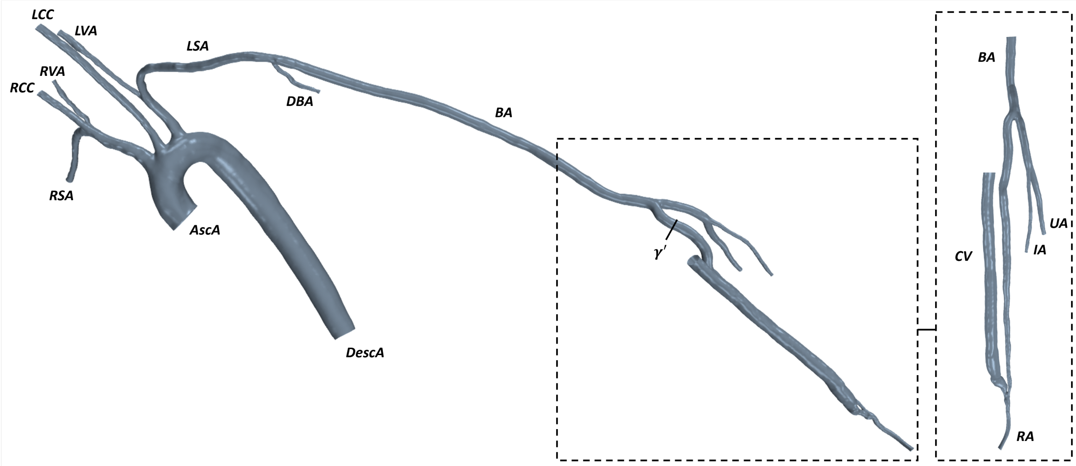

Fig. B.10 Annotated post-AVF geometry, where AscaA - Ascending aorta, DescA - Descending aorta, RSA - Right subclavian artey, RCC - Right common carotid, RVA - Right vertebral artery, LCC - Left common carotid, LVA - Left vertebral artery, LSA - Left subclavian artery, DBA - Deep brachial artery, BA - Brachial artery, RA - Radial artery, IA - Interosseous artey, UA - Ulnar artery, CV - Cephalic vein, γ’ is the feeding artery phase-contrast scan location.

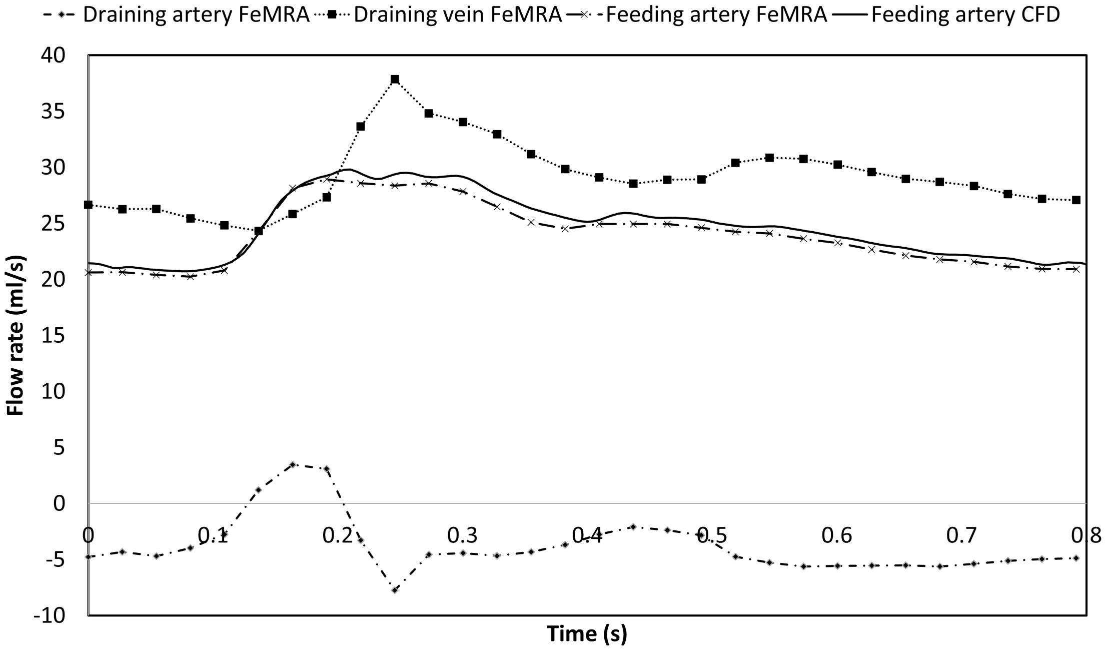

Fig. B.11 Phase-contrast waveforms ascertained through FeMRA scanning, in addition to flow obtained through CFD simulation at feeding artery cross section (γ' in Fig. B8)

B.9 Non-Newtonian Blood model

A non-Newtonian generalised Carreau-Yasuda model [295, 296] was used for approximating the properties of blood in the simulations; as per:

$$\mu(\dot{\gamma}) = \mu_\infty + (\mu_0 - \mu_\infty)(1 + (\lambda\dot{\gamma})^a)^{(n-1)/a} \tag{B.29}$$

where μ is the fluid viscosity, a is the shear-thinning control parameter, λ is the relaxation time, μ_0 is the zero shear viscosity, μ_∞ is the infinite shear viscosity, n is the power constant, and $\dot{\gamma}$ is the shear rate. The parameters used in the simulations were as follows: a = 0.5, λ = 46.5/s, μ_0 = 150mPas, μ_∞ = 3.5mPas, n = 0.342.

B.10 Scale-resolving hybrid model

The scale-resolving hybrid (SRH) turbulence model is a hybrid (RANS-LES Reynolds-Averaged Navier-Stokes, Large Eddy Simulation) model which permits the computation of unsteady large-scale turbulence structures whilst having a computational expense similar to that of the RANS models.

As described in the main paper, the equations solved in the SRH model are ascertained using a spatial-temporal filtering; i.e. each variable ϕ is decomposed into a filtered $\overline{\tilde{\phi}}$ and a subfiltered value ϕ' as per:

$$\phi = \overline{\tilde{\phi}} + \phi' \tag{B.30}$$

where ϕ is representative of quantities such as velocity components, pressure, and energy. This is given in the main paper.

The SRH filtering results in transport equations being equivalent to the RANS equations for a large filter time-width, and LES equations for a short filter-width. The decomposed solution variables are input into the Navier-Stokes equations to yield filtered transport equations of mass, momentum, and energy. These transport equations are solved for RANS and LES. The sub-filtered scale stresses are representative of the stress tensor, T_{SFS}, which is modeled as per:

$$T_{SFS} = 2\mu_t S - \frac{2}{3}\rho k_{SFS} I \tag{B.31}$$

where S is the strain rate tensor computed from the resolved velocity field $\overline{\tilde{v}}$, ρ is density, k_{SFS} is subfilter scale turbulent kinetic energy, I is the identity tensor. Turbulent eddy viscosity μ_t is defined by the respective RANS model and is a function of the turbulent time scale and kinetic energy.
The mean strain rate (S) is given by:

$$S = \frac{1}{2}(\nabla\overline{v} = \nabla\overline{v}^T) \tag{B.32}$$

where $\overline{v}$ is the mean velocity.

For more information regarding the SRH model utilsied in this study, the reader is referred to Duffal et al. (2019) [218].

B.11 Resource required for the workflow

The resource required for completing segmentation and meshing, and the computational resource required for CFD simulation are given in Table 6. These times were ascertained in a '2nd run through' by an experienced user of the softwares.

B.12 Boolean methodologies implemented within Meshmixer

The Boolean methods mentioned in the text refer to the use of Boolean union techniques in Meshmixer (Autodesk Meshmixer, https://www.meshmixer.com/). Boolean composition tools in Meshmixer permit a structured approach for combining solid geometries. The

Table B.5 Time required for completing the workflow

Task	Time taken (Computational resource)
Segmentation: chest scan	20 mins
Segmentation: upper arm scan	24 mins
Segmentation: lower arm scan	26 mins
Reconstruction and mesh generation	20 mins
CFD simulation (for 4 cardiac cycles)	227 mins (16 processors)
Post-processing	30 mins
Total	347 mins (5 hours 47mins)

three segmentations are combined using logic operations. First the segmentations are aligned at common bifurcations (Fig. B.10). The daughter bifurcations of the common bifurcation are aligned and so that two common points of the same diameter are obtained (Positions 1 and 2 in Fig. B.10). Following this, the angle of the parent bifurcation of the distal segmentation is modified so that all three vessels are aligned. This approach gives 1 degree of freedom in the positioning of the segmentations.

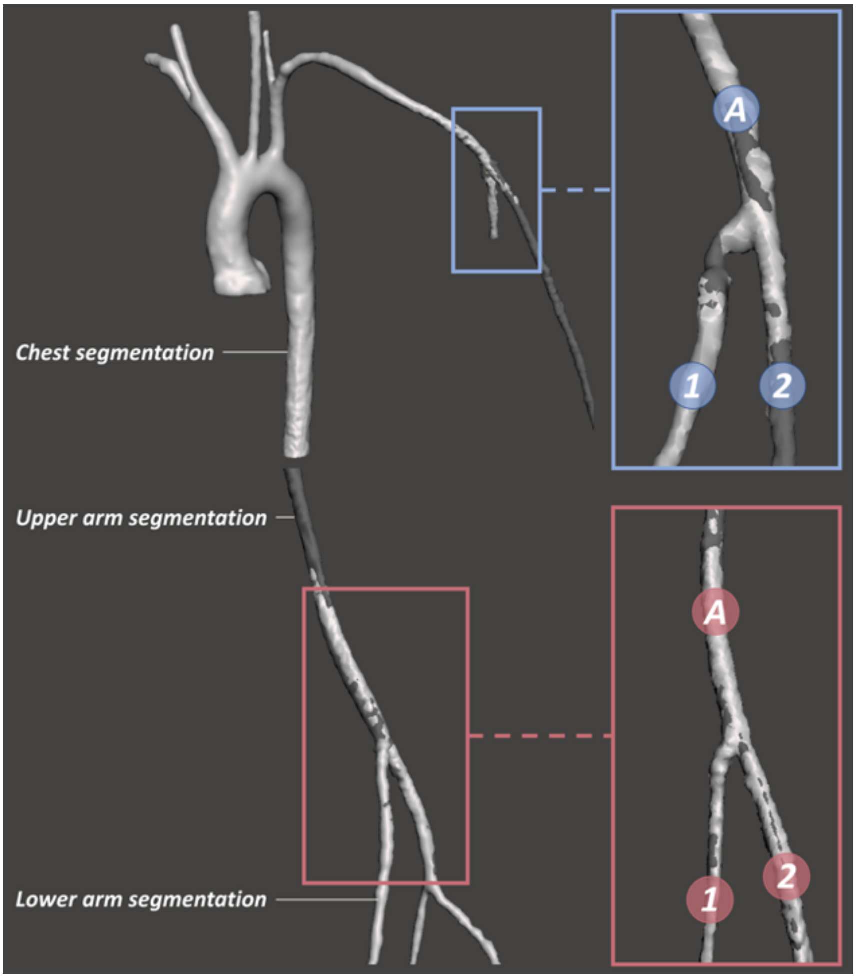

Fig. B.12 Positioning of segmentations for constructing the computational domain. Where the blue labels represent the locations for positioning the upper arm segmentation towards the chest segmentation, and the red label represent the locations for positioning the lower arm segmentation towards the upper arm segmentation. Positions 1 and 2 represent common points between the segmentations of the daughter bifurcations, whereas position A represents a position where the angle of the parent bifurcation is changed so that the segmentations align.

After positioning the segmentations with respect to one another (Fig. B.10), boolean methodologies are utilised for generating the computational domain (Fig. B.11). At the interface between each segmentation, the following mesh-editing steps occur:

- Manual tidy-up of segmentation are completed to remove obvious errors
- A booloean union (also known as 'combine') function is utilised for generating a single geometry comprised of multiple surface
- The surface is homogenised into a surface with uniform mesh density. This is achieved by:

- Ensuring the position of the two surfaces is correct (Fig. B.11Ci)
- More triangles being added to the intersecting region (Fig. B.11Cii)
- Strips of triangles removed from each object (to generate clean boundary loop either side of the intersection). This removes areas not belonging to the result. The open boundaries are matched up to yield the final surface mesh. This step has the effect of 'sliding' the boundaries on the underlying input surfaces (Fig. B.11Ciii)

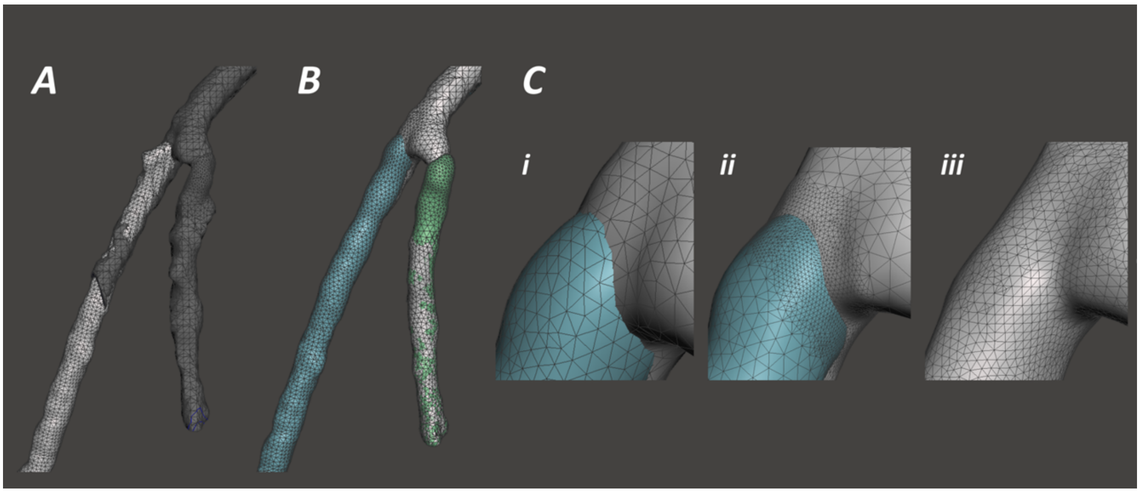

Fig. B.13 The boolean process for generating the surface of the computational domain. Where (A) shows the position of the segmentations, (B) shows the combined segmentation following manual 'clean up' of segmentation, (Ci-iii) shows the boolean process of unifying multiple segmentation surface into a singular computational domain.

Appendix C

Supplementary material for Chapter 4

C.1 Boundary conditions

In Chapter 4, the flow at each inlet and outlet patch was specified using waveforms from phase-contrast data. This is an approach useful for replicating known flow rates and conditions at the inlet and outlets, rather than predicting them.

The flowrates within the AVF vessels were imaged above and below the location of the anastomosis (Fig. C.1). This permitted the inlet and outlet waveforms of the computational models to be assigned for the entire cardiac cycle. The PC-MRI waveform data was extracted using the freely available software Segment version 3.0 R7946 (http://segment.heiberg.se). Within Simcenter STAR-CCM+ the flow waveforms are assigned as mass flow waveforms, which meant converting the flow rates to mass flows using the cross-sectional area of the vessels. One complication of this approach is when the sum total of the outlet waveforms does not equal the inlet waveform mass flow magnitude at each timestep (Fig. C.1).

This can arise due to limitations in the resolution of the PC-MRI. In order to maintain continuity in each simulation, the distal arterial outlet (DAO) was computed as the feeding artery inlet (FAI) minus the distal venous outlet (DVO). This was specified due to the greater visualisation and pixel resolution of the phase-contrast data in the proximal region of the arm. This occurs largely due to vessel cross-sectional area and the flow rates being greater in this region of the arm. Uniform inlets wre used due to the entrace lengths and resolution of the flow waveform inlet profile (Fig, C.2).

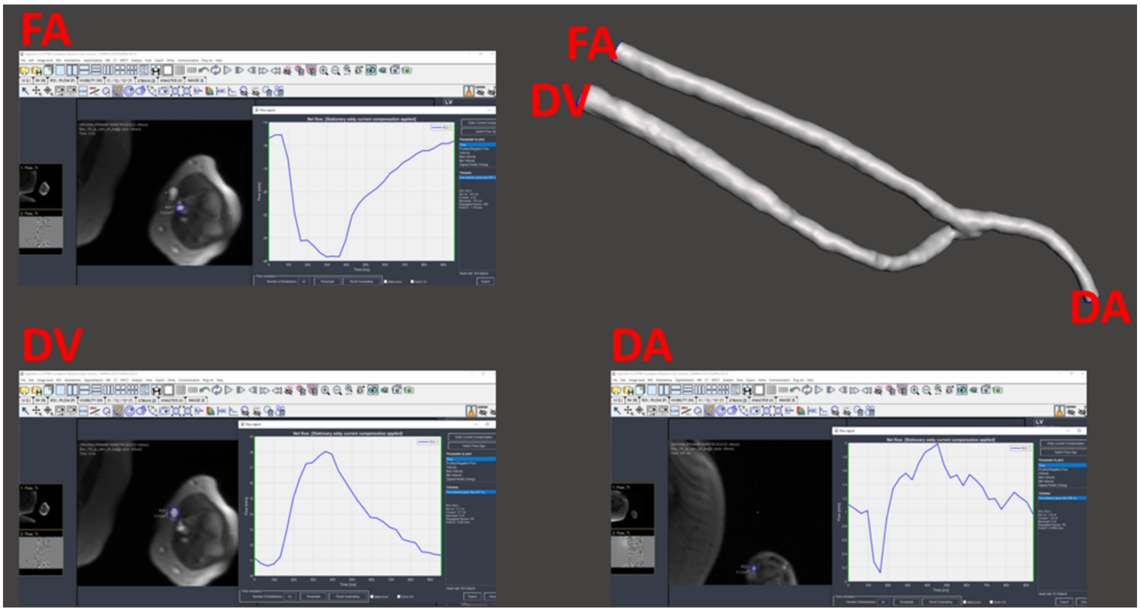

Fig. C.1 Phase contrast waveforms extracted at the point of the AVF vessels (example of case 6 shown).

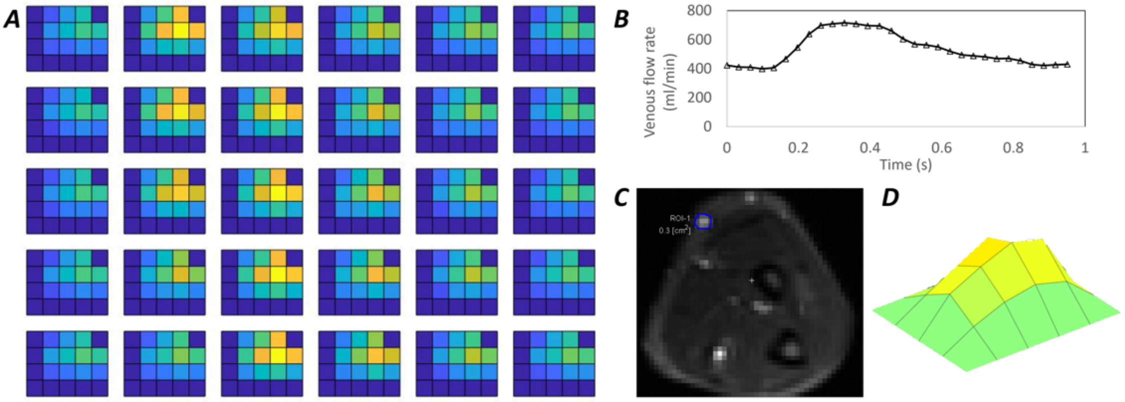

Fig. C.2 Flow waveform profile example from the PC-MRI using FeMRA.

C.2 Mesh independence analysis

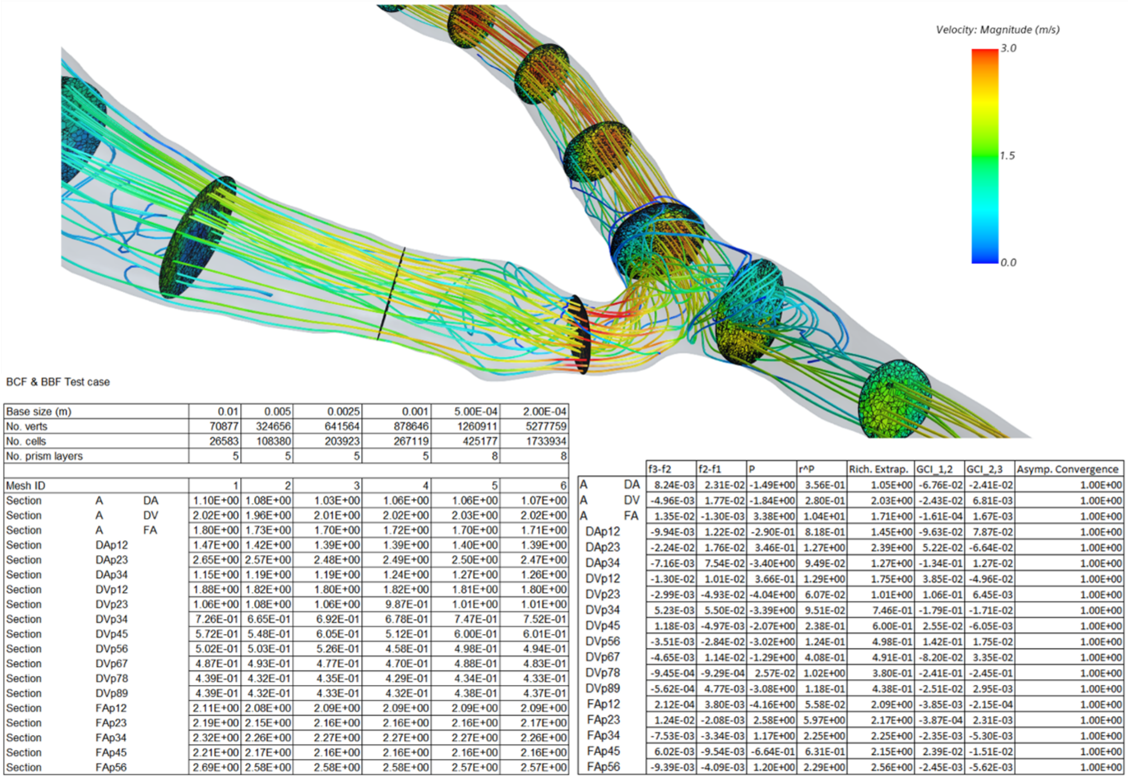

BCF & BBF Test case

Base size (m)			0.01	0.005	0.0025	0.001	5.00E-04	2.00E-04
No. verts			70877	324656	641564	878646	1260911	5277759
No. cells			26583	108380	203923	267119	425177	1733934
No. prism layers			5	5	5	5	8	8
Mesh ID			1	2	3	4	5	6
Section	A	DA	1.10E+00	1.08E+00	1.03E+00	1.06E+00	1.06E+00	1.07E+00
Section	A	DV	2.02E+00	1.96E+00	2.01E+00	2.02E+00	2.03E+00	2.02E+00
Section	A	FA	1.80E+00	1.73E+00	1.70E+00	1.72E+00	1.70E+00	1.71E+00
Section	DAp12		1.47E+00	1.42E+00	1.39E+00	1.39E+00	1.40E+00	1.39E+00
Section	DAp23		2.65E+00	2.57E+00	2.48E+00	2.49E+00	2.50E+00	2.47E+00
Section	DAp34		1.15E+00	1.19E+00	1.19E+00	1.24E+00	1.27E+00	1.26E+00
Section	DVp12		1.88E+00	1.82E+00	1.80E+00	1.82E+00	1.81E+00	1.80E+00
Section	DVp23		1.06E+00	1.08E+00	1.06E+00	9.87E-01	1.01E+00	1.01E+00
Section	DVp34		7.26E-01	6.65E-01	6.92E-01	6.78E-01	7.47E-01	7.52E-01
Section	DVp45		5.72E-01	5.48E-01	6.05E-01	5.12E-01	6.00E-01	6.01E-01
Section	DVp56		5.02E-01	5.03E-01	5.26E-01	4.58E-01	4.98E-01	4.94E-01
Section	DVp67		4.87E-01	4.93E-01	4.77E-01	4.70E-01	4.88E-01	4.83E-01
Section	DVp78		4.39E-01	4.32E-01	4.35E-01	4.29E-01	4.34E-01	4.33E-01
Section	DVp89		4.39E-01	4.32E-01	4.33E-01	4.32E-01	4.38E-01	4.37E-01
Section	FAp12		2.11E+00	2.08E+00	2.09E+00	2.09E+00	2.09E+00	2.09E+00
Section	FAp23		2.19E+00	2.15E+00	2.16E+00	2.16E+00	2.16E+00	2.17E+00
Section	FAp34		2.32E+00	2.26E+00	2.27E+00	2.27E+00	2.27E+00	2.26E+00
Section	FAp45		2.21E+00	2.17E+00	2.16E+00	2.16E+00	2.16E+00	2.16E+00
Section	FAp56		2.69E+00	2.58E+00	2.58E+00	2.58E+00	2.57E+00	2.57E+00

		f3-f2	f2-f1	P	r^P	Rich. Extrap.	GCI_1,2	GCI_2,3	Asymp. Convergence
A	DA	8.24E-03	2.31E-02	-1.49E+00	3.56E-01	1.05E+00	-6.76E-02	-2.41E-02	1.00E+00
A	DV	-4.96E-03	1.77E-02	-1.84E+00	2.80E-01	2.03E+00	-2.43E-02	6.81E-03	1.00E+00
A	FA	1.35E-02	-1.30E-03	3.38E+00	1.04E+01	1.71E+00	-1.61E-04	1.67E-03	1.00E+00
DAp12		-9.94E-03	1.22E-02	-2.90E-01	8.18E-01	1.45E+00	-9.63E-02	7.87E-02	1.00E+00
DAp23		-2.24E-02	1.76E-02	3.46E-01	1.27E+00	2.39E+00	5.22E-02	-6.64E-02	1.00E+00
DAp34		-7.16E-03	7.54E-02	-3.40E+00	9.49E-02	1.27E+00	-1.34E-01	1.27E-02	1.00E+00
DVp12		-1.30E-02	1.01E-02	3.66E-01	1.29E+00	1.75E+00	3.85E-02	-4.96E-02	1.00E+00
DVp23		-2.99E-03	-4.93E-02	-4.04E+00	6.07E-02	1.01E+00	1.06E-01	6.45E-03	1.00E+00
DVp34		5.23E-03	5.50E-02	-3.39E+00	9.51E-02	7.46E-01	-1.79E-01	-1.71E-02	1.00E+00
DVp45		1.18E-03	-4.97E-03	-2.07E+00	2.38E-01	6.00E-01	2.55E-02	-6.05E-03	1.00E+00
DVp56		-3.51E-03	-2.84E-02	-3.02E+00	1.24E-01	4.98E-01	1.42E-01	1.75E-02	1.00E+00
DVp67		-4.65E-03	1.14E-02	-1.29E+00	4.08E-01	4.91E-01	-8.20E-02	3.35E-02	1.00E+00
DVp78		-9.45E-04	-9.29E-04	2.57E-02	1.02E+00	3.80E-01	-2.41E-01	-2.45E-01	1.00E+00
DVp89		-5.62E-04	4.77E-03	-3.08E+00	1.18E-01	4.38E-01	-2.51E-02	2.95E-03	1.00E+00
FAp12		2.12E-04	3.80E-03	-4.16E+00	5.58E-02	2.09E+00	-3.85E-03	-2.15E-04	1.00E+00
FAp23		1.24E-02	-2.08E-03	2.58E+00	5.97E+00	2.17E+00	-3.87E-04	2.31E-03	1.00E+00
FAp34		-7.53E-03	-3.34E-03	1.17E+00	2.25E+00	2.25E+00	-2.35E-03	-5.30E-03	1.00E+00
FAp45		6.02E-03	-9.54E-03	-6.64E-01	6.31E-01	2.15E+00	2.39E-02	-1.51E-02	1.00E+00
FAp56		-9.39E-03	-4.09E-03	1.20E+00	2.29E+00	2.56E+00	-2.45E-03	-5.62E-03	1.00E+00

Fig. C.3 Mesh independence study completed for the BBF and BCF sub-groups. Demonstrated on test case (subject 69).

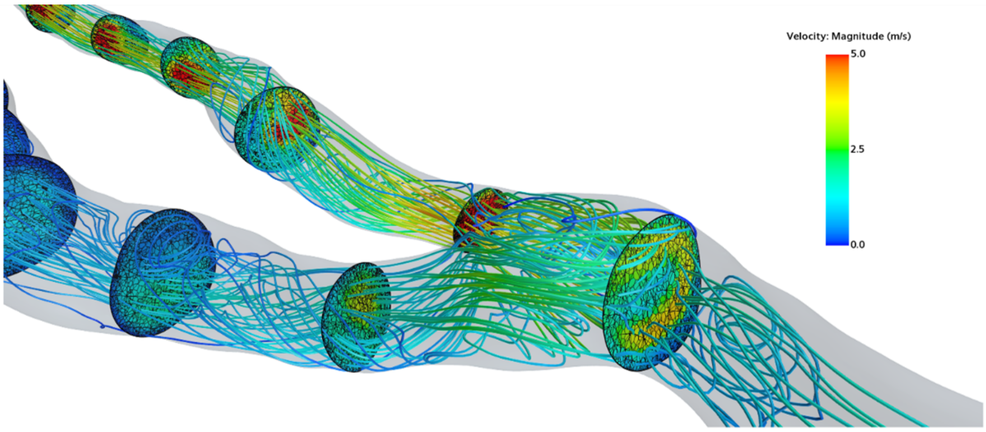

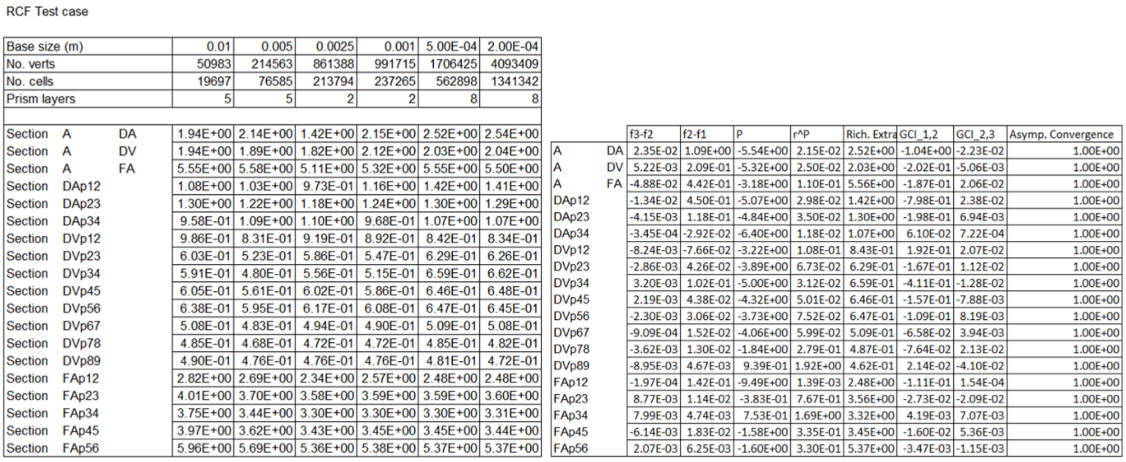
RCF Test case

Base size (m)			0.01	0.005	0.0025	0.001	5.00E-04	2.00E-04
No. verts			50983	214563	861388	991715	1706425	4093409
No. cells			19697	76585	213794	237265	562898	1341342
Prism layers			5	5	2	2	8	8
Section	A	DA	1.94E+00	2.14E+00	1.42E+00	2.15E+00	2.52E+00	2.54E+00
Section	A	DV	1.94E+00	1.89E+00	1.82E+00	2.12E+00	2.03E+00	2.04E+00
Section	A	FA	5.55E+00	5.58E+00	5.11E+00	5.32E+00	5.55E+00	5.50E+00
Section	DAp12		1.08E+00	1.03E+00	9.73E-01	1.16E+00	1.42E+00	1.41E+00
Section	DAp23		1.30E+00	1.22E+00	1.18E+00	1.24E+00	1.30E+00	1.29E+00
Section	DAp34		9.58E-01	1.09E+00	1.10E+00	9.68E-01	1.07E+00	1.07E+00
Section	DVp12		9.86E-01	8.31E-01	9.19E-01	8.92E-01	8.42E-01	8.34E-01
Section	DVp23		6.03E-01	5.23E-01	5.86E-01	5.47E-01	6.29E-01	6.26E-01
Section	DVp34		5.91E-01	4.80E-01	5.56E-01	5.15E-01	6.59E-01	6.62E-01
Section	DVp45		6.05E-01	5.61E-01	6.02E-01	5.86E-01	6.46E-01	6.48E-01
Section	DVp56		6.38E-01	5.95E-01	6.17E-01	6.08E-01	6.47E-01	6.45E-01
Section	DVp67		5.08E-01	4.83E-01	4.94E-01	4.90E-01	5.09E-01	5.08E-01
Section	DVp78		4.85E-01	4.68E-01	4.72E-01	4.72E-01	4.85E-01	4.82E-01
Section	DVp89		4.90E-01	4.76E-01	4.76E-01	4.76E-01	4.81E-01	4.72E-01
Section	FAp12		2.82E+00	2.69E+00	2.34E+00	2.57E+00	2.48E+00	2.48E+00
Section	FAp23		4.01E+00	3.70E+00	3.58E+00	3.59E+00	3.59E+00	3.60E+00
Section	FAp34		3.75E+00	3.44E+00	3.30E+00	3.30E+00	3.30E+00	3.31E+00
Section	FAp45		3.97E+00	3.62E+00	3.43E+00	3.45E+00	3.45E+00	3.44E+00
Section	FAp56		5.96E+00	5.69E+00	5.36E+00	5.38E+00	5.37E+00	5.37E+00

		f3-f2	f2-f1	P	r^P	Rich. Extra	GCI_1,2	GCI_2,3	Asymp. Convergence
A	DA	2.35E-02	1.09E+00	-5.54E+00	2.15E-02	2.52E+00	-1.04E+00	-2.23E-02	1.00E+00
A	DV	5.22E-03	2.09E-01	-5.32E+00	2.50E-02	2.03E+00	-2.02E-01	-5.06E-03	1.00E+00
A	FA	-4.88E-02	4.42E-01	-3.18E+00	1.10E-01	5.56E+00	-1.87E-01	2.06E-02	1.00E+00
DAp12		-1.34E-02	4.50E-01	-5.07E+00	2.98E-02	1.42E+00	-7.98E-01	2.38E-02	1.00E+00
DAp23		-4.15E-03	1.18E-01	-4.84E+00	3.50E-02	1.30E+00	-1.98E-01	6.94E-03	1.00E+00
DAp34		-3.45E-04	-2.92E-02	-6.40E+00	1.18E-02	1.07E+00	6.10E-02	7.22E-04	1.00E+00
DVp12		-8.24E-03	-7.66E-02	-3.22E+00	1.08E-01	8.43E-01	1.92E-01	2.07E-02	1.00E+00
DVp23		-2.86E-03	4.26E-02	-3.89E+00	6.73E-02	6.29E-01	-1.67E-01	1.12E-02	1.00E+00
DVp34		3.20E-03	1.02E-01	-5.00E+00	3.12E-02	6.59E-01	-4.11E-01	-1.28E-02	1.00E+00
DVp45		2.19E-03	4.38E-02	-4.32E+00	5.01E-02	6.46E-01	-1.57E-01	-7.88E-03	1.00E+00
DVp56		-2.30E-03	3.06E-02	-3.73E+00	7.52E-02	6.47E-01	-1.09E-01	8.19E-03	1.00E+00
DVp67		-9.09E-04	1.52E-02	-4.06E+00	5.99E-02	5.09E-01	-6.58E-02	3.94E-03	1.00E+00
DVp78		-3.62E-03	1.30E-02	-1.84E+00	2.79E-01	4.87E-01	-7.64E-02	2.13E-02	1.00E+00
DVp89		-8.95E-03	4.67E-03	9.39E-01	1.92E+00	4.62E-01	2.14E-02	-4.10E-02	1.00E+00
FAp12		-1.97E-04	1.42E-01	-9.49E+00	1.39E-03	2.48E+00	-1.11E-01	1.54E-04	1.00E+00
FAp23		8.77E-03	1.14E-02	-3.83E-01	7.67E-01	3.56E+00	-2.73E-02	-2.09E-02	1.00E+00
FAp34		7.99E-03	4.74E-03	7.53E-01	1.69E+00	3.32E+00	4.19E-03	7.07E-03	1.00E+00
FAp45		-6.14E-03	1.83E-02	-1.58E+00	3.35E-01	3.45E+00	-1.60E-02	5.36E-03	1.00E+00
FAp56		2.07E-03	6.25E-03	-1.60E+00	3.30E-01	5.37E+00	-3.47E-03	-1.15E-03	1.00E+00

Fig. C.4 Mesh independence study completed for the RCF sub-groups. Demonstrated on test case (subject 87).

C.3 Interpolation of data using polynomials for ROC analysis: Separate excluded data

Due to the limited number of datasets in the pilot study, polynomials were used for generating more ‘virtual’ datasets uby interpolating datapoints over he polynomials fitted to the raw datapoins (n=17). The results generated did not differ significantly in the majority of the metrics, however, the assumptions made with the polynomials were not deemed to be appropriate for including the results in the study.

C.3 Interpolation of data using polynomials for ROC analysis: Separate excluded data

Table C.1 Area under curve (AUC) of ROC curves using raw and interpolated data.

Characteristic	**AUC (raw data)**	AUC (interpolated data)
Angle	0.6667	0.787
Draining vein curvature	0.4583	0.7015
Draining artery curvature	0.7014	0.8736
Feeding artery curvature	0.8194	0.8810
Draining vein diameter	0.7361	0.7814
Draining artery diameter	0.7222	0.7632
Feeding artery diameter	0.7639	0.9726
Systolic blood pressure	0.6528	0.7301
Heart rate	0.7014	0.7815
BMI	0.7083	0.7134
Age	0.6042	0.6917

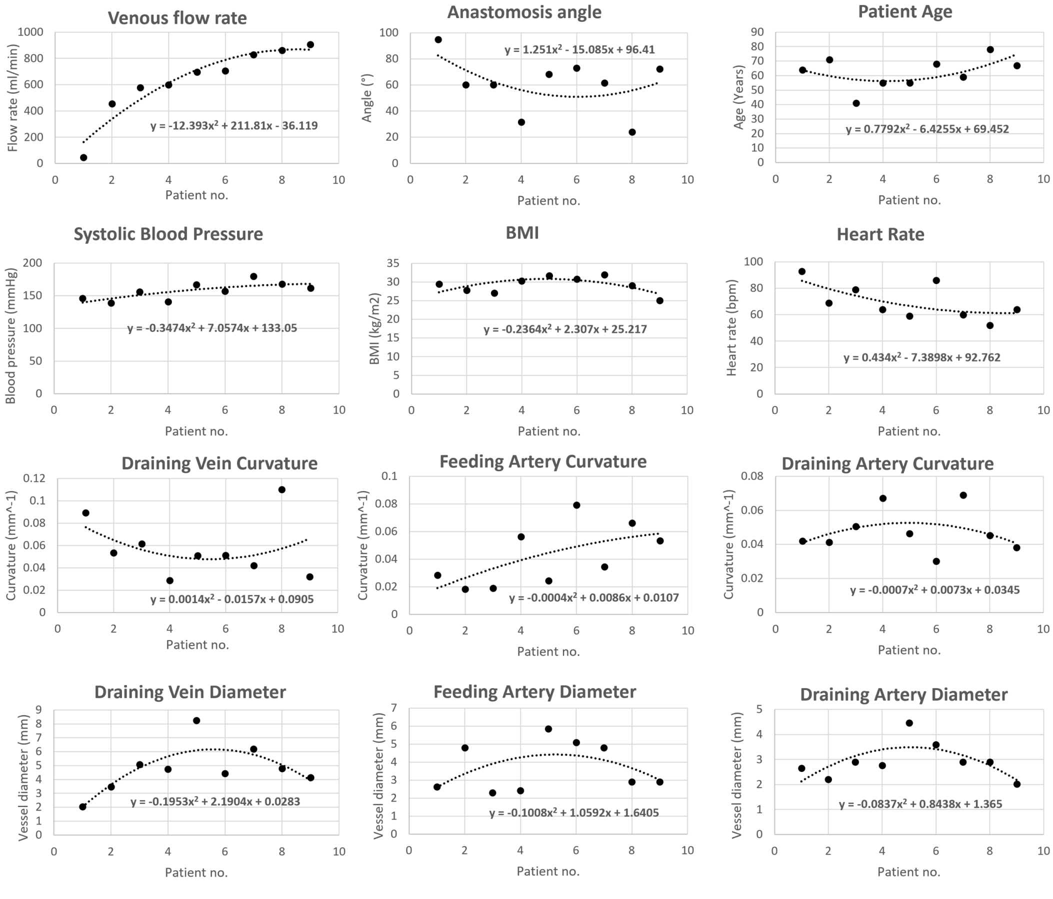

Fig. C.5 Low-flow polynomials fitted to the low-flow (<1000ml/min) datapoints

C.3 Interpolation of data using polynomials for ROC analysis: Separate excluded data

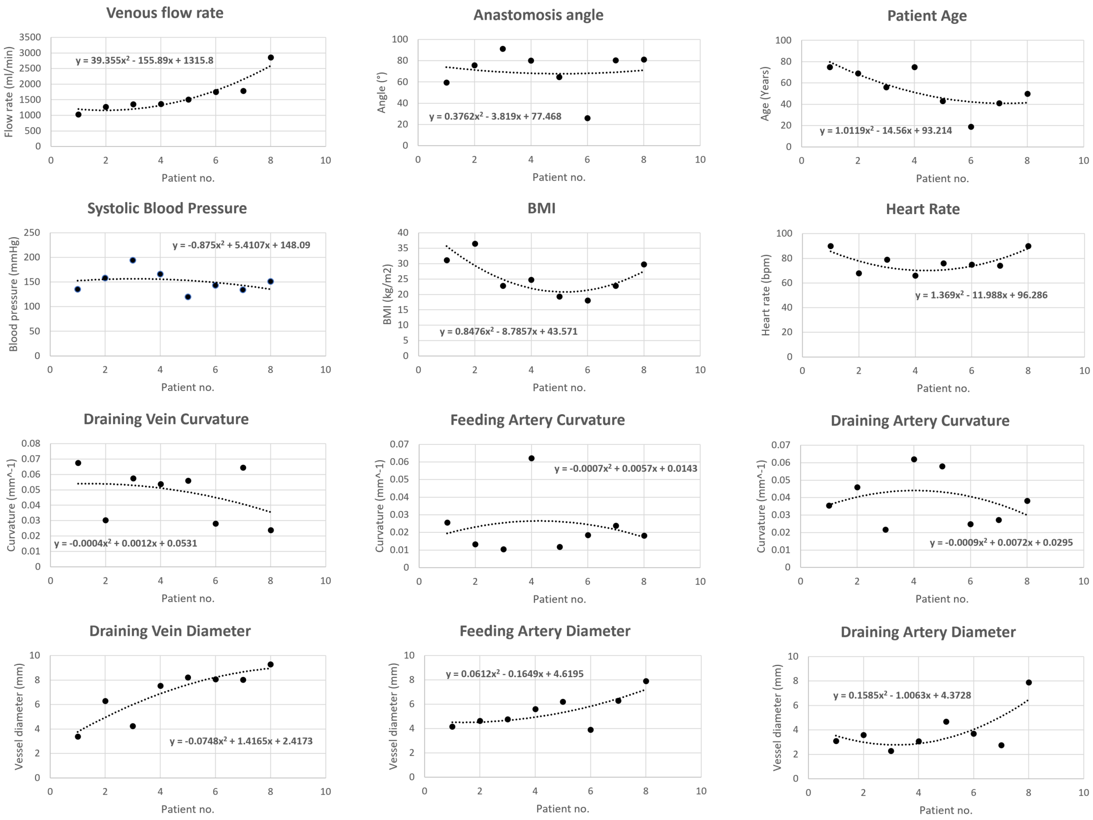

Fig. C.6 High-flow polynomials fitted to the high-flow (>1000ml/min) datapoints

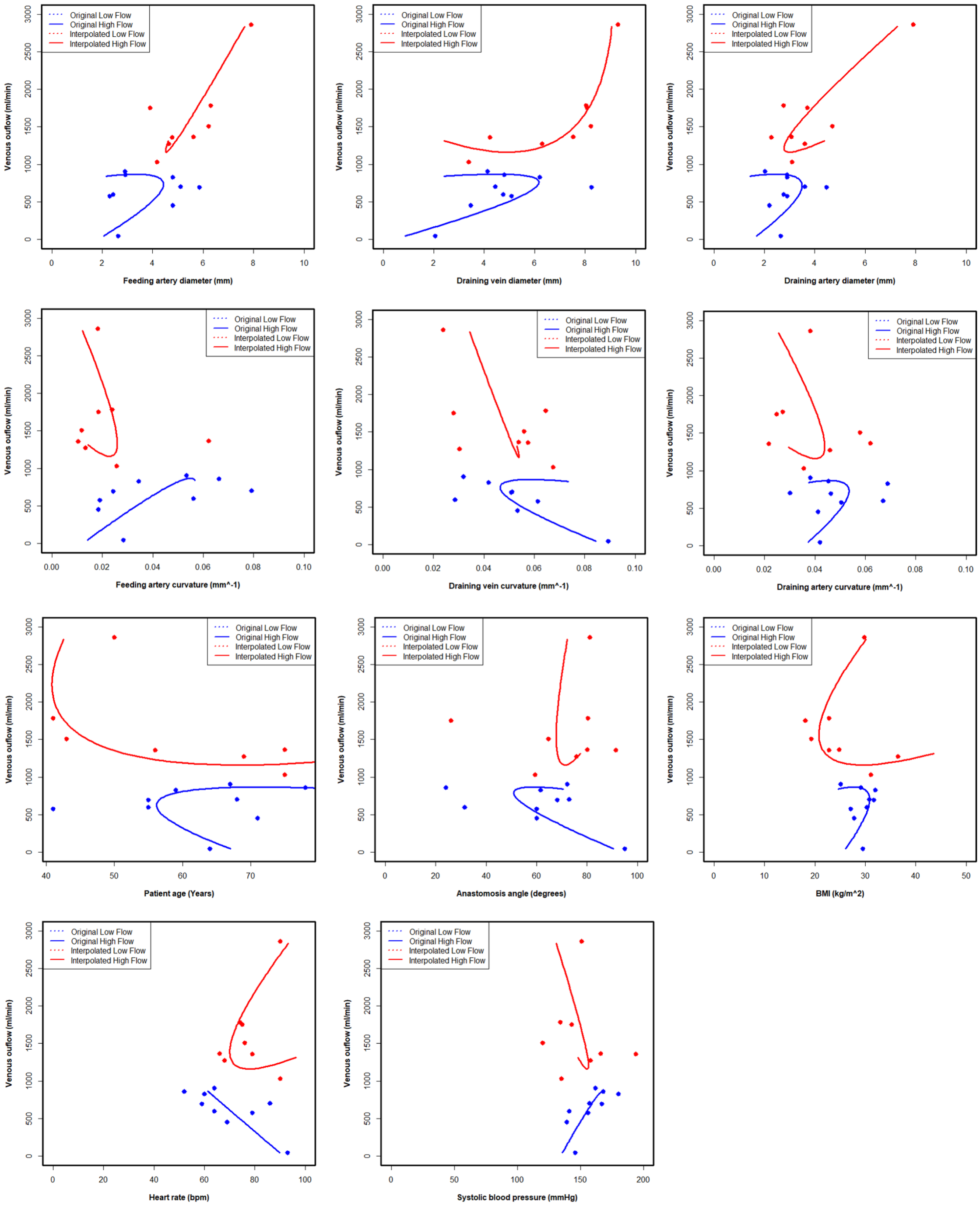

Fig. C.7 Interpolated vs Original dataset datapoints

C.4 Code used for ROC analysis

The lines of code utilised for performing the ROC analysis within R is presented herein.

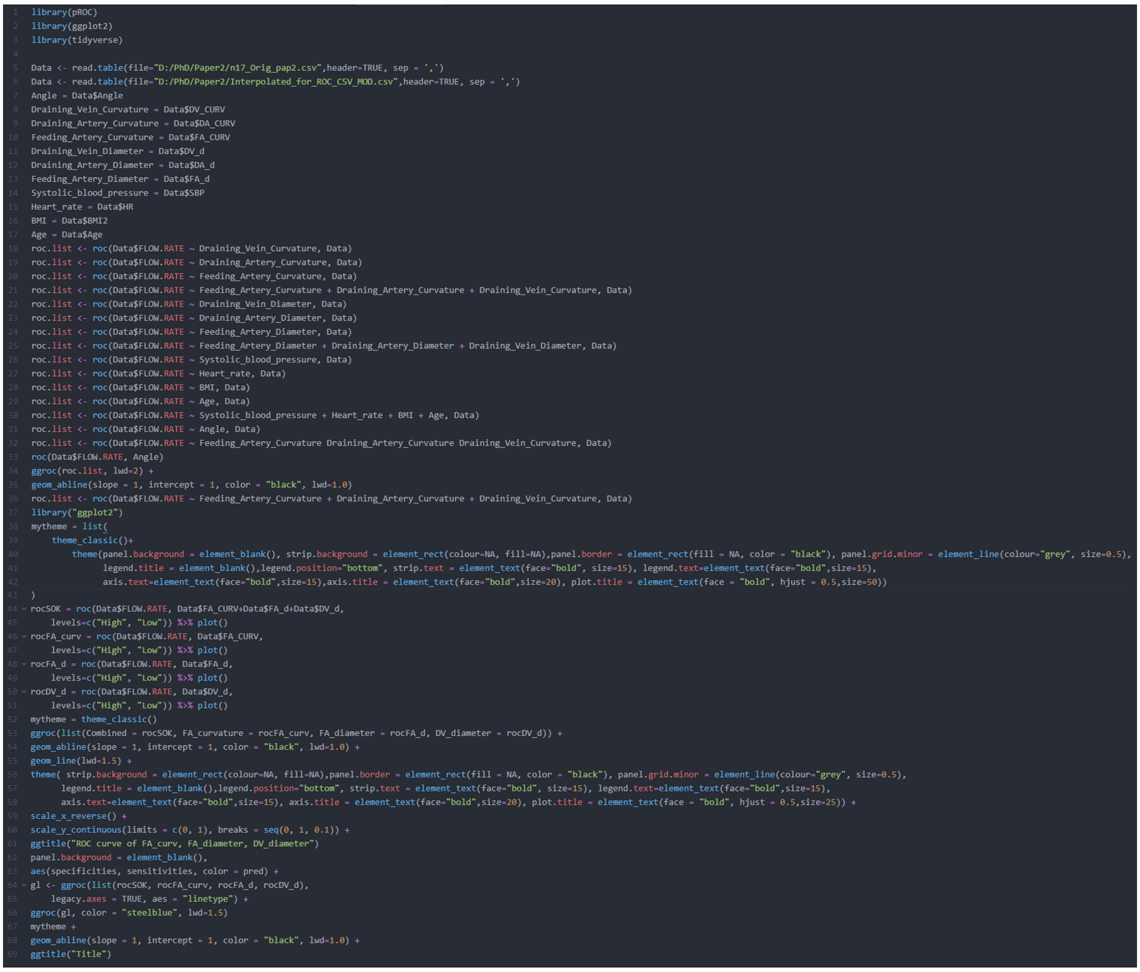

```
library(pROC)
library(ggplot2)
library(tidyverse)

Data <- read.table(file="D:/PhD/Paper2/n17_Orig_pap2.csv",header=TRUE, sep = ',')
Data <- read.table(file="D:/PhD/Paper2/Interpolated_for_ROC_CSV_MOD.csv",header=TRUE, sep = ',')
Angle = Data$Angle
Draining_Vein_Curvature = Data$DV_CURV
Draining_Artery_Curvature = Data$DA_CURV
Feeding_Artery_Curvature = Data$FA_CURV
Draining_Vein_Diameter = Data$DV_d
Draining_Artery_Diameter = Data$DA_d
Feeding_Artery_Diameter = Data$FA_d
Systolic_blood_pressure = Data$SBP
Heart_rate = Data$HR
BMI = Data$BMI2
Age = Data$Age
roc.list <- roc(Data$FLOW.RATE ~ Draining_Vein_Curvature, Data)
roc.list <- roc(Data$FLOW.RATE ~ Draining_Artery_Curvature, Data)
roc.list <- roc(Data$FLOW.RATE ~ Feeding_Artery_Curvature, Data)
roc.list <- roc(Data$FLOW.RATE ~ Feeding_Artery_Curvature + Draining_Artery_Curvature + Draining_Vein_Curvature, Data)
roc.list <- roc(Data$FLOW.RATE ~ Draining_Vein_Diameter, Data)
roc.list <- roc(Data$FLOW.RATE ~ Draining_Artery_Diameter, Data)
roc.list <- roc(Data$FLOW.RATE ~ Feeding_Artery_Diameter, Data)
roc.list <- roc(Data$FLOW.RATE ~ Feeding_Artery_Diameter + Draining_Artery_Diameter + Draining_Vein_Diameter, Data)
roc.list <- roc(Data$FLOW.RATE ~ Systolic_blood_pressure, Data)
roc.list <- roc(Data$FLOW.RATE ~ Heart_rate, Data)
roc.list <- roc(Data$FLOW.RATE ~ BMI, Data)
roc.list <- roc(Data$FLOW.RATE ~ Age, Data)
roc.list <- roc(Data$FLOW.RATE ~ Systolic_blood_pressure + Heart_rate + BMI + Age, Data)
roc.list <- roc(Data$FLOW.RATE ~ Angle, Data)
roc.list <- roc(Data$FLOW.RATE ~ Feeding_Artery_Curvature Draining_Artery_Curvature Draining_Vein_Curvature, Data)
roc(Data$FLOW.RATE, Angle)
ggroc(roc.list, lwd=2) +
geom_abline(slope = 1, intercept = 1, color = "black", lwd=1.0)
roc.list <- roc(Data$FLOW.RATE ~ Feeding_Artery_Curvature + Draining_Artery_Curvature + Draining_Vein_Curvature, Data)
library("ggplot2")
mytheme = list(
    theme_classic()+
        theme(panel.background = element_blank(), strip.background = element_rect(colour=NA, fill=NA),panel.border = element_rect(fill = NA, color = "black"), panel.grid.minor = element_line(colour="grey", size=0.5),
              legend.title = element_blank(),legend.position="bottom", strip.text = element_text(face="bold", size=15), legend.text=element_text(face="bold",size=15),
              axis.text=element_text(face="bold",size=15),axis.title = element_text(face="bold",size=20), plot.title = element_text(face = "bold", hjust = 0.5,size=50))
)
rocSOK = roc(Data$FLOW.RATE, Data$FA_CURV+Data$FA_d+Data$DV_d,
    levels=c("High", "Low")) %>% plot()
rocFA_curv = roc(Data$FLOW.RATE, Data$FA_CURV,
    levels=c("High", "Low")) %>% plot()
rocFA_d = roc(Data$FLOW.RATE, Data$FA_d,
    levels=c("High", "Low")) %>% plot()
rocDV_d = roc(Data$FLOW.RATE, Data$DV_d,
    levels=c("High", "Low")) %>% plot()
mytheme = theme_classic()
ggroc(list(Combined = rocSOK, FA_curvature = rocFA_curv, FA_diameter = rocFA_d, DV_diameter = rocDV_d)) +
geom_abline(slope = 1, intercept = 1, color = "black", lwd=1.0) +
geom_line(lwd=1.5) +
theme( strip.background = element_rect(colour=NA, fill=NA),panel.border = element_rect(fill = NA, color = "black"), panel.grid.minor = element_line(colour="grey", size=0.5),
      legend.title = element_blank(),legend.position="bottom", strip.text = element_text(face="bold", size=15), legend.text=element_text(face="bold",size=15),
      axis.text=element_text(face="bold",size=15), axis.title = element_text(face="bold",size=20), plot.title = element_text(face = "bold", hjust = 0.5,size=25)) +
scale_x_reverse() +
scale_y_continuous(limits = c(0, 1), breaks = seq(0, 1, 0.1)) +
ggtitle("ROC curve of FA_curv, FA_diameter, DV_diameter")
panel.background = element_blank(),
aes(specificities, sensitivities, color = pred) +
gl <- ggroc(list(rocSOK, rocFA_curv, rocFA_d, rocDV_d),
    legacy.axes = TRUE, aes = "linetype") +
ggroc(gl, color = "steelblue", lwd=1.5)
mytheme +
geom_abline(slope = 1, intercept = 1, color = "black", lwd=1.0) +
ggtitle("Title")
```

Fig. C.8 ROC code used for vessel curvature, diameter, patient characteristics, and anastomosis angle. Note: Lines included which are commented out during running the code for various characteristics.

C.5 Vessel diameter and velocity waveforms applied at the computational domain patches

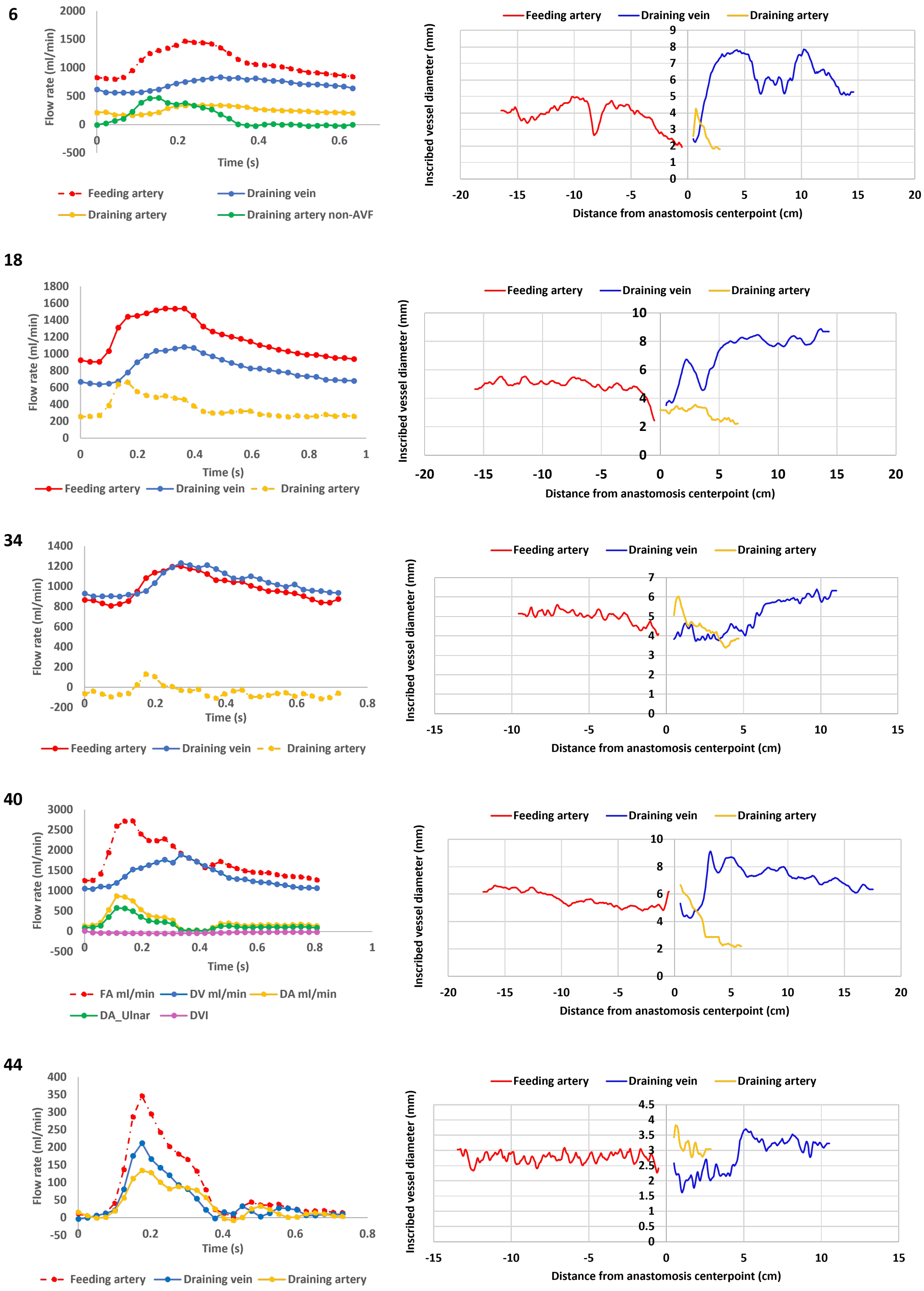

Fig. C.9 Vessel diameter and velocity waveforms and computational domain patches (for cases 6-44)

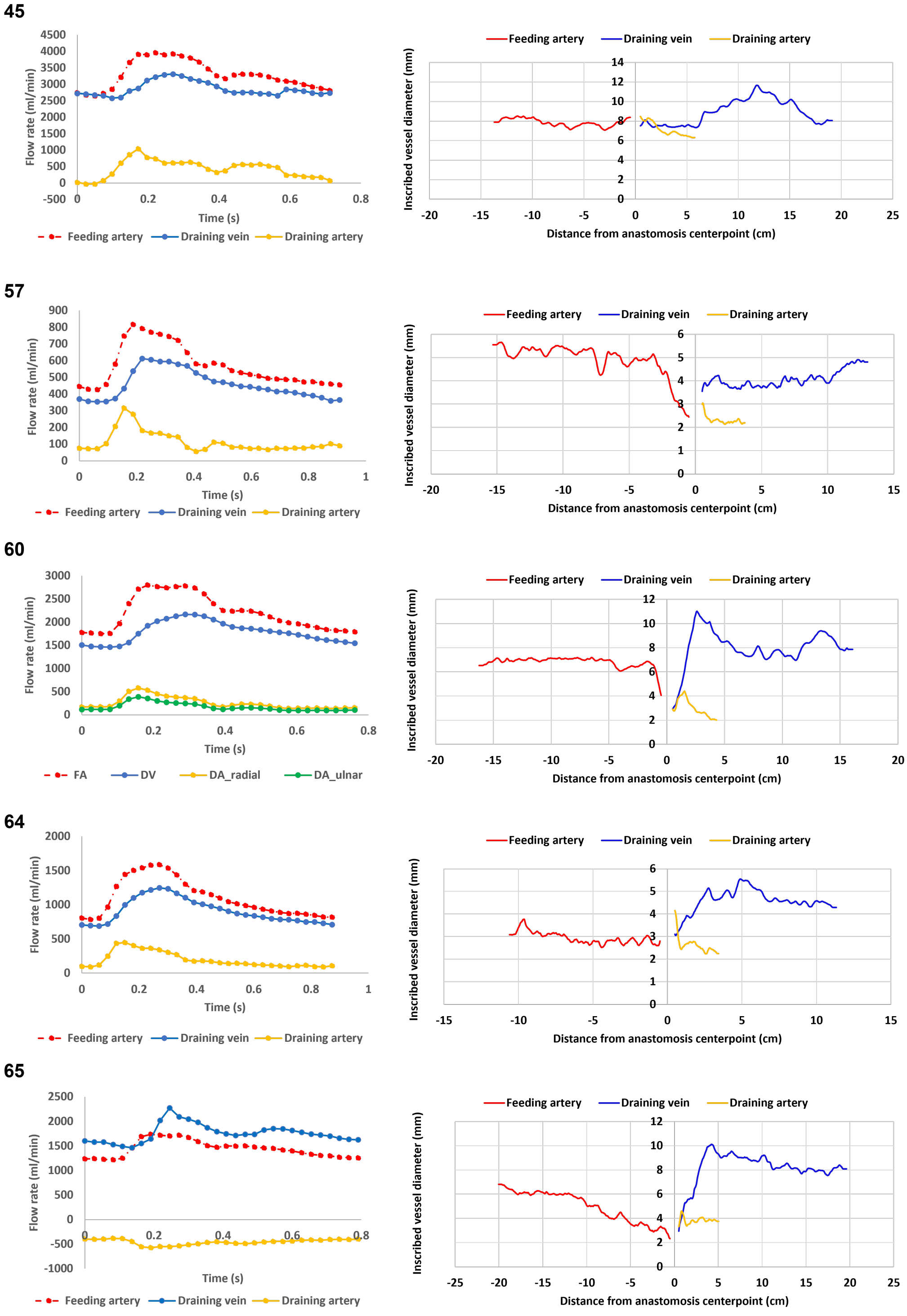

Fig. C.10 Vessel diameter and velocity waveforms and computational domain patches (for cases 45-65)

69

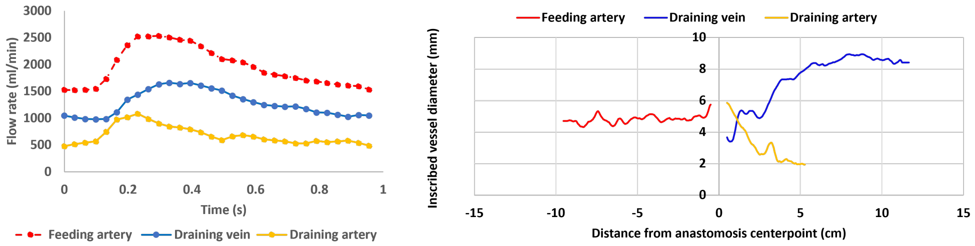

71

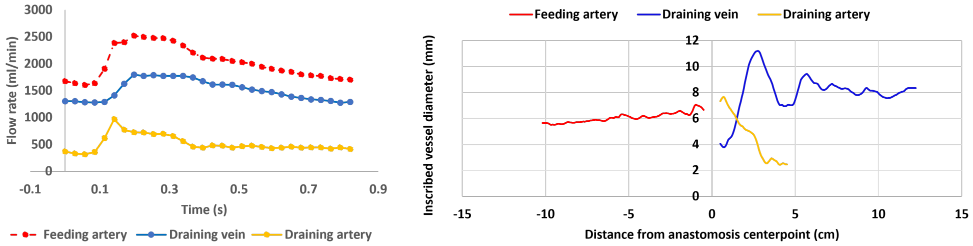

72

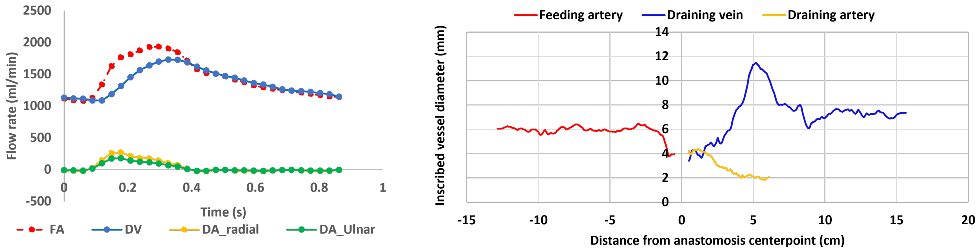

77

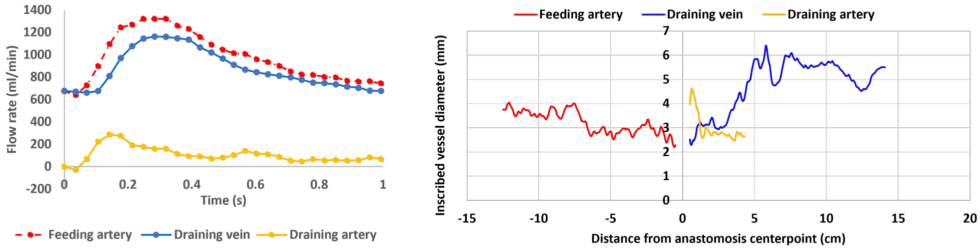

79

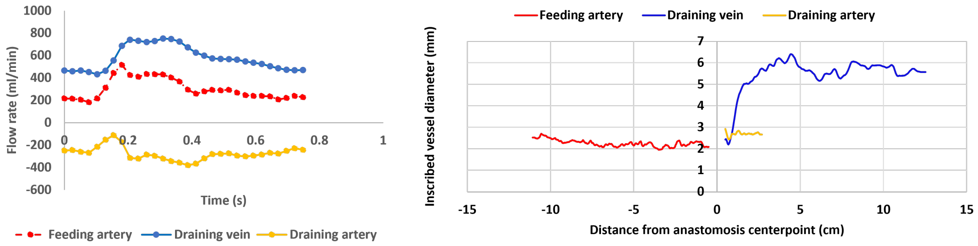

Fig. C.11 Vessel diameter and velocity waveforms and computational domain patches(for cases 69-79)

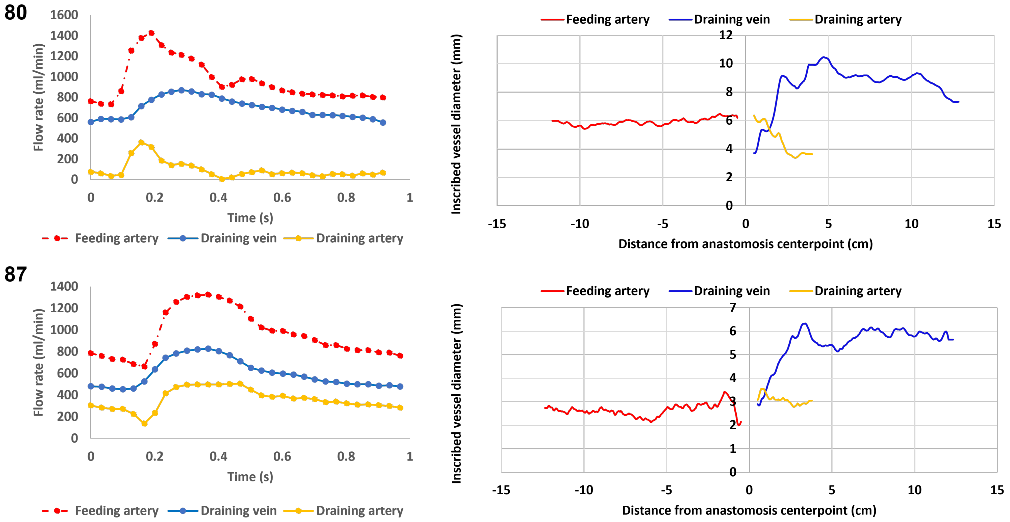

Fig. C.12 Vessel diameter and velocity waveforms and computational domain patches(for cases 80-87)

C.6 AVF contour plots not presented in main body of thesis

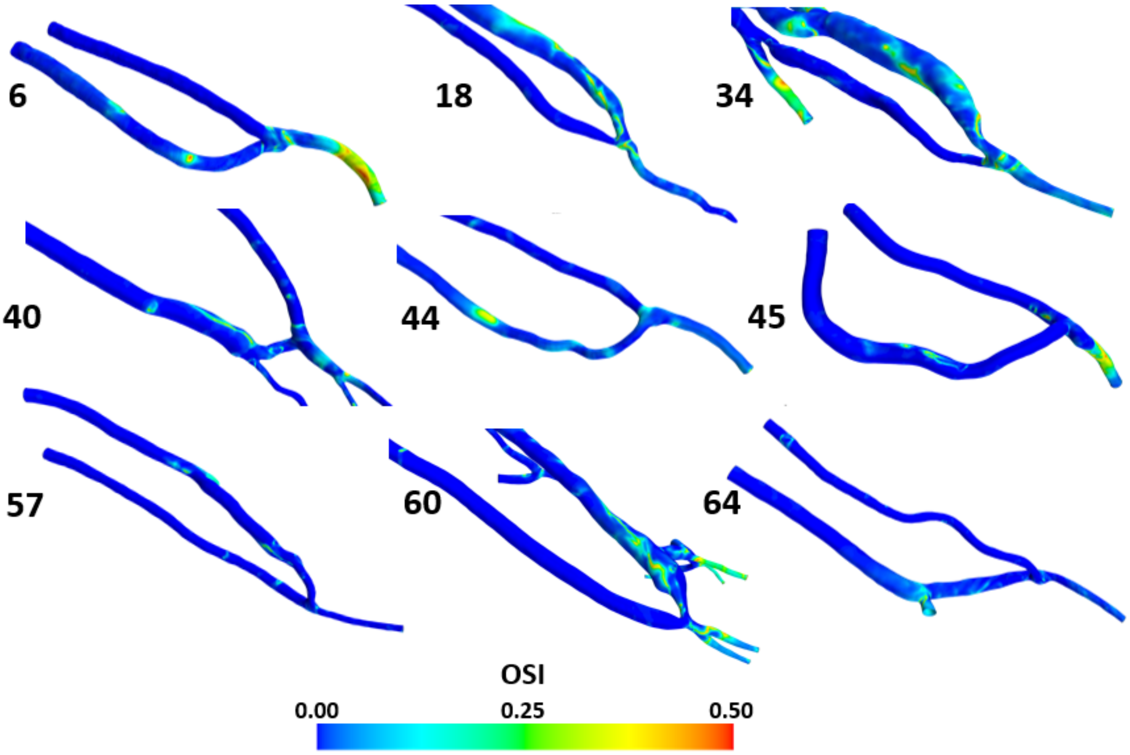

Fig. C.13 OSI contour plots for AVFs for subjects 6-64.

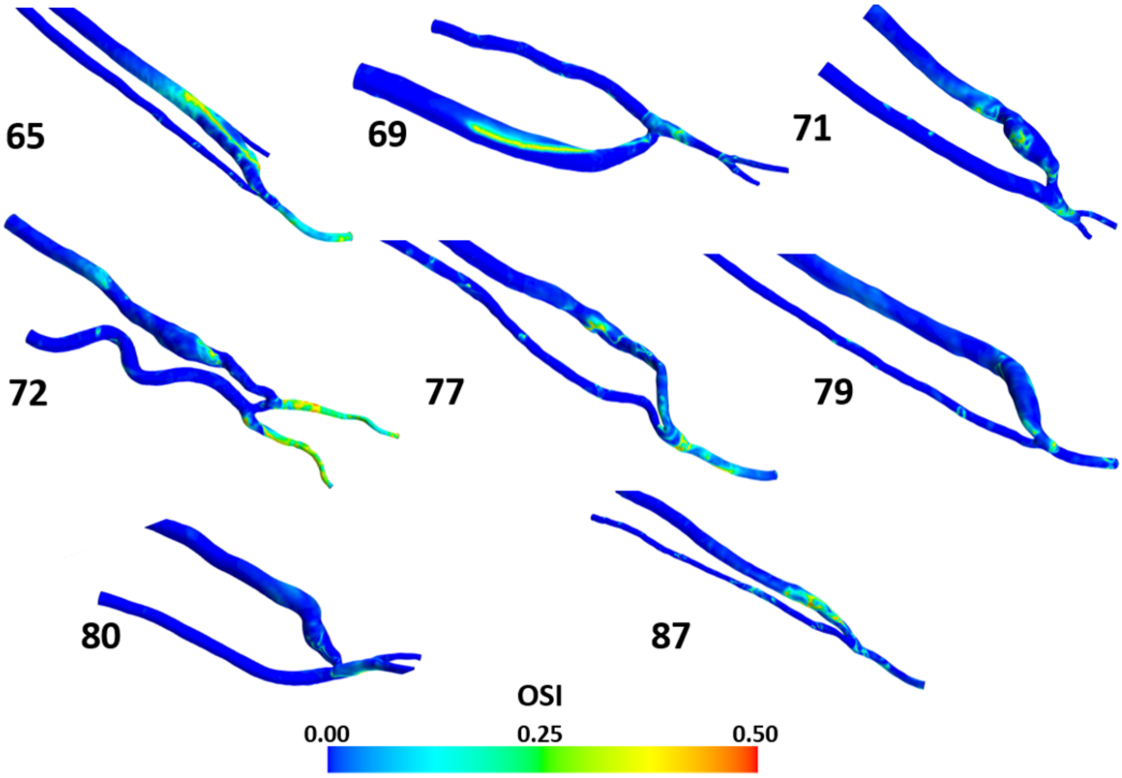

Fig. C.14 OSI contour plots for AVFs for subjects 65-87.

C.7 Further details of cohort in Chapter 4

Table C.2 Cohort information referred to in Chapter 4 and presented within Figs. 4.11-4.12.

FEMRA Dataset	Classification	SBP	HR	Sat O2	BMI	Age	CO (l/min)
45	SucBBF$_A$	151	90	0.96	29.8	50	7.1
69	SucBCF$_A$	158	68	0.94	36.5	69	5.4
40	SucBCF$_A$	194	79	0.98	22.8	56	9.7
71	SucBCF$_A$	120	76	0.99	19.3	43	7.1
60	SucBCF$_A$	134	74	0.97	22.8	41	7.4
57	SucRCF$_A$	139	69	0.97	27.8	71	7.4
87	SucRCF$_A$	141	64	0.96	30.3	55	9.3
34	SucRCF$_A$	157	86	0.99	30.8	68	7.3
18	SucRCF$_A$	180	60	0.95	32	59	5.7
77	SucRCF$_A$	168	52	0.975	29.1	78	5.9
64	SucRCF$_A$	162	64	0.97	25.1	67	9.5
6	SucRCF$_A$	135	90	0.94	31.1	75	10.8
65	SucRCF$_A$	143	75	0.99	18.1	19	5.1
44	UnsucBCF$_A$	146	93	0.95	29.5	64	6.4
80	UnsucBCF$_A$	167	59	0.97	31.7	55	4.4
79	UnsucRCF$_A$	156	79	0.98	27.1	41	10.4
72	UnsucRCF$_A$	166	66	0.95	24.8	75	8.9

Appendix D

Supplementary material for Chapter 5

D.1 Boundary conditions

D.1.1 Prescribed flow-splits

In Chapter 6 there was limited flow data available, which infers the use of ‘flow-splitting’ methods. There are several approaches previously utilised in prior computational haemodynamic studies for assigning outlet flow rates as a percentage of the inlet waveform. Notable examples of this include Murray’s law, where the diameters around bifurcations are computed to estimate flow divisions. A modified version of Murray’s law proposed in Chanafa et al. (2018) [222] was the ‘flow-splitting’ method considered in this research. In this approach the ratio of the daughter vessel diameters is computed against the feeding vessel diameter to allocate a percentage of the flow to each daughter vessel. The flow divisions leading to each outlet are summed to yield the estimate percentage of the inlet waveform at the outlet. However, Murray’s law and such approaches are suited towards to physiologically related flow distributions in the vascular network. The presence of the AVF in the cases presented in Chapter 6, makes these inapplicable.

In order to produce ‘flow-splits’ which account for the presence of the AVF (which produces ‘non-physiological’ flow rates) whilst also producing physioligcally sound split for the rest of the network, a modified ‘flow-split’ method was created in Chapter 5. This method utilised initial flow-split estimates based on values from literature.

D.2 Mesh independence analysis

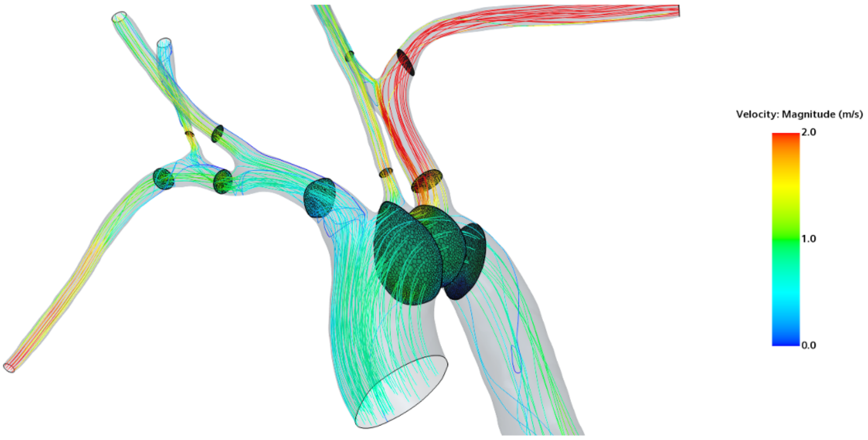

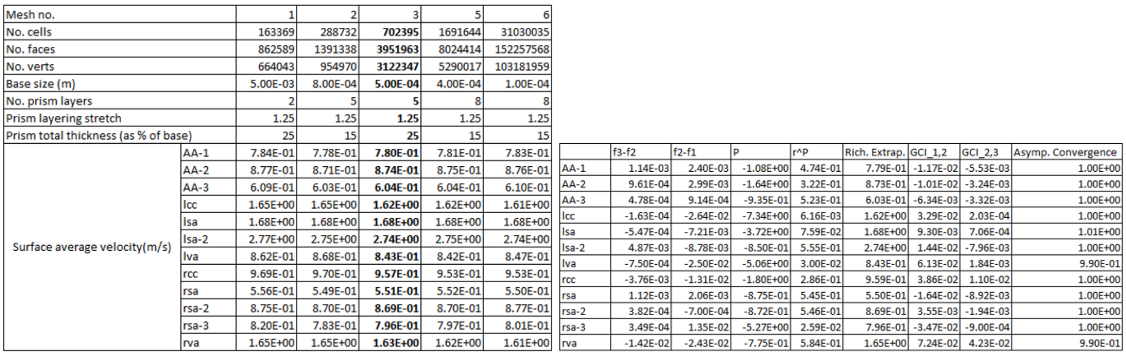

Mesh no.		1	2	3	5	6
No. cells		163369	288732	**702395**	1691644	31030035
No. faces		862589	1391338	**3951963**	8024414	152257568
No. verts		664043	954970	**3122347**	5290017	103181959
Base size (m)		5.00E-03	8.00E-04	**5.00E-04**	4.00E-04	1.00E-04
No. prism layers		2	5	**5**	8	8
Prism layering stretch		1.25	1.25	**1.25**	1.25	1.25
Prism total thickness (as % of base)		25	15	**25**	15	15
Surface average velocity(m/s)	AA-1	7.84E-01	7.78E-01	**7.80E-01**	7.81E-01	7.83E-01
	AA-2	8.77E-01	8.71E-01	**8.74E-01**	8.75E-01	8.76E-01
	AA-3	6.09E-01	6.03E-01	**6.04E-01**	6.04E-01	6.10E-01
	lcc	1.65E+00	1.65E+00	**1.62E+00**	1.62E+00	1.61E+00
	lsa	1.68E+00	1.68E+00	**1.68E+00**	1.68E+00	1.68E+00
	lsa-2	2.77E+00	2.75E+00	**2.74E+00**	2.75E+00	2.74E+00
	lva	8.62E-01	8.68E-01	**8.43E-01**	8.42E-01	8.47E-01
	rcc	9.69E-01	9.70E-01	**9.57E-01**	9.53E-01	9.53E-01
	rsa	5.56E-01	5.49E-01	**5.51E-01**	5.52E-01	5.50E-01
	rsa-2	8.75E-01	8.70E-01	**8.69E-01**	8.70E-01	8.77E-01
	rsa-3	8.20E-01	7.83E-01	**7.96E-01**	7.97E-01	8.01E-01
	rva	1.65E+00	1.65E+00	**1.63E+00**	1.62E+00	1.61E+00

	f3-f2	f2-f1	P	r^P	Rich. Extrap.	GCI_1,2	GCI_2,3	Asymp. Convergence
AA-1	1.14E-03	2.40E-03	-1.08E+00	4.74E-01	7.79E-01	-1.17E-02	-5.53E-03	1.00E+00
AA-2	9.61E-04	2.99E-03	-1.64E+00	3.22E-01	8.73E-01	-1.01E-02	-3.24E-03	1.00E+00
AA-3	4.78E-04	9.14E-04	-9.35E-01	5.23E-01	6.03E-01	-6.34E-03	-3.32E-03	1.00E+00
lcc	-1.63E-04	-2.64E-02	-7.34E+00	6.16E-03	1.62E+00	3.29E-02	2.03E-04	1.00E+00
lsa	-5.47E-04	-7.21E-03	-3.72E+00	7.59E-02	1.68E+00	9.30E-03	7.06E-04	1.01E+00
lsa-2	4.87E-03	-8.78E-03	-8.50E-01	5.55E-01	2.74E+00	1.44E-02	-7.96E-03	1.00E+00
lva	-7.50E-04	-2.50E-02	-5.06E+00	3.00E-02	8.43E-01	6.13E-02	1.84E-03	9.90E-01
rcc	-3.76E-03	-1.31E-02	-1.80E+00	2.86E-01	9.59E-01	3.86E-02	1.10E-02	1.00E+00
rsa	1.12E-03	2.06E-03	-8.75E-01	5.45E-01	5.50E-01	-1.64E-02	-8.92E-03	1.00E+00
rsa-2	3.82E-04	-7.00E-04	-8.72E-01	5.46E-01	8.69E-01	3.55E-03	-1.94E-03	1.00E+00
rsa-3	3.49E-04	1.35E-02	-5.27E+00	2.59E-02	7.96E-01	-3.47E-02	-9.00E-04	1.00E+00
rva	-1.42E-02	-2.43E-02	-7.75E-01	5.84E-01	1.65E+00	7.24E-02	4.23E-02	9.90E-01

Fig. D.1 Mesh independence study for Chapter 5, demonstrated on the test case (subject 65).

D.3 Velocity streamline figures

Velocity streamline contour plots of the flow waveforms induced at peak systole, mid-deceleration, and peak diastole are presented herein in this section.

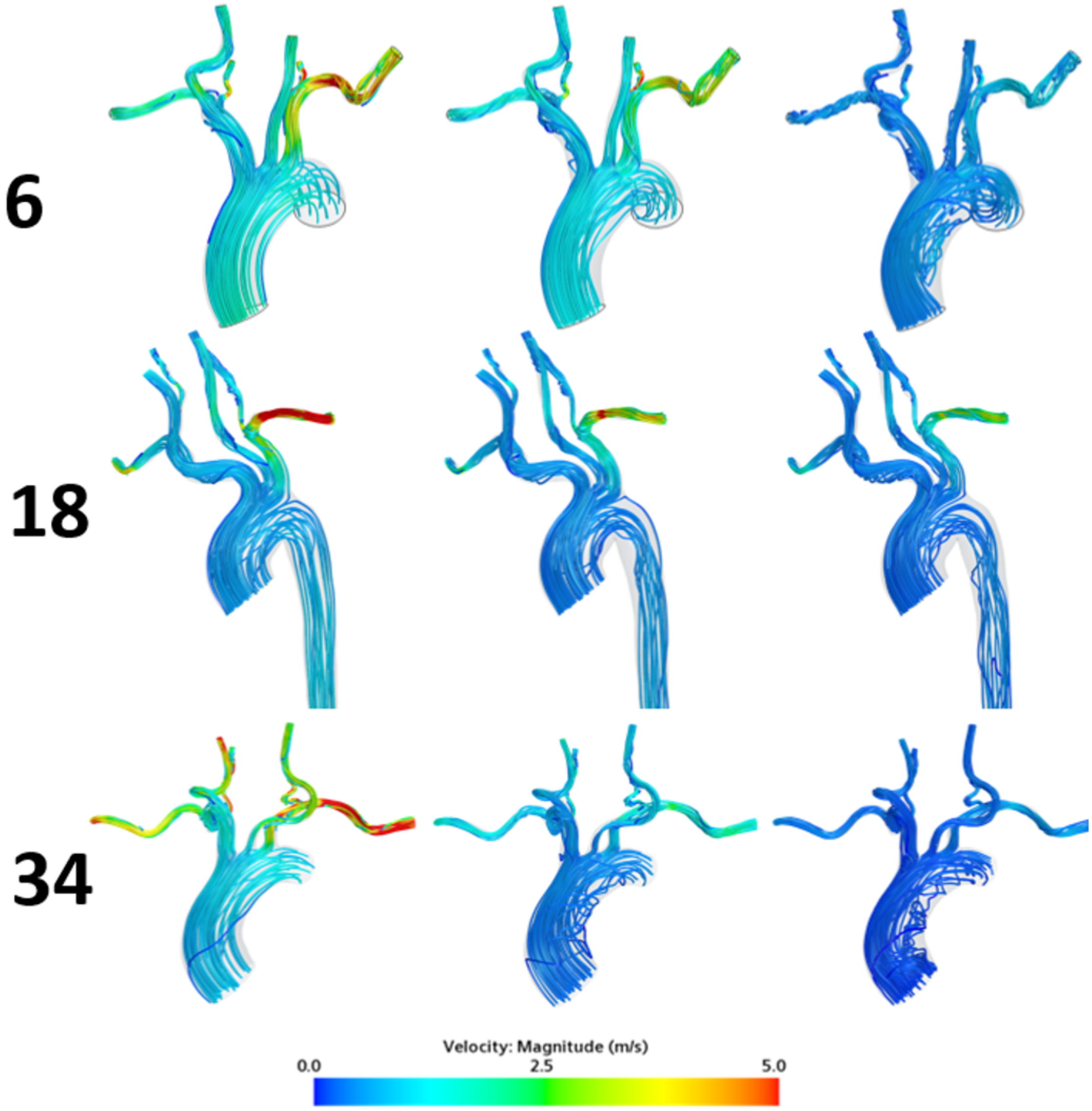

Fig. D.2 Velocity magnitude streamline contour plots for peak systole (left), mid-deceleration (centre), and peak diastole (right) for datasets 6-34.

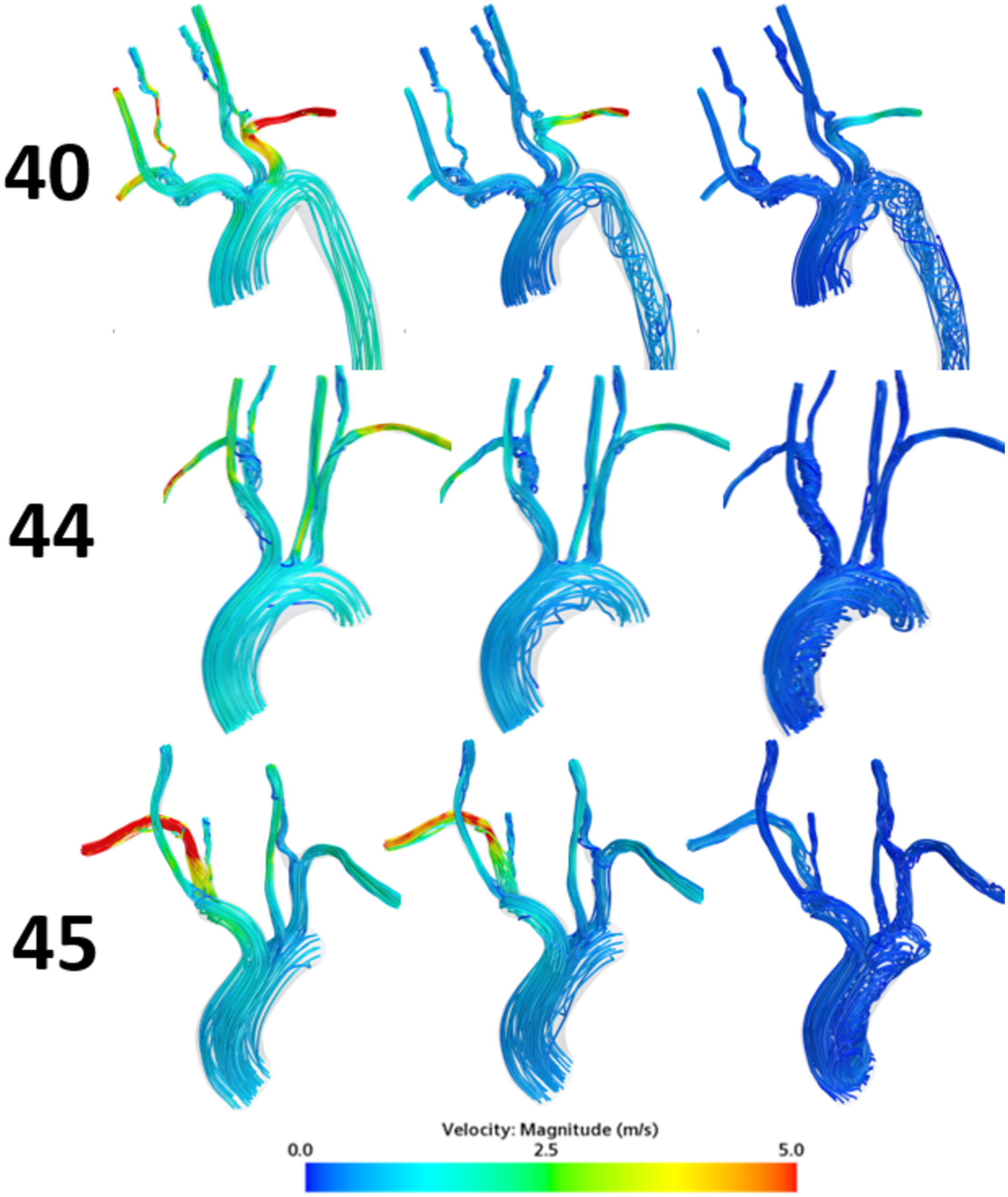

Fig. D.3 Velocity magnitude streamline contour plots for peak systole (left), mid-deceleration (centre), and peak diastole (right) for datasets 40-45.

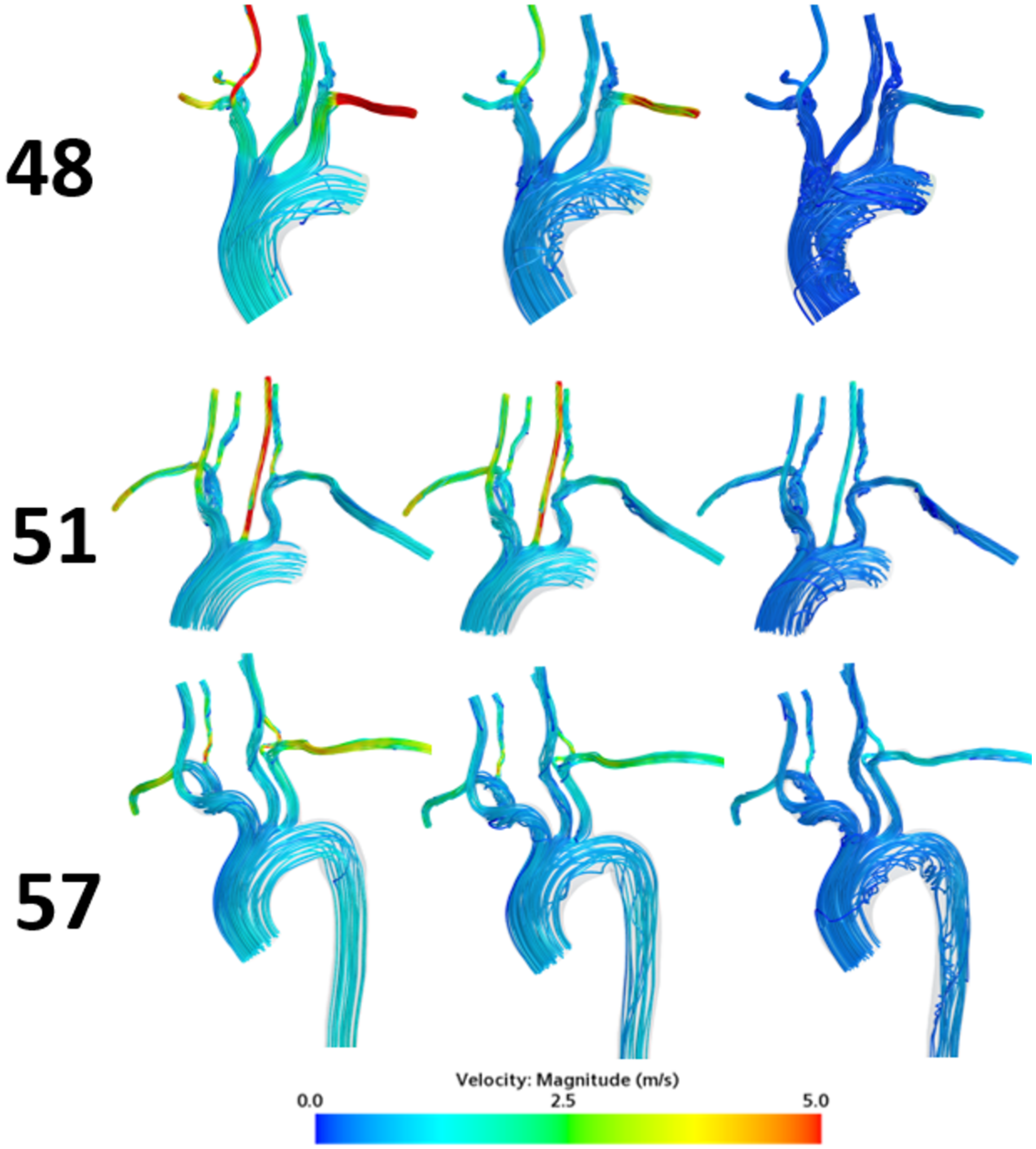

Fig. D.4 Velocity magnitude streamline contour plots for peak systole (left), mid-deceleration (centre), and peak diastole (right) for datasets 48-57.

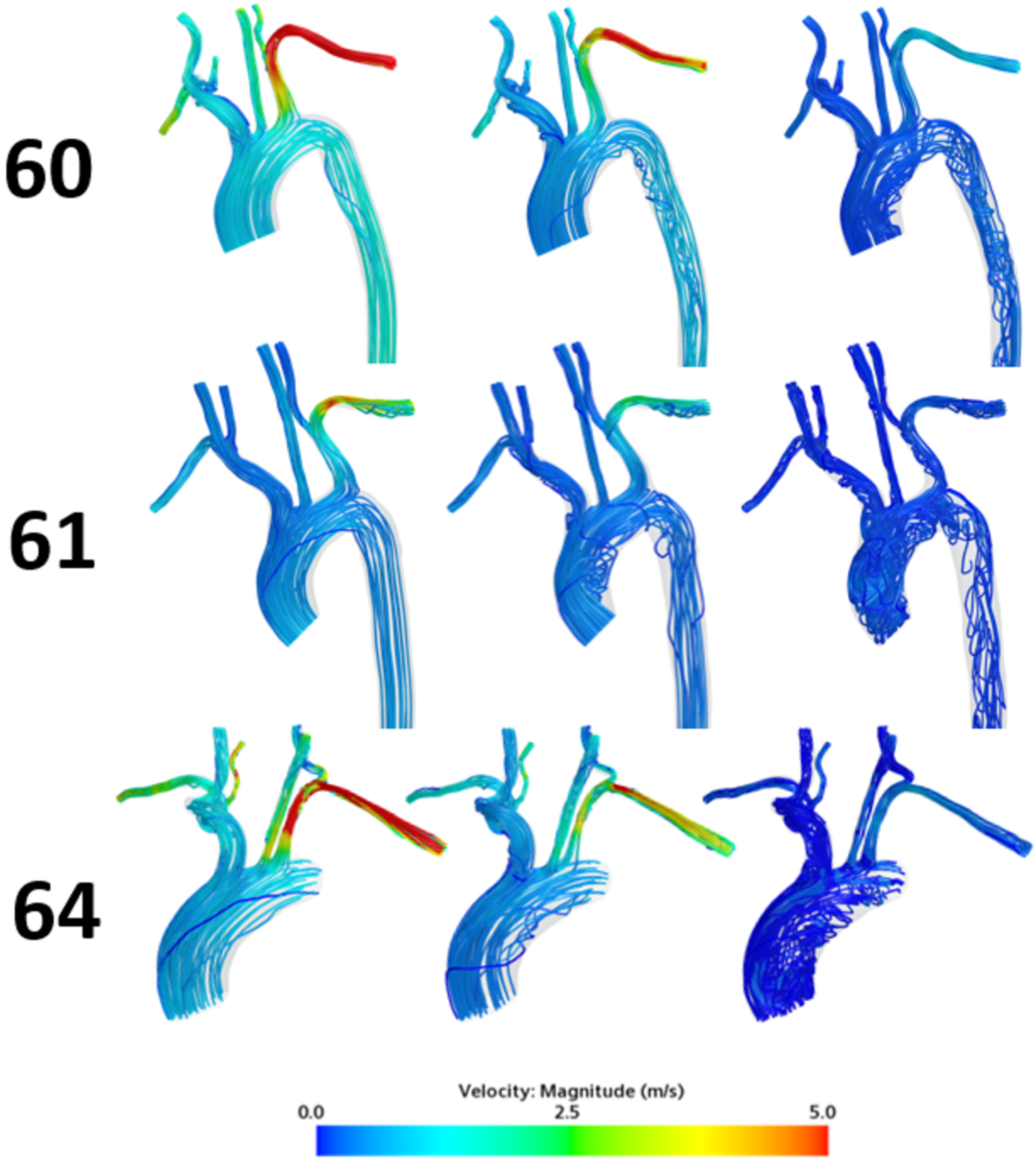

Fig. D.5 Velocity magnitude streamline contour plots for peak systole (left), mid-deceleration (centre), and peak diastole (right) for datasets 60-64.

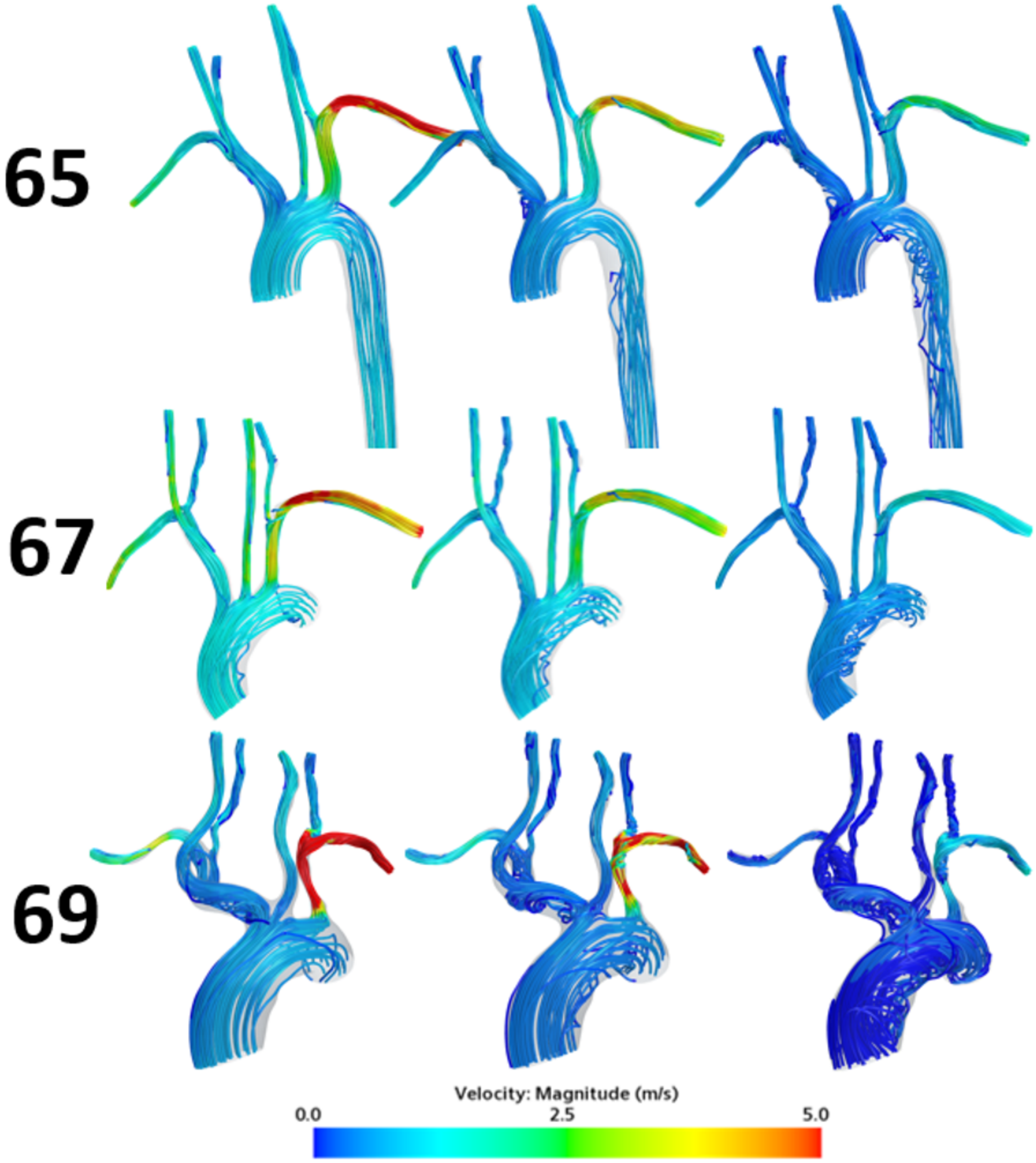

Fig. D.6 Velocity magnitude streamline contour plots for peak systole (left), mid-deceleration (centre), and peak diastole (right) for datasets 65-69.

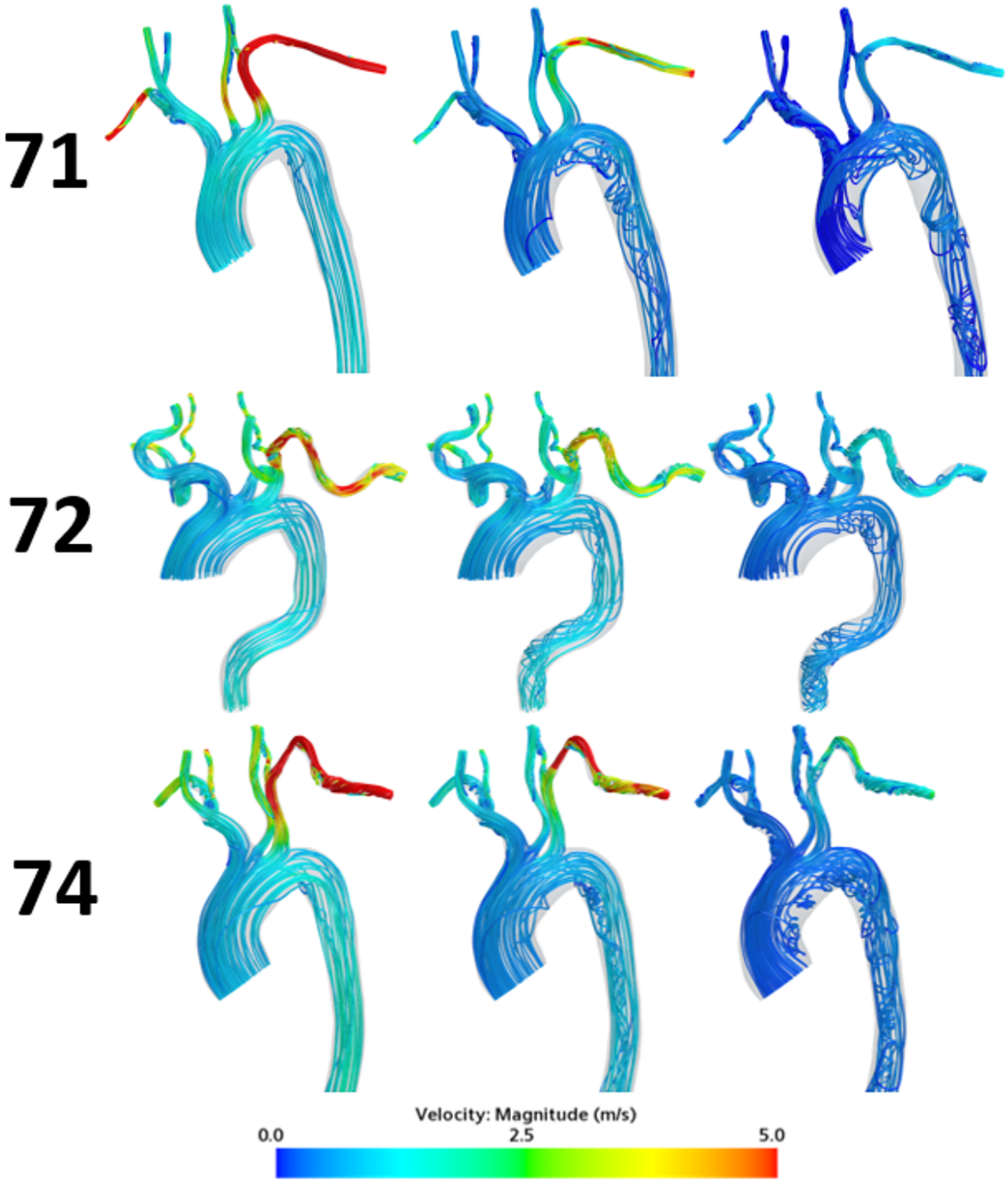

Fig. D.7 Velocity magnitude streamline contour plots for peak systole (left), mid-deceleration (centre), and peak diastole (right) for datasets 71-74.

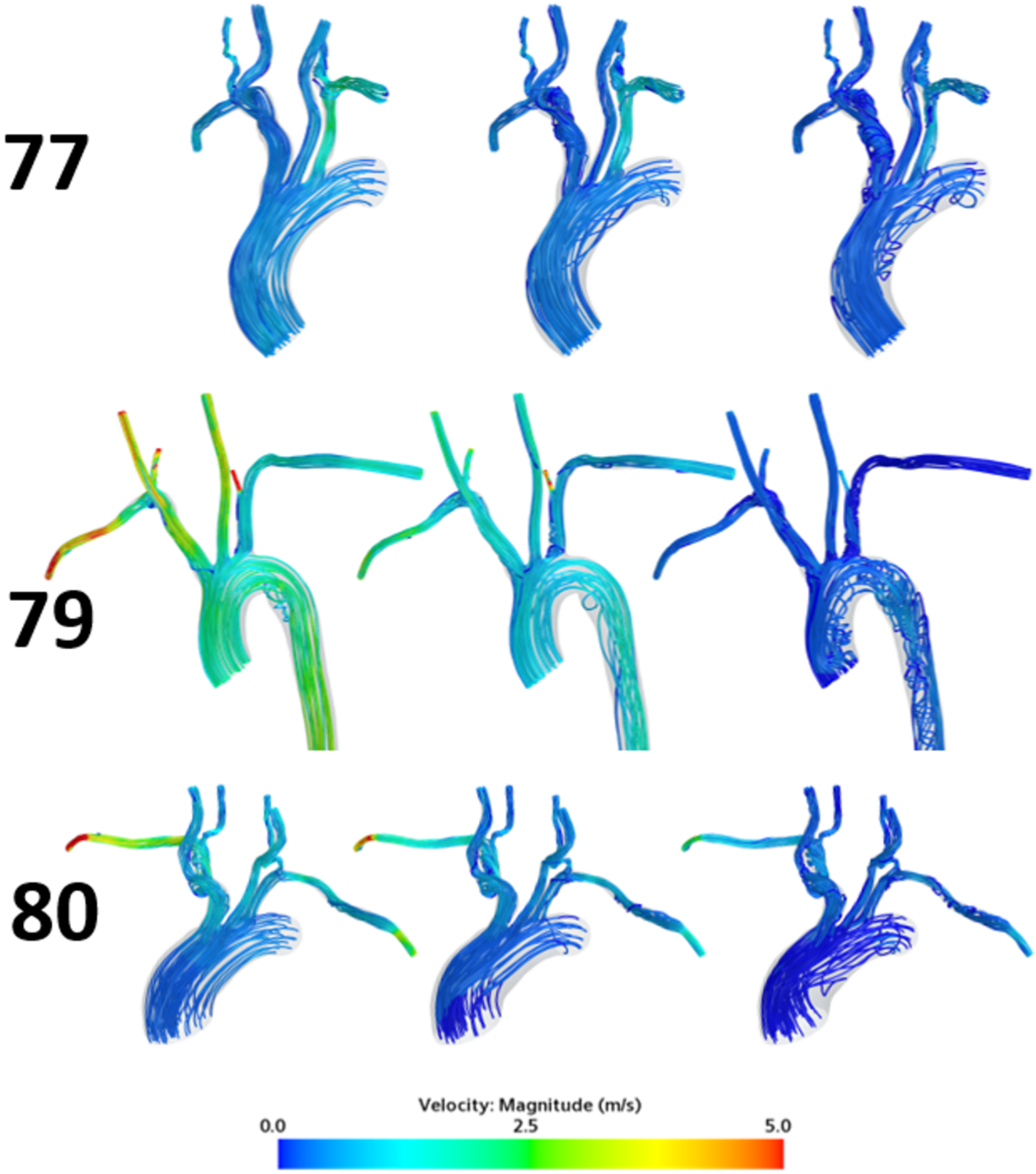

Fig. D.8 Velocity magnitude streamline contour plots for peak systole (left), mid-deceleration (centre), and peak diastole (right) for datasets 77-80.

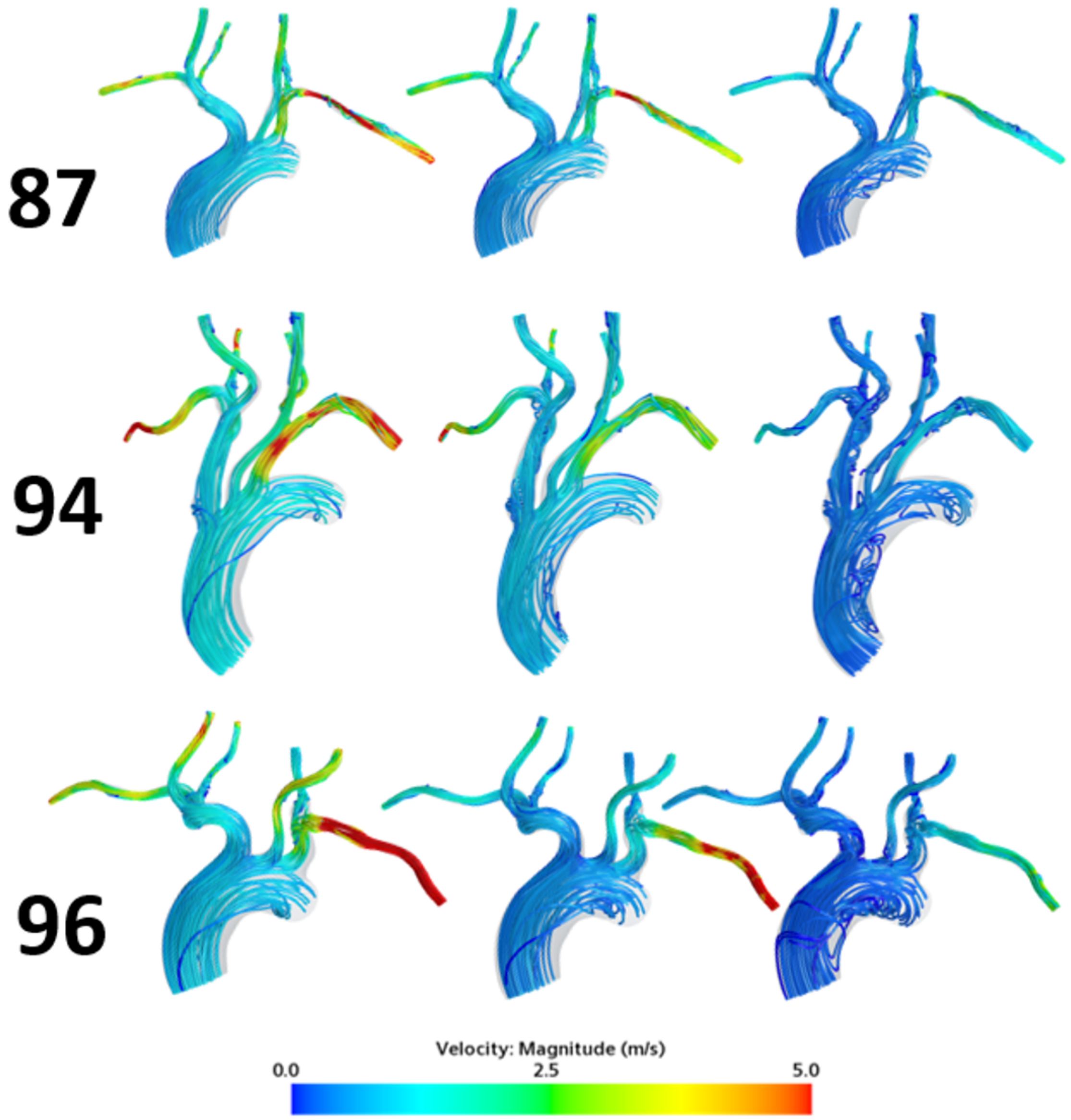

Fig. D.9 Velocity magnitude streamline contour plots for peak systole (left), mid-deceleration (centre), and peak diastole (right) for datasets 87-96.

D.4 Pressure figures

Normalised pressure figures at peak-systole for the geometries presented in Chapter 5 are presented herein, where normalised pressure is calculated through dividing pressure by half of the fluid density ($\frac{P}{0.5\rho}$).

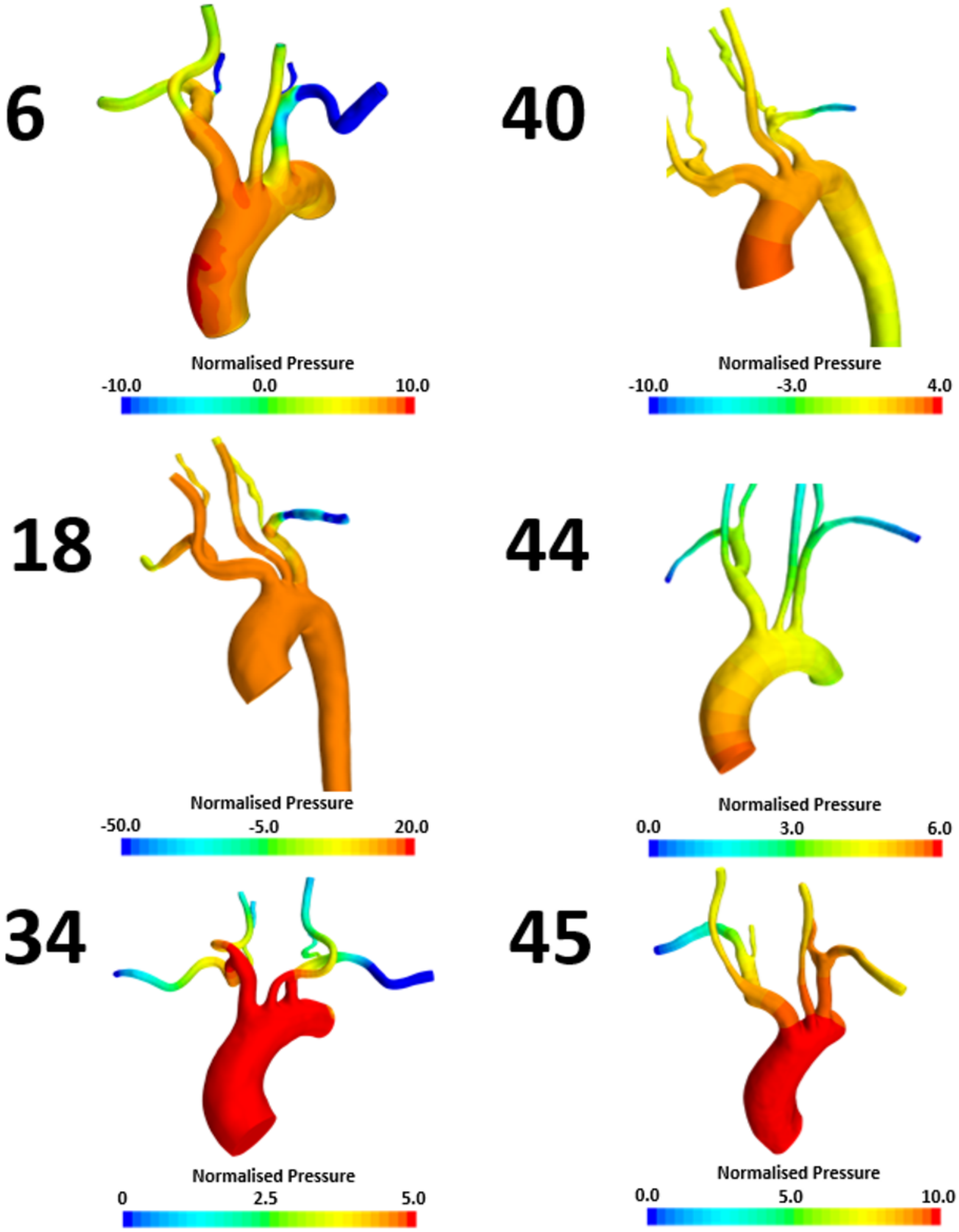

Fig. D.10 Normalised pressure contour plot at peak systole for datasets 6-45.

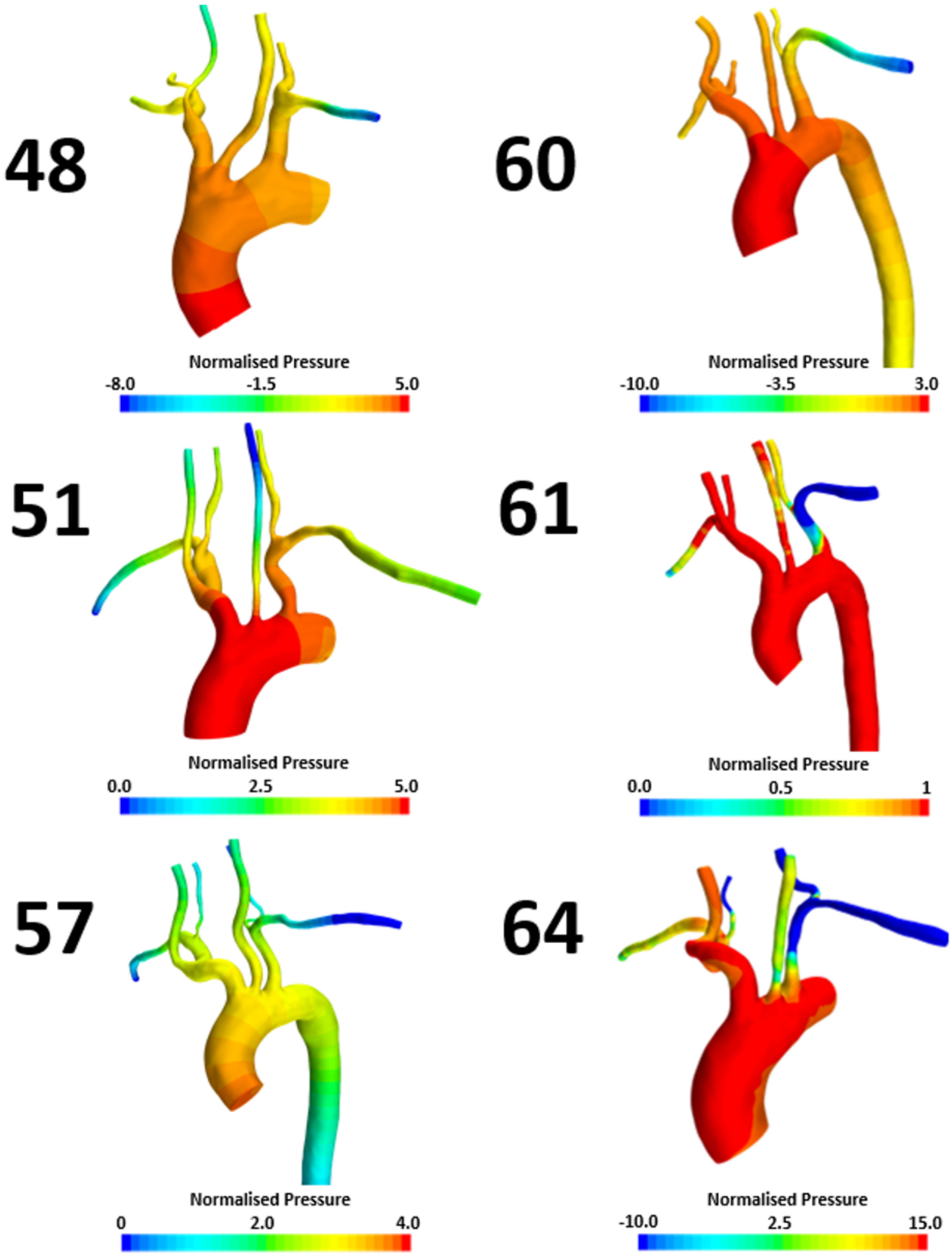

Fig. D.11 Normalised pressure contour plot at peak systole for datasets 48-64.

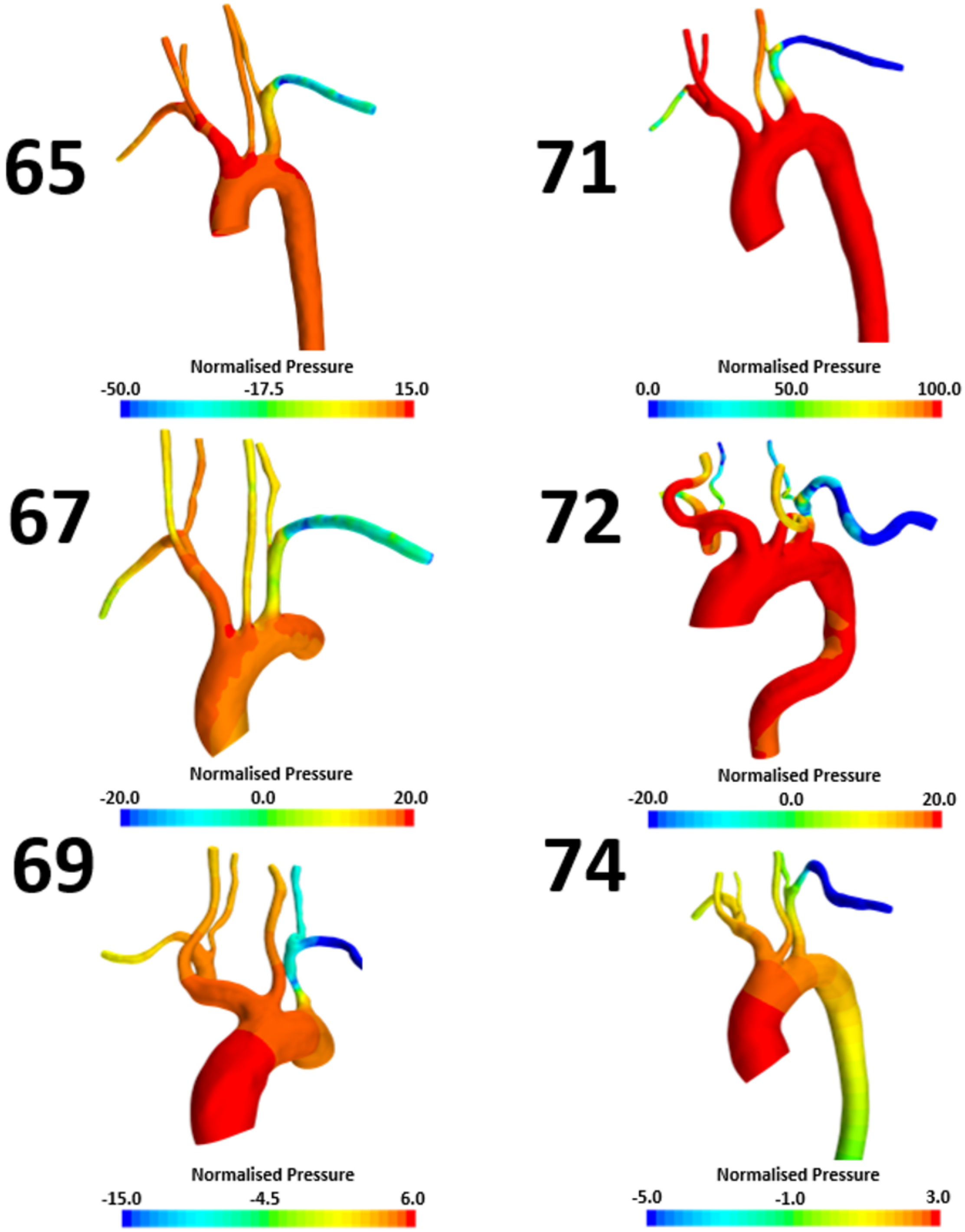

Fig. D.12 Normalised pressure contour plot at peak systole for datasets 65-74.

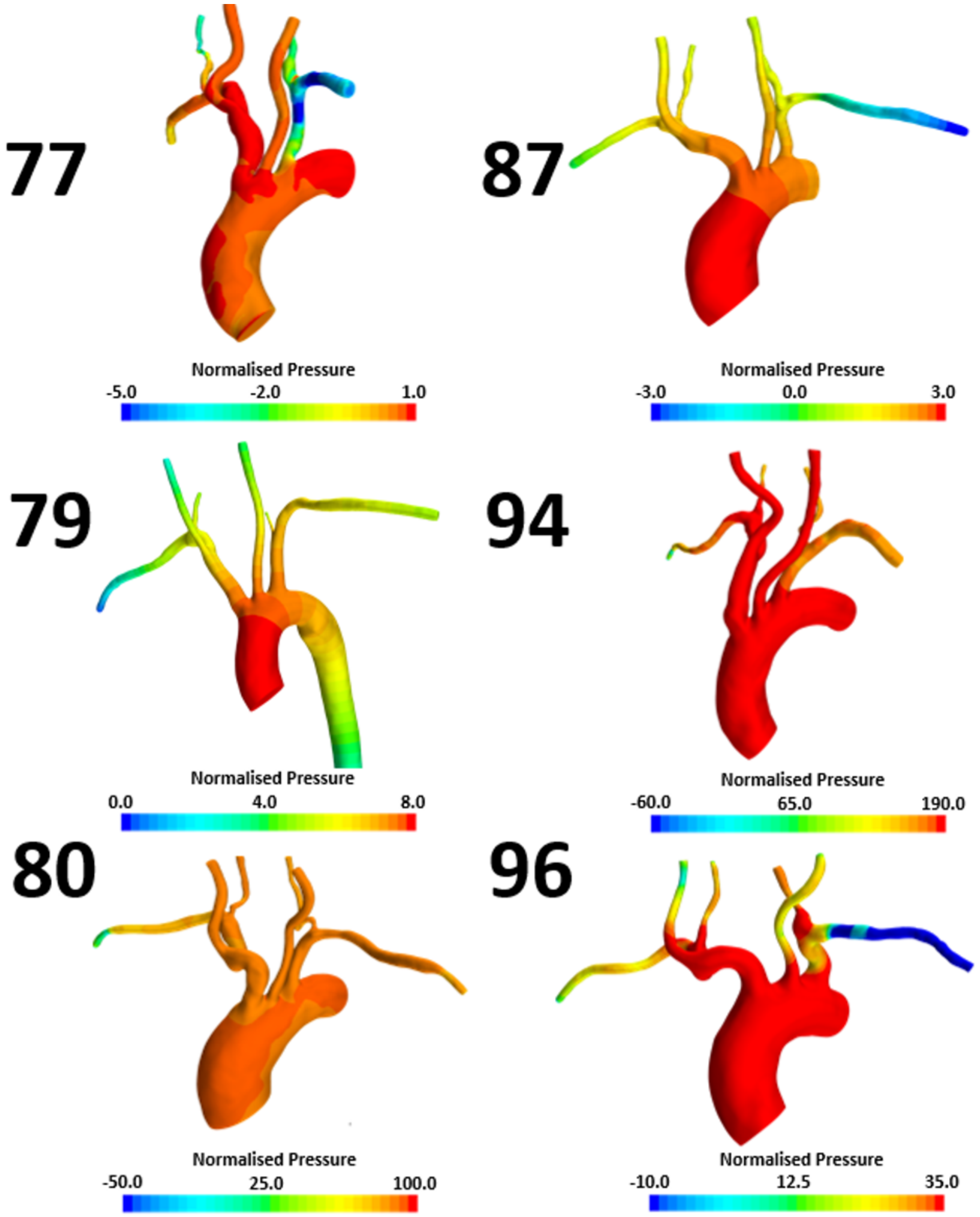

Fig. D.13 Normalised pressure contour plot at peak systole for datasets 77-96.